Revealing Interfacial Reactions and Charge Transfer Kinetics in Electrochemical Energy Storage and Conversion

By

Yirui Zhang

M.S. Mechanical Engineering
Massachusetts Institute of Technology, 2019

Submitted to the Department of Mechanical Engineering
in Partial Fulfillment of the Requirements for the Degree of

Doctor of Philosophy

at the

MASSACHUSETTS INSTITUTE OF TECHNOLOGY

February 2023

Author: ……
Department of Mechanical Engineering
September 15, 2022

Certified by: ……
Prof. Yang Shao-Horn
JR East Professor of Engineering
Thesis Supervisor

Accepted by:……
Prof. Nicolas Hadjiconstantinou
Professor of Mechanical Engineering
Graduate Officer, Department of Mechanical Engineering

Revealing Interfacial Reactions and Charge Transfer Kinetics in Electrochemical Energy Storage and Conversion

by

Yirui Zhang

Submitted to the Department of Mechanical Engineering
on September 15, 2022 in Partial Fulfillment of the
Requirements for the Degree of Doctor of Philosophy in
Mechanical Engineering

ABSTRACT

Climate change demands the development of clean energy technologies. Renewable energy sources such as solar or wind energy are intermittent, and it is necessary to develop advanced energy storage and conversion devices to complete the sustainable eco-system, where Li-ion batteries and fuel cells promise a bright future. Batteries and fuel cells also play essential roles in electrifying transportation in replacement of internal combustion engines. Central to these electrochemical systems is the electrode-electrolyte interface, where (electro)chemical surface reactions or intercalation reactions occur, and its thermodynamic and kinetic properties determine the energy density, power density, and lifetime of the electrochemical devices. However, the molecular structures at the interface and how they promote or suppress the desired reactions remain unclear. Furthermore, microscopic-level understandings of reaction mechanisms and electrochemical processes are still lacking, hindering the rational design of electrode-electrolyte interfaces to improve the performance of electrochemical devices.

This thesis focuses on the fundamental understanding of the interfacial (electro)chemical reaction mechanisms at the molecular level and charges transfer kinetics at the electrified interfaces. First, an *in situ* Fourier-transform infrared spectroscopy (FT-IR) method was developed to examine the parasitic reactions between carbonate electrolytes and lithium nickel, manganese and cobalt oxides (NMC) in Li-ion batteries, and unique evidence for dehydrogenation reactions on Ni-rich NMC was revealed, which accounted for interface impedance build-up and battery capacity fading. Based on the proposed mechanism, strategies to suppress battery degradation were further demonstrated and discussed. Next, the kinetic mechanism for Li-ion intercalation was investigated, and experimental evidence from a charge-adjusted electrochemical method showed that ion intercalation occurs by coupled ion-electron transfer (CIET), which governs the current-dependent maximum capacity and power density of intercalation batteries. Further, the thesis extended *in situ* interface characterization and kinetic models to electrocatalytic reactions central to fuel cell technologies. Protic ionic liquids with different acid dissociation constants in an interfacial layer were found to enhance the oxygen-reduction reaction (ORR), attributed to strengthened hydrogen bonds between ORR products and ionic liquids, revealed by *in situ*

surface-enhanced infrared absorption spectroscopy (SEIRAS) and density functional theory (DFT) calculations. Promoting hydrogen bonding between interfacial water molecules also facilitated proton-coupled electron transfer (PCET) kinetics, resulting in favorable hydrogen evolution reaction (HER) in controllable organic confinements. This thesis has laid a solid foundation for the rational design of electrochemical interfaces employing the physical chemistry of electrodes and electrolytes, for next-generation electrochemical storage devices with improved energy and power density and cycle life.

Thesis Supervisor:
Professor Yang Shao-Horn
JR East Professor of Engineering
Mechanical Engineering, Materials Science and Engineering, MIT

Thesis Committee Members:
Professor Martin Z. Bazant
E. G. Roos (1944) Professor of Chemical Engineering
Professor of Mathematics
Chemical Engineering, Mathematics, MIT

Professor Jeffrey C. Grossman
Morton and Claire Goulder and Family Professor in Environmental Systems
Professor of Materials Science and Engineering
Materials Science and Engineering, MIT

Professor Kripa Varanasi
Professor of Mechanical Engineering
Mechanical Engineering, MIT

Acknowledgement

The work in this thesis would not have been possible without the support of all the wonderful people, whom I have worked with and who accompanied me in the past five years.

Firstly, I am incredibly grateful to my advisor, Prof. Yang Shao-Horn, for her guidance throughout my research and for all the merits I have learnt from her as a researcher. Thank you for providing me with the opportunity and freedom to work on a wide range of interesting research projects. Her passion to keep learning new knowledge and rigor for high standards of research have undoubtedly influenced me in my professional growth.

I would also like to express my great gratitude towards Prof. Martin Z. Bazant, whom I have worked with closely and who is on my thesis committee. Thank you for all the insights, valuable guidance, and supports on my research. I am also grateful to Prof. Jeffrey C. Grossman and Prof. Kripa Varanasi for serving on my thesis committee and for providing constructive feedback throughout my thesis research.

During my PhD, I have been privileged to work with and learn from many supportive and amazing colleagues in Electrochemical Energy Laboratory. I would like to thank Prof. Ryoichi Tatara for teaching me electrochemistry experiments and always providing his help generously, Prof. Livia Giordano, Dr. Shuting Feng, and Dr. Soo Kim for teaching me calculations, Prof. Yu Katayama for introducing me to FT-IR, Dr. Dimitrios Fraggedakis for sharing his knowledge and helping me understand theories with patience, and Prof. Tao Wang and Dr. Botao Huang for introducing me to electrocatalysis research.

Many other people in the lab have also supported and helped me intellectually and personally. I would like to thank Dr. Yang Yu, Dr. Yunguang Zhu, Daniel J. Zheng, Hongbin Xu, Daniel Wang, Dr. Jen-Hung Fang, Dr. Nicolò Minafra, Dr. Bin Liu, Dr. Thaneer Narayanan, Dr. Graham Leverick, Dr. Abhishek Aggarwal, Dr. Bryce Tappan, Dr. Kiarash Gordiz, Dr. Benjamin Paren, Dr. Yaolin Xu, Dr. Sunmoon Yu, Dr. Cristina Grosu, Dr. Eva Mikaela Gorlin, Jame Guangwen Sun, Christian Plaza-Rivera, Dr. Pjotrs Zguns, Dr. Kuei-Lin Chan, Dr. Shuai Yuan, Dr. Bo Qiao, Dr. Jeff Lopez, Michael Stolberg, Dr. Reshma R. Rao, Dr. Jonathan Hwang, Dr. Karthik Akkiraju, Dr. Muy Sokseiha, Dr. Nenian Charles, Dr. Dongwook Lee, Dr. Chaoyu Li, Christopher T Mallia, as well as Dimitrios, Botao, Tao, Ryoichi, Shuting, and Yu, with many of whom we have become very close friends. Also thank you to all other members in EEL who have provided me with a wonderful environment for research.

I would like to acknowledge our collaborators outside the lab, including Dr. Weijiang Xue, Dr. Tao Gao, and Debbie Zhuang for the amazing collaborations, our industrial collaborators Dr. Ryan Stephens and Dr. Filippo Maglia for the fruitful discussions and their insights from the industrial perspective, and Shell and BMW who funded my research. Furthermore, the research was enabled by the contribution of undergraduate researchers that I have had the privilege to mentor, including Sravani Duggirala, Tomasz J Slusarczyk, Eryn Cornelius, and Leah Soldner.

In addition, I am grateful to many people in the department who have supported my PhD study through their dedication and generous help. Dr. Sarah McKeever and Abby Reynolds have supported our lab administration and thank you Sarah for helping with all the applications! Leslie and Saana have been great Grad Officers that we can rely on. Prof. Ming Guo, Prof. Betar Gallant, and Prof. Carlos Portela have generously provided me with suggestions and discussions on my future research and careers.

I would like to thank my friends and life mentors in Boston and far away who have accompanied me spiritly in this journey: Dr. Maureen Reitman, Lu Mi, Sijie Chen, Xiaotong Zhang, Qian Li, Jinwen Zhang, Xinjian Shi, and many others. Further, I would like to thank my undergraduate advisors Prof. Liran Ma, Prof. Tairan Fu, and Prof. Dameng Liu (Tsinghua University), Prof. David Bogy (UC Berkeley), and Prof. Xiaolin Zheng (Stanford), for leading me into research, stimulating my interests, and making it possible for me to come to MIT.

Last but not the least, many thanks to my boyfriend, Jiayue Wang, for supporting me and making my life so joyful. And I want to send my love and deepest thanks to my parents, Yanling Liu and Yufeng Zhang, for their continued love and support, devotion and encouragements, as well as my aunts. I could never thank them enough throughout the journey.

Table of Contents

Chapter 1. Introduction

1.1 Clean Energy Technology and Renewables

Greenhouse gas emissions have increased sharply since the 1900s, primarily from fossil fuel combustion and industrial processes[1], and climate change demands the development of clean energy technologies. Affordable and clean energy is also among the United Nations' 17 sustainable development goals to transform our world[2]. Under current and planned policies, energy-related CO_2 emissions would increase to at least 35 Gt in 2050 [3], while emissions need to drop to 9.7 Gt in 2050 [3] to meet the target of limiting global average temperature increase to below 2 °C [4]. To accomplish the reduction in emission, the share of renewable energy in total primary energy supply would need to rise from 14% in 2021 to 63% in 2050 [3]. It is therefore essential to scale up renewable energy to sharply reduce energy-related CO_2 emissions.

Renewable energy sources, including solar or wind energy, are intermittent, which means that the time period that electricity can be generated is limited. To overcome the intermittency, it is necessary to develop advanced energy storage and conversion devices to complete the sustainable eco-system. Among different energy storage and conversion technologies, Li-ion batteries and fuel cells provide higher energy and power densities compared to conventional lead-acid or Ni-MH batteries[5,6] (Fig. 1-1), promising a bright future of renewable energies to replace fossil fuels. Batteries and fuel cells can not only serve as critical components in stationary grid applications to store excess energy when solar panels are producing electricity and feed it into the grid when they are not[7,8], but they also play essential roles in electrifying transportation and replacing conventional internal

combustion engines, which reduces the emissions that contribute to climate change and smog.[9] However, current Li-ion batteries and fuel cell technologies still pose challenges to realizing the energy transition due to either high cost[10], poor cycling durability[11], or low efficiency[12]. It is therefore critical to develop better energy devices with cheaper materials, longer lifetimes, and higher energy and power densities.

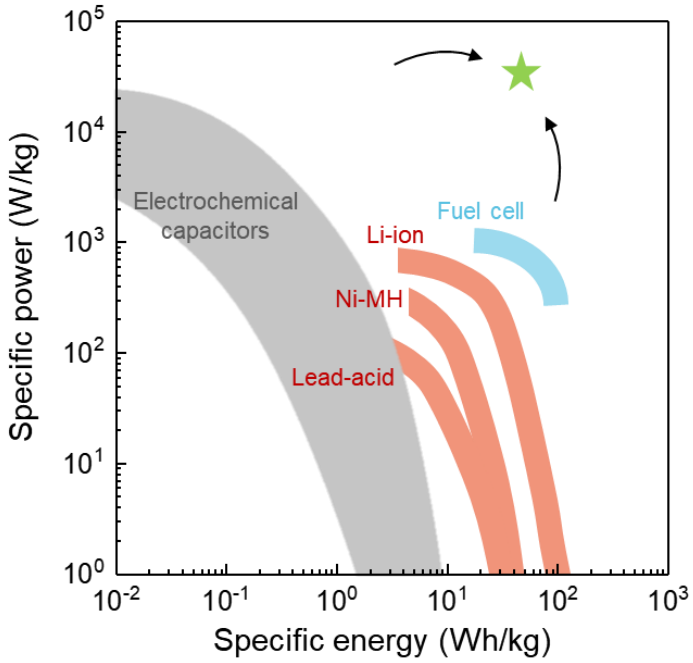

Fig. 1-1 Ragone plot of specific power density versus energy density of various storage methods, including electrochemical capacitors (grey), rechargeable batteries (red), and fuel cells (blue). Data from refs. [5,6,13–15]

1.2 Li-ion batteries and current challenges[1]

As recognized by the 2019 Nobel Prize in Chemistry to Goodenough, Whittingham and Yoshino, Li-ion batteries have already revolutionized portable electronics and are poised

[1] Reproduced in part, with permission from Zhang, Y., Katayama, Y., Tatara, R., Giordano, L., Yu, Y., Fraggedakis, D., Sun, J.G., Maglia, F., Jung, R., Bazant, M.Z. and Shao-Horn, Y., 2020. Revealing electrolyte oxidation via carbonate dehydrogenation on Ni-based oxides in Li-ion batteries by in situ Fourier transform infrared spectroscopy. *Energy & Environmental Science*, 13(1), pp.183-199. Copyright © The Royal Society of Chemistry 2020

to enable widespread electrified transportation[16]. They function by shuttling Li-ions and electrons between two electrodes, the positive electrode (or commonly called as "cathode") and negative electrode (or "anode"), Fig. 1-2. The positive electrode is usually made of lithium transition metal oxide in a layered structure (such as $LiCoO_2$), or lithium iron phosphate ($LiFePO_4$) of an olivine type structure. The negative electrode is usually graphite (LiC_6) with a layered structure in commercial applications. Both electrodes are Li-ion hosts, where Li-ions are able to intercalate into and de-intercalate from the crystal structures. The liquid electrolyte in between is usually a mixture of organic carbonates, such as ethyl methyl carbonate (EMC) and ethylene carbonate (EC), with Li-salts. It is ionically conducting while electronically insulating, serving as a media where Li-ions travel back and forth between the two electrodes. During discharging, Li-ion de-intercalates from the negative electrode, travels through the electrolyte, and intercalates into the positive electrode; at the same time, same charge amount of electrons flow through the outside circuit from negative electrode to the positive electrode. The overall cell reaction is as follows:

$$LiMO_2 + C_6 \underset{\text{discharging}}{\overset{\text{charging}}{\rightleftharpoons}} Li_{1-x}MO_2 + Li_xC_6$$

There is an increasing need to develop cheaper and higher energy density batteries due to some limitations of conventional Li-ion batteries. For instance, $LiCoO_2$ positive electrode materials rely heavily on cobalt, which is not only expensive but also has supply chain and mining issues.[17] $LiFePO_4$ is cheaper yet having much lower energy densities compared to layered oxides. Recent developments have focused on a family of layered oxide materials

$LiNi_xMn_yCo_{1-x-y}O_2$ (NMC), which provide high capacities and potentially lower costs for use in electric vehicles.[18–22] Increasing Ni content in NMC from $LiNi_{1/3}Co_{1/3}Mn_{1/3}O_2$ (NMC111), $LiNi_{0.6}Co_{0.2}Mn_{0.2}O_2$ (NMC622) to $LiNi_{0.8}Co_{0.1}Mn_{0.1}O_2$ (NMC811) can greatly increase initial discharge capacities[11,18,19]; however, the capacity retention and energy density decrease significantly during cycling for Ni-rich materials[11], and the cycle life is much shorter.

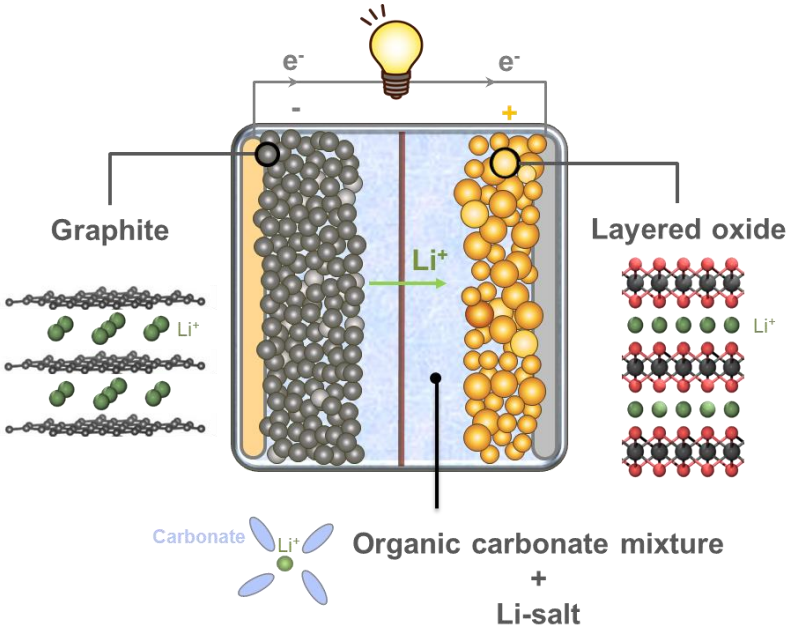

Fig. 1-2: Components in Li-ion batteries and schematics during discharging.

To achieve high energy density and long cycle life of Ni-rich NMCs, the stability of the electrode-electrolyte interface (EEI) in Li-ion batteries is critical. It is well known that carbonate-based electrolytes are reduced on negative electrode materials to form solid electrolyte interphase (SEI)[23,24], which is electronically insulating but lithium-ion conducting to enable reversible lithium intercalation, but their possible (electro)chemical reactions on positive electrode materials are poorly understood. It is therefore essential to

understand the interfacial reactions at the interface and their thermodynamics to improve battery cyclability and capacity.

Moreover, besides the needs to improve the energy density, it is also desirable to reach high power densities, which is related to the kinetics and charging/discharging rates. There is a common trade-off between energy and power densities (Fig. 1-1), while commercial applications desire improvements in both (marked by the green star in Fig. 1-1). Unfortunately, the studies and understanding of intercalation kinetics are much limited to the Butler-Volmer model[25–29], and the microscopic reaction mechanism has not yet been established. Experimentally, electrochemical impedance spectroscopy (EIS) is commonly used to study the charge transfer in Li-ion batteries, combined with equivalent circuits analysis and Butler-Volmer kinetics[30,31]. However, EIS analysis only applies to near-equilibrium kinetics, and the impedance originates from multiple processes including ion migration, ion (de)solvation, ion adsorption (desorption) apart from charge transfer[31], making it difficult to deconvolute the impedance. Besides, the Butler-Volmer kinetics used to analyze the EIS charge transfer impedance is not accurate to describe the intercalation process in far-equilibrium conditions. As a result, the reported kinetic parameters for a same material have huge discrepancies, ranging more than 5 orders of magnitudes[32,33]. Hence there is urgent drive to develop both new theoretically frameworks and experimental methods to systematically investigate intercalation kinetics to enable high-power batteries.

1.3 Water electrolyzers, fuel cells, and their current challenges

Low-temperature fuel cells are an attractive energy technology to produce electricity by direct electrochemical conversion of hydrogen and oxygen into water (Fig. 1-3).[34] Hydrogen oxidation reaction (HOR) occurs at the anode ($H_2 \rightarrow 2H^+ + 2e^-$ in acid, or $H_2 + 2OH^- \rightarrow 2H_2O + 2e^-$ in alkaline solutions), while oxygen reduction reaction (ORR) happens at the cathode ($O_2 + 4H^+ + 4e^- \rightarrow 2H_2O$ in acid, or $O_2 + 2H_2O + 4e^- \rightarrow 4OH^-$ in alkaline solutions).

The overall cell produces water, and the electrons flow through an external circuit. They are environmentally friendly, producing low emissions and exhibiting high energy conversion efficiency and high power density.[13,35] Unfortunately, fundamental catalytic limitations that have plagued fuel cells still remain: the slow kinetics of the ORR can induce large overpotentials and significant efficiency losses in fuel cells[12], requiring larger amount of Pt catalyst loading than the HOR side. Similar problems of high overpotentials exist for the reverse oxygen evolution reaction (OER) in water electrolyzers.[36] Better catalyst designs are therefore necessary to enable high-efficiency fuel cells.

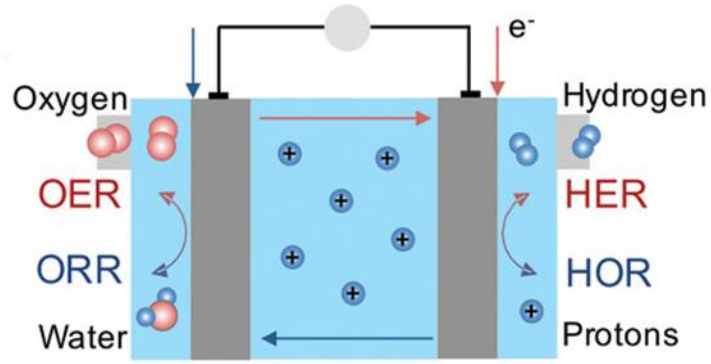

Fig. 1-3: Schematic of a two-electrode fuel cell or water electrolyzer.[37]

Previous studies to improve the catalysts are mainly based on tuning the surface electronic structures[38], such as screening different metals[39], alloys of Pt and Ni[40,41] and Pt-rare earth alloys[42–44] for ORR. Based on the binding energy of surface intermediates, the ORR or OER activities follow a volcano trend (Fig. 1-4A & B), and materials at the top of the volcanos are desired. Recently, there is increasing interest in modifying electrolytes, such as cations[45] or pH[46,47], to tune the catalytic activities. Nevertheless, the mechanistic understanding on the role of pH, cations and non-covalent interactions in proton-coupled electron transfer (PCET) reactions is still lacking. As a result, it is not apparent how to control the catalytic activity of OER/ORR using this strategy.

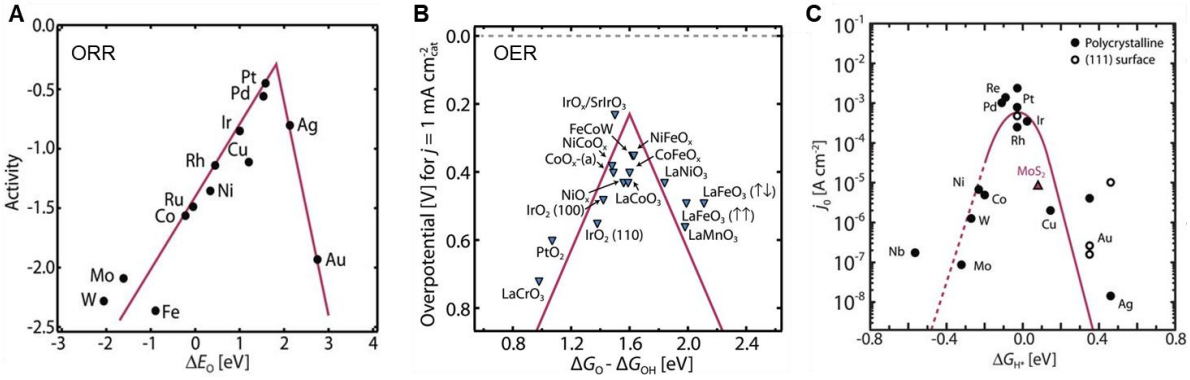

Fig. 1-4: Volcano plots for various reactions.[37] (A) ORR volcano plot for metals. (B) OER volcano plot for metal oxides. (C) HER volcano plot for metals and MoS_2. Adapted with permission from Ref. **[39]**.

Apart from OER and ORR, controlling the hydrogen evolution reaction (HER) has also been critical. In the production of molecular hydrogen as energy carriers[48], a high HER activity is desirable, while in applications like aqueous batteries[49], electrochemical CO_2 reduction[50,51], or electrochemical N_2 reduction[52], suppressing HER is desired. It is critical to tailor and control the water activity properly towards designed applications. Pt is at the

top of the volcano for HER (Fig. 1-4C) to yield the highest activity, while it is challenging to go beyond Pt and even further tune the water activity through electrolyte design. Water plays dual roles in aqueous electrolytes during HER, both as solvents and as reactants, which complicates the physical picture. Consequently, the mechanisms at play in the electrochemical double-layer for HER are poorly understood,[53] and it is not yet clear how to control water structures at the electrified interface and how to tune their activities accordingly. Hence it is crucial to simplify the physical picture and isolate the role of water to understand HER kinetics, so as to achieve precise tailoring of water activities for desired applications.

1.4 Thesis scope[2]

In this thesis, I aim to tackle the challenges above related to both the energy density and power density of batteries, and electrocatalytic activities critical to fuel cell technologies. I first focus on developing the fundamental understanding of the interfacial (electro)chemical reaction mechanisms in the molecular level and charge transfer kinetics at the electrified interfaces, where I develop in situ characterizations and novel electrochemical methods to advance the understand. Based on the mechanisms, I further propose design principles employing physical chemistry of electrolytes and solvation

[2] Reproduced in part, with permission from Zhang, Y., Katayama, Y., Tatara, R., Giordano, L., Yu, Y., Fraggedakis, D., Sun, J.G., Maglia, F., Jung, R., Bazant, M.Z. and Shao-Horn, Y., 2020. Revealing electrolyte oxidation via carbonate dehydrogenation on Ni-based oxides in Li-ion batteries by in situ Fourier transform infrared spectroscopy. *Energy & Environmental Science*, 13(1), pp.183-199. Copyright © The Royal Society of Chemistry 2020; Wang, T. †, Zhang, Y. †, Huang, B., Cai, B., Rao, R.R., Giordano, L., Sun, S.G. and Shao-Horn, Y., 2021. Enhancing oxygen reduction electrocatalysis by tuning interfacial hydrogen bonds. *Nature Catalysis*, *4*(9), pp.753-762. († denotes equal contribution.) Copyright © Springer Nature Limited 2021.

structures to improve the energy density, power density, and lifetime of batteries, and control the activity and kinetics of common electrocatalytic reactions.

In **Chapter 2**, I reveal the mechanism of battery degradation for $LiNi_{0.8}Mn_{0.1}Co_{0.1}O_2$ (NMC811) electrodes, which accounts for their capacity fading and poor cycle life. I develop an *in situ* FT-IR method and reveal dehydrogenation pathways of carbonate solvents in the electrolyte (EMC/EC with $LiPF_6$) on composite NMC811 electrodes. While ethylene carbonate (EC) was stable against oxidation on Pt up to 4.8 V_{Li}, at voltages as low as 3.8 V_{Li}, dehydrogenation of EC starts to show up, accompanied with huge growth in the charge transfer impedance measured from EIS. These observations are in agreement with density functional theory (DFT) results. Finally, I propose the pathways and mechanisms for carbonate-based electrolyte decomposition on NMC811 that account for impedance growth and capacity fading.

Based on the findings, in **Chapter 3,** I then discuss various strategies to prevent electrolyte oxidation and enhance the cyclability of Li-ion batteries, demonstrated from *in situ* FT-IR. Carbonate dehydrogenation can be suppressed by decreasing surface oxygen reactivity of Ni-based oxides, decreasing carbonate activity, or by substituting with fluorinated solvents, where no dehydrogenation was found from *in situ* FT-IR measurements. The electrode–electrolyte combinations without dehydrogenation further did not show significant impedance growth. Therefore, minimizing carbonate dehydrogenation on the NMC surface by tuning electrode reactivity and electrolyte reactivity is critical to develop high-energy Li-ion batteries with long cycle life. These findings highlight the importance of *in situ*

studies to capture reaction intermediates and suggest design strategies for more stable high-energy positive electrode materials.

In **Chapter 4**, I focus on the other aspect of Li-ion batteries, *i.e.* the power density that is governed by intercalation kinetics. We provide experimental and theoretical evidence that ion intercalation occurs by coupled ion-electron transfer (CIET), in which classical ion transfer into the solid host is coupled with quantum-mechanical electron transfer to a weakly coupled reduced state. In contrast to the empirical Butler-Volmer equation, CIET theory predicts curved Tafel plots that vary with ion concentration, as well as reaction-limited battery capacity that decreases in proportion to increasing insertion rate. We verify these predictions by collapsing data for many popular cathodes, anodes and electrolytes at different compositions and temperatures onto universal theoretical curves and performing Bayesian model selection. These results open the possibility of designing high-rate battery interfaces by maximizing the CIET reaction-limited current.

Starting from **Chapter 5**, I extend my research to electrocatalysis, leveraging physical chemistry of liquid electrolytes and non-covalent interactions to tune electrocatalytic activities. Proton activity at the electrified interface is central to the kinetics of proton-coupled electron transfer (PCET) reactions for making chemicals and fuels. We employ a library of protic ionic liquids in an interfacial layer on platinum and gold to alter local proton activity, where the intrinsic oxygen-reduction reaction (ORR) activity is enhanced up to fivefold, exhibiting a volcano-shaped dependence on the pK_a of the ionic liquid. The enhanced ORR activity is attributed to strengthened hydrogen bonds between ORR

products and ionic liquids with comparable pK_as, resulting in favourable PCET kinetics. This proposed mechanism is supported by in situ surface-enhanced Fourier-transform infrared spectroscopy. These findings highlight opportunities for using non-covalent interactions between hydrogen-bonded structures and solvation environments at the electrified interface to tune the kinetics of ORR and beyond.

In **Chapter 6**, I apply electrolyte design and non-covalent interactions to hydrogen evolution reaction (HER) and hydrogen oxidation reaction (HOR). I isolate the role of water as solely reactants by confining water in organic matrixes, and systematically tune the hydrogen-bonding networks by changing the water concentration and altering the donor number of organic solvents. Water reduction onset potentials are found to be dependent on both water-to-organic ratio and organic solvents, where high donor number solvents suppress HER and lower the onset potential more significantly, by stabilizing isolated water and suppressing hydrogen-bonded water at the electrified interface. Poisoning effects of different organic solvents are quantified, but they are found not to be the cause for the difference in solvent effects. Surface-enhanced infrared absorption spectroscopy (SEIRAS) measurements provide further support for the changes in interfacial hydrogen bonding during the reactions.

Finally, **Chapter 7** summarizes the combined results and learnings from this thesis on interfacial reactions and charge transfer kinetics for Li-ion batteries and electrocatalysis. It further discusses perspectives on the rational design of electrodes and electrolytes to

improve both the energy density, power density, and lifetime of electrochemical energy storage devices.

Chapter 2. Revealing electrolyte oxidation via carbonate dehydrogenation on Ni-based oxides in Li-ion batteries by in situ Fourier transform infrared spectroscopy[3]

2.1 Introduction

Understanding the (electro-)chemical reactions at the electrified interface between positive electrodes and electrolyte is crucial to develop Li-ion batteries with high cycle life and safety.[54–57] Layered lithium metal oxides are the most common positive electrode materials, among which $LiNi_xMn_yCo_{1-x-y}O_2$ (NMC) provides high capacities and potentially lower costs for use in electric vehicles.[18–22] While increasing Ni content in NMC from $LiNi_{1/3}Co_{1/3}Mn_{1/3}O_2$ (NMC111), $LiNi_{0.6}Co_{0.2}Mn_{0.2}O_2$ (NMC622) to $LiNi_{0.8}Co_{0.1}Mn_{0.1}O_2$ (NMC811) can greatly increase initial discharge capacities,[11,18,19] the capacity retention decreases during cycling,[11] which is accompanied by earlier onset for gas (O_2 and CO_2) evolution[11,58]. Although the mechanistic details of electrolyte reactivity and reaction pathways on Ni-rich positive electrodes[59–61] are not well understood, modifying electrode surfaces by ceramic coatings such as Al_2O_3[62–66], creating Ni-poor surfaces through concentration gradients[67–70] and introducing additives in the carbonate electrolytes[71–76] can greatly increase the capacity retention of Ni-rich electrodes, such as NMC811.

[3] Reproduced in part, with permission from Zhang, Y., Katayama, Y., Tatara, R., Giordano, L., Yu, Y., Fraggedakis, D., Sun, J.G., Maglia, F., Jung, R., Bazant, M.Z. and Shao-Horn, Y., 2020. Revealing electrolyte oxidation via carbonate dehydrogenation on Ni-based oxides in Li-ion batteries by in situ Fourier transform infrared spectroscopy. *Energy & Environmental Science*, 13(1), pp.183-199.

Multiple reaction mechanisms on carbonate electrolyte oxidation have been proposed, including nucleophilic attack reactions between oxides and carbonate molecules,[77–79] electrophilic attack,[80,81] and dehydrogenation reactions, including EC dissociation by breaking C-H bond,[82,83] and dissociation with oxygen vacancy formation.[80] However, recent density functional theory (DFT) results[59] show that EC dissociation on layered Ni-rich oxides is more energetically favorable than the other processes reported. The enhanced oxide-electrolyte reactivity for Ni-rich oxides[11,58,84,85] can be attributed to having more metal-oxygen covalency or more oxygen p states pinned at the Fermi level,[24,59,86] where there is greater driving force for the surface oxygen to dissociate or oxidatively dehydrogenate more carbonate solvents such as EC to form surface protic species ($C_3O_3H_4 \rightarrow {}^*C_3O_3H_3^+ + {}^*H^+$) and reduce transition metal ions[59,80]. For example, DFT calculations have shown that the dissociation energetics of EC (~-2.6 eV) on NMC811 is thermodynamically favorable.[59] Such proposed dehydrogenation of carbonate solvents is supported by *ex situ* diffuse reflectance infrared Fourier transform spectroscopy (DRIFTS) and Raman spectroscopy, where EC dissociation on charged NMC is more visible with increasing Ni content in NMC or increasing lithium de-intercalation in NMC811.[59] The protic species produced by dehydrogenation such as surface hydroxyl groups, can further react with $LiPF_6$ salt, forming lithium nickel oxyfluorides,[60] PF_3O,[87] $Li_xPF_yO_z$[60] and HF species,[60] validated by online electrochemical mass spectrometry and X-ray photoelectron spectroscopy (XPS).[60,88,89]

Previous *ex situ* techniques only provided information on oxidative products from the electrolyte that remain on oxide surfaces, while soluble species and dynamic changes of

surface reaction intermediates formed as a function of potential are not captured.[90] *In situ* FT-IR measurements, instead, would be ideal to probe the reaction pathway of organic electrolytes on oxide surfaces, as it is highly sensitive to covalent bonds, such as those in battery electrolytes.[91] While there are a few *in situ* FT-IR techniques previously reported in understanding the reduction[92–94] or oxidation[95,96] stability of organic electrolytes in lithium-ion batteries,[92–95] it is not straightforward to apply these methods to study oxide powders, especially Ni-rich NMCs used in practical Li-ion batteries. For example, Kanamura et al.[96] have developed a method for thin-film electrodes such as $LiFePO_4$[97] and $LiCoO_2$[98,99], while Aurbach *et al.* have used a technique that purges the gaseous products from an electrochemical cell to an optical IR cell[100], which can detect gaseous species such as CO_2 and CO from ionic liquid-based electrolyte with $LiNi_{0.8}Co_{0.15}Al_{0.05}O_2$ electrodes. However, they are either not applicable to various composite electrodes of oxide powders due to the difficulty in synthesizing thin film electrodes for Li-containing Ni-rich NMCs[101], or cannot detect interfacial species or solution phase species. Consequently, the exact oxidation products and mechanistic details are not revealed. Other techniques including *in situ* DRIFTS[102] or surfaced-enhanced Raman spectroscopy (SERS)[103] have also been applied to the study of EEI formation for Li-Rich oxides ($Li_{1.2}Ni_{0.2}Mn_{0.6}O_2$) and Lewis acid or Lewis base initiated EC decompositions have been proposed. However, *in situ* studies and direct evidence for interface reaction mechanisms on Ni-rich high-covalent NMCs are still missing.

In this study, we have designed a new *in situ* FT-IR setup to examine the parasitic reactions between carbonate electrolytes and composite NMC powder electrodes used in practical

Li-ion batteries as a function of voltage (or time) during galvanostatic (or potentiostatic) measurements. We study $LiPF_6$ in EC, and LP57 electrolyte (1 M $LiPF_6$ in 3:7 EC/EMC), and examine their reactivity with NMC811 as a function of voltage. The spectra assignments are validated by DFT simulated spectra. Next, we correlate the oxidation of electrolytes through carbonate dehydrogenation on NMC811 with charge transfer impedance measured from electrochemical impedance spectroscopy (EIS). Finally, we propose the pathways and mechanisms for carbonate-based electrolyte decomposition on NMC that account for impedance growth and capacity fading. Through the *in situ* spectra on NMC surfaces, we track the interfacial reactions and understand the electrolyte decomposition mechanism on composite NMC powder surfaces in practical battery operations during galvanostatic charging.

2.2 Results and Discussion

2.2.1 *In situ* FT-IR measurements of NMC811-mediated oxidation of EC upon charging

While EC with 1.5 M $LiPF_6$ was stable against (electro)chemical oxidation up to 4.8 V_{Li} on Pt, species derived from dehydrogenation of EC, including dehydrogenated EC (de-H EC, one hydrogen removed), vinylene carbonate (VC, two hydrogens removed), and oligomers with EC-like rings, were detected *in situ* upon charging NMC811 at voltages as low as 3.8 V_{Li}. FT-IR spectra were first collected *in situ* at selected voltages with Pt only as the positive electrode, as the voltage of Li/Pt cells was linearly swept from open circuit voltage (OCV) at 3.1 V_{Li} to 4.8 V_{Li} (Fig. A-1). Since the C=O stretching region gives the strongest signal and is the most sensitive to molecule structure changes, the focus is to probe this C=O stretching region. Voltage-dependent difference spectra obtained by

subtracting each spectrum by the spectrum at OCV revealed no new peaks appearing upon charging to 4.8 V_{Li} (Fig. A-1B), indicating no significant electrolyte oxidation. This result is consistent with previous theoretical[104–106] and experimental results[107–109] for linear sweep voltamograms showing that carbonate electrolytes are stable against oxidation below 5 V_{Li} on inert metals.

Unfortunately, upon charging NMC811 from OCV to 4.4 V_{Li} (Fig. 2-1 B), significant changes were observed in the difference spectra (Fig. 2-1 C) obtained from IR spectra collected *in situ*, indicative of oxidative instability. Broad intensities in the wavenumber range from 1850 to 1750 cm^{-1} were found to grow significantly from 3.8 V_{Li} to 4.4 V_{Li} , where individual peaks between 1830 and 1800 cm^{-1} became resolved at 3.8 V_{Li} and grew in intensity. Two pronounced peaks in the C=O region at ~1800 cm^{-1} and ~1773 cm^{-1} were revealed, corresponding to C=O stretching in EC and Li^+-coordinated EC[60,93], respectively. This assignment is in agreement with attenuated total reflection (ATR) measurements of 1.5 M $LiPF_6$ in EC (Fig. 2-1 C) and DFT-simulated spectra (Fig. 2-1 A). In addition, two small, sharp peaks at ~1773 and ~1763 cm^{-1} became visible upon charging from 3.9 V_{Li} to 4.4 V_{Li}. Upon further oxidation from 4.4 V_{Li} to 4.8 V_{Li} (Fig. A-2), the difference spectra remained unchanged. The peak at ~1830 cm^{-1} that appeared at 3.8 V (Fig. 2-1 C) could be assigned to VC, having two hydrogens removed from EC to form a C=C bond in the ring, which assignment was supported by experimental ATR spectrum of VC-containing 1.5 M $LiPF_6$ in EC (Fig. 2-1 C), and calculated spectrum of VC by DFT (Fig. 2-1 A). The peaks at ~1800 cm^{-1} and ~1773 cm^{-1} came from the C=O stretching in EC and Li^+-EC, respectively, and the greater peak intensity of EC grew with increasing voltage, possibly

because bulk EC from electrolyte were attracted to surface during the adsorption and oxidation of EC on surface which could create a concentration gradient of EC in the electrolyte. The increased intensity ratio of VC to EC from 3.8 V_{Li} to 4.8 V_{Li} (Fig. A-2 C) indicate more VC formed on the surface with increasing voltage. In addition, the peaks in the broad feature between 1820 to 1810 cm^{-1} and the peak at ~1763 cm^{-1} (black arrow in Fig. 2-1 C) can be attributed to small oligomers with EC-like rings, which could come from EC ring opening and polymerization.[110–112] This assignment is supported by the DFT spectra (Fig. A-2 D and Fig. 2-1 A) of oligomers including $C_6H_8O_6$ (computed 1813 and 1755 cm^{-1}), $C_9H_{14}O_8$ (computed 1819 and 1757 cm^{-1}), and $C_7H_{10}O_6$ (computed 1813 and 1750 cm^{-1}). Further support came from time-dependent intensity measurements at OCV in Fig. 2-1 E, which will be discussed below. Moreover, the feature around 1813 cm^{-1} (convoluted between 1820 to 1810 cm^{-1}, black arrow in Fig. 2-1 C) that appeared the earliest at ~3.8 V_{Li} could also contain C=O stretching of dehydrogenated EC (de-H EC), having one hydrogen removed from EC and whose formation was energetically favorable with driving force around 2.6eV (Fig. 2-1 F).[59,60] This peak position of de-H EC fell between EC and VC, which is in agreement with DFT (Fig. 2-1 A), and the assignment was further supported by time-dependent intensity measurements at OCV in Fig. 2-1 E to be discussed later. The deconvoluted peak areas of VC and oligomers were found to grow comparably with increasing voltage, indicating that they were gradually generated from EC and/or de-H EC, while the peak area of de-H EC grew less with increasing voltage (Fig. 2-1 B), which might due to its consumption to further generate VC and oligomers. In summary, the appearance and growth of new peak features at ~1830, ~1820 to 1810 cm^{-1}, and ~1763 cm^{-1} provided direct evidence of electrolyte oxidation via EC dehydrogenation

on charged NMC811 starting at voltages as low as ~3.8 V_{Li}, where EC could dissociate on electrode surface to remove one hydrogen and generate de-H EC, further remove another hydrogen to form VC, or combine with another EC to form oligomers.

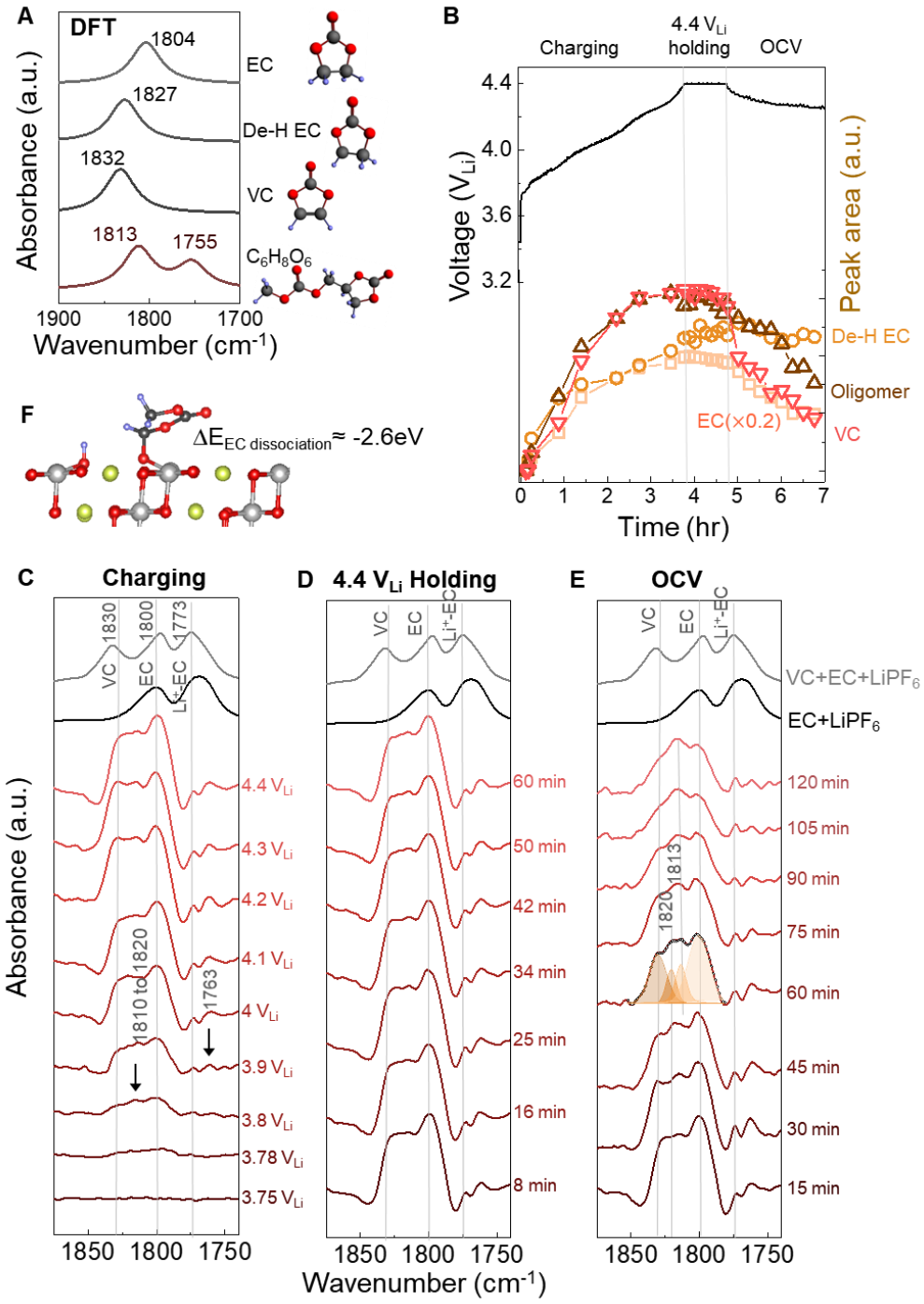

Fig. 2-1 *In situ* FT-IR measurements on NMC811 surface in EC with 1.5 M $LiPF_6$. (A) DFT-simulated spectra of EC, de-H EC, VC and oligomer $C_6H_8O_6$. (B) Voltage profile (black) of NMC811 galvanostatically charged to 4.4 V_{Li}, potentiostatically holding at 4.4 V_{Li}, and resting at OCV, in 1.5 M $LiPF_6$ / EC electrolyte, with the *in situ* FT-IR cell, at a current of 27.5 mA/g; Deconvoluted peak areas (red) of EC and its decomposed products at ~1813 cm^{-1} (de-H EC), ~1820 cm^{-1} (oligomers with EC-like rings) and 1830 cm^{-1} (VC), during charging, potentiostatic holding and OCV. During the OCV, peak intensities of VC and oligomers decreased dramatically while de-H EC stayed almost the same in amount. (C) *In situ* FT-IR difference spectra (C=O stretching region, in red) on NMC811 surface during galvanostatic charging to 4.4 V_{Li}, (D) potentiostatic holding at 4.4 V_{Li}, (E) resting at OCV in EC with 1.5 M $LiPF_6$ electrolyte, and ATR spectra for 1.5 M $LiPF_6$ in EC and 1.5 M $LiPF_6$ in EC/VC (5:1) electrolyte solution (in black). (F) Diagram of EC dehydrogenation on $LiNiO_2$ (similar to NMC811) and its energetics.

While no significant changes were noted for the C=O stretching region (1900 to 1700 cm^{-1}) in the difference spectra during voltage holding at 4.4 V_{Li} (Fig. 2-1 D), most peaks were reduced in intensity with increasing time upon OCV following the 4.4 V_{Li} voltage hold (Fig. 2-1 B, E). These potentiostatic and open circuit voltage measurements were conducted followed by charging to 4.4 V_{Li} to examine whether the species could stick on surface or could diffuse or dissolve away from surface**.** The spectrum at OCV (after 60 min) could be splitted into four features, VC at ~1830 cm^{-1}, de-H EC at ~ 1813 cm^{-1}, and oligomers at ~1820 cm^{-1} (and 1763 cm^{-1}) and EC at 1800 cm^{-1}. The peaks of VC, oligomers and EC were reduced rapidly with increasing time at OCV, indicating these species diffused away from charged NMC811 into the electrolyte. Of significance to note that VC intensity was reduced faster than oligomers and EC, indicative of greater diffusivity or solubility, which is in agreement with the fact that VC was not detected in the *ex situ* DRIFT spectra.[60] In contrast, the peak intensity of de-H EC (~1813 cm^{-1}) did not change significantly with increasing time (Fig. 2-1 B, E), and it became the most dominant feature after resting for 60 minutes, suggesting de-H EC was anchored on the oxide surface, presumably by a $C\text{-}O_{surface}$ bond formed during EC dehydrogenation on surface oxygen of

NMC811[59] (Fig. 2-1 F), which is in agreement with the observation of this species in *ex situ* DRIFT spectra of charged NMC811 electrodes dried and removed from electrochemical cells[60].

2.2.2 *In situ* FT-IR measurements of LP57 during charging and discharging on NMC811

Similarly in LP57 (1 M $LiPF_6$ in EC/EMC) – a commonly used electrolyte for Li-ion batteries, we have observed similar NMC811-mediated oxidation of EC. While LP57 (1 M $LiPF_6$ in EC/EMC) was stable against oxidation on Pt, *in situ* FT-IR spectra revealed that EC was dehydrogenated to form de-H EC, vinylene carbonate (VC), and oligomers during galvanostatic charging similar to those discussed earlier for 1.5 M $LiPF_6$ in EC. Spectra collected on NMC811 from OCV (3 V_{Li}) to 4.8 V_{Li} was subtracted from the OCV spectrum to yield differential spectra (Fig. 2-2 B) which revealed new peaks of EC-derived dehydrogenation species at voltages greater than 3.8 V_{Li}, including de-H EC (~1813 cm^{-1}, greater than 3.9 V_{Li}), VC (~1830 cm^{-1}, greater than 4.1 V_{Li}), and oligomers with EC-like rings (~1820 and ~1763 cm^{-1}, greater than 4.1 V_{Li}) similar to Fig. 2-1. Changes in the difference spectra unique to the dehydrogenation of EMC during galvanostatic charging of NMC811 was not observed, which can be interpreted by the convolution of de-H EMC with bulk EMC and with EC-derived oligomers, and/or having EC preferentially adsorbed on the NMC811 surface than linear alkyl carbonate EMC[113,114] due to its higher dielectric constant[105]. Previous sum frequency generation studies show that EC occupies over 90 mole% on lithium metal oxide ($LiCoO_2$) surfaces in mixed carbonate solutions such as EC+DEC or EC+DMC, much higher than that in the bulk solution (43 mole%)[114]. After charging, we also discharged the cell and the difference spectra (Fig. 2-2 D) showed that

upon discharging from 4.8 V_{Li} to 2 V_{Li}, VC peak (1830 cm^{-1}) and oligomer peaks (1820 and 1763 cm^{-1}) gradually decreased in intensity, which agrees with the results during OCV (Fig. 2-1 E) that VC and oligomers could diffuse or dissolve away. De-H EC still anchored on the surface, which is also in agreement with the results at OCV. Another interesting finding is that Li^+-EC (1773 cm^{-1}) peaks gradually grew larger, which was not observed during OCV, and this was probably because during discharge, Li^+ migrated from bulk electrolyte to oxide surface to be intercalated, making more EC to become coordinated.

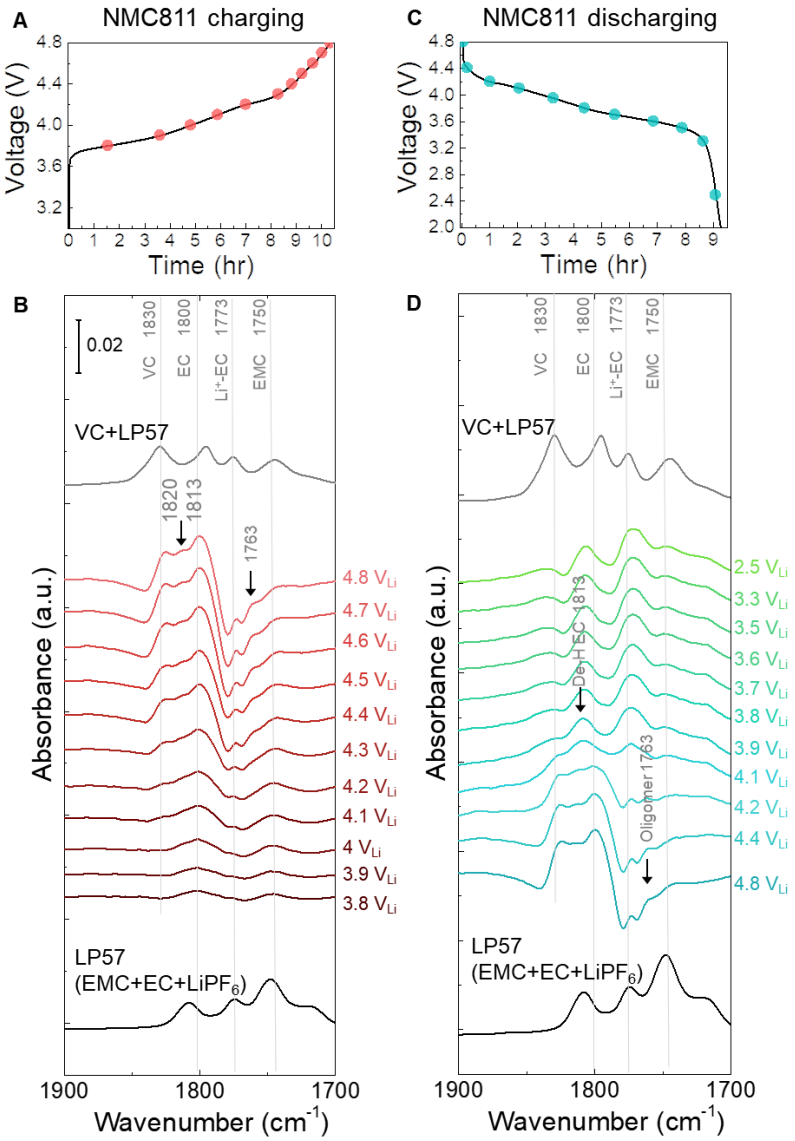

Fig. 2-2 *In situ* FT-IR measurements on NMC811 surface in LP57. (A) Voltage profile of NMC811 galvanostatically charged to 4.8 V_{Li}. (B) *In situ* FT-IR difference spectra (C=O stretching region, in red) and ATR spectra for LP57 (in black). (C) Voltage profile of NMC811 galvanostatically discharged to 2 V_{Li}. (D) *In situ* FT-IR difference spectra (C=O stretching region, in red) and ATR spectra for LP57 (in black).

2.2.3 Correlating impedance growth with carbonate solvent dehydrogenation

While *in situ* FT-IR spectra revealed the dehydrogenation of solvents on NMC *in situ* as a function of voltage/time, we employed EIS to further reveal that the charge transfer and EEI impedance on NMC811 grew much more significantly than on NMC111 with increasing voltage, which could be attributable to dehydrogenated products on NMC811 surfaces. For stable interfaces such as NMC111, NMC622 with surface coating, and NMC811 in the concentrated electrolyte (3.1 M $LiPF_6$ in EC/EMC) exhibit no significant impedance growth in contrast to NMC811 in LP57 (Fig. 2-3).

EIS on NMC811 positive electrode collected at 3.9 V_{Li}, 4 V_{Li} and up to 4.6 V_{Li} during the 1st cycle charging in LP57 showed huge growth in the low-frequency semicircle (right-hand side semicircle in Fig. 2-3 A), which can be attributed to the charge transfer and EEI resistance (R_{CT+EEI}, low-frequency resistance)[31] (Fig. 2-3 C), growing from ~10 to over 300 Ohm during charging. The R_{CT+EEI} impedance at 4.6 V_{Li} was beyond the detected amplitude in this frequency range (down to 100 mHz) because it was almost at the end of charge. Similarly, for NMC811 in other non-concentrated electrolytes including EC with 1.5 M $LiPF_6$, EMC with 1 M $LiPF_6$, and EMC/EC with 1 M $LiClO_4$, R_{CT+EEI} all grew dramatically from ~10 Ohm to ~400 Ohm (Fig. 2-3 C). The difference in R_{CT+EEI} between EC with $LiPF_6$, EMC with $LiPF_6$, and LP57 at each voltage could come from the different dielectric

constants[115] and physical properties such as ionic conductivity and viscosity, which could affect the solvation and de-solvation processes during charge transfer. This great increase of R_{CT+EEI} upon NMC811 charging in all four 1 M or 1.5 M electrolytes can be correlated with the dehydrogenation and/or oligomerization products detected by *in situ* FT-IR reported above for 1 M or 1.5 M electrolyte cases, indicating that these organic products likely formed a resistive layer on NMC811 which passivated the surface and impeded charge transfer. The comparable impedance growth and similar dehydrogenation reactions between the PF_6^--based electrolyte and ClO_4^--based electrolyte noted for NMC811 further supports the hypothesis that solvent (carbonate) decomposition contributed most to the impedance growth, rather than commonly-perceived salt decomposition. Although $LiPF_6$ salt could be attacked by surface protic species to form metal fluorides (MF)[60,99,116] and resistive LiF,[78] our result of a non-PF_6^- electrolyte revealed that even without severe salt decomposition, solvent dehydrogenation itself could account for great impedance growth on NMC811 in the ClO_4^--based electrolyte.

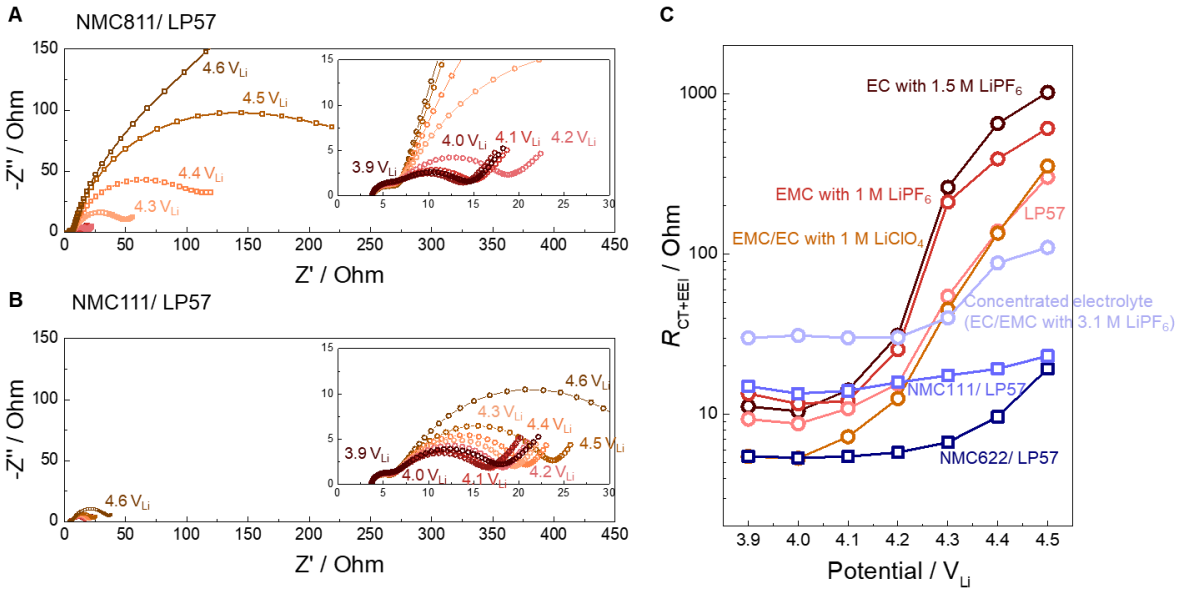

Fig. 2-3. EIS measurement on NMC composite electrode during the first charging. Nyquist plot at different voltages for (A) NMC811 and (B) NMC111 charged in LP57. Inset figures show the enlarged Nyquist plot. (C) Charge transfer and EEI resistances (R_{CT+EEI}) at different voltages measured by EIS, for NMC811 charged in EC with 1.5 M $LiPF_6$, EMC with 1 M $LiPF_6$, LP57, EMC/EC with 1 M $LiClO_4$ and the concentrated electrolyte (3.1 M $LiPF_6$ in EC/EMC), and for NMC111 and NMC622 charged in LP57. Those curves in (c) without specifying the electrode correspond to NMC811 electrode.

2.2.4 Mechanistic discussion on electrolyte oxidation on Ni-rich NMC

The detailed mechanisms of electrolyte oxidative decomposition on layered Ni-rich metal oxide positive electrodes are proposed based on *in situ* FT-IR experiments and their correlated contribution to EEI impedance growth and capacity loss, shown in Fig. 2-4. EC molecules dehydrogenate and form de-H EC that bonds with surface oxygen, which is energetically favorable as supported by DFT (Fig. 2-1 F). EC can also further dehydrogenate a second hydrogen on the other carbon and form VC. De-H EC could go through ring opening, or form oligomers with EC-like rings. Eventually, the dehydrogenation products may also be further oxidized to CO_2.[11] Organic products from carbonate decomposition can form a passivating layer on the oxide surface, and therefore R_{CT+EEI} shows great impedance growth during charging of NMC811 (Fig. 2-3 C). The dehydrogenation of EC and EMC also generates protic species on the surface,[59,117,11] which can further trigger reactions[116] with the widely used $LiPF_6$ salt. Salt decomposition might also contribute to EEI impedance, but our comparable results between LP57 (EMC/EC with 1 M $LiPF_6$) and EMC/EC with 1 M $LiClO_4$ show that solvent decomposition plays a much larger role. Combining *in situ* FT-IR spectra and EIS reveals that when there is undesirable dehydrogenation of solvents, there is great interfacial impedance growth at

higher voltage, eventually leading to the loss of capacity when NMC811 is cycled to high voltages.

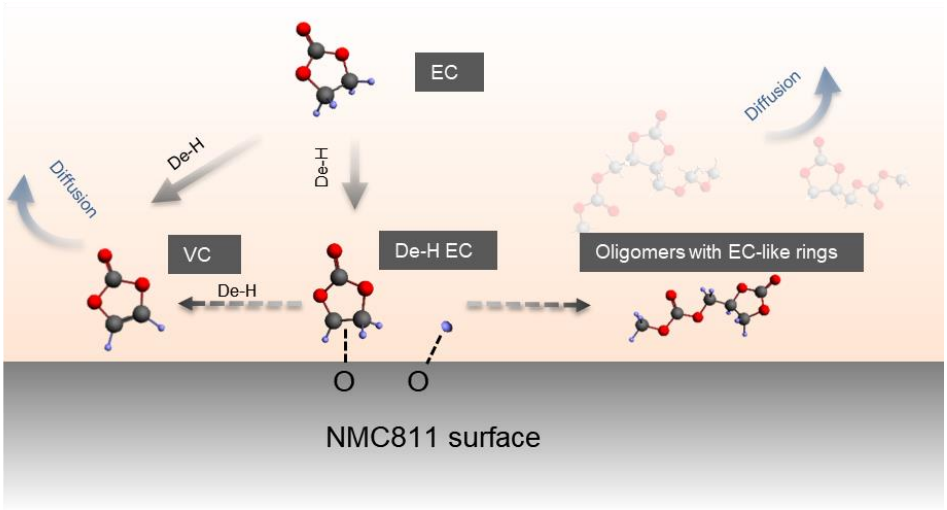

Fig. 2-4 Proposed mechanism and pathways of EC oxidation on NMC811.

2.3 Conclusions

In this study, we developed an FT-IR method, which allowed the *in situ* studies on the reactivity of the electrolyte on NMC surfaces as a function of voltage. While ethylene carbonate (EC) remained stable against (electro)chemical oxidation on Pt up to 4.8 V_{Li}, we found unique evidence for dehydrogenation of EC on NMC811 surface at voltages as low as 3.8 V_{Li}. Three unique dehydrogenated species from EC were observed on the NMC811 surface, which included dehydrogenated EC (de-H EC, anchored on oxides), vinylene carbonate (VC), and dehydrogenated oligomers with EC-like rings, while the latter two can diffuse away from the NMC811 surface into the electrolyte. These observations indicate that electrolyte oxidation on NMC811 might not generate a protective film unlike the solid electrolyte interface (SEI) formed by EC reduction on graphite. Similar dehydrogenation

was observed for LP57 electrolytes on NMC811. Such oxidative dehydrogenation tendencies on the oxide chemistry are in good agreement with the driving force for EC dehydrogenation on surface oxygen of NMC predicted by recent density functional theory (DFT) calculations, which increased with lower Fermi level into the oxygen p band of oxides associated with greater Ni and less lithium in NMC. Dehydrogenation of carbonates (EC and EMC) on the NMC811 surface was found to accompany with rapid growth of interfacial impedance with increasing charging voltage measured from EIS. Therefore, it is crucial to minimize carbonate dehydrogenation on the NMC surface by tuning electrode reactivity and electrolyte reactivity for improving the cycle life and high energy of lithium-ion batteries.

2.4 Methods

The *in situ* FT-IR cell was designed and machined on a piece of Teflon (Fig. 2-5). The optical window is a calcium fluoride (CaF_2) hemisphere (Diameter 20mm, Pier optics), with 15-30 nm of Pt sputtered on top as the current collector (sputtered at ~0.3 Å/s). The optical window was attached to the Teflon cell body through a metal holder with O ring sealing. The cell was assembled in an argon-filled glovebox ([H_2O] and [O_2]<0.5 ppm, MBraun).

Inside the cell, composite NMC on glassy fiber substrates (Whatman 934-AH, 10 mm in diameter) was the positive electrode (electrode preparation method is described in Appendix A), and a lithium metal foil (11 mm in diameter) was the negative electrode, separated by two pieces of separators (2325 Celgard or Whatman GF/A). 100 μL

electrolyte was added in total between electrodes and separators. They were then covered by a stainless steel spacer, and a spring was compressed by a top plate.

During measurements, the top part of the cell was able to conduct currents and perform charging and discharging; at the same time, the bottom optical part was able to collect FT-IR spectra at the NMC/electrolyte interface through internal reflection. *In situ* FT-IR measurements were performed on a Tensor II (Bruker) FT-IR equipped with deuterated triglycine sulfate (DTGS) detector inside the glovebox. The FT-IR spectra were acquired in the single-reflection mode using an attentuated total reflection (ATR) accessory (Pike Vee-Max II, Pike Technologies) at an incident angle of 50 degrees. The spectral resolution was 4 cm^{-1} and the scan velocity was 1.6 kHz. Each spectrum was measured by superimposing 32 interferograms. All spectra were presented in the form of absorbance according to $\log(I_0/I_1)$, where I_0 and I_1 are the spectrum of background (blank Pt surface without electrolytes) and *in situ* spectrum of the sample, respectively.

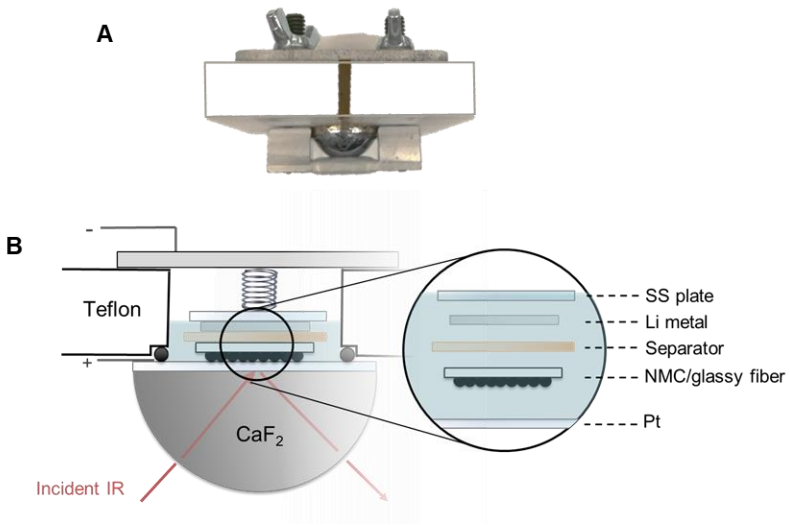

Fig. 2-5 *In situ* FT-IR spectro-electrochemical cell. (A) Photo of the cell setup. (B) Schematics of cell components. Composite NMC drop-casted on glassy fiber substrate is the positive electrode, with NMC particles faced towards the prism.

Chapter 3. Strategies for EEI design by tuning electrode and electrolyte reactivity[4]

3.1 Introduction

The understanding on degradation pathways in Chapter 2 paves the way for rational design of more stable, more durable, and cheaper Li-ion batteries. Previous attempts to improve the lifetime or energy densities were mainly based on trial-and-error, such as using inert coatings[63] or additives[71] in electrolytes to improve the cyclability of NMC811, but it was unclear how to rationally improve them or what fundamentally limits their lifetime. Based on the findings in Chapter 2, which focused on understanding the microscopic processes lead to the battery degradation, I have revealed that carbonate dehydrogenation is the first and key reaction that accounts for interfacial impedance build-up and capacity fading for NMC811. It is a natural strategy to suppress the parasitic dehydrogenation reaction which is not desired, so as to prevent battery degradation and increase lifetime. In this Chapter, I demonstrate a few approaches on how carbonate oxidative dehydrogenation is suppressed by lowering the electrode or electrolyte reactivity, or through fluorinated solvents or electrolyte additives to form a stable EEI instead. The physical origins of these effective approaches for Ni-rich NMCs are also discussed in the context of driving forces of

[4] Reproduced in part, with permission from Zhang, Y., Katayama, Y., Tatara, R., Giordano, L., Yu, Y., Fraggedakis, D., Sun, J.G., Maglia, F., Jung, R., Bazant, M.Z. and Shao-Horn, Y., 2020. Revealing electrolyte oxidation via carbonate dehydrogenation on Ni-based oxides in Li-ion batteries by in situ Fourier transform infrared spectroscopy. *Energy & Environmental Science*, 13(1), pp.183-199. Copyright © The Royal Society of Chemistry 2020; Karayaylali, P.*, Zhang, Y.*, Giordano, L., Katayama, Y., Tatara, R., Yu, Y., Maglia, F., Jung, R. and Shao-Horn, Y., 2020. The role of diphenyl carbonate additive on the interfacial reactivity of positive electrodes in Li-ion batteries. *Journal of The Electrochemical Society*, *167*(4), p.040522. (* denotes corresponding author) © 2020 The Electrochemical Society ("ECS").

dehydrogenation and EEI formation, supported by *in situ* FT-IR. Unlike empirical and trial-and-error studies, I first uncover the fundamental microscopic mechanisms, and then identify dominant factors that would enable improvements in lifetime and power densities, bridging the gap between applications and scientific understandings. These findings provide science-driven, innovative design of long-living and high-power energy devices, with cheaper materials for decarbonization.

3.2 Lowering electrode covalency and suppressing carbonate activity[5]

The dehydrogenation tendency of EC in LP57 on Ni-based oxide electrode is decreased either by decreasing metal-oxygen covalency[59,118], or suppressing the carbonate activity. We have screened a library of inorganic compounds commonly used in Li-ion batteries, and computed the hydrogen adsorption (dissociation) energetics on the surface to predict electrolyte stability in Li-ion batteries (Fig. 3-1 A). Using first-principle density functional theory (DFT) calculations[59,119], the hydrogen adsorption energy was found to be higher when decreasing metal-oxygen covalency, *i.e.* moving the Fermi level away from the oxygen p band center (Fig. 3-1 B), especially for high-band-gap materials, attributed to a lower energy level associated with adsorbed hydrogen relative to the bottom of the conduction band (Fig. 3-1 C). There materials, such as Al_2O_3 and low-Ni content layered oxides, are therefore promising candidates, being unfavorable for EC dehydrogenation, while NMC811 (represented by $LiNiO_2$ in computations) is favorable for the parasitic

[5] Reproduced in part, with permission from Zhang, Y., Katayama, Y., Tatara, R., Giordano, L., Yu, Y., Fraggedakis, D., Sun, J.G., Maglia, F., Jung, R., Bazant, M.Z. and Shao-Horn, Y., 2020. Revealing electrolyte oxidation via carbonate dehydrogenation on Ni-based oxides in Li-ion batteries by in situ Fourier transform infrared spectroscopy. *Energy & Environmental Science*, 13(1), pp.183-199. Copyright © The Royal Society of Chemistry 2020

reaction. I further apply *in situ* FT-IR to investigate the tendency of EC dehydrogenation on these materials with lower metal-oxygen covalency.

3.2.1 *In situ* FT-IR measurements of NMC111- and NMC622-mediated oxidation of LP57 upon charging

Unlike NMC811, where EC was dehydrogenated upon charging to voltages as low as 3.8 V_{Li} in the first cycle, no new peaks were found for difference spectra collected for NMC111 upon the first galvanostatic charging from OCV to 4.8 V_{Li} (Fig. 3-2 A-B), indicative of no obvious solvent oxidation upon first cycle charging for NMC111, which is in agreement with recent *ex situ* FT-IR studies.[60] In the subsequent third cycle, still no new peaks were found for difference spectra collected for NMC111 upon galvanostatic charging from OCV to 4.8 V_{Li} (Fig. 3-2 C-D). The difference in the dehydrogenation of EC or oxidation of LP57 between NMC811 and NMC111 observed in the *in situ* FT-IR measurements provides further experimental evidence to support previous DFT results, where the driving force for EC dehydrogenation on NMC811 with greater metal-oxygen covalency and more oxygen 2p states pinned at the Fermi level is much greater than that on NMC111[60,61,120,121].

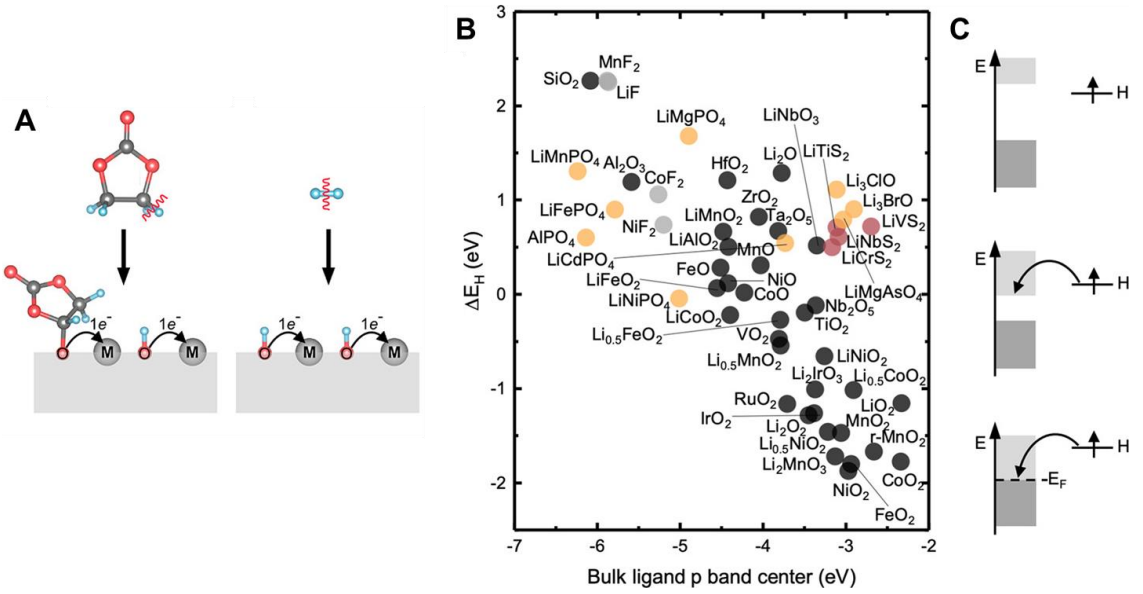

Fig. 3-1 DFT-computed hydrogen adsorption energy. (A) Analogy between EC dissociative adsorption and hydrogen adsorption on transition metal oxides, which both involve the reduction of the oxide transition metal ions. (B) Hydrogen adsorption energy with respect to the bulk ligand p band center, referred to the Fermi level for metals and midgap for semiconductors and insulators. (C) Schematic charge transfer between adsorbed hydrogen and surfaces for high-band-gap insulators, semiconductors, and metals. *Figures adapted with permission.*[119] *Copyright © 2019 American Chemical Society.*

While NMC622 did not show any evidence for carbonate dehydrogenation during the 1st cycle (Fig. 3-3 B), dehydrogenated EC products including de-H EC (~1813 cm^{-1}, marked in black arrow), VC (~1830 cm^{-1}), and oligomers with EC-like rings (~1820 and ~1763 cm^{-1}, marked in black arrows) were detected in the FT-IR difference spectra obtained upon the third charge (Fig. 3-3 D). In contrast, the dehydrogenation of LP57 was not detected for NMC622 coated with Al_2O_3 in the 3rd charging (Fig. 3-3 F). This difference in the dehydrogenation of LP57 between coated and uncoated NMC622 demonstrates the effect of surface coating layers[122,123] such as Al_2O_3,[124,125] ZrO_2,[126] HfO_2[127] on eliminating electrolyte oxidation. Oxides such as Al_2O_3 were less thermodynamically favorable for dissociative adsorption of EC, and lowered the driving force to dehydrogenate

carbonates,[59,119,128,129] which is in agreement with former studies that coatings the electrode surfaces with Al_2O_3,[124,125,129] ZrO_2[126] or HfO_2[127], or creating a Ni-poor surface to decrease M-O covalency[67–69] can improve cycling performance. Coated Ni-rich NMC electrodes with greater capacity retention[123–125,129] can be attributed to enhanced stability against dehydrogenation compared to electrodes without coatings.

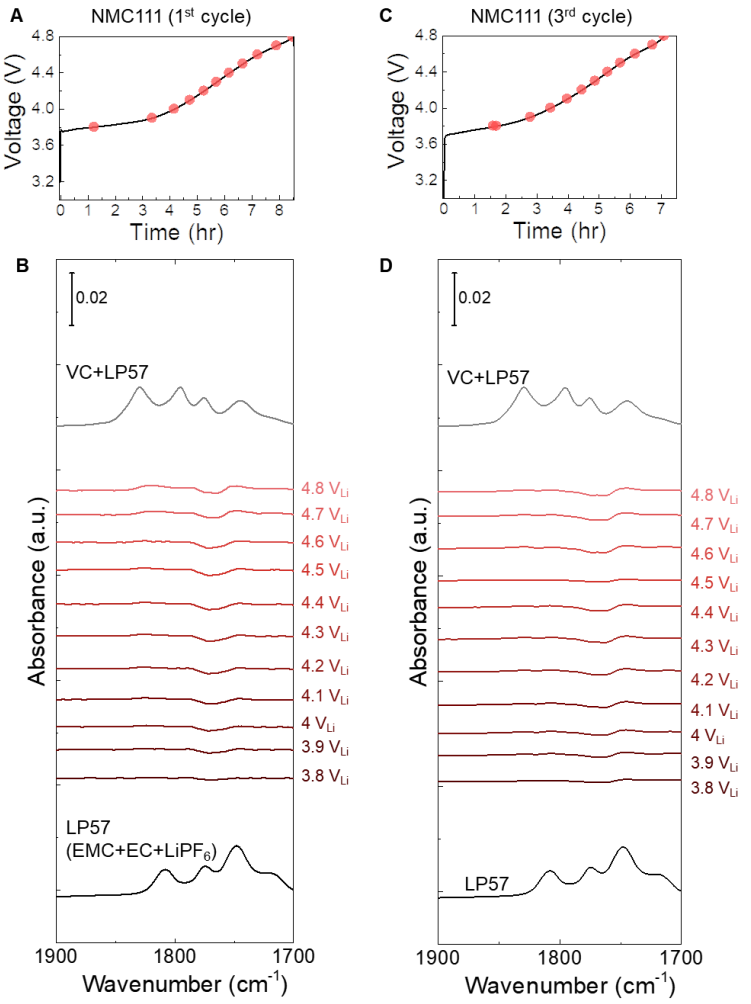

Fig. 3-2 *In situ* FT-IR measurements on NMC111 surface in LP57, during the 1st and the 3rd cycle. Voltage profile of NMC111 galvanostatically charged to 4.8 V_{Li} during the (A) first cycle and (C) third cycle. *In situ* FT-IR difference spectra (C=O stretching region, in red) and ATR spectra for LP57 (in black) during the (B) first cycle and (D) third cycle.

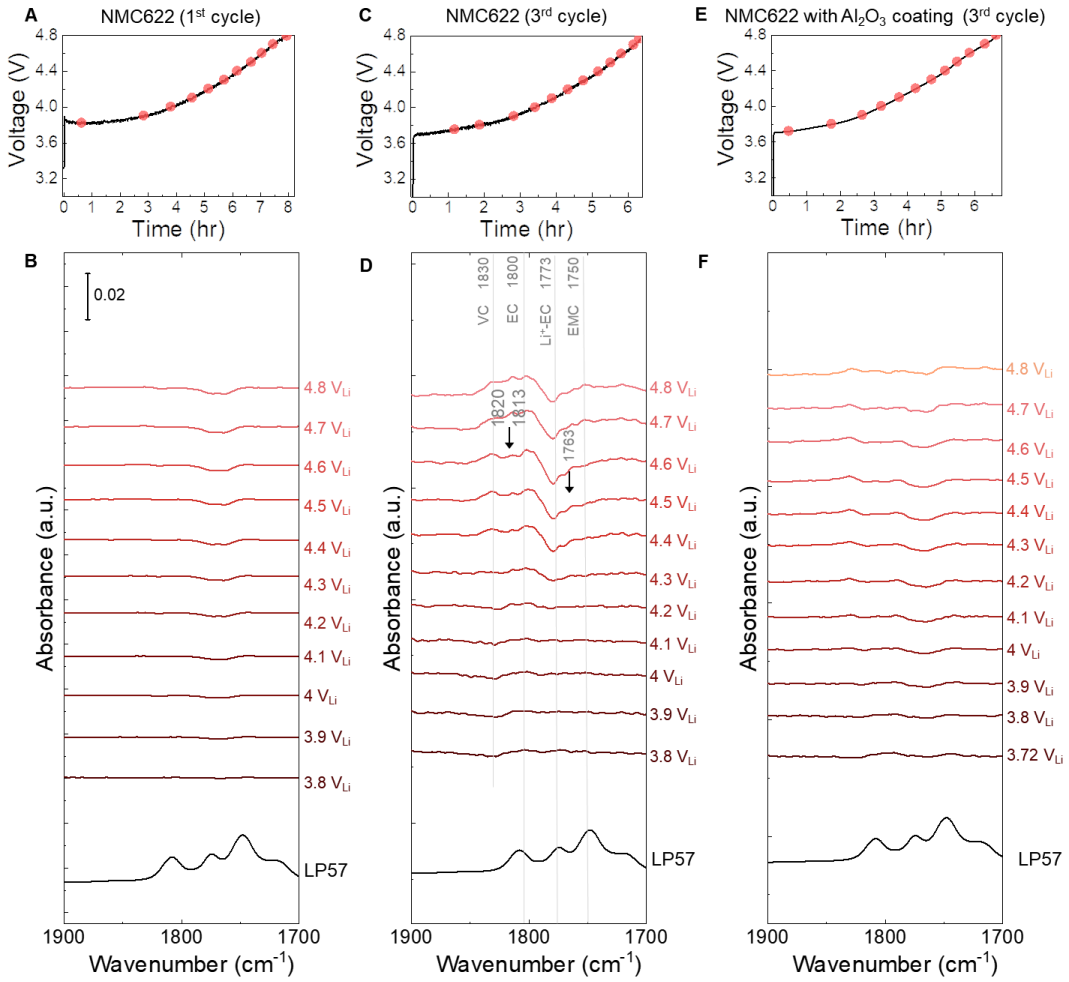

Fig. 3-3 *In situ* FT-IR measurements on NMC622 surfaces with and without surface coating upon the 1st and 3rd cycle charging to 4.8 V_{Li} in LP57. (A, C, E) Voltage profile during charging of NMC622, NMC622 with Al_2O_3 coating. (B, D, F) *In situ* FT-IR difference spectra in C=O stretching region on NMC622, NMC622 with Al_2O_3 coating electrodes during the 1st and 3rd cycle charging in LP57 electrolyte. ATR spectra (in black) for LP57 solutions.

3.2.2 *In situ* FT-IR measurements of concentrated electrolytes on NMC811 upon charging

We further examine the influence of carbonate solvent activity on the oxide-mediated electrolyte oxidation by changing electrolyte salt concentrations. Increasing the salt concentration in the electrolyte was found to reduce NMC811-mediated dehydrogenation of EC upon charging. *Ex situ* ATR spectra (Fig. 3-4 B & D) of EC:EMC 3:7 with 3.1 M

$LiPF_6$ revealed that increasing the salt concentration resulted in more Li^+-coordinated solvent molecules (Li^+-EC/EMC) but fewer free EC/EMC solvent molecules (low carbonate activity), in agreement with previous work.[130–133] NMC811 charged in the concentrated electrolyte (3.1 M $LiPF_6$ in EC/EMC), which contained fewer free EC or free EMC (molar fraction of free solvent in general concentrated electrolyte with dissociative salt is reported to be less than 10%)[134–138], did not show dehydrogenation or oligomerization products from EC or EMC in the FT-IR difference spectra (Fig. 3-4D) upon charging to 4.8 V_{Li}, unlike in LP57 (with 1 M $LiPF_6$) where EC became dehydrogenated as discussed before (Fig. 3-4B). Increasing the Li^+ salt concentration in the electrolyte decreased the carbonate activity in the electrolyte and enhanced the solvent stability against oxidative dehydrogenation on NMC811, which could potentially lead to stable cycling and longer cycle life for NMC811. This observation can interpret recent findings that increasing the $LiBF_4$[139–141] or $LiPF_6$ [142,143] concentration can increase capacity retention of Ni-rich NMC[139–141], and enhance the cycle life[142,144] since the dehydrogenation is suppressed by the decrease of free EC or EMC solvent activity in the concentrated electrolytes.

While NMC811 in LP57 showed large impedance growth during the first cycle charging, NMC811 in the concentrated electrolyte did not exhibit as large impedance growth and R_{CT+EEI} remained around 30-100 Ohm (Fig. 2-3c), which could be also be correlated with the more stable interface and lack of dehydrogenation from FT-IR result (Fig. 3-4D). This observation further supports the role of undesirable carbonate dehydrogenation in passivating the surface and increasing interfacial impedance, suggesting that lowering free

solvent activity could facilitate stable cycling of NMC811. For NMC111 and NMC622, R_{CT+EEI} stayed less than 50 Ohm through all the voltages (Fig. 2-3C) during the first cycle, which matched well with *in situ* FT-IR spectra that there was no profound solvent dehydrogenation in the first charging. The more stable interface and lower impedance growth is also in agreement with the better cycling stability of NMC111 and NMC622 than NMC811.[20]

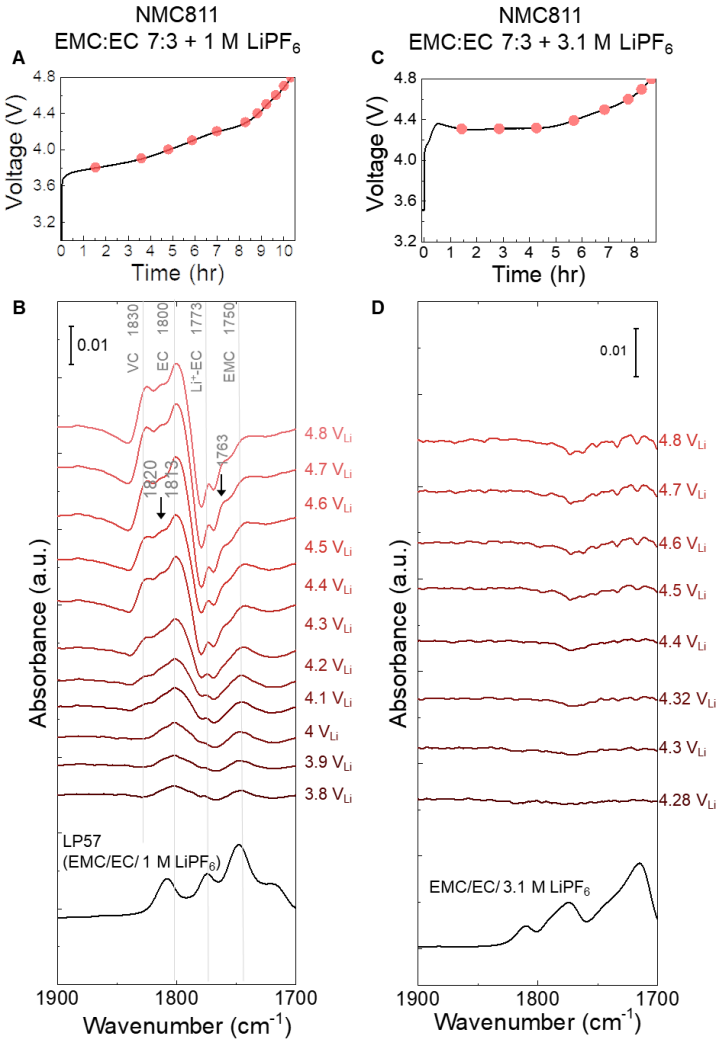

Fig. 3-4 *In situ* FT-IR measurements on NMC811 surfaces upon charging to 4.8 V_{Li} in 1 M $LiPF_6$ and in a concentrated (3.1 M) electrolyte. Voltage profile during charging of NMC811 (A) in LP57 and (C) concentrated electrolyte (EMC:EC with 3.1 M $LiPF_6$). (B, D) *In situ* FT-IR difference spectra in C=O stretching region (in red) on NMC811

during charging in the two electrolytes. *Ex situ* ATR spectra of LP57 and EMC:EC 7:3 with 3.1 M $LiPF_6$ are shown in black at the bottom of figures.

3.3 Stable EEI with fluorinated solvents and electrolyte additives[6]

In addition to other mitigation strategies, like coating[145] and Ni concentration gradient[22,68], several researchers have shown that additives[71,146,147] and fluorinated solvents[148] can be used to reduce impedance growth and increase capacity retention of Ni-rich NMC such as NMC811. For instance, electrolyte additives such as phenyl carbonates[73,149], i. e. methyl phenyl carbonate (MPC) and diphenyl carbonate (DPC), nitriles[72,150], prop-1-ene-1,3-sultone (PES)[75,151,152], and vinylene carbonate[151–154] have shown improved cycling performance of NMC111[72,73,154], NMC422[72,151] and NMC811[75,149,152] electrodes. Of significance, Dahn et al. have shown reduced impedance growth and better coulombic efficiency for NMC111/graphite[73] and NMC811/graphite[149] pouch cells by adding 1 wt% diphenyl carbonate additive in LP57 electrolyte (1 M $LiPF_6$ EC:EMC (3:7 wt:wt)). However, there is a lack of understanding on how additives modify the positive electrode/electrolyte interface (EEI) composition. The electrolyte additives can improve the cycling performance by hindering parasitic reactions at the positive electrode surfaces by developing a protective, stable electrode/electrolyte interface formed upon the additive electrochemical oxidation, as additives typically have lower electrochemical oxidation potentials than typical carbonate solvents such as ethylene carbonate (EC) and ethyl methyl

[6] Reproduced in part, with permission from Karayaylali, P.*, Zhang, Y.*, Giordano, L., Katayama, Y., Tatara, R., Yu, Y., Maglia, F., Jung, R. and Shao-Horn, Y., 2020. The role of diphenyl carbonate additive on the interfacial reactivity of positive electrodes in Li-ion batteries. *Journal of The Electrochemical Society*, *167*(4), p.040522. (* denotes corresponding author) © 2020 The Electrochemical Society ("ECS").

carbonate (EMC)[155]. Here we investigate and correlate the effect of additives on the electrode/electrolyte interface in the LP57 electrolyte (1 M $LiPF_6$ EC:EMC (3:7 wt:wt)). We selected diphenyl carbonate as a model additive system due to its enhanced cycling performance of NMC811 shown by Dahn et al.[149,73] We performed in situ FT-IR to understand the decomposition products of diphenyl carbonate additive and N,N-Dimethyl-trifluoromethane-sulfonamide ($DMCF_3SA$).

3.3.1 *In situ* FT-IR measurements on NMC811 electrodes using diphenyl carbonate additive

In-situ FTIR measurement (C=O region) on NMC811 surfaces further supported the suppression of EC dehydrogenation and stable EEI layer formation on these oxide surfaces when DPC additive is added to the electrolyte. In-situ FTIR NMC811/Li metal cell was charged to 4.4 V_{Li} (Fig. B-1 A) and 4.8 V_{Li} (Fig. 3-5 A). One small sharp peak at 1824 cm^{-1} became visible upon charging from OCV to 4.4 V_{Li} and became more pronounced with increasing potential, which is accompanied by a reduced intensity of diphenyl carbonate peaks at 1773 and 1760 cm^{-1}, indicating the electrochemical oxidation of DPC at earlier potentials (3.9 V_{Li}). The diphenyl carbonate electrochemical oxidation can be further supported by *in situ* FTIR spectra of Pt/Li metal cell[156], where it revealed onset potential of DPC oxidation around 4 V_{Li}, which is much earlier than EC or EMC oxidation. Unlike our previous work on in-situ FTIR cell[157] on NMC811 electrodes charged with LP57 electrolyte, in situ IR spectra with diphenyl carbonate additive revealed no evidence of EC dehydrogenation (1813 cm^{-1}) and oligomer formation (1820 cm^{-1}) on NMC811 surfaces. No significant changes were noted for the C=O region in the FTIR spectra during voltage

holding at 4.4 V_{Li} (Fig. B-1 B) or resting at OCV (Fig. B-1 C) after charging to 4.4 V_{Li}. The peak intensity of 1824 cm^{-1} peak did not change significantly with increasing time suggesting these species, which are related to DPC electrochemical oxidation, were anchored on the NMC811 surfaces (not diffused away), suggesting the formation of a stable EEI layer which prevents EC dehydrogenation on these surfaces. Next we discuss the possible physical origin for 1824 cm^{-1} peak on NMC811 surfaces.

Benzene derivatives, such as biphenyl[155] or diphenyl sulfide (DPDS)[158] have been reported as additives for positive electrodes, since their aromatic parts can polymerize to form a stable layer on positive electrode surfaces[159,160]. Zuo et al.[158] showed the formation of stable EEI layer through electrochemical oxidation of DPDS and DPDS polymerization on $Li_{1.2}Mn_{0.54}Ni_{0.13}Co_{0.13}O_2$ positive electrodes using X-ray Diffraction (XRD), Scanning Electron Microscope (SEM) and Energy-dispersive X-ray Spectroscopy (EDS). Abe et al.[155] reported less salt decomposition on $LiCoO_2$ surfaces when biphenyl is added to 1M $LiPF_6$- EC/MEC (3:7/ w:w) using X-ray Photoelectron Spectroscopy (XPS) and linked the lower salt decomposition with the earlier oxidation of biphenyl additive and the formation of a thin layer of organic species on $LiCoO_2$ surfaces. Similar to these previous works discussed above, we propose the formation of radicals through electrochemical oxidation of DPC, where these radicals can react with another DPC or EC molecule, forming polymers or oligomers. The formation of these polymers or oligomers through DPC electrochemical oxidation might be the physical origin of 1824 cm^{-1} peak in in situ FTIR measurements. These stable organic species can passivate the NMC surfaces and prevent EC dehydrogenation, which is detrimental for positive electrode surfaces. This hypothesis

is further supported by Dahn et al.'s[73,149] work where they showed lowest impedance growth using 1 wt % diphenyl carbonate additive for NMC111/graphite and NMC811/graphite pouch cells.

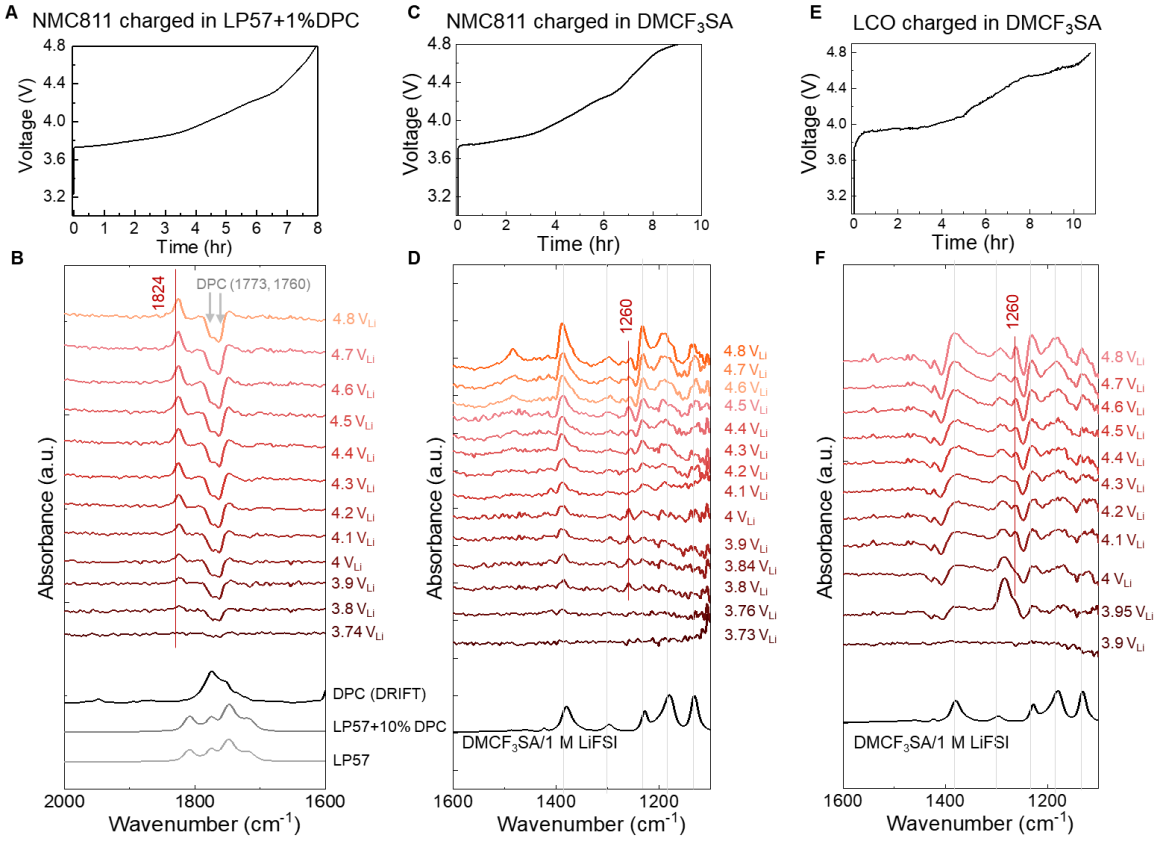

Fig. 3-5 Voltage profiles and *in situ* FT-IR for NMC811 and LCO with electrolyte additives and with fluorinated solvents. (A) Charging curve and (B) *in situ* FT-IR difference spectra from OCV to 4.8 V_{Li} for NMC811 in LP57 with 1 wt % DPC. (C, E) Charging curve and (D, F) *in situ* FT-IR difference spectra from OCV to 4.8 V_{Li} for NMC811 and LCO, respectively, in $DMCF_3SA$ with 1 M LiFSI. *Figures adapted with permission.*[156,161] *Copyright © 2020 The Electrochemical Society ("ECS"). Copyright © The Royal Society of Chemistry 2021.*

3.3.2 *In situ* FT-IR measurements on NMC811 and $LiCoO_2$ electrodes using $DMCF_3SA$-based electrolytes

There has been significant progress recently on a new class of electrolytes based on sulfonamides[79,162], with molecular structures similar as lithium imide salts such as lithium bis(trifluoromethanesulfonyl) imide (LiTFSI) and lithium bis(fluorosulfonyl)imide (LiFSI). Recent studies showed that *N*,*N*-Dimethyl-trifluoromethane-sulfonamide[148,162] ($DMCF_3SA$) based electrolyte could improve capacity retention for NMC811[148] and $LiCoO_2$ (LCO)[161] by suppressing cracking and improving their structural stability.

To understand the oxidation process of $DMCF_3SA$ based electrolyte on NMC811 surfaces, we performed *in situ* FT-IR to characterize the evolution of EEIs during galvanostatic charging to 4.8 V_{Li}. Upon charging NMC811 from OCV to 4.8 V_{Li} (Fig. 3-5 C), a peak at ~1260 cm^{-1} in the S=O region in the IR spectra was observed from 3.8 V_{Li} to 4.8 V_{Li} (Fig. 3-5 D). It could be attributed to the decomposition of LiFSI or $DMCF_3SA$ since they both have the S=O groups. This peak is electrode-independent: in LCO we similarly charged the electrode to 4.8 V_{Li} (Fig. 3-5 E), the same peak at ~1260 cm^{-1} was noted (Fig. 3-5 F), with obvious changes in the IR spectra from 3.9 V_{Li} to 4.2 V_{Li}. Upon further charging from 4.2 V_{Li} to 4.8 V_{Li} (Fig. 3-5 F), the spectra almost remained unchanged, indicating good chemical stability of the EEIs against oxidation.

The stability of the EEI was further confirmed by holding the potential at 4.8 V_{Li} for one hour and subsequent resting at OCV for one hour, where there was no significant change for the new species at 1260 cm^{-1} in the *in situ* spectra (Fig. 3-6). It indicates that once the EEI species is formed, it remains stable on the surface, which is similar to the case of LP57 with DPC additives.

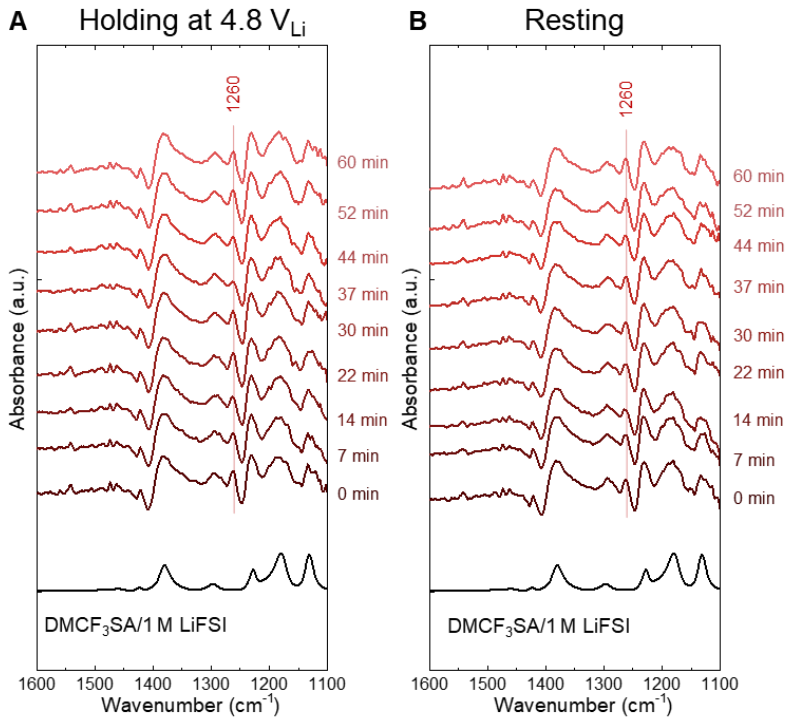

Fig. 3-6 *In situ* FT-IR for LCO in $DMCF_3SA$ with 1 M LiFSI, during (A) potential holding and (B) resting at OCV. *Figures adapted with permission.*[161] *Copyright © The Royal Society of Chemistry 2021.*

3.4 Conclusions

We interpreted the strategies for EEI design by tuning electrode and electrolyte activity, and through modified electrolytes to achieve a stable EEI. Through the *in situ* spectra on NMC surfaces, we tracked the interfacial reactions and understood the electrolyte decomposition mechanism on composite NMC811 powder surfaces in practical battery operations during galvanostatic charging. The decomposition was oxide-dependent, and no dehydrogenation was found for NMC111 or modified NMC surface by coatings such as Al_2O_3. For low-covalency electrode materials such as NMC111 or Al_2O_3, which are less reactive, carbonate is more stable against dehydrogenation, and the undesirable reactions to form passivating layers barely happen, leading to lower impedance and better capacity

retention. Further, the dehydrogenation of EC was not observed in the concentrated electrolyte (EC/EMC with 3.1 M $LiPF_6$) on NMC811, indicating that the dehydrogenation of carbonates can be suppressed by increasing lithium coordination with solvents. Finally, DPC additives or $DMCF_3SA$ solvents could form a stable EEI on NMC811 or LCO surfaces, preventing further oxidation of electrolytes and stabilize the interface. While dehydrogenation of carbonates (EC and EMC) on the NMC811 surface was found to accompany with rapid growth of interfacial impedance with increasing charging voltage measured from EIS, those electrode-electrolyte combinations without dehydrogenation were found to have no significant impedance growth. These findings provide rational design of Ni-rich positive electrodes, such as NMC811, for Li-ion batteries with high cycling stability.

Chapter 4. Lithium intercalation by coupled ion-electron transfer

4.1 Introduction

Ion intercalation chemistry is central to various emerging technologies that address critical needs in energy, sustainability and computation [163]. As recognized by the 2019 Nobel Prize in Chemistry to Goodenough, Whittingham and Yoshino, Li-ion batteries have already revolutionized portable electronics and are poised to enable widespread electrified transportation [16]. Ion-intercalation materials also driving advances in other types of rechargeable batteries [164], electrocatalysis [165], electrochromics [166], ionic separations [167], and artificial synapses [168].

Despite the importance of ion intercalation, its reaction mechanism has not yet been established. Interfacial charge transfer is still difficult to simulate at the molecular scale (in contrast to solid-state charge transport, which can be predicted from first principles [169]). Instead, the empirical Butler-Volmer (BV) equation is widely used to infer intercalation rates from current-voltage data or electrochemical impedance spectroscopy [27] based on a classical model of ion transfer (IT) [170], but fitted values of the exchange current density can differ by orders of magnitude for the same materials (Table C-1,C-2) and are often not identifiable [171], suggesting the need for an improved microscopic model.

In this study, we perform systematic experiments to determine the reaction mechanism for lithium intercalation in battery electrodes. Our work is motivated by the recent hypothesis that ion intercalation may be limited by electron transfer (ET) to a redox state in the host solid [172]. In the original theory, honored by the 1992 Nobel Prize in Chemistry [173], Marcus

[174] postulated that ET occurs by quantum tunneling in response to solvent reorganization in polar liquids [175], but similar ideas can also be applied to solid electrodes. In the case of carbon-coated $LiFePO_4$ (LFP), a popular Li-ion battery cathode material, it was proposed the Li^+ intercalation may be limited by ET from the metallic carbon coating to the Fe^{3+}/Fe^{2+} redox site in the $FePO_4$ crystal [172]. Marcus-Hush-Chidsey (MHC) kinetics for ET at metal electrodes [176–178] was shown to predict the curvature of Tafel plots at different temperatures (obtained by fitting chronoamperometry data for LFP porous electrodes to a population dynamics model [179]) using only the predicted outer-sphere reorganization energy [173] without any adjustable parameters [172].

Despite this evidence, however, the theory of ET-limited lithium intercalation was not widely accepted. Another study soon showed that nonlinear impedance data for LFP could be fitted to BV kinetics, albeit with an empirical "film resistance" [180] (also considered below). Evidence also grew that IT influences Li-ion battery nonequilibrium thermodynamics [170], since the ET hypothesis (by itself) fails to predict the strong "electro-autocatalytic" concentration-dependence of the ion intercalation rate [181], revealed by *in operando* x-ray imaging and shown to control interfacial stability [182–184]. Auto-inhibitory lithium insertion was shown to suppress phase separation in LFP nanoparticles [182], while autocatalytic lithium extraction was shown to drive heterogeneity in metal-oxide porous electrodes [183] (as we also observe in our experiments below).

These debates led to the idea that ET and IT might occur simultaneously. A general theory of coupled ion-electron transfer (CIET) was recently developed and applied to LFP [185]. In

contrast to coupled proton-electron transfer (CPET) [186–188], where both protons and electrons obey quantum mechanics, the ions in CIET are treated classically via non-equilibrium thermodynamics (16). The theory accurately predicts the concentration-dependent exchange current from x-ray imaging [182], as well as the raw data from LFP chronoamperometry [172], which cannot be fitted by the BV model with film resistance *(13)*. CIET kinetics were also implemented in Multiphase Porous Electrode Theory (MPET) for Li-ion battery simulations [189], prior to the development of the microscopic theory [185]. Nevertheless, the BV equation is still ubiquitous in battery modeling with fitted series resistances that may mask the true underlying reaction kinetics.

Here, we provide the first comprehensive experimental evidence that lithium intercalation occurs by CIET for a wide range of Li-ion battery materials. First, we develop a voltage-pulse method to measure lithium insertion and extraction rates versus over-potential, ion concentration and temperature for a variety of common battery electrode and electrolyte materials. We find a remarkable collapse of all the data with CIET theory using only three parameters per electrode/electrolyte pair, the Marcus reorganization energy and a rate-constant pre-factor that depends on both ET (reorganization) and IT energies. Bayesian analysis clearly selects CIET over BV with film resistance as the most likely model to describe all the data with the fewest adjustable parameters. Next, we analyze a key prediction of the theory that the reaction-limited current varies linearly with lithium vacancy concentration. This implies a linear decrease in reaction-limited battery capacity with increasing current, which we verify for eight popular battery materials in porous-electrode cells. These results provide a fundamental understanding of ion intercalation

kinetics and new directions for interfacial engineering of Li-ion batteries to boost their power density.

4.2 Kinetics of Li^+ intercalation in layered-oxide

We first determine the lithium-ion insertion and extraction rates as a function of overpotential and lithium concentration (x) in thin Li_xCoO_2 (LCO) and $Li_xNi_{1/3}Co_{1/3}Mn_{1/3}O_2$ (NMC111) porous electrodes using a three-electrode setup (Fig. 4-1A) with Li-metal counter and reference electrodes. Currents are measured for a series of applied potential steps (Fig. 4-1B) over a range of lithium concentrations (Fig. C-1, C-2). For each voltage step, the cell is first discharged/charged potentiostatically and then gradually charged/discharged to restore the lithium concentration, as verified by the corresponding equilibrium voltages (V_{eq}) (Fig. C-3). (See Materials and Methods for more details.) The measurements are not limited by lithium-ion diffusion since the maximum operating currents are at least an order of magnitude below both the solid and liquid diffusion-limited currents (Fig. C-4). We further exclude rate limitation from the Li-metal counter electrode, as it exhibits much smaller overpotentials than the working electrodes (Fig. C-5).

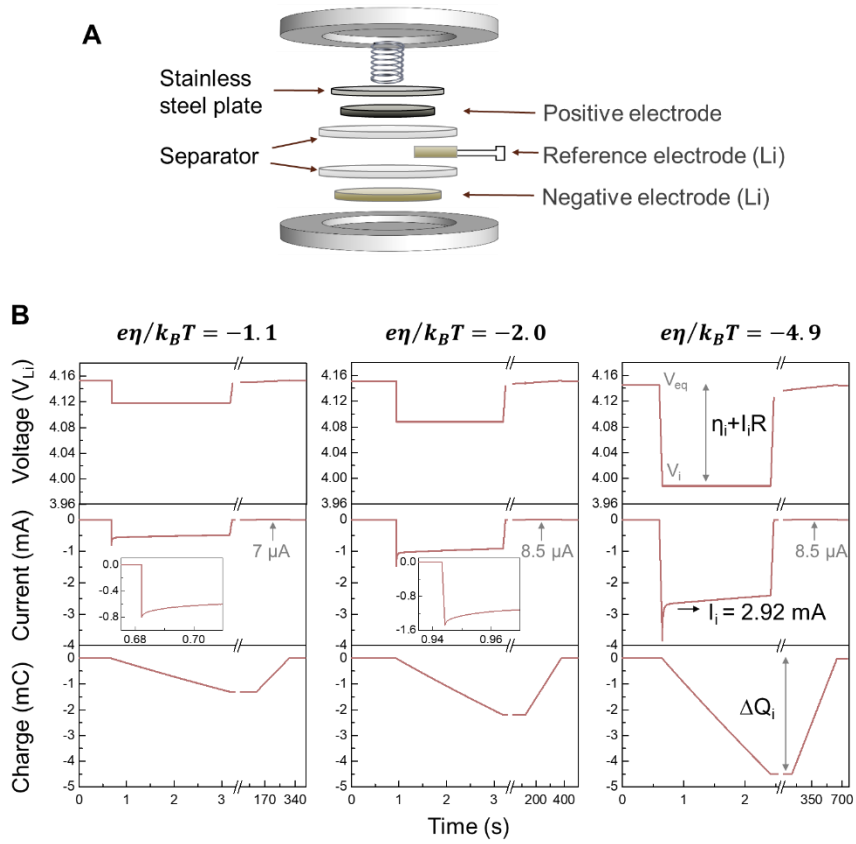

Fig. 4-1 Experimental measurements for concentration-dependent kinetics of Li^+ intercalation in Li_xCoO_2 or NMC111. (A) Three-electrode cell setup for current-voltage response measurements. (B) Schematics for three representative charge-adjusted voltage steps at a fixed Li^+-concentration (x=0.5) for $Li_{0.5}CoO_2$, corresponding to a fixed equilibrium voltage ($\boldsymbol{V_{eq}}$). (Note different time scales on the x-axis.) Zoomed-in current responses within the initial 50 ms and electrochemical impedance spectra (EIS) are provided in Figs. C-1, C-2, and C-6. During the time period when the initial current response is taken, the change in x is $\Delta x < 10^{-4}$ (Fig. C-3 D-E). Loading of Li_xCoO_2 in the positive electrode is 1.3 mg/cm$^2_{geo}$, and the electrolyte is EMC:EC (7:3) with 1 M $LiClO_4$ salt.

The Tafel plots (Fig. 4-2 A-B) for lithium-ion insertion/extraction in LCO and NMC111 exhibit similar curved shapes, consistent with ET limitation [172,177], as well as a clear ion concentration dependence which was not resolved in the original experiments on LFP [172]: The insertion current density (normalized to the oxide surface area) decreases linearly with

increasing lithium concentration ($x = 0.5$, 0.6, 0.7, and 0.8), while extraction shows a similar, but somewhat weaker concentration dependence. Moreover, the reaction kinetics are strongly influenced by the electrolyte composition, where the rate measured in EC:EMC (3:7) with 1 M $LiClO_4$ is much greater than in 1 M $LiPF_6$ for the same electrodes (Fig. 4-2 A-B, Fig. C-7).

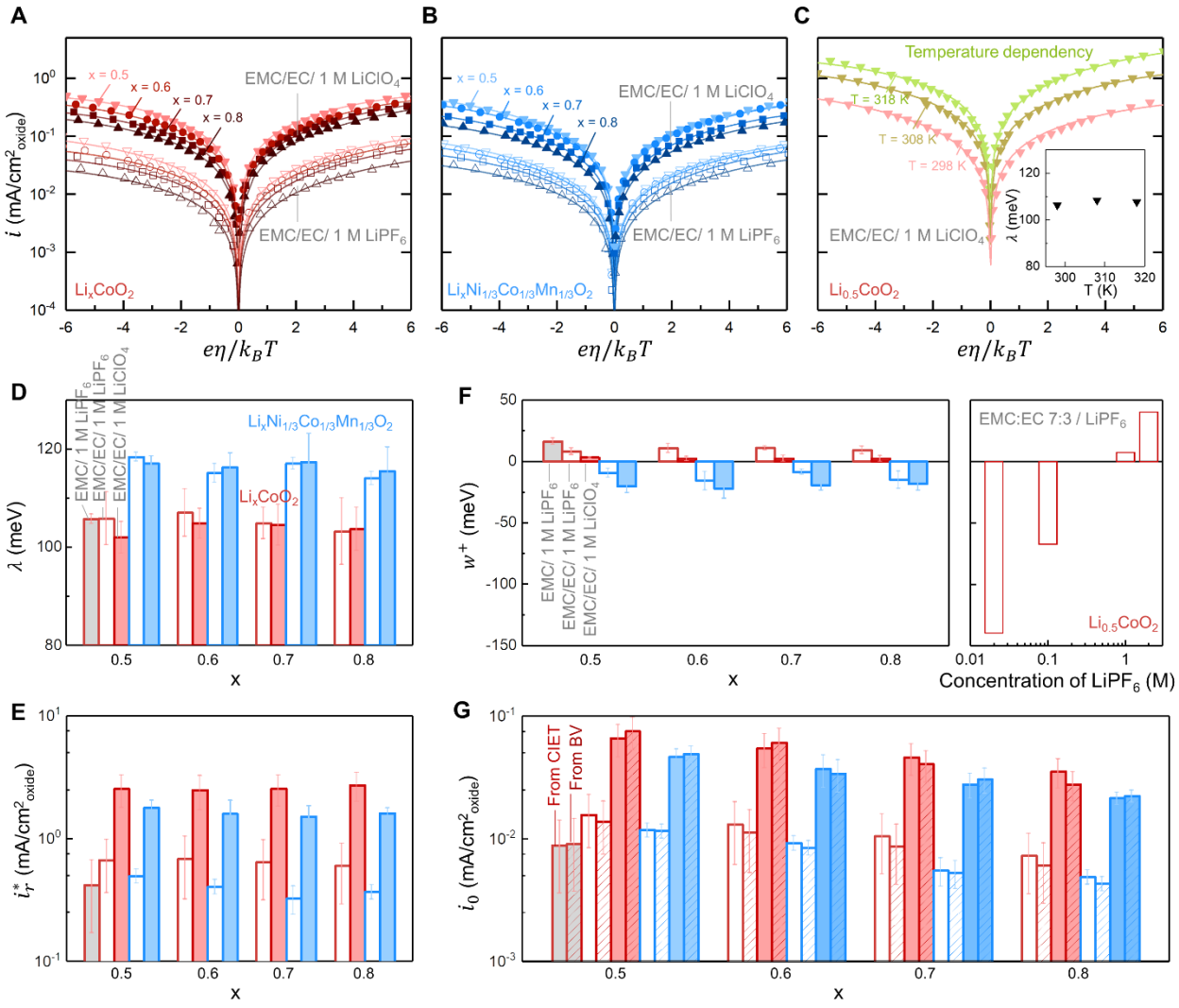

Fig. 4-2 Intercalation current versus overpotential at different lithium-ion concentrations and fitted parameters from CIET. (A and B) Electrochemical response of Li_xCoO_2 (LCO) and $\mathbf{Li_xNi_{1/3}Co_{1/3}Mn_{1/3}O_2}$ (NMC111) from the charge-adjusted Tafel analysis (▽ for $\mathbf{x = 0.5}$; ○ for $\mathbf{x = 0.6}$; □ for $\mathbf{x = 0.7}$; △ for $\mathbf{x = 0.8}$). Two sets of

electrolytes are used, 1 M $LiClO_4$ (filled symbols) and 1 M $LiPF_6$ (open symbols) with solvent EMC:EC = **7**:**3**, respectively. Electrode loadings are 1-2 mg_{active}/cm^2_{geo} (Table C-3). Current densities are calculated from specific surface areas estimated by nitrogen adsorption. The lines represent the CIET theory predictions, from which the reaction-limited current $\boldsymbol{i_r^*}$, reorganization energy $\boldsymbol{\lambda}$, and work of Li^+ surface adsorption $\boldsymbol{w_+}$ are obtained. (C) Electrochemical response for $Li_{0.5}CoO_2$ at three different temperatures in 1M $LiClO_4$ with solvent EMC:EC = **7**:**3** with nearly constant values of the reorganization energy $\boldsymbol{\lambda}$ (inset). (D-F) Fitted reorganization energy $\boldsymbol{\lambda}$, current density prefactor $\boldsymbol{i_r^*}$, and work of Li^+ surface adsorption $\boldsymbol{w_+}$, for CIET in Li_xCoO_2 (red) and NMC111 (blue) for different electrolytes including 1 M $LiClO_4$ in EMC:EC (**7**:**3**) (color filled), 1 M $LiPF_6$ in EMC:EC (**7**:**3**) (empty filled), and 1 M $LiPF_6$ in EMC (grey filled). (G) Predicted exchange current density $\boldsymbol{i_0}$ from CIET for Li_xCoO_2 (red) and NMC111 (blue), and $\boldsymbol{i_0}$ fitted from Butler-Volmer kinetics plotted beside with lightly-textured bars. Electrolyte shadings in (G) follow those in (D-F). All error bars are obtained from at least two independent measurements.

Existing models of ET and IT are unable to explain the data. Pure BV kinetics of IT are invalidated by significant deviations from constant Tafel slopes at large overpotentials, $|\eta| > 2 \quad k_BT/e$ (Figs. C-8, C-9). Adding an empirical film resistance for each concentration [177] (BV+film) allows the Tafel curvature to be reproduced (Fig. C-10A and Fig. C-11A), but the fitted resistances vary strongly with the solid-state ion fraction *x* (Fig. C-10D and Fig. C-11D) and thus cannot be attributed to a resistive "film" on the solid surface. In contrast, the Tafel curvature can be captured by MHC kinetics [177,190] (Fig. C-12, Fig. C-13) by fitting a single reorganization energy λ for each electrode material, consistent with ET limitation in the solid [172], but again the strong ion-concentration dependence, inter-twined with the overpotential dependence, cannot be explained.

4.3 Proposed reaction mechanism and theory of coupled ion-electron transfer

The theory of CIET [185] resolves these paradoxes by postulating that IT and ET occur in a concerted fashion. The CIET mechanism is governed by a two-dimensional free-energy landscape (Fig. 4-3A) of excess chemical potential [170] with an ion-position coordinate ξ

for classical IT and a solvent-reorganization coordinate *y* for quantum-mechanical ET [185]. In the case of lithium insertion into a transition metal oxide (Fig. 4-3), solvated Li^+ from the electrolyte reservoir is first adsorbed at the solid/electrolyte interface via a fast reaction to form the oxidized (Ox) state of the Faradaic reaction [170], together with the oxidized cation in the solid, M^{z_M}, such as cobalt in $Co^{4+}(O^{2-})_2$ (Fig. 4-3B). The reduced state (Red) of the reaction is a neutral polaron [185], consisting of an inserted lithium ion and a neighboring reduced cation, M^{z_M-1}, such as Li^+-$Co^{3+}(O^{2-})_2$.

In response to a negative overpotential (an applied increase in the chemical potential of Ox versus Red per negative electron charge [170]), adsorbed Li^+can shed the remainder of its solvation shell and transfer into a nearby vacancy in the host crystal. At the same time, the surroundings of M^{z_M} near the transferring ion, including electronic wavefunctions around the cation and phonons in the crystal lattice, can become spontaneously reorganized to facilitate ET (Fig. 4-3C). Since electron transfer is known to occur by quantum tunneling only if the Ox and Red states share at least one energy level [175,191], the reduction of M^{z_M} is mostly likely to occur when the Li^+ ion reaches the CIET transition-state position, and a polaron pair, Li^+-M^{z_M-1}, is formed in the solid (Fig. 4-3D) [185]. States with only IT (Fig. 4-3E) or only ET (Fig. 4-3F) are at much higher energy levels, dominated by the electrostatic energy of the separated polaron, and therefore not favored.

Although the preceding example involves localized ET to a reduced solid cation, the theory also applies for ET to delocalized states in a metallic or semi-conducting intercalation host [185]. For example, when lithium intercalates into graphite, an electron is donated to the π-

orbital conduction band, but there are also significant lattice distortions and redistributed electron density in the valence band that form a polaron with the inserted Li^+ ion [192,193]. The theory only assumes that that the reduced and oxidized electronic states are weakly coupled.

Theory of CIET

The Faradaic reduction current density for symmetric CIET at an electrode has the general form [185,189]:

$$i = i_r \int_{-\infty}^{\infty} \left[\tilde{c}_O \, n_e(\varepsilon) \, p_{red}(\varepsilon) - \tilde{c}_R \left(1 - n_e(\varepsilon)\right) p_{ox}(\varepsilon)\right] \rho(\varepsilon) d\varepsilon \qquad \text{(Eq. 1)}$$

where $\tilde{c}_O$ and $\tilde{c}_R$ are the dimensionless concentrations of the oxidized and reduced ionic states; $n_e(\varepsilon) = 1/(1 + e^{\varepsilon/k_B T})$ is the Fermi distribution; $\rho(\varepsilon)$ is the electronic density of states (band structure) of the electrode; and $p_{red}(\varepsilon)$ and $p_{ox}(\varepsilon)$ are the normalized ET probabilities of reduction and oxidation, respectively, involving an electron of energy ε relative to Fermi level. The prefactor can be approximated as [185], $i_r = (e k_0 H_{DA}^2 / \hbar \nu_{\ddagger}) e^{-\mu_{\ddagger}^{ex}/k_B T}$, where k_0 is a reaction rate constant, proportional to the attempt frequency; H_{DA} is the electronic coupling between the electron donor and acceptor in the oxidized and reduced states, respectively; h is Planck's constant ($\hbar = h/2\pi$); $\nu_{\ddagger}$ is the vibrational frequency along the harmonic ET reaction coordinate (y); and $\mu_{\ddagger}^{ex}$ is the ionic excess chemical potential of the CIET transition state. In the harmonic approximation of Marcus for weakly coupled electronic states, the ET probabilities take the following Gaussian form [173–176]:

$$p_{\frac{red}{ox}} = \frac{1}{\sqrt{4\pi\lambda k_B T}} \exp\left[-\frac{\left(\lambda \pm e\eta_f \mp \varepsilon\right)^2}{4\lambda k_B T}\right] \qquad \text{(Eq. 2)}$$

where λ is the reorganization energy of the solid host; η is the applied overpotential, which shifts the electronic band structure with respect to equilibrium; and η_f is the "formal overpotential" [175,185],

$$\eta_f = \eta + \frac{k_B T}{e} \ln\left(\frac{\tilde{c}_O}{\tilde{c}_R}\right) + i\, R_c \qquad \text{(Eq. 3)}$$

which excludes contributions from dilute-solution entropies of the redox species [170], as well as the voltage drop across the ionic resistance R_c of any surface coating on the electrode, such as carbon on LFP [172]. (The theory does not include any "film resistance" for uncoated electrodes.)

In the case of lithium intercalation, we write $\tilde{c}_O = \tilde{c}_+$, the fractional coverage of reactive surface sites by adsorbed Li^+, and $\tilde{c}_R = x$, the filling fraction of inserted Li^+ in the electrode host material. Assuming that surface adsorption is fast relative to CIET (the proposed rate-limiting step), the surface coverage of ions is related to thermodynamic properties of the nearby bulk electrolyte by an equilibrium isotherm, such as the Langmuir isotherm for non-interacting surface sites [170],

$$\tilde{c}_+ = \frac{a_+(\tilde{c},T)\, e^{-\tilde{w}_+}}{1 + a_+(\tilde{c},T)\, e^{-\tilde{w}_+}} \qquad \text{(Eq. 4)}$$

where $a_+(\tilde{c},T)$ is the activity and $\tilde{c}$ is the molar concentration of the Li^+ in the bulk electrolyte ($a_+ = \tilde{c}$ in the dilute limit) and w_+ is the work of Li^+ surface adsorption ($\tilde{w}_+ = w_+/k_B T$), which accounts for partial de-solvation and Frumkin effects of ion transfer across the electric double layer [194].

We now describe the CIET transition state for lithium intercalation. Our key approximation, $\mu_{\ddagger}^{ex} = \Delta E_{\ddagger} - s\, k_B \mathrm{T} \ln(1-x)$, expresses that the transition state excludes one site ($s = 1$) in the host solid, or equivalently, requires one vacancy [170] (Fig. 4-3G). In addition, material properties of the electrode/electrolyte interface, such as dielectric constants and crystal structure, enter through the CIET energy barrier, $\Delta E_{\ddagger} \approx \alpha_{IT} \Delta E_{IT}$, , which may be approximated as a fraction α_{IT} of the ion-transfer energy, ΔE_{IT}, typically dominated by the electrostatic energy of separating the ion-electron pair [185]. This allows us to write $i_r = i_r^* (1-x)$, where $i_r^* = (e k_0 H_{DA}^2 / \hbar v_{\ddagger}) e^{-\alpha_{IT} \Delta E_{IT} / k_B T}$ (Eq. S2).

Finally, we consider a metallic electrode (or coating [172]), $\rho(\varepsilon)$ =constant and approximate the integral in Eq. (1) for $\lambda > k_B T$ [185,189,190] to arrive at our final CIET rate expression,

$$i(\eta, x, \tilde{c}_+) \approx i_r^* (1-x) \left(\frac{\tilde{c}_+}{1+e^{\tilde{\eta}_f}} - \frac{x}{1+e^{-\tilde{\eta}_f}} \right) \mathrm{erfc} \left[\frac{\tilde{\lambda} - \sqrt{1+\sqrt{\tilde{\lambda}}+\tilde{\eta}_f^2}}{2\sqrt{\tilde{\lambda}}} \right] \qquad \text{(Eq. 5)}$$

where $\tilde{\eta}_f = e\eta_f / k_B T$ and $\tilde{\lambda} = \lambda / k_B T$. In contrast to BV kinetics, the CIET rate is non-separable in the variables $(\eta, x, \tilde{c}_+)$ and predicts reaction-limited currents for large positive and negative overpotentials:

$$i(\eta, x, \tilde{c}_+) \sim \begin{cases} i_r^* (1-x) \tilde{c}_+, & \text{as } \eta \to -\infty \quad (\mathrm{Li}^+ \text{ insertion}) \\ -i_r^* (1-x) x\,, & \text{as } \eta \to \infty \quad (\mathrm{Li}^+ \text{ extraction}) \end{cases} \qquad \text{(Eq. 6)}$$

The exchange current density is also non-separable

$$i_0 = i_r^* (1-x) x \left(\frac{\tilde{c}_+}{x+\tilde{c}_+} \right) \mathrm{erfc} \left[\frac{\tilde{\lambda} - \sqrt{1+\sqrt{\tilde{\lambda}}+\ln^2\left(\frac{\tilde{c}_+}{x}\right)}}{2\sqrt{\tilde{\lambda}}} \right] \qquad \text{(Eq. 7)}$$

for CIET at small overpotentials ($-i \sim i_0\tilde{\eta}$ as $|\tilde{\eta}| \to 0$, $\tilde{\eta} = e\eta/k_BT$). (For more general formulae, see Supplementary Notes 1 and 2.)

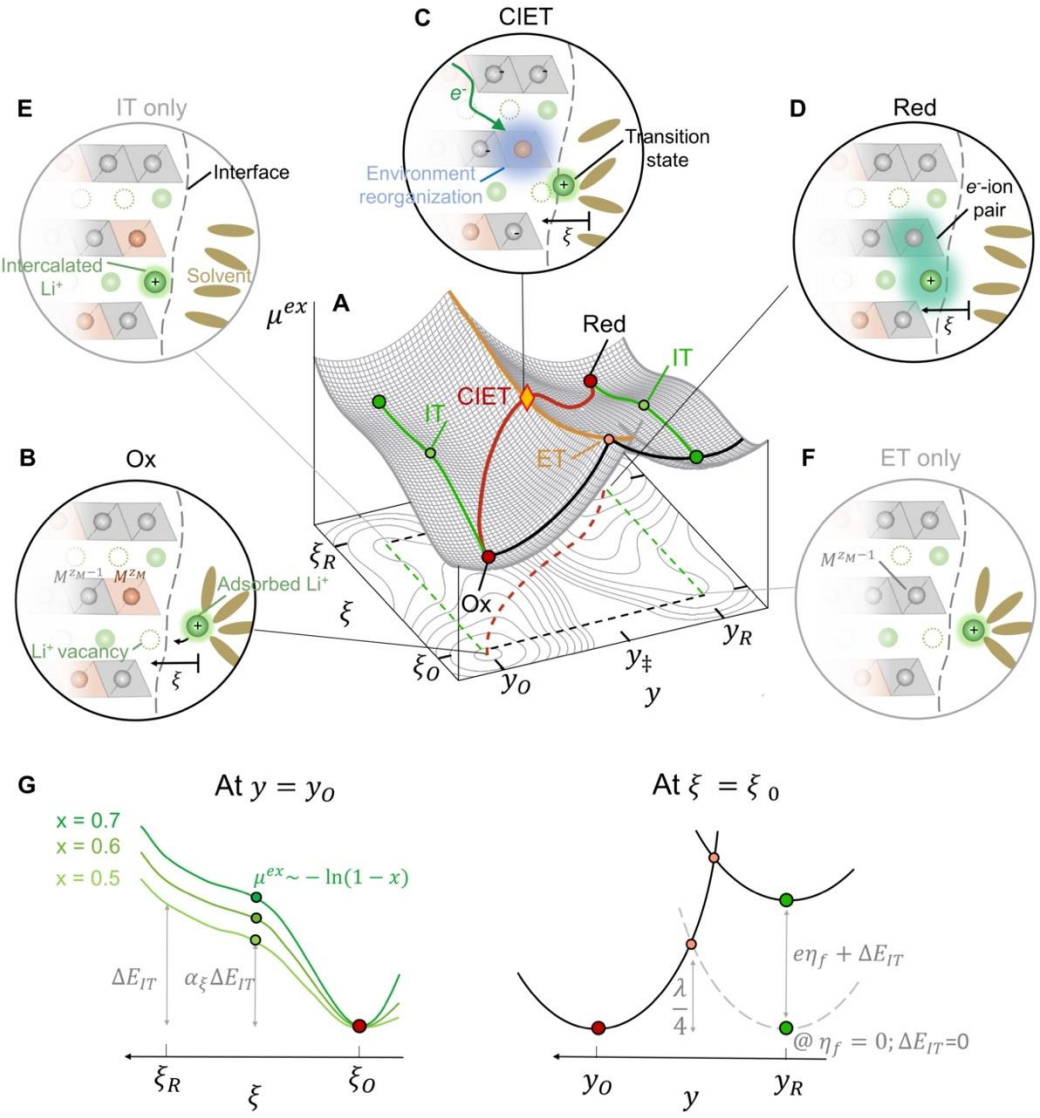

Fig. 4-3 Proposed mechanism for lithium intercalation. (A) Two-dimensional landscape of excess chemical potential in the Faradaic reaction [170] expressed in terms of a Li^+ position coordinate **ξ** for classical ion transfer (IT) and an reorganization coordinate ***y*** for quantum-mechanical electron transfer (ET) [185], adapted from *(1)*. There are four local minima: (B) the oxidized state (Ox), consisting of an adsorbed Li^+ on the electrode surface and a delocalized electron in the electrode or coating; (D) the reduced state (Red), consisting of an inserted Li^+ forming a polaron with the donated electron and local lattice distortion; (E) a high-energy state of Li^+ IT without ET on the (green) path of constant y; and (F) another high-energy state of ET without IT on the (black) path at constant **ξ**.

The lowest energy barrier (C) occurs along the (red) path of coupled ion-electron transfer (CIET). (G) Projected two-dimensional energy landscape for only the IT at $\boldsymbol{y = y_O}$ (green, left), or for only the ET at $\boldsymbol{\xi = \xi_O}$ (black, right), adapted from Ref [185], where $\boldsymbol{\Delta E_{IT}}$ is the IT energy which contributes a fraction $\boldsymbol{\alpha_\xi \Delta E_{IT}}$ to the CIET barrier, $\boldsymbol{\mu_\ddagger^{ex} \sim -\ln(1-x)}$ is entropic contribution for a vacancy, and $\boldsymbol{\eta_f}$ is the formal overpotential.

In summary, our model of ion intercalation, Eqs. 3-5, has only two parameters for the CIET reaction – the reorganization energy, $\tilde{\lambda}$, for ET into the solid electrode [172] and the reaction-limited current prefactor, i_r^*, which depends on the classical IT barrier and the quantum ET coupling [185] – and one parameter for fast ion adsorption from the electrolyte to the reaction site – the work of surface adsorption, $\widetilde{w}_+$. (If a surface coating is present, its ionic resistance, R_c, is an optional fourth parameter). Each parameter is rooted in microscopic physics, which can be predicted from first principles or inferred from experimental data.

4.4 Discussion

4.4.1 Statistical analysis for diverse electrodes and electrolytes

In order to test the CIET hypothesis, we first perform non-linear regression on the current-overpotential data using the theory (Eq. 5) with three adjustable parameters for each electrode/electrolyte pair and each temperature (for all lithium concentrations): the reorganization energy λ, current density prefactor i_r^*, and work of Li^+ surface adsorption w_+ (Fig. 4-2 D-F). Notably, we do not fit any series resistance R_c for uncoated electrode materials. The CIET fits for LCO and NCM111 shown in Fig. 4-2 A-B are in excellent agreement with the experimental data. In particular, the concentration dependence at large overpotentials is clearly described by the limits in Eq. 6, including the prefactor of (1-x) representing a crystal vacancy for IT. For all combinations of electrodes, electrolytes, and

temperatures, the ratios of experimental and best-fit CIET current densities (without taking logarithms) are all centered around 1.0 with standard deviation less than 11% (Fig. C-14 and Fig. 4-4D right inset). The largest relative errors arise as $\tilde{\eta} \to 0$ due to division by small uncertain numbers, but typical errors are very small (<7.5% for $|\tilde{\eta}| > 2$, Fig. C-14).

Further support to the CIET formulism for the (de)intercalation kinetics comes from temperature-independent reorganization energy (Fig. 4-2C) of $Li_{0.5}CoO_2$ measured at different temperatures ($T = 298$, 308, and 318 K) in 1 M $LiClO_4$ with EMC:EC (7:3), as expected for classical Marcus electron transfer theory [173,175,195] and consistent with prior results on LFP [172]. Fitting the temperature dependent plots with BV+film, however, yields varying film resistances without any theoretical explanation (Fig. C-15).

Next, we perform Bayesian inference to determine which model is most likely to predict the data, using the fewest adjustable parameters to achieve the best overall fit (Supplementary Note 3). Compared to existing models (BV, BV+film, BV+film with fixed α = 0.5), CIET has the lowest value of the Bayesian information criterion (BIC) for all the LCO and NCM111 data (Fig. 4-4D left inset) and fits considerably better (Fig. C-16), while BV+film models overfit the data with an adjustable film resistance for each curve. CIET also fits well to experiments upon expanding our dataset to span a representative set of Li-ion battery materials (Fig. 4-4A, Fig. C-17 to Fig. C-22), including four popular cathodes, LCO, NMC111 (Fig. 4-2), $Li_xNi_{0.8}Mn_{0.1}Co_{0.1}O_2$ (NMC811, Fig. C-17), LFP (Fig. 4-4A, Fig. C-18, Fig. C-19), and the standard graphite anode, Li_xC_6 (Fig. C-20 to Fig. C-22), in the same EMC:EC (7:3) with 1 M $LiClO_4$ electrolyte. For LFP, which has carbon coating,

and Li_xC_6, which has a solid-electrolyte interphase, CIET with film resistance R_c is more physically meaningful and indeed yields the lowest BIC values (Fig. C-19D, Fig. C-22D). Finally, we visually demonstrate the accuracy of CIET theory by scaling the data to the reaction-limited currents for each electrode/electrolyte pair. The scaled data collapses at large overpotentials (Fig. 4-4D) and falls onto the predicted master curves (shown in Fig. C-23 with offsets for clearly), governed by the fitted reorganization energies (below). The somewhat larger spread of the data for ion extraction ($\eta > 0$) versus insertion ($\eta < 0$) insertion is likely due to particle size heterogeneity (Fig. C-24) and concentration heterogeneity from electro-autocatalysis [181–183].

4.4.2 Physical validation of the fitted parameters

The fitted parameters (λ, i_r^*, w_+) are generally consistent with estimates from CIET theory. A key prediction is that the reorganization energy λ is a constant material property of the electrode. We have already seen that λ is temperature independent (Fig. 4-2C), and we find no dependence on lithium concentration or the electrolyte (Fig. 4-2D). Moreover, the fitted values (Fig. 4-4C) are similar for LCO ($\lambda \simeq 4.08\, k_BT = 0.104$ eV), NMC111 ($\lambda \simeq 4.53\, k_BT = 0.116$ eV), and NMC811 ($\lambda \simeq 4.84\, k_BT = 0.124$ eV), and larger for LFP ($\lambda \simeq 5.70\, k_BT = 0.147$ eV) and Li_xC_6 ($\lambda \simeq 7.17\, k_BT = 0.184$ eV). Intercalation materials with smaller λ (LCO, NMC111, NMC811) exhibit smaller Tafel curvatures and larger normalized current densities in Fig. 4-4D than those with larger λ (LFP, graphite). Consistent with CIET in a crystal lattice [172], fitted λ is close to the predicted Marcus outer-sphere reorganization energy (Eq. S9) for all electrodes (Table C-4) [175]. For example, using Co-O bond length of $LiCoO_2$ (0.19 nm)[196] as a_0 and d (Supplementary Note 4), we estimate

$\lambda \simeq 3.5\ k_BT = 0.9$ eV for $LiCoO_2$, in good agreement with the fitted value. As expected, the crystal reorganization energies are smaller than liquid outer-sphere reactions, such as $[Fe(CN)_6]^{3-}/[Fe(CN)_6]^{4-}$ redox (0.2-0.6 eV) [197], and inner-sphere hydrogen evolution and oxidation reactions (0.4-1.2 eV) [198].

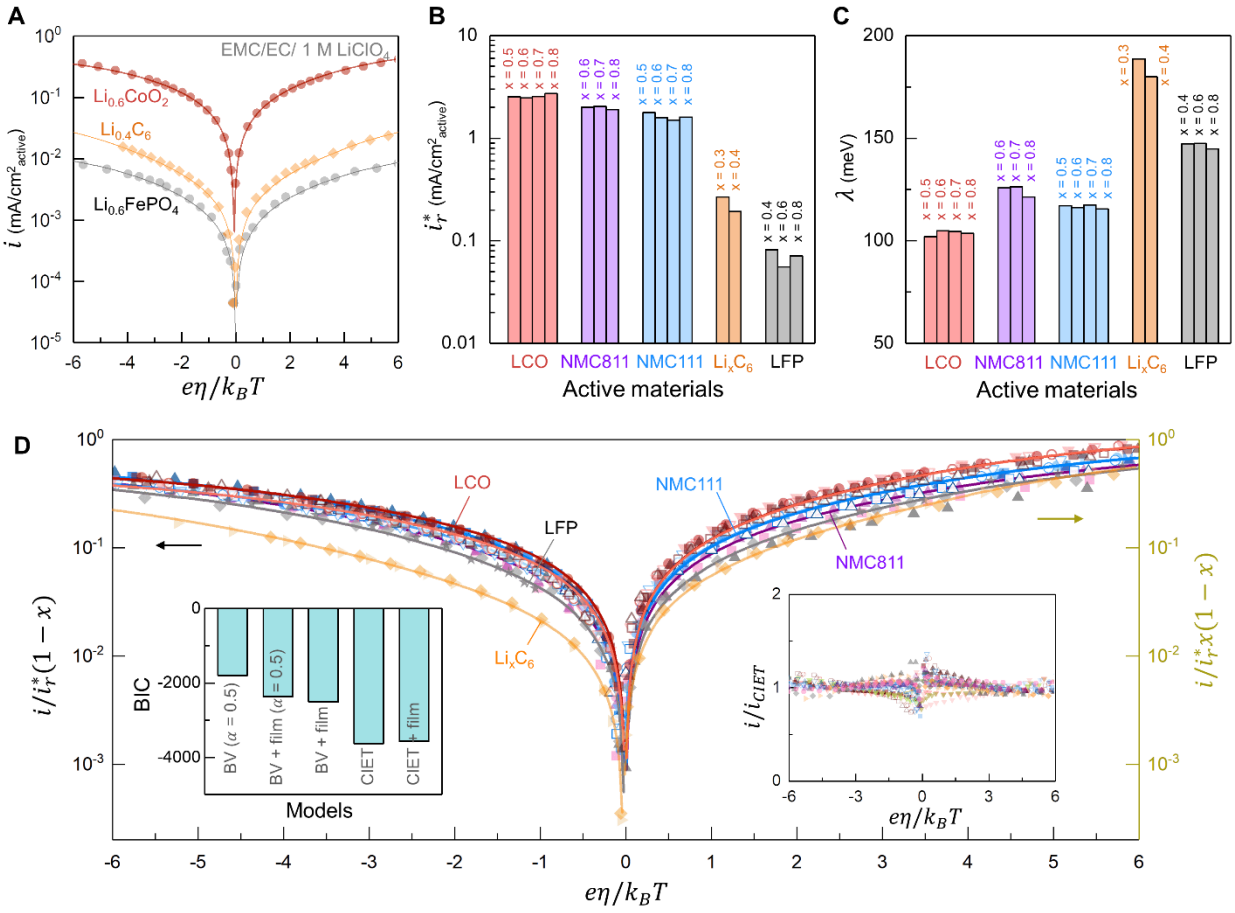

Fig. 4-4 Fitted parameters, data collapse and Bayesian model selection. (A) Comparison of electrochemical response of $Li_{0.6}CoO_2$, $Li_{0.6}FePO_4$, and $Li_{0.4}C_6$. All other concentrations measured are provided in Fig. C-18 to Fig. C-21. For graphite, the applied potential for intercalation is kept above 0 V_{Li} ($\boldsymbol{e\eta/k_BT > -4}$) to avoid Li plating. Electrolyte is 1 M $LiClO_4$ in EMC:EC (**7**: **3**). (B-C) Fitted $\boldsymbol{i_r^*}$ and $\boldsymbol{\lambda}$ for LCO, NMC111, NMC811, LFP, and graphite. (D) Data collapse with CIET theory. Current density divided by the fitted $\boldsymbol{i_r^*}$ times (1-x) for Li^+ insertion ($\boldsymbol{e\eta/k_BT < 0}$ on the left), or $\boldsymbol{i_r^*}$ times x(1-x) for Li^+ extraction ($\boldsymbol{e\eta/k_BT > 0}$ on the right) for $\mathbf{Li_xCoO_2}$ (red), NMC111 (blue), NMC811 (purple), $\mathbf{Li_xFePO_4}$ (grey), and $\mathbf{Li_xC_6}$ (yellow) at different Li content *x*. Symbols for $\mathbf{Li_xCoO_2}$, NMC111, NMC811, and $\mathbf{Li_xC_6}$ in (E) follow those of Figs. 4-2 A-B and Fig.

C-17 to Fig. C-22, and lines follow those of Fig. C-23. Li_xFePO_4 data marked by filled symbols are measured in this work (♦ for x=0.4 and ▲ for x=0.8), while the points marked by ☆ are taken from former work [172] where x was not specified and its *i* was normalized with respect to its total current prefactor. Left inset of (D) shows the computed Bayesian Information Criterion (BIC) values for all the experiments on LCO and NMC111, comparing different models (BV with fixed α = 0.5, BV + film resistance with fixed α = 0.5, BV + film resistance, CIET, and CIET+ film resistance). Detailed BIC analysis for each of the data sets was shown in Fig. C-16, Fig. C-19D, and Fig. C-22D. Right inset of (D) shows the goodness of fit for the CIET fitting of all materials in Fig. 4-2, Fig. 4-4A, and Figs. C-17, C-18, C-21, expressed as the ratio of experimental current densities and the best-fitted current densities from CIET. Electrode loadings are 1-2 mg_{active}/cm^2_{geo} (Table C-3).

While the prefactor i_r^* is independent of *x* (Fig. 4-2E, Fig. 4-4B), it does depend on the electrode/electrolyte interface, having a higher value for Li_xCoO_2 (2.6 mA/cm^2_{oxide}) than Li_xC_6 (0.23 mA/cm^2_{active}) and LFP (0.065 mA/cm^2_{oxide}) with 1 M $LiClO_4$ in EMC:EC (7:3) (Fig. 4-4B), and lower values with 1 M $LiPF_6$ in EMC:EC (7:3) (with 0.65 mA/cm^2_{oxide} for Li_xCoO_2) (Fig. 4-2E). The differences in i_r^* are partly attributable to variations in ion-transfer energy, ΔE_{IT}. Indeed, a simple electrostatic estimate of ΔE_{IT} (Supplementary Note 5, Eq. S12) predicts that LCO has 0.06 eV lower ΔE_{IT} than LFP and therefore at least 11 times higher i_r^* (Eq. S13), thus qualitatively explaining the experimental trend (40 times higher i_r^*). The temperature dependence of i_r^* (Fig. C-25A) has an activation energy ~0.89 eV for LCO (Fig. C-25B) that is also comparable to ΔE_{IT} (0.47 eV estimated from Eq. S12). The electrolyte dependence of i_r^* on different anions (Fig. 4-2E) or $LiPF_6$ concentrations (Fig. C-26) is more complicated, however, since it also reflects differences in quantum coupling for ET and charged double-layer structure for IT. For example, it has been shown that surface functionalization of $LiFePO_4$ with negative sulfide or nitride groups can increase i_r^* by up to 1.5 times by lowering the Li^+ binding energy on surface and decreasing ΔE_{IT} calculated from first-principle calculations.[199].

The trends in exchange current density (Fig. 4-2G) are also consistent with CIET theory. Extrapolating from Eq. 7 predicts that i_0 decreases from 0.066 mA/cm$^2_{\text{oxide}}$ at $x = 0.5$ to 0.035 mA/cm$^2_{\text{oxide}}$ at x=0.8 for Li_xCoO_2, and from 0.046 mA/cm$^2_{\text{oxide}}$ at $x = 0.5$ to 0.021 mA/cm$^2_{\text{oxide}}$ at x=0.8 for NMC111, both with 1 M $LiClO_4$ in EMC/EC (Fig. 4-2G). These values from CIET are comparable with those extracted from Bulter-Volmer (Fig. 4-2G, Fig. C-8 and C-9), MHC (Fig. C-12 and Fig. C-13) or EIS (Fig. C-27 and Fig. C-28), and comparable with some of the reported values from experimental studies [200,201] (Table C-1). In contrast, much larger exchange current densities are used in models with BV kinetics (Table C-2), thereby promoting (sometime spurious) diffusion limitation in battery simulations. These exchange current densities are also smaller than the well-known outer-sphere $[Fe(CN)_6]^{3-}/[Fe(CN)_6]^{4-}$ redox (0.1-10 mA/cm$^2_{\text{geo}}$)[197] and inner-sphere hydrogen evolution and oxidation reactions (0.1-10 mA/cm$^2_{\text{geo}}$)[198].

Trends in the work of Li^+ surface adsorption w_+ are also consistent with properties of the electrode/electrolyte interface. $LiPF_6$-containing electrolytes are found to have slightly larger w_+ than $LiClO_4$-containing electrolytes (Fig. 4-2F), consistent with their higher Li^+ solvation numbers (~4) compared to $LiClO_4$-containing electrolytes (~3.5) in EMC:EC 7:3 [133,202], which presumably require more work to break Li^+-solvent/anion interactions during surface adsorption (Fig. C-29 A-B). Comparing different solvents with $LiPF_6$ (Fig. C-29 B-C), EMC-only solvent has lower dielectric constant compared to EMC:EC 7:3, leading to more Li-PF_6 ion pairs in the solvation shell ($[Li^+\text{-}(EMC)_{2.8}\ (PF_6^-)_{1.1}]$) [202–204], which presumably also leads to larger w_+ (Fig. 4-2F). The increasing w_+ in the order of EMC

with 1 M $LiPF_6$ > EMC:EC 7:3 with 1 M $LiPF_6$ > EMC:EC 7:3 with 1 M $LiClO_4$ might lead to decreasing i_r^*, while future studies from first-principle calculations will be needed to understand the trends for w_+. When decreasing the $LiPF_6$ concentration in EMC:EC 7:3 from 2 M to 0.02 M (Fig. C-26), w_+ decreased significantly (Fig. 4-2F) indicating preferred Li^+ adsorption, which is possibly related to the higher degree of dissociation for $LiPF_6$ when decreasing its concentration in carbonates.[205]

Finally, the ionic resistance of surface coating R_c is introduced for LFP with carbon coating and graphite with solid-electrolyte interphase (SEI). Nanoscale variations in carbon-coating thickness on LFP have been shown to correlate inversely with the local reaction rate inferred from x-ray images [184], while SEI has a similar macroscopic effect on graphite [206]. The fitted R_c is around 20 Ω for LFP (Fig. C-18F), consistent with prior estimates of 10-35 Ohm for LFP carbon coatings [207,208]. The fitted value for graphite, 30 Ω (Fig. C-21E), is the range of reported SEI resistances, 6-200 Ohm [206,209]. The validity of fitting CIET with R_c for materials with surface coatings is also confirmed by slightly decreased BIC values for LFP and graphite (Fig. C-19D, Fig. C-22D).

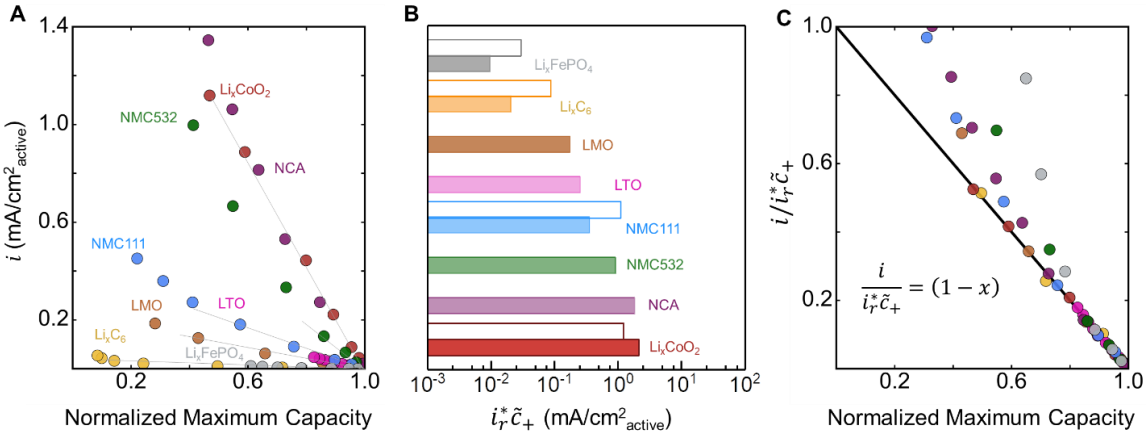

Fig. 4-5 Reaction-limited capacity of Li-ion batteries. (A) Constant insertion current *i* versus normalized capacity at the voltage cutoff (Fig. C-30) for thin, reaction-limited electrodes loaded at 1-2 mg_{active}/cm^2_{geo} (Table C-5) for eight different active materials in 1 M $LiPF_6$ DEC:EC (1:1, v/v) electrolyte. (B) Kinetic prefactors $\boldsymbol{i_r^*\tilde{c}_+}$ obtained by fitting the data in A to Eq. 6 (shaded bars). Values of $\boldsymbol{i_r^*\tilde{c}_+}$ from Tafel kinetic measruements are plotted for comparison (unshaded bars). (C) Collapse of all the data in A using the fitted prefactors in B onto the predicted linear scaling for CIET.

4.4.3 Implications for Li-ion batteries

A novel prediction of CIET theory is a limiting current for ion insertion (Eq. 6) that is proportional to the vacancy concentration, $i \sim i_r^*\tilde{c}_+(1-x)$ as $\tilde{\eta} \to -\infty$. Inverting this relation implies a reaction-limited capacity that decreases linearly with increasing (constant) current, $x_{\mathrm{r,lim}} \sim 1 - i/(i_r^*\tilde{c}_+)$. We tested this prediction by measuring the current-dependent maximum capacity for eight common Li-ion battery anodes and cathodes (Fig. C-30) in thin reaction-limited cells: Li_xCoO_2, Li_xFePO_4, Li_xC_6, NMC111, $Li_xNi_{0.5}Mn_{0.3}Co_{0.2}O_2$ (NMC532), $Li_{4+3x}Ti_5O_{12}$ (LTO), $Li_xNi_{0.8}Co_{0.15}Al_{0.05}O_2$ (NCA), $Li_xMn_2O_4$ (LMO). The achieved capacity normalized to its lowest-rate value for each electrode indeed decreases linearly with applied current density (Fig. 4-5A). The values of $i_r^*\tilde{c}_+$ inferred from the linear fits (Fig. 4-5B) are in good agreement with those obtained from Tafel measurements (Fig. 4-2), and lead to data collapse of $i/i_r^*\tilde{c}_+$ vs. $x_{\mathrm{r,lim}}$ for all eight electrodes (Fig. 4-5C). Deviations from linear scaling at large applied currents in Fig. 4-5C can be attributed to concentration heterogeneities in the porous electrodes, as predicted by MPET simulations using the fitted CIET reaction kinetics (Supplementary Note 6, Fig. C-31).

By revealing the reaction mechanism, our results suggest new avenues to improve the rate capability, lifetime and safety of Li-ion batteries. CIET theory relates the observed variations in i_r^* across different electrodes (Fig. 4-4B, Fig. 4-5B) to the reorganization and ion-transfer energies, which can by predicted by *ab initio* simulations and used to guide surface modifications [199]. The theory also predicts reaction-limited capacity losses from crystal defects that eliminate lithium vacancies, such as nickel disorder in NMCs and iron anti-site defects in LFP [210]. Guided by the theory, battery operation can be constrained to avoid parasitic side reactions, such as lithium plating and electrode-electrolyte interface (EEI) growth [157,209], so as to avoid CIET reaction limitation [211].

4.5 Conclusions

In this study, we have developed a method to measure the kinetics of ion intercalation electrode materials Li_xCoO_2 and NMC111, and the intercalation current density is proportional to $(1-x)$, *i.e.* it decreases with the available Li-ion vacancies in electrode materials. λ is independent of electrolytes and temperatures, and is only dependent on the solid electrodes. Normalizing the current density by the fitted i_r^* and Li vacancy fraction $1-x$ leads to a collapsed master curve for each material, whose curvature is depicted by λ. Additionally, rate capability measurements on eight electrode materials show the linear decrease of the maximum (fractional) capacity at the cut-off voltage with increased discharge current, further supporting by the theory. The experimental results provide direct evidence to the theory of coupled ion-electron transfer, where microscopically both ions and electrons are transferred in a concerted way. Our findings suggest that the proposed

microscopic mechanism applies to a variety of intercalation materials in energy storage, and governs the power density at low and moderate applied current densities.

4.6 Material and Methods

Materials and Electrode preparation

The composite positive electrode for Tafel measurements was composed of 80 wt% active materials (LCO from Sigma Aldrich, NMC111 or NMC811 from Umicore, LFP and graphite from MTI corp.), 10wt% acetylene black (Chevron) as an electrically conductive carbon, and 10 wt% poly(vinylidene fluoride) (PVDF, Kynar) as the binder. The materials were mixed thoroughly with N-methylpyrrolidone (NMP, Aldrich) using a vibratory micro mill (Fritsch Pulverisette 23). The obtained slurry was applied with a blade applicator onto an aluminum foil and dried at 70 °C. Then, the sheet was punched with a 0.5 inch diameter (1.27 cm) punch, compressed at 6.3 T/cm^2 using a hydraulic press, and further dried in vacuum at 120 °C prior to cell assembling. The active material loading was 0.6~1.5 mg/cm$^2_{geo}$ (Table C-3). Electrode thickness is all around 5 μm and active material porosity is all around 50 - 70%. In this study, the electrolyte was 1 M $LiClO_4$ (> 99.99%, battery-grade, Aldrich) in a 3: 7 wt:wt ethylene carbonate (EC): ethyl methyl carbonate (EMC). The electrolyte was prepared by simple mixing of $LiClO_4$ and EC/EMC in an argon-filled glove box ([H2O] and [O2] < 0.5 ppm, MBraun). The residual water contents in the electrolytes were measured by Karl Fischer titration and were less than 10 ppm.

The rate capability of different intercalation materials (purchased from MTI corp.) are measured with coin cells. The material is first mixed with carbon black and PVDF

(dissolved in NMP) in a mass ratio of $80:10:10$, and the slurry is coated onto an aluminum foil to form a thin film. The film is first dried in air overnight and then in a vacuum oven at 70 °C for 8 hours. After that, the film is punched into small disks of 12.7 mm diameter. In order to avoid liquid-diffusion limitations, the thin porous electrodes have low active material loading around 1 mg/cm^2.

Tafel kinetic measurements

Tafel analysis widely adopted in electrocatalytic reactions enables the study of non-equilibrium kinetics by directly relating the current of an electrochemical reaction to the applied overpotential. The analysis is applicable to fitting into different kinetic models beyond Butler-Volmer, including Marcus equation[178] and Marcus-Hush-Chidsey (MHC) equation[176,177], which give rise to non-equilibrium material properties such as reorganization energy[190]. There have been a few studies and experimental practices to extract Tafel-like plots for Li-ion batteries. For example, West *et.al.* have performed Tafel polarization measurements by applying a linear voltage sweep on $Li_{1.17}Mn_{0.56}Ni_{0.135}Co_{0.135}O_2$ and compared different temperatures.[212] Munakata *et.al.* galvanostatically charged a $LiFePO_4$ single particle electrode at various currents, and plotted the potential at the half discharged state against the logarithm of each discharge current to fit Butler-Volmer equation.[213] However, the overpotential was not well defined, and the state of charge changed during the measurement, so the methods do not allow Tafel analysis at a fixed Li^+ concentration in the electrode. Bai *et.al.* have performed chronoamperometry experiments on $LiFePO_4$ porous electrodes and fit transient currents into a phase transformation statistical model,[172] to achieve Tafel analysis of the reaction

rates and compare with different kinetic models. The overpotential was more well-defined, but the corresponding current was not straightforward to capture.

In this study, we have developed a new charge-adjusted methodology, which enables Tafel measurements for Li-ion battery electrodes at a specific state of charge. The Tafel measurements were performed in a three-electrode cell. The three-electrode cell was assembled in the glove box, with a Li metal foil (D=15 mm) as the negative electrode, 2 pieces of Celgard 2325 D=19 mm) as the separators, a Li strip as reference electrode (5 mm× 3 mm), two pieces of Celgard 2325 (D = 19 mm) again, and LCO or NMC111 composite electrode ($\phi = 0.5$ inch) as the positive electrode from bottom to top (Fig. 4-1A). $150\mu L$ of electrolyte was added to the cell.

Galvanostatic charging and potentiostatic measurements were performed using a VMP3 potentiostat (Biologic). The LCO or NMC working electrode was charged (or later discharged) to specific Li concentrations Li_xMO_2 ($x \in (0.5,0.8)$) (Fig. C-3), at ~ 28 mA/g ($C/10$ rate based on theoretical capacity, which corresponds to full lithium deintercalation ($LiMO_2 \leftrightarrows Li^+ + e^- + MO_2$), followed by a charge-adjusted potentiostatic measurement to obtain (i, η) points for Tafel plots.

In Li-ion batteries the state of charge changes continuously during operation; therefore, to obtain Tafel plots at a fixed x, we need to adjust the charge after each measurement so that x and the equilibrium voltage are kept the same. We developed the charge-adjusted potentiostatic measurement methodology (Fig. 4-1B), to keep both the open-circuit voltage

V_{eq} (OCV) and x constant for all (i, η). More specifically, for each measurement of a single (i, η) point at a specified x, the cell was first rested at OCV or V_{eq}, which is constant at a corresponding x (Fig. C-1 B-C). We then discharged the cell potentiostatically at V_{applied} for 2-3 s, which led to changes in the charge (ΔQ_i). The current was taken according to the timescale from electrochemical impedance spectra (EIS), where the second semicircle started (Fig. C-6). The timescale for which the currents were taken is smaller than 0.5 s, and the change in x during this time is negligible with $\Delta x < 10^{-4}$ (Fig. C-3 D-E).

Finally, ΔQ_i was charged back with a small current (Fig. 4-1B) to bring the charge and x to the initial value. The voltage difference between V_{applied} and V_{eq} defines the overpotential η_i, and also the current i_i at the end of potentiostatic corresponds to η_i. Since the charge was pre-adjusted before each measurement, V_{eq} and x were kept constant for the measuring (i, η). The potential and overpotentials have been corrected considering iR-drop (resistance R is typically around 5 to 10 Ω from electrochemical impedance spectra).

Fitting procedure

The coupled ion-electron transfer model has two free parameters, the reorganization energy λ and the reaction rate prefactor i_r^*. Given the form of Eq. 1, it is clear that the dependence of i in terms of λ is non-linear, as it appears in both the numerator and in the exponential term of $i_{red/ox}$. Thus, to fit the model to the experimental results of Fig. 4-2 A-C, we perform a standard non-linear regression. In particular, to find the values of (i_r^*, λ) we minimize the following cost function

$$C[\mathbf{i}_{\text{exp}}, \boldsymbol{\eta}_{\text{exp}}; i_r^*, \lambda] = \sum_{i=1}^{N_{\text{exp}}} \left(\log\left(\frac{i_{\text{exp},i}}{i_{\text{model}}(\eta_{\text{exp},i}; i_r^*, \lambda)} \right) - 1 \right)^2$$

where N_{exp} are the experimental data points included in the fitting process, $\mathbf{i}_{\text{exp}}$ and $\boldsymbol{\eta}_{\text{exp}}$ are the values of the experimentally accessible current density and overpotential, respectively, and i_{model} is evaluated using Eq. 1. We carried the minimization procedure using Gauss-Newton method[214], while the derivative with respect to the parameters of the model for evaluating the Hessian matrix $\mathbf{H} = \nabla_{\boldsymbol{\theta}} \nabla_{\boldsymbol{\theta}} C$, with $\boldsymbol{\theta} = (i_r^*, \lambda)$, were evaluated using automatic differentiation[215]. The minimization process is stopped when the cost function becomes less than 5×10^{-2}. Bulter-Volmer (BV) and conventional MHC fitting follow the same programs as our previous work. [197]

Rate capability experiment

The rate capability of different intercalation materials is measured with coin cells, where Li foil is used as the counter/reference electrode. The electrolyte is 1M $LiPF_6$ in (1: 1) EC:DEC. The separator is Celgard 3501 separator. To avoid diffusion limitation at high rate, all the electrodes are controlled to have a thickness $< 5\ \mu$m by using cold compression. The thickness of the cell guarantees that liquid-diffusion limitations will be negligible compared to reaction and solid-diffusion limitations. In particular, the liquid diffusion timescale for $D_{eff,Li^+} \simeq \phi^{1.5} D_{Li^+} \simeq 3 \times 10^{-10}$ m^2/s corresponds to $\tau_{diff,liq} \simeq 0.09$ s, while the operation of the cells never exceeds 10 C Rates (~ 360 s). The liquid Li^+ diffusivity is taken from literature[216], the porosity of the electrodes is approximately $\phi \simeq 0.8$, while for the effective diffusivity we consider Bruggeman's relation[29].

Before the rate capability test, the coin cell is first discharged/charged at $C/10$, which is defined by theoretical capacity, for three cycles to fully activate the materials. During the rate capability test, the cell is charged at $C/10$ and discharged at different C rates using the same cell.

Particle size distribution

Powders were first immersed in ethanol and subsequently ultrasonicated for 20 minutes to disperse the powder particles. The suspensions were then drop-casted on a copper substrate, and the dried particles were observed with a scanning electron microscope (Zeiss Merlin high-resolution SEM, with secondary electron detector at accelerating voltage of 5 kV). The histogram of particles is obtained from 250 randomly selected spherical particles in the SEM micrographs (Fig. C-24).

Chapter 5. Enhancing oxygen reduction electrocatalysis by tuning interfacial hydrogen bonds[7]

5.1 Introduction

Understanding proton coupled electron transfer (PCET) processes are critical to control the reaction kinetics in bio[217], organic[218], inorganic[219], environmental chemistry[220] and electrochemistry[221]. In particular, PCET steps have been used extensively in recent research on catalysts for making energy carriers or solar fuels[222] including water splitting[223], and for converting energy carriers in fuel cells to generate work[219,221] including oxygen reduction reaction (ORR)[221]. Current thinking of the ORR mechanism[34,221] involves PCET steps on surface metal sites, which can involve one key intermediate on metals such as Au[224] for two-electron ORR ($O_2 + 2H^+ + 2e^- \rightarrow H_2O_2$, 0.68 V_{RHE}), -OOH[224,225], and three key intermediates on metals such as Pt[34,226], -OOH, -O and -OH for four-electron ORR ($O_2 + 4H^+ + 4e^- \rightarrow 2H_2O$, 1.23 V_{RHE})[227]. Conventional designs of catalysts involve the tuning of the surface electronic structure and covalent interactions with reaction intermediates[34,227] (surface binding or adsorption strength), which has led to significant advances in the intrinsic ORR activity by tuning strain[228,229], the ligand effect[230,231], and surface orientation[232–234]. For example, $Pt_3Ni(111)$[235] is shown to exhibit intrinsic ORR activity ten times greater than Pt (111) at 0.9 V_{RHE}, and polycrystalline PtGd[44] exhibit five times enhancement than polycrystalline Pt.

---

[7] Reproduced in part, with permission from Wang, T. †, Zhang, Y. †, Huang, B., Cai, B., Rao, R.R., Giordano, L., Sun, S.G. and Shao-Horn, Y., 2021. Enhancing oxygen reduction electrocatalysis by tuning interfacial hydrogen bonds. *Nature Catalysis*, *4*(9), pp.753-762. († denotes equal contribution.) Copyright © Springer Nature Limited 2021.

Recent studies have shown that changing electrolyte compositions can significantly alter the kinetics of electrochemical reactions such as oxygen reduction reaction (ORR) [236–239] and hydrogen oxidation reaction[45,240–242], highlighting new opportunities in noncovalent interactions via the chemical physics of electrolytes to control activity. While the pH of electrolyte, which represents proton activity, does not greatly alter the ORR activity of metals such as Pt[243], increasing pH can significantly increase the ORR activity on weakly interacting metals such as Au[46,47], where the activity in base is much higher than that in acid[46]. Moreover, modifying Pt-based catalysts with protic ionic liquids[40,237,244] is shown to enhance the ORR activity in acid, where ionic-liquid-modified PtNi nanoparticles have ~3 times greater intrinsic ORR activity than pristine PtNi[237], and ~20 times greater than commercial Pt/C[40]. Although this increase in the ORR activity has been attributed to the increase of hydrophobicity at the interface between Pt and ionic liquids[244] and oxygen solubility in ionic liquids[237], it is not apparent on how to design new catalysts to control the catalytic activity of ORR and other reactions using this strategy. Considering these ionic liquids used in these previous studies[40,237,244] have different pK_a from the acidic electrolyte and the ΔpK_a values between cations and anions were found correlated with open circuit potential in H_2/O_2 fuel cell[245], it is postulated that interfacial proton activity of ionic liquids can alter proton transfer or proton-coupled electron transfer (PCET) kinetics on metals such as Pt and Au, and thus ORR activity, which is the focus of this work.

Here we employ a library of protic ionic liquids in an interfacial layer to tune ORR kinetics of Pt and Au in acid. We hypothesize that the protic cations in the ionic liquids can serve as intermolecular proton relay between proton in the bulk electrolyte and that near the metal

surface (Scheme 5-1), where altering of protic cation with different proton activity (or pK_a) provides opportunities to examine how local proton activity near the active sites can influence the ORR kinetics. A library of protic cations with different pK_a values were used (Scheme 1) $[C_4C_1im]^+$ pK_a=23.3[246], $[TMPim]^+$ pK_a=21.3[246], $[MTBD]^+$ pK_a=15.0[247], $[DBU]^+$ pK_a=13.5[247], $[DEMA]^+$ pK_a=10.3[248], $[TEMEDA]^+$ pK_a=8.9[249], $[C_4Him]^+$ pK_a=7.1[250] to influence the ORR activity of Au and Pt, which catalyzes ORR via the $2e^-$[251] and $4e^-$ [252] pathway in acid, respectively. The ORR activity of Au and Pt was found to increase with the presence of protic cations, where the maximum enhancement was obtained when the pK_a values of protic cations and the reaction intermediate in the ORR rate-limiting step are similar. The ORR activity enhancement can be attributed to the stronger hydrogen bond between protic cations and the rate-limiting ORR intermediate, which is supported by *in situ* attenuated total reflection surface-enhanced infrared absorption spectroscopy (ATR-SEIRAS). Our work reveals the role of local pK_a and interfacial H-bond strength on the kinetics of PCET and electrochemical reactions, which highlight new opportunities to further enhance electrocatalytic activity of ORR, reduction of CO_2 and N_2, and beyond by tuning how local proton activity near the active sites.

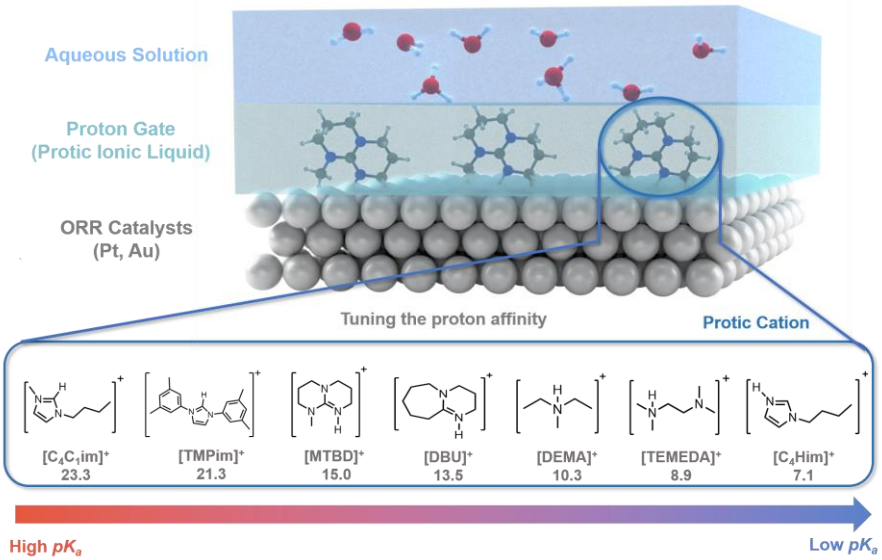

Scheme 5-1. Tuning local proton activity for ORR catalyzed on the surface of metallic catalysts by adding a thin layer of protic ionic liquids, where the pK_a value can range from 7.1 to 23.3. The anion of all ionic liquids used was NTf_2 in this work.

5.2 pK_a-dependent ORR activity of protic-cation-modified catalysts

The ORR activity of Au/C (6.0 nm Au) and Pt/C (TKK, 19wt% 1.7 nm Pt) with and without protic cations was measured using rotating disk electrode measurements, as shown in Fig. 5-1A and 1B, respectively. The ionic liquid layer thickness with protic cations on the surface of Au/C and Pt/C was estimated to ~1 nm (details in Fig. D-1). The catalysts with protic cations showed enhanced activity compared to those without, as indicated by the positive shifts in the half-wave potential in the voltammetry data. ORR kinetic currents were extracted from the data in Fig. 5-1A, 1B and Fig. D-2 using the Koutecky–Levich analysis, from which the specific and mass activity was obtained by normalizing the kinetic ORR current (Fig. D-3) by the electrochemically surface area from CV measurements (Fig. D-4-5) and metal mass (Fig. D-6), respectively. The specific ORR activity for Au/C at 0.4 V_{RHE} can be enhanced up to ~5 times with protic cations relative to pristine Au/C shown

in this work while that of Pt/C at 0.9 V_{RHE} can be increased by ~3 times compared to pristine Pt/C (TKK 19%, ~190 $\mu A/cm^2_{Pt}$) shown in this work and previous studies[12,253–256]. Similar activity trends and enhancement were found for polycrystalline Au (~4 times at 0.3V_{RHE}, Fig. D-7A) and Pt (~2 times at 0.9 V_{RHE}, Fig. D-7B). The exchange current density of ORR was extracted for Au/C ($O_2 + 2H^+ + 2e^- \Rightarrow H_2O_2$, 0.68 V_{RHE}) and for Pt/C ($O_2 + 4H^+ + 4e^- \Rightarrow 2H_2O$, 1.23 V_{RHE}) using Butler-Volmer in Fig. D-8 and Fig. D-9 respectively. These observations suggest that the local proton activity at the metal/electrolyte interface can considerably influence the ORR kinetics.

The ORR activity of both Au/C and Pt/C was found to first increase and then decrease, exhibiting a volcano trend, as a function of the pK_a value of protic cations, as shown in Fig. 5-1C and Fig. 5-1D, respectively. The maximum ORR activity enhancement for Au/C was found for [DEMA][NTf_2] with pK_a of 10.3, which is similar to the ORR product on Au, H_2O_2 of pK_a of 11.6 [257]. The production of H_2O_2 on Au/C and ionic-liquid-modified Au/C was measured by RRDE (Fig. D-10), which revealed that the number of electron transfer for ORR on ionic-liquid-modified Au/C and pristine Au/C is all in the range from 2.0 to 2.2. These results confirm that H_2O_2 is the main product for ionic-liquid-modified Au/C as well, being consistent with Au/C. In acid, the first PCET step of ORR on Au ($O_2 + H_3O^+ + e^- \Rightarrow OOH_{Au} + H_2O$) has similar kinetics to the second step ($OOH_{Au} + H_3O^+ + e^- \Rightarrow H_2O_2 + H_2O$), as indicated by the 0.09 eV difference in activation barrier from DFT[258]. As increasing pH is shown to promote the rate of the first step by several orders of magnitude[47], the second step becomes rate-limiting to the overall kinetics with increasing local pH. Therefore, we propose that the ORR kinetics on Au with interfacial ionic liquids are limited

by the PCET kinetics of OOH_{Au} to form H_2O_2 ($OOH_{Au} + N\text{-}H^+ + e^- \Rightarrow H_2O_2 + N$)[224] (the detailed kinetic analysis depicted in Fig. D-11). This hypothesis is in agreement with previous kinetic measurements of ORR in organic solvents, where the first electron transfer step ($O_2 + e^- \Rightarrow O_2^-$) [259] is more than 10^3 times faster than the second PCET step ($O_2^- + e^- + H_2O \Rightarrow OOH^- + OH^-$)[260]. Further support comes from the observation that OOH_{Au} has been detected as the stable ORR intermediate accumulating on Au by *in situ* ATR-SEIRAS[225] and *in situ* surface enhanced Raman[261]. Therefore, it is proposed that different pK_a altered the kinetics of the second PCET step for ORR on Au in ionic liquid ($OOH_{Au} + N\text{-}H^+ + e^- \Rightarrow H_2O_2 + N$) and tuned the overall ORR kinetics consequently. This hypothesis departs from the decoupled proton-electron transfer mechanism outlined by Koper,[221] where increasing kinetics with increasing pH for one-electron reduction can be attributed to enhanced electron-transfer kinetics on the RHE scale.

The maximum ORR activity enhancement for Pt/C occurred for [MTBD][NTf_2] with pK_a of 15.0, which is similar to the ORR product in the rate-limiting step, water with pK_a of 15.7 [257]. Previous DFT studies have shown that PCET of adsorbed OH on Pt to form H_2O is rate-limiting ($OH_{Pt} + H^+ + e^- \Rightarrow Pt + H_2O$),[34] which is supported by ambient pressure X-ray photoelectron spectroscopy[262] and *in situ* electrochemical surface-enhanced Raman spectroscopy[226]. The coverage of intermediates (O_{Pt} and OH_{Pt} on Pt) is about 20-30% at ORR relevant potentials [262]and that of cations was estimated to be 17-30% on Pt (Table D-1), we suggested the coverage of cations is comparative with the coverage of ORR intermediates when we consider the ORR intermediates on the surface grabbing proton from ionic liquids. Therefore, these results show that the kinetics of ORR on Au and Pt

could be regulated by the pK_a of protic cations at the interface, which can work as the proton donor near the active sites catalyzing the rate-limiting PCET, having the maximum ORR activity obtained with minimum pK_a difference between the protic ionic liquid (proton donor) and rate-limiting ORR product (proton acceptor). This observation is further supported by the measurement on Au/C in 0.1M $NaClO_4$ and Ag/C in 0.1M $HClO_4$, of which the number of electron transfer for ORR is close to 3, having both H_2O_2 and H_2O in ORR products (Fig. D-12 (C, D)). The maximum ORR activity enhancement was found for [DBU][NTf_2] with pK_a of 13.5 (Fig. D-12 (E, F)), which is between the pK_a of H_2O and H_2O_2. Therefore, the results further support our opinion that pK_a of cation can affect the ORR kinetics and it is correlated with the intermediates of ORR pathway.

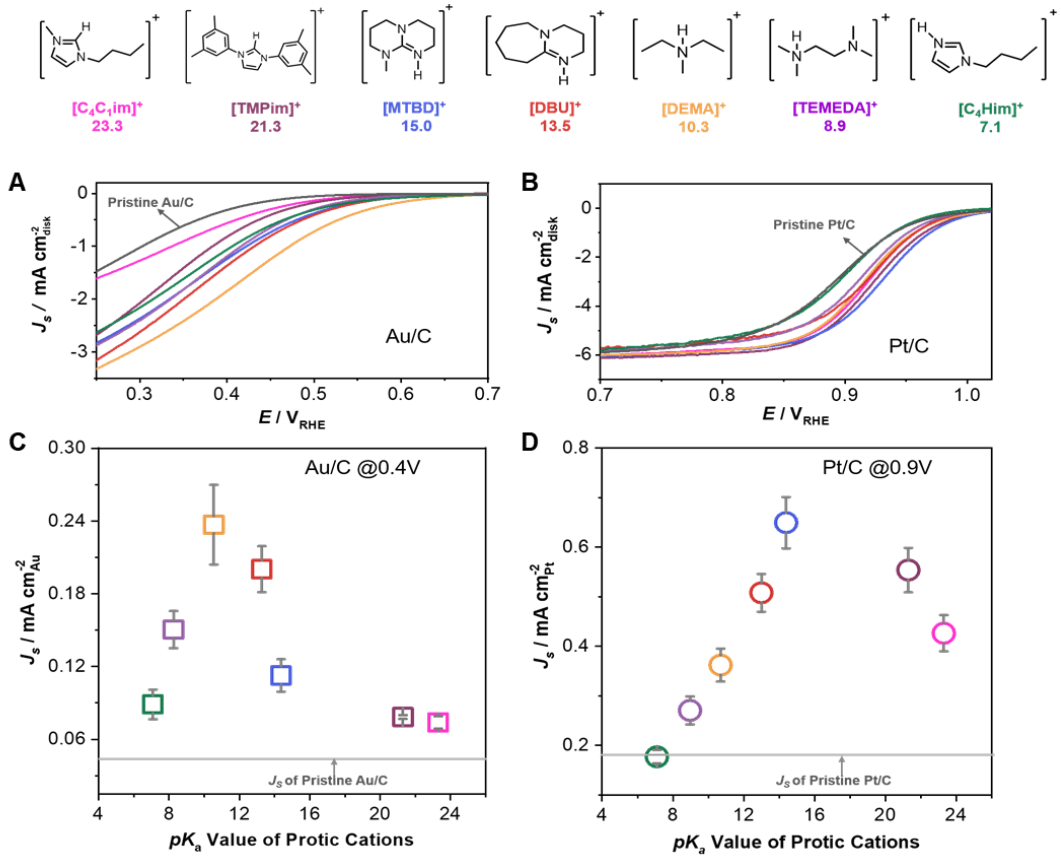

Fig. 5-1 pK_a-dependent ORR activity on Au/C and Pt/C measured in O_2-saturated 0.1 M $HClO_4$, with a scan rate of 10 mV/s and the rotation speed is 1600 rpm. (A and B)

Background and *IR* corrected ORR polarization curves of ionic-liquids-modified Au/C (A), Pt/C (B). (C and D) The relationship between the enhancement in ORR specific kinetic currents on ionic-liquids-modified Au/C (C), Pt/C (D) as a function of the pK_a value of protic cations in ionic liquids. Error bars represent standard deviations (SDs) of at least three independent measurements. The loading of Pt was controlled at 20 $\mu g \cdot cm^{-2}$ and the loading of Au were controlled at 40 $\mu g \cdot cm^{-2}$. 0.05wt% Nafion was added to the catalytic layer.

As the thermodynamic driving force of proton coupled electron transfer (PCET) reactions diminishes with minimized pK_a difference between the proton donor and acceptor[263], and the reorganization energies (λ) fitted by Marcus-Hush-Chidsey (MHC) theory were found similar in different ionic liquids (Fig. D-13), we propose that the enhancement in the ORR activity with different ionic liquids can be attributed to difference in the interfacial hydrogen bond structure as predicted previously by PCET theory for homogeneous reactions[219], which will be examined by *in situ* ATR-SEIRAS experiments and computation below.

5.3 pK_a-dependent interfacial H-bond detected by *in situ* ATR-SEIRAS

In situ ATR-SEIRAS was performed on Au and Pt thin-film chemically deposited on Si prism, which detected ORR intermediates and revealed the interactions between protic cations in ionic liquids and ORR intermediates by monitoring the stretching frequency of H-bonded species of protic cations as influenced by the formation of ORR intermediates and product as a function of potential. Potential-dependent *in situ* ATR-SEIRA spectra were collected from [MTBD][NTf_2]-modified Au thin-film surface (estimated to have a thickness of ~ 50 nm for Au and ~20 μm for [MTBD][NTf_2]). Differential spectra subtracted by that collected at OCV are shown in Fig. 2, along with that of bulk [MTBD][NTf_2] and [MTBD][NTf_2] with water (0.5 M water). Two sharp peaks at 1632

cm^{-1} and 1603 cm^{-1} (Fig. 5-2A), resulting from the stretching mode of C=N-H^+ and C=N in the cation[264], respectively, grew with decreasing potential. The increased peak intensities can be attributed to having more protic cations on the Au surface with decreasing potential, which is in agreement with increasing peak intensities of C-N stretching[265,266] from protic cations at 1231 cm^{-1} (Fig. 5-2B). Similar peaks to those found on Au were found on [MTBD][NTf_2]-modified Pt thin-film surface (Fig. D-14), which also grew with decreasing potential.

Two new peaks, at 1263 cm^{-1} and 3238 cm^{-1} emerged (Fig. 5-2B and 2C) with decreasing potential, which can be assigned to the bending (H-O-O) of HOO-adsorbed on Au[225] and the stretching of N-H^+···OOH_{Au} of [MTBD][NTf_2], respectively. The assignment of the broad feature at 3238 cm^{-1} is supported by DFT calculations, where computed N-H^+···OOH_{Au} stretching of [MTBD][NTf_2] was determined to be 3267 cm^{-1} (Table D-2), in good agreement with the experimental observation. This new broad peak at ~3238 cm^{-1} is redshifted compared to the N-H^+ stretching of bulk [MTBD][NTf_2] with and without water added (~3400 cm^{-1} in Fig. 5-2C), indicating the presence of hydrogen bond interactions between protic cation and ORR intermediates such as [MTBD]N-H^+···OOH_{Au}. These two peaks at 1263 cm^{-1} and 3238 cm^{-1} grew at the expense of the peak at 3583 cm^{-1}, attributable to the O-H stretching of water dissolved in the [MTBD][NTf_2] in Fig. 5-2C and Fig. D-14, which indicated reduction of water adsorbed on the surface with decreasing potential.

Changing the pK_a of protic cations was found to redshift the N-H^{+}···OOH_{Au} stretching at ORR-relevant potentials (Fig. 5-3 and Fig. D-15 and 16). The N-H^{+}···OOH_{Au} stretching frequency decreased from 3429 cm^{-1} for [C_4Him][NTf_2] with pK_a of 7.1 in Fig. 5-3C, 3238

cm^{-1} for [MTBD][NTf_2] with pK_a of 15.0 in Fig. 5-3A, to ~3000 cm^{-1} for [DEMA][NTf_2] with pK_a of 10.3 in Fig. 5-3B, at 0.2 V_{RHE}. These assignments are supported by DFT calculations (Table D-2), which also show the two fine peak features at ~3000 cm^{-1} for [DEMA][NTf_2] with the maximum ORR activity, having the feature at 2985 cm^{-1} to the stretching of [DEMA]N-H^+···OOH_{Au} and the feature at 3024 cm^{-1} to [DEMA]N-H^+···OHOH. Further support to these assignments came from the observed peak growth as expected for increasing ORR intermediates with decreasing potential (Fig. D-15, D-16 and D-17). Weakening the N-H^+ (proton donor) stretching of N-H^+···OOH_{Au} from [C_4Him][NTf_2] to [DEMA][NTf_2] indicates stronger hydrogen bond interactions in N-H^+···OOH_{Au} as shown from previous IR spectroscopy studies of hydrogen-bonded (H-Bond) species[267,268], suggesting the strongest hydrogen bond found for [DEMA][NTf_2] with a similar pK_a (10.3) to H_2O_2 (11.6). This observation is in agreement with general trends that the H-bond would become stronger when the difference between the pK_a value of proton donor and acceptor decreases as shown from thousands of H-bond structures from the Cambridge Structural Database including the N-H^+···O, N-H^+···N etc.[269] Therefore, the maximum ORR activity found on Au in presence of [DEMA][NTf_2] is associated with the strongest H-bond interaction between N-H^+···OOH (Fig. 5-3G). Considering the rate of ORR on Au is limited by PCET from OOH_{Au} to form H_2O_2 on Au in ionic liquids (OOH_{Au} + N-H^+ + e^- = H_2O_2 + N), strengthening H···OOH facilitated by protic cations with comparable pK_a such as [DEMA]N-H^+ would enhance ORR kinetics.

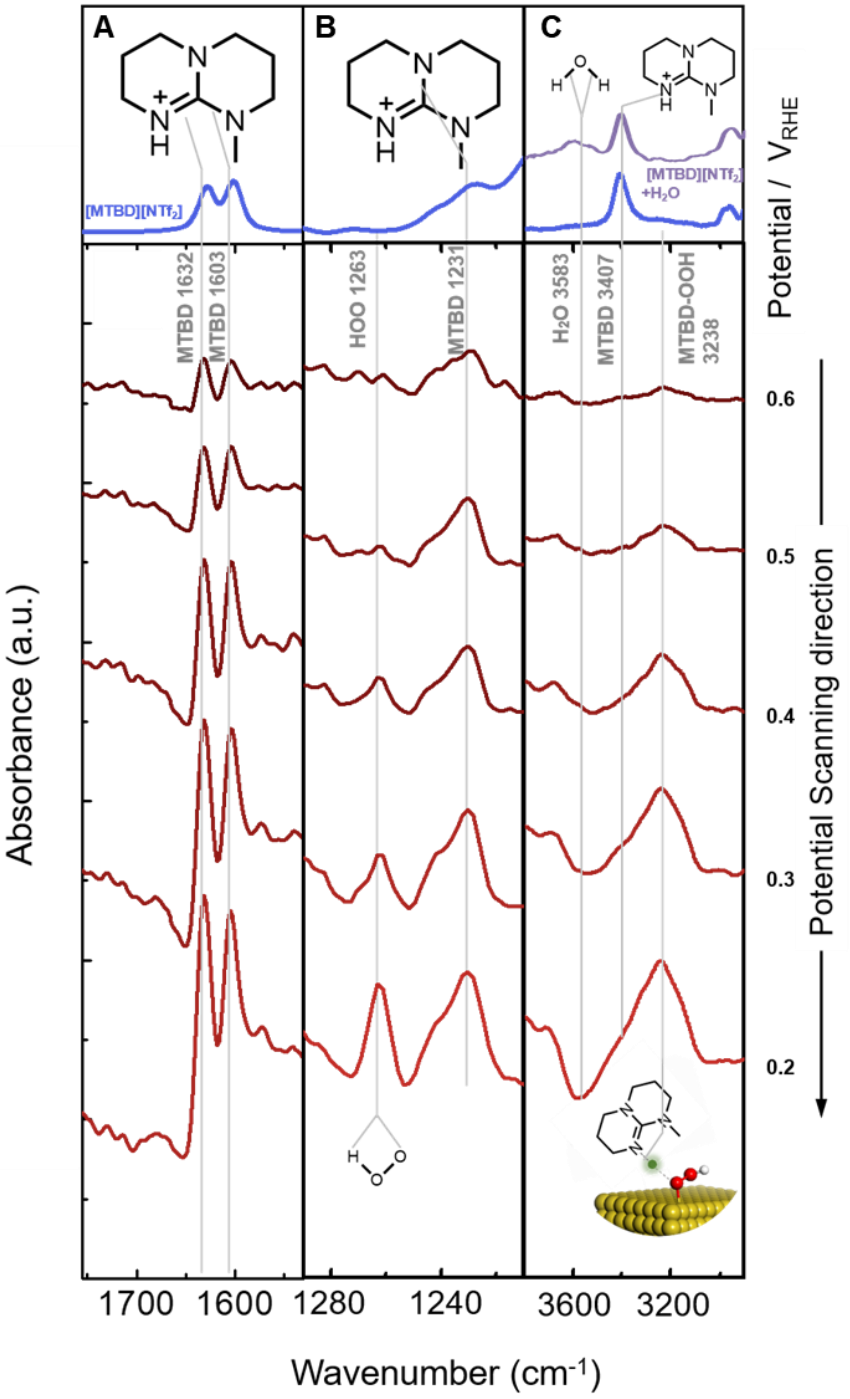

Fig. 5-2 *In situ* ATR-SEIRAS measurement on a [MTBD][NTf_2]-modified Au electrode in oxygen-saturated 0.1 M $HClO_4$. (A) C=N stretching region, (B) O-O-H bending region and (C) X-H (X=N, O) stretching region were obtained during potential steps swept from 0.2 V_{RHE} to 0.6 V_{RHE} in 0.1 M $HClO_4$. The blue curves show the IR spectrum of pristine [MTBD][NTf_2] and the purple curve shows the IR spectrum of pristine [MTBD][NTf_2] with 0.5M water. The cumulative number of 256 was used at a 4 cm^{-1}

resolution. Spectra were subtracted with respect to a reference spectrum obtained at OCV in 0.1 M $HClO_4$.

Similar to Au, the maximum ORR activity found on Pt in presence of [MTBD][NTf_2] is associated with the strongest H-bonding interaction between N-H^+ and OH of species such as N-H^+···OH_{Pt} among the protic cations examined in this study, as shown in Fig. 5-3D-F, Fig. 5-3H and Fig. D-18-20. This assignment is in agreement with the detection of Pt-OH as the dominant ORR intermediate by *in situ* SERS and XPS[226,262] and previous DFT findings that PCET of OH adsorbed on Pt is rate-limiting for ORR[264]. Further support came from the agreement between experimentally observed and DFT calculated (Table D-2) wavenumber for N-H^+ stretching, where the computed value for [MTBD]N-H^+···OH_{Pt}, [DEMA]N-H^+···OH_{Pt} and [C_4Him]N-H^+···OH_{Pt} was found to be 3089 cm^{-1}, 3188 cm^{-1} and 3335 cm^{-1}, respectively. Like Au, the N^+-H stretching for the protic cation with the maximum ORR activity has one additional feature to [MTBD]N-H^+···OH_{Pt} at 3089 cm^{-1}, which can be attributed to [MTBD]N-H^+···OH_2 at 3215 cm^{-1} as supported by DFT (Table D-2), revealing the presence of the ORR intermediate (OH_{Pt} and final product (H_2O) in the rate-limiting step. Considering the PCET from OH_{Pt} to form H_2O (OH_{Pt} + N-H^+ + e^- = H_2O + N) is rate-limiting, strengthening H···OH facilitated by protic cations with comparable pK_a such as [MTBD]N^+-H would enhance ORR kinetics. In addition, in order to discuss the potential effect of water in ionic liquid, we have measured the water solubility of different ionic liquids, where the results are depicted in Table D-3. We found there was no apparent correlation between bulk water content in ionic liquids and ORR activity. Considering the water content at interface, we further examined water signal at the electrode interface by *in situ* ATR-SEIRAS. When ORR current density increased with

decreasing potential, the IR intensity of OH stretching (3600-3300 cm^{-1}) and H-O-H bending (1600-1700cm^{-1}) of water decreased and the signal of cation increased (Fig. D-14 to D-16 and D-18 to D-20). This phenomenon indicated that cations could accumulate on metal surface and kicked water out during ORR. This opinion agrees with previous works on interface between Au and humid ionic liquids, where cations of ionic liquid was found accumulate on Au surface at ORR relevant potential [270], and there is no adsorption of water at Au surface at the potential window of -0.4 to 0.4V [271]. Therefore, based on our ATR results and previous works [270,271], we suggest that water adsorption in ionic liquid at ORR relevant potential is insignificant, the variation of ORR activity of different ionic liquids is mainly dependent on the change of H-bonding structure between cations and ORR intermediates.

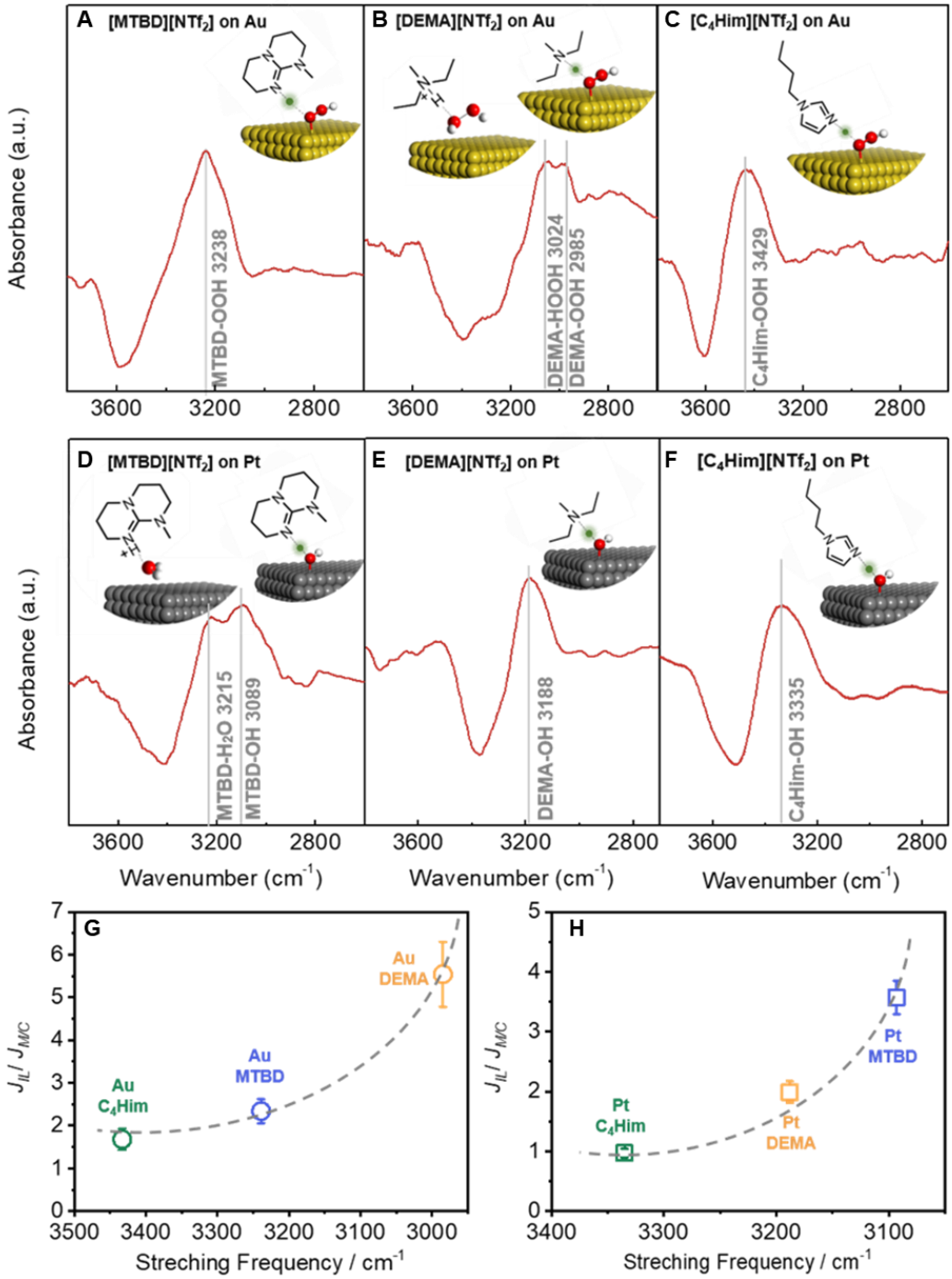

Fig. 5-3 *In situ* ATR-SEIRAS measurement on an ionic-liquid-modified Au and Pt electrode in 0.1 M $HClO_4$. X-H (X=N, O) stretching region of (A) [MTBD][NTf_2]-modified Au, (B) [DEMA][NTf_2]-modified Au, (C) [C_4Him][NTf_2]-modified Au, (D) [MTBD][NTf_2]-modified Pt, (E) [DEMA][NTf_2]-modified Pt and (F) [C_4Him][NTf_2]-modified Pt. The spectra were acquired at 0.2 V_{RHE} for Au and 0.5V_{RHE} for Pt. The peak position of the H-bonded species indicates the strength of H-bond forming during the ORR

process; (G, H) the relationship between the stretching frequency of the H-bonding species and the ionic liquid enhancement for ORR catalyzed by Au/C (G) and Pt/C (H), which is defined by $J_{IL\text{-}M/C}/J_{M/C}$ ($J_{IL\text{-}M/C}$ is the ORR current density of ionic-liquid-modified sample, $J_{M/C}$ is the current density of pristine Pt/C or Au/C). Error bars represent SDs of at least three independent measurements. The relationship indicates stronger H-bond would lead to higher ORR activity. The curve only serves as a guide to eyes.

5.4 Conclusions

This study shows that ORR activity forms a volcano relationship with pK_a of ion liquids (serving as proton donor) on the surface of Au and Pt in acid. The optimized pK_a for proton donor is around 15 and close to the pK_a value of water for Pt while the optimized pK_a for proton donor on Au is around 11 and close to the pK_a value of H_2O_2. *In situ* ATR-SEIRAS provides direct evidence for red-shifted stretching frequency of X-H with decreasing ΔpK_a, which is associated with enhanced ORR activity. This work shows compelling evidence for pK_a-dependent hydrogen bond structures and their impact on the kinetics of proton tunneling and the rate-limiting PCET of ORR on Pt and Au, where altering the pK_a of proton donor at the catalyst surface can change the H-bonding interaction with ORR intermediates. Our findings highlight new opportunities beyond conventional catalyst design strategies of surface electronic structure tuning to control catalytic activity by tuning H-bond structures and/or solvation environments at the electrified interface.

5.5 Methods

In situ SEIRAS measurements

We used a working electrode composed of a thin (~50 nm) Au or Pt film deposited on the Si prism (radius 22 mm, Pier optics) by electroless deposition[272,273]. The prism was then assembled to a three-electrode cell along with an Ag/AgCl reference electrode and a

platinum wire counter electrode. The SEIRAS experiments were conducted on a FT-IR Vertex 70 (Bruker) FT-IR equipped with an MCT detector. The optical path was fully filled with N_2 gas. The FTIR spectra were acquired in the attenuated total reflection (ATR) mode using a single-reflection ATR accessory (Pike Vee-Max II, Pike Technologies) at an incident angle of 68 degrees. The spectral resolution was 4 cm^{-1} and the scan velocity was 7.5 kHz. Each spectrum was measured by superimposing 256 interferograms. During each experiment, O_2 was bubbled through the electrolyte, and the prism surface was then cleaned by cyclic voltammetry between 0 and 1.0 V_{RHE}. After cleaning, the spectra were collected while applying potentiostatic potentials. All spectra were presented in the form of absorbance according to $\log(I_0/I)$, where I_0 and I are the spectra of background (at open circuit potential) and at the potentiostatic potential, respectively.

Electrochemical characterization, determination of kinetic currents, and fitting of exchange current density of ORR are discussed in Ref. [274].

FTIR frequency calculations

The computed the vibrational frequency shifts for hydrogen-bonded species were simulated by DFT from the vibrational frequencies of individual ionic liquid cations, and with interaction of individual cations with a H-bond from a nearby OH or OOH, in an implicit solvation model (PCM), and 2-Pentanone (dielectric constant=15.5) was used as solvent[275]. We used the B3LYP functional and 6-311++G** basis set, as implemented in the Gaussian (g16) suite[276]. It should be noted that the effects of the metal surface and the applied potential were neglected in these calculations, which should not influence. In

general, these effects can be significant, but the qualitative trends for the vibrational frequencies of ionic liquid cation bonded with OH or OOH.

Chapter 6. Water-in-confinement modulated hydrogen evolution and hydrogen oxidation reactions

6.1 Introduction

Designing electrochemical water splitting and its reverse process is crucial for producing hydrogen and achieving high efficiencies for fuel cells. Controllable water activity is essential for electrochemical systems. In applications such as the production of molecular hydrogen[48], higher water activity is desirable, while in other applications like aqueous batteries[49], electrochemical CO_2 reduction[50,51], or electrochemical N_2 reduction[52], suppressing HER is desired. Therefore, it is critical to tailor and control the water activity properly, which remains a challenge. While conventional design of catalysts has focused on tuning the surface electronic structures of electrodes[39,277,278] and binding strength of intermediates[39,48,279], recent studies show that changing electrolyte compositions, such as spectator cations and pH[198,241], can also significantly alter catalytic activity and kinetics by orders of magnitude, highlighting new opportunities in tuning non-covalent interactions in the electrolytes to control catalytic activities. However, water plays dual roles in aqueous electrolytes during HER, both as solvents and as reactants, complicating the physical picture, and the mechanisms at play in the electrochemical double-layer for HER are poorly understood.[53] Isolating the sole role of water as a reactant will therefore be promising to simplify the physical picture and understand the PCET kinetics, which could be achieved through confinements.[49,53,280]

To further develop design principles for electrolyte engineering and unravel the role of interfacial hydrogen bonding, here we employ a series of water-in-solvent electrolytes for hydrogen evolution and oxidation reactions (HER/HOR). We systematically confine water in organic matrixes, including acetonitrile (ACN) and dimethyl sulfoxide (DMSO), and tune the hydrogen-bonding networks by changing the water concentration (2% - 100% molar ratio) and altering the donor number of organic solvents. Similar to the concept of "water-in-salt" electrolytes, which have larger electrochemical windows than 1.23 V[49], here these "water-in-solvent" electrolytes are expected to suppress water reduction. We conduct *ex situ* FT-IR and NMR measurements to quantify the bulk water structures of water confined in organic solvents. We then use RDE experiments to study the HER/HOR kinetics for these "water-in-solvent" electrolytes, and quantify the organic poisoning effects. Finally the observations on water content and solvent effects are justified through interfacial water structures, supported by *in situ* SEIRAS.

We found that water molecules became more isolated when decreasing the water-to-organic ratio, and water reduction shifted to a more negative potential. The shifts in onset potentials were solvent-dependent, where DMSO-containing electrolytes suppressed HER and lowered the onset potential compared to ACN-containing electrolytes. The suppression effect of HER with DMSO is attributed to its stabilization effect of isolated and weakly H-bonded water as a result of the high donor number, while the enhancement effect of HER with ACN is due to the promotion of interfacial highly hydrogen-bonded water. Surface-enhanced infrared absorption spectroscopy (SEIRAS) measurements provided further support for the changes in interfacial hydrogen bonding during the reactions, highlighting

the role of interfacial hydrogen bonds between organic solvents and water in controlling HER/HOR kinetics.

These findings open up immense opportunities for using non-covalent hydrogen bonding interactions at the electrified interface to control the kinetics of ORR, HER, and beyond. The understanding would also be impactful across other reactions crucial to improving decarbonizing efforts in energy storage, such as electrochemical N_2 reduction, CO_2 reduction, and aqueous batteries.

6.2 Bulk structure of water confined in organic solvents

Ex situ FT-IR and nuclear magnetic resonance (NMR) of bulk water structures for water-in-solvents and dilute electrolytes showed that water molecules became more isolated from other water molecules when decreasing the water content, indicated from a shift to higher wavenumber for OH stretching in FT-IR, and a lower chemical shift value in ^{1}H NMR.

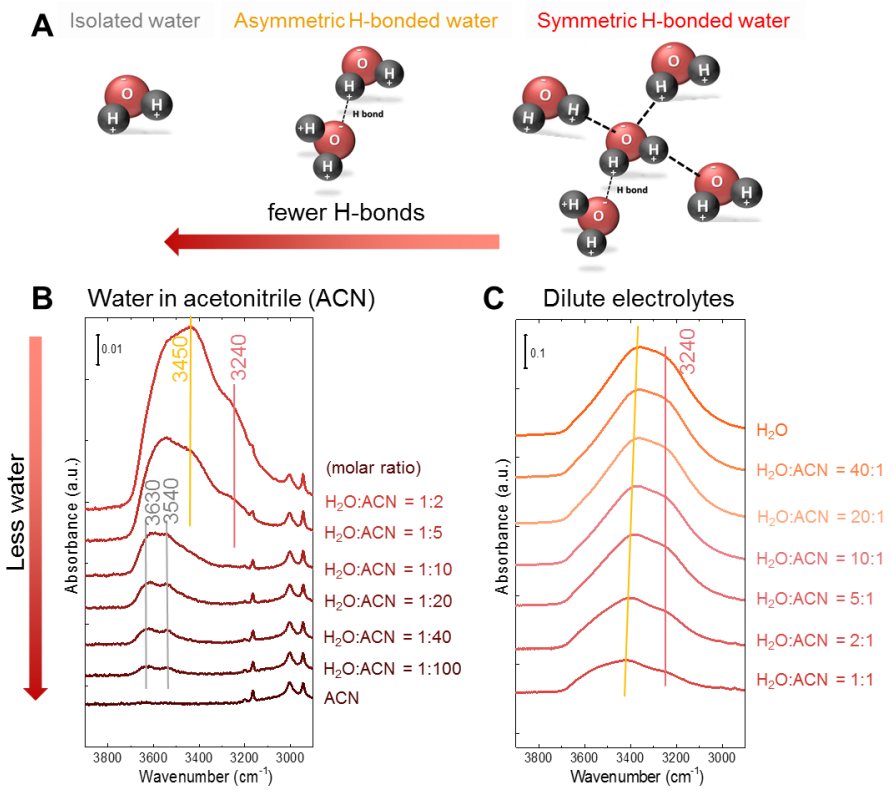

Fig. 6-1 FT-IR for bulk structure of water confined in ACN. (A) Schematic of three types of hydrogen-bonded water. The number of hydrogen bonds between water decreased from symmetric H-bonded water, asymmetric H-bonded water, to isolated water. *Ex situ* FT-IR spectra for (B) water confined in ACN, where H_2O-to-ACN molar ratio is smaller than 1; and (C) dilute electrolytes, where H_2O-to-ACN molar ratio is larger than 1.

FT-IR quantifies the hydrogen-bonding network of water, where in the OH stretching region the peaks at higher wavenumbers correspond to fewer hydrogen bonds, denoted as "isolated water"[197,198,281,282] (Fig. 6-1A). For water confined in ACN, when decreasing the H_2O:ACN molar ratio from 1:2 to 1:100 (Fig. 6-1B), the OH stretching band for water shifted from 3450 and 3240 cm^{-1}, representing asymmetric H-bond[197,198,281,282] and symmetric H-bonded (ice-like) water[197,198,281,282], respectively, to mainly 3630 and 3540 cm^{-1}, which represented isolated water[197,198,281,282]. Both 3630 and 3540 cm^{-1} arose from isolated water but were different modes - symmetric and asymmetric OH stretching of

isolated water[283], respectively. Note that the "isolated water" meant that the water molecule was isolated from other water molecules, but not necessarily isolated from any molecules. In fact, it was surrounded by and interacted with other organic species, which will be discussed later. For the dilute electrolytes where H_2O:ACN molar ratio is larger than 1 (Fig. 6-1C), their spectra look similar to that of pure water, dominated by 3450 and 3240 cm^{-1} peaks, indicating the hydrogen bonding network gradually recovers a bulk-like feature.

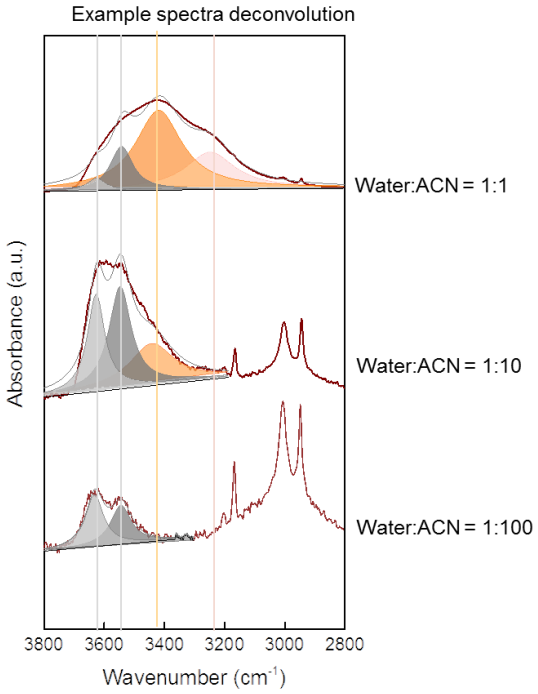

Fig. 6-2 Example of spectra deconvolution for water confined in ACN. Light and dark grey bands correspond to isolated water, with peak center at 3630 cm^{-1} and width 75 cm^{-1} (light grey), and peak center at 3540 cm^{-1} and width 85 cm^{-1} (dark grey). The yellow band represents symmetric H-bonded water, with peak center at 3420±20 cm^{-1} and width 190 cm^{-1}. The light red band corresponds to symmetric H-bonded water, with peak center at 3240 cm^{-1} and width 210 cm^{-1}.

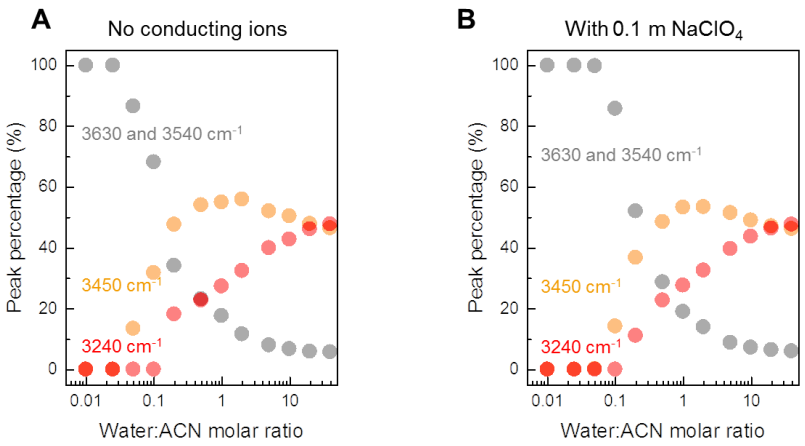

Fig. 6-3 Deconvoluted peak percentage of three types of water for water confined in ACN, (A) without and (B) with 0.1 m $NaClO_4$ conducting ions. Percentage was calculated by integrating the areas of each water band and calculating their ratios. Grey points are the sum of two isolated water peaks at 3630 cm^{-1} and 3540 cm^{-1}.

Deconvoluting the spectra (Fig. 6-2, Fig. 6-3 A) according to the assignments above further confirmed the higher percentage of isolated water when decreasing the water molar ratio, while lower percentage of hydrogen-bonded water. The C≡N stretching of ACN shifted to higher wavenumbers when increasing the water concentration (Fig. 6-4), indicating that water started to interact with other water molecules through hydrogen bonding instead of interacting with ACN, and hence ACN became more isolated from water clusters and shifted to higher wavenumbers. Adding 0.1 m $NaClO_4$ salts ("m" denotes molality) as conducting ions in the solution did not have obvious impact on the FT-IR spectra, where all the peak positions are the same as the ones without ions (Fig. 6-5), and the deconvoluted peak percentage was also similar to that without ions (Fig. 6-3 B).

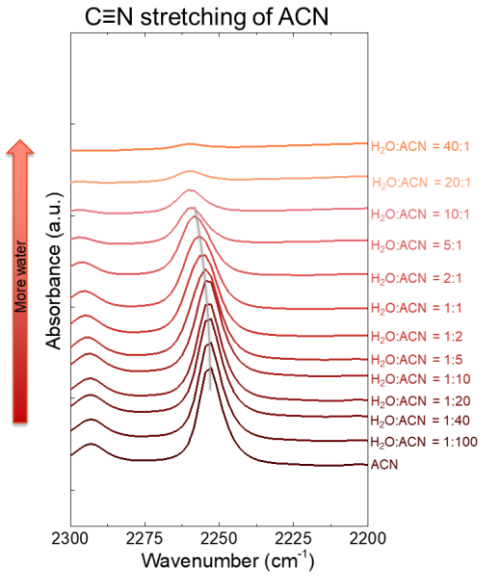

Fig. 6-4 C≡N stretching region of FT-IR spectra for water confined in ACN.

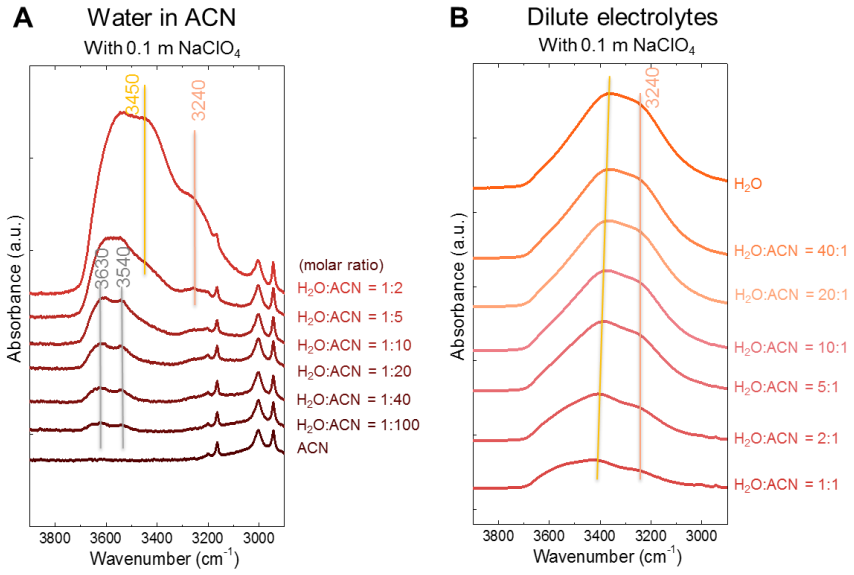

Fig. 6-5 FT-IR for water confined in ACN with added 0.1 m $NaClO_4$ as conducting ions. *Ex situ* FT-IR spectra for (B) water confined in ACN, where H_2O-to-ACN molar ratio is smaller than 1; and (C) dilute electrolytes, where H_2O-to-ACN molar ratio is larger than 1.

NMR spectra of bulk electrolytes for water confined in ACN (Fig. 6-6A) were conducted in a coaxial NMR configuration (Fig. 6-6B) to avoid deuterated solvent (D_2O) from

affecting the solvation structures of the water-in-solvent solutions. When decreasing the water-to-ACN ratio, ^{1}H NMR chemical shift for the water peak gradually shifted to a lower value, from 4.7 ppm to 3 ppm (Fig. 6-6C), indicating that the proton on water is more shielded[284], having a higher electron density from the tighter O-H bond on isolated water molecules. The lower chemical shift at low water content also meant that water had a higher pK_a value[285] and harder deprotonation when they were isolated.

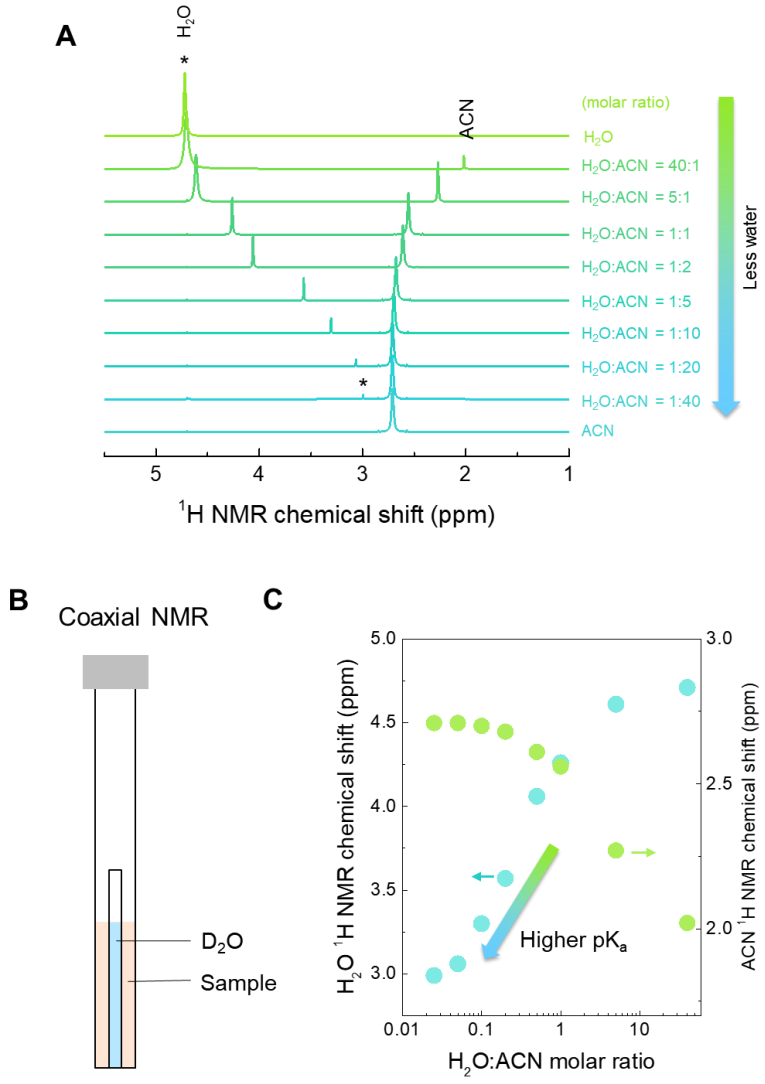

Fig. 6-6 Bulk NMR for water confined in ACN. (A) ^{1}H NMR spectra for water confined in ACN, where the water peak is marked by *. (B) Coaxial NMR sample schematics. (C) ^{1}H NMR chemical shift of water peaks as a function of water to ACN molar ratios.

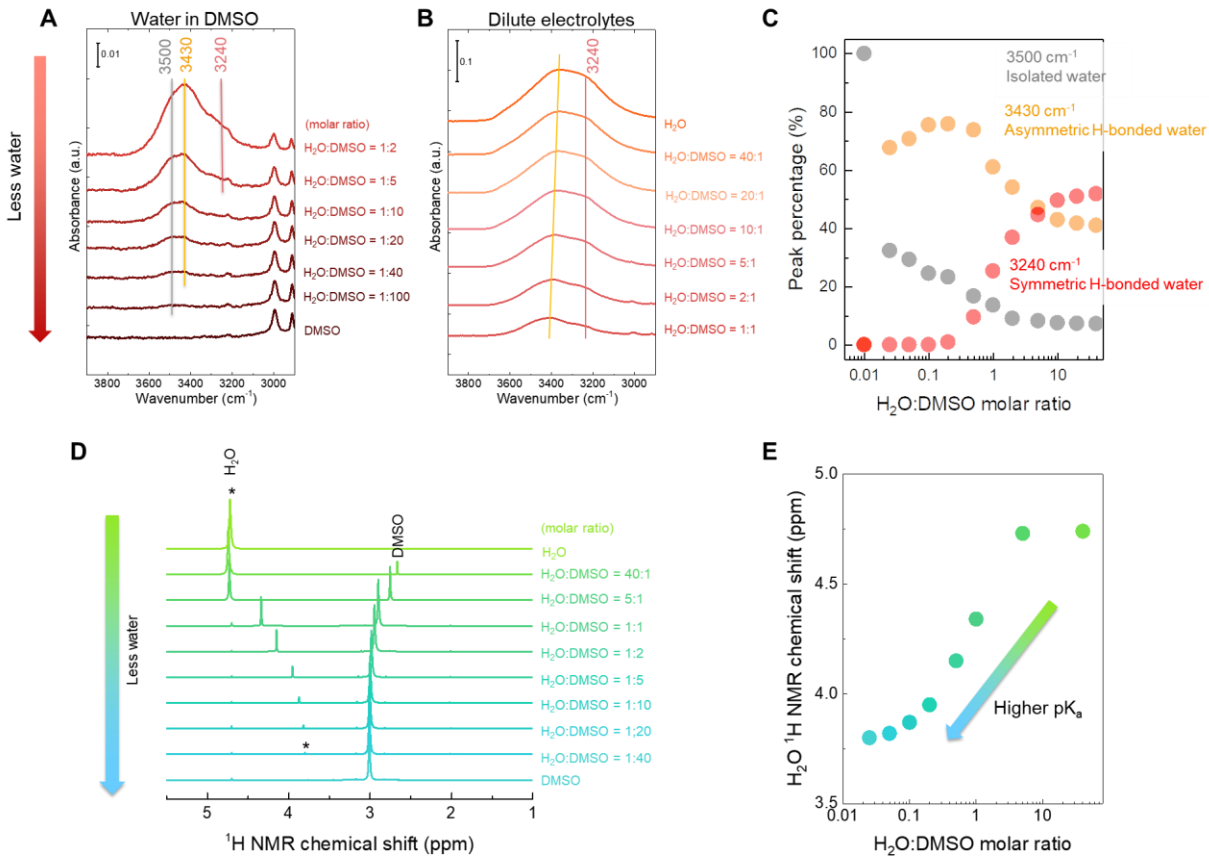

Fig. 6-7 Bulk FT-IR and NMR for water/DMSO mixtures. *Ex situ* FT-IR spectra for (A) water confined in DMSO, where H_2O-to-DMSO molar ratio is smaller than 1; and (C) dilute electrolytes, where H_2O-to-DMSO molar ratio is larger than 1. (D) ^1H NMR spectra for water/DMSO mixtures, where the water peak is marked by *. (E) ^1H NMR chemical shift of water peaks as a function of water to DMSO molar ratios.

We further screened a library of organic solvents that are aprotic and miscible or soluble with water, including ACN, DMSO, dimethoxyethane (DME), dimethylacetamide (DMA), dimethylformamide (DMF), diethylene glycol dimethyl ether (G2), triethylene glycol dimethyl ether (G3), and tetrahydrofuran (THF). Water in DMSO exhibited similar concentration dependency to water in ACN, where decreasing water-to-DMSO ratio also led to fewer H-bonds between water with decreasing, indicated by higher OH stretching frequency in FT-IR (Fig. 6-7 A-C) and lower ^1H NMR chemical shift (Fig. 6-7 D-E). Water

in the other organic solvents had similar trend that when water-to-organics ratio was smaller than 1 (Fig. 6-8), isolated water peaks at high wavenumbers dominated the OH stretching region. As water content increased, asymmetric H-bonded water peak arose (Fig. 6-8) and gradually shifted to lower wavenumbers up to 3430 cm^{-1} (Fig. 6-9). When water-to-organics ratio was increased to larger than 1, the OH stretching region gradually recovered pure water features dominated by asymmetric and symmetric H-bonded water.

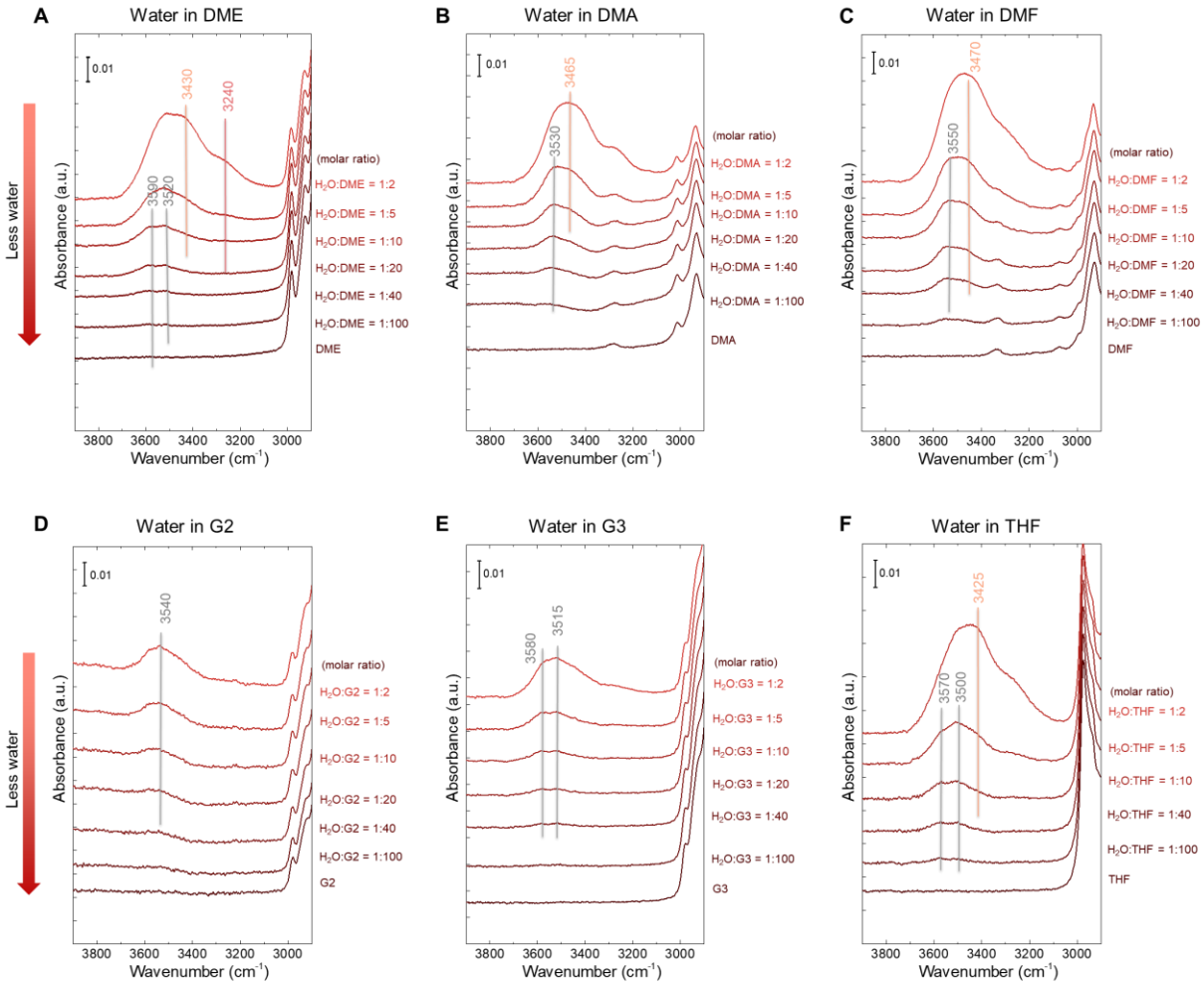

Fig. 6-8 FT-IR for bulk electrolyte of water confined in organics, where H_2O-to-organic molar ratio is smaller than 1. Spectra for water in (A) DME, (B) DMA, (C) DMF, (D) G2, (E) G3, and (F) THF. Grey lines mark the peak centers of isolated water, yellow

lines mark the centers of asymmetric H-bonded water, and red lines mark symmetric H-bonded water.

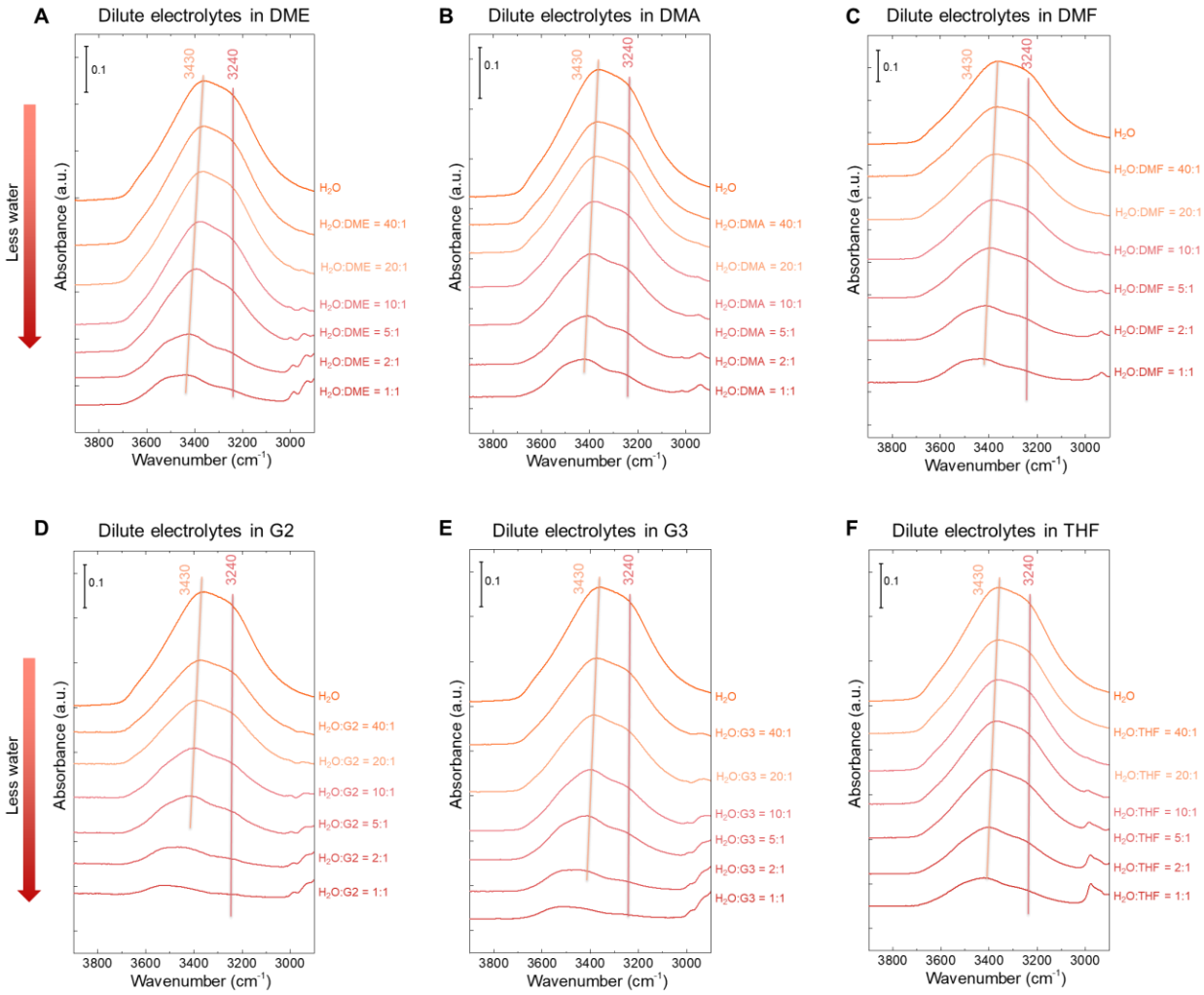

Fig. 6-9 FT-IR for bulk electrolyte of water with organics, where H_2O-to-organic molar ratio is larger than 1 (dilute electrolytes). Spectra for water in (A) DME, (B) DMA, (C) DMF, (D) G2, (E) G3, and (F) THF. Yellow lines mark the peak centers of asymmetric H-bonded water, and red lines mark symmetric H-bonded water.

It is interesting to note that the peak positions of isolated water (Fig. 6-1B, Fig. 6-7A, Fig. 6-8) varied among different organic solvents, located at higher frequency for water in ACN (3630 and 3540 cm^{-1}, Fig. 6-10A-B) while at lower frequency for water in DMSO (3500 cm^{-1}, Fig. 6-10A-B). The isolated water OH stretching wavenumber (taking the highest

frequency one if there were two peaks) was found to correlate with the solvent donor number (DN), shown in Fig. 6-10C. Higher-DN solvent like DMSO had a strong interaction with isolated water through the hydrogen bonding between O (on DMSO S=O) and H (on water), weakening the O-H bond strength on isolated water and shifting it to lower frequency (Fig. 6-10C). On the contrary, lower-DN solvent like ACN, had weaker interactions with isolated water and therefore the OH stretching of water remained strong and high-frequency. Next, we took ACN and DMSO as representative solvents to investigate the HER/HOR kinetics for confined water, since these two solvents were on the two ends of the spectra (Fig. 6-10C) among screened organics.

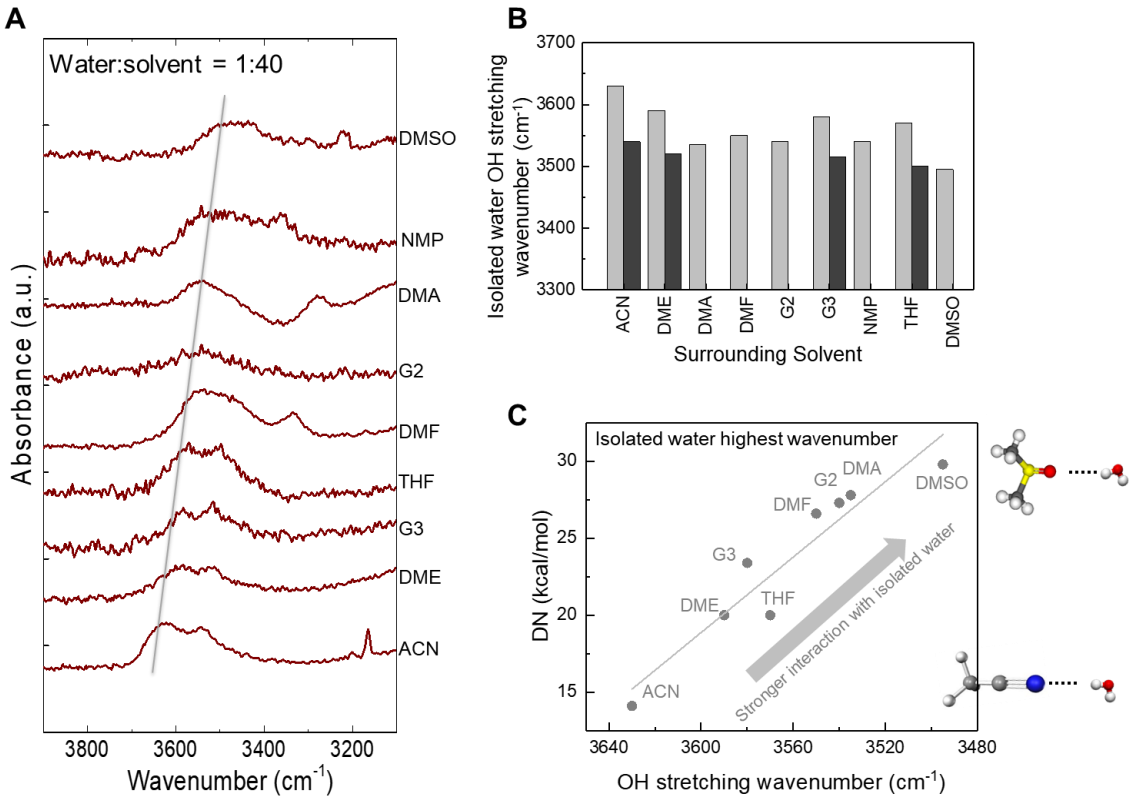

Fig. 6-10 FT-IR for bulk electrolyte of water confined in organics, with H_2O-to-organics molar ratio = 1:40. (A) Spectra for water in organic solvents, where the grey line marked the highest wavenumber of isolated water. (B) Plot of isolated water O-H stretching frequencies for different surrounding solvents. Black corresponded to a second peak for water some solvents, arising from different modes of O-H stretching. (C)

Correlation between OH stretching frequency of isolated water and the donor number of solvents. For the cases where isolated water had two peaks, the high wavenumber one was taken.

6.3 HER/HOR activity for water-in-solvents

6.3.1 HER/HOR activity for water confined in DMSO

The HER/HOR activity were measured on Pt using a rotating disk electrode (RDE). The typical cyclic voltammograms (CV) for water-in-DMSO (1:40 molar ratio) on Pt (Fig. 6-11) showed that HER started at around -1.5 V_{SHE} while HOR started at around -0.25 V_{SHE}. Further, HOR in H_2 is rotation rate dependent, indicating that H_2 gas diffusion was limiting and needed correction from the Koutecký–Levich equation, while HER is not dependent on the rotation rate or H_2 *vs.* Ar atmosphere. It is noted the organic solvent themselves (ACN or DMSO) had a large electrochemical stability window, -3 to 1.7 V_{SHE} for DMSO and -2.5 to 3.2 V_{SHE} for ACN (Fig. E-2), and thus did not contribute to the current we observed here.

During the forward scan (Fig. 6-11A), one positive peak appeared after HER and before HOR when measured in H_2 gas, while it did not show up in the backward scan or in Ar atmosphere (Fig. 6-11). The peak was also rotation dependent (Fig. 6-11A), and we believe this peak is related to H_2 gas diffusion/removal from the following analysis. Moving the lower cutoff to a higher value from -1.61 V_{SHE} to -1.5 V_{SHE} (Fig. E-3A) decreased the HER current, and meanwhile decreased the positive peak area and peak width. It seemed that the area and width of the positive peak directly scaled with the HER current density before it

(Fig. E-3A), indicating the peak was related to the amount of H_2 generated. It is possible that with more H_2 generated, it would take longer for H_2 gas to desorb or diffuse away from the surface, leading to a larger and broader peak. This hypothesis is consistent with the rotation rate dependency (Fig. 6-11A) that the peak was broader at low rotation rates, as the removal or diffusion of H_2 gas would be slower at slower rotation.

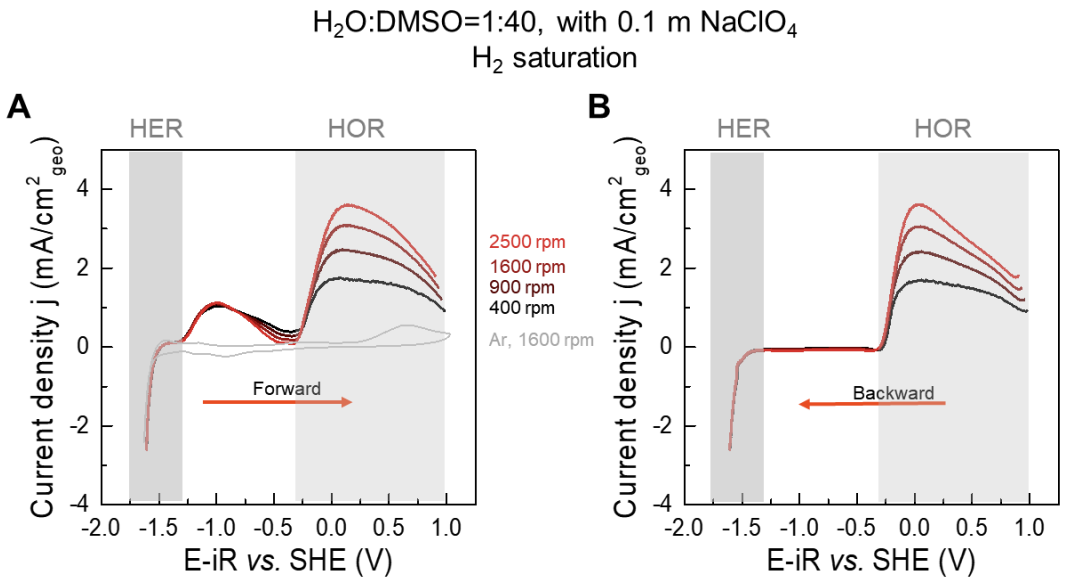

Fig. 6-11 Typical CV for water-in-DMSO (H_2O:DMSO=1:40) on Pt. (A) Forward and (B) backward scans of CV. Curves were measured at four rotation rates from 2500 rpm to 400 rpm in H_2 gas (red lines), and at 1600 rpm in Ar (grey lines). Electrolytes contained 0.1 m $NaClO_4$ as conducting ions. Shaded areas corresponded to the HER and HOR reaction regions.

Varying the upper cutoffs in CV affected slightly the HOR and HER current densities (Fig. E-3B). Lowering the upper cutoff from 0.9 V_{SHE} to -0.4 V_{SHE} led to a decrease in HOR and a slight decrease in HER current densities, which is due to the slight poisoning effect of DMSO on Pt surfaces if cutting off at a low potential. DMSO was likely to only get

removed from the surface when scanning to high potentials to recover a clean Pt surface. Quantifications of the organic poisoning effects will be discussed in Session 6.2.4.

As HOR current density was dependent on rotation rates, we next extracted the HOR kinetic current density. First, the HOR kinetics was found distinguishable from the calculated Nernstian diffusion overpotential of hydrogen[286] (Fig. 6-12A), meaning that kinetic current density was able to be extracted from measured current densities at various rotation rates by the Koutechy-Levich equation[287], shown in Fig. 6-12B.

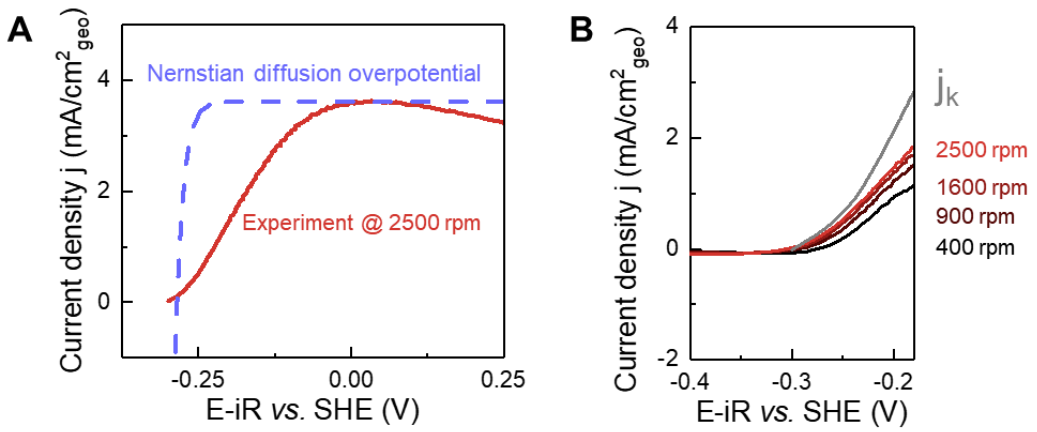

Fig. 6-12 Nernstian diffusion overpotential comparison and Koutecky-Levich analysis on HOR current density. (A) Calculated Nernstian diffusion overpotential[286] and measured HOR polarization curves in H_2O:DMSO=1:40 with 0.1 m $NaClO_4$electrolyte are compared. (B) HOR kinetic current density extracted from measured current density by the Koutechy-Levich equation.

6.3.2 Water content- and solvent- dependent HER/HOR activity

We first investigated the HER/HOR activity when varying water content in DMSO. Water reduction (HER) shifted to more negative potentials with decreasing water content in

DMSO (Fig. 6-13A), where the HER onset potential (the potential at which the current density reached -0.2 mA/cm^2_{geo}) shifted from around -0.5 V_{SHE} for the pure aqueous electrolyte to around -1.6 V_{SHE} for the water-in-DMSO (H_2O:DMSO=1:40) electrolyte. To take into account of the thermodynamic shift due to changes in water activity or pH, we have calculated the thermodynamic equilibrium potential for HER/HOR based on the Nernst equation[287]. The thermodynamic potential, however, only shifted slightly from -0.45 V_{SHE} to -0.55 V_{SHE} across the concentration range (Fig. 6-13B), much smaller than the experimental shift, which indicated that the experimental shift in HER onset potential came largely from kinetics rather than pure thermodynamics. We then shifted all the HER polarization curves with respect to the thermodynamic potentials (Fig. 6-13C), *i.e.* zero overpotentials corresponded to the thermodynamic potentials for each electrolytes, so that the overpotentials represented the kinetic barriers. Decreasing the water content to H_2O:DMSO 1:40, the onset overpotential went to as large as -1 V (Fig. 6-13C).

Unlike HER which showed strong dependency on water content, the HOR side did not show large shifts in the onset potentials (Fig. 6-14A), and were all close to the thermodynamic potential around -0.5 V_{SHE}. The maximum HOR current densities varied among different water content, which could be related to the different solubility of H_2 gas in DMSO and water[288], and the occupation of DMSO on some Pt sites. Kinetic current densities were extracted from measurements at 4 rotation rates (2500 rpm, 1600 rpm, 900 rpm, and 400 rpm) using the Koutechy-Levich equation (Fig. 6-14B), which showed that the kinetic currents did not vary significantly either. There was a slight decrease in j_k from pure water to dilute electrolytes containing DMSO, but stayed almost unchanged after

adding more DMSO and confining water. Tafel plots for the HOR side (Fig. 6-14C) were generated based on the kinetic currents and the thermodynamic potentials calculated, and the curves for different water-to-DMSO ratios were mostly collapsed with each other, again confirming that HOR had weak dependency on water content.

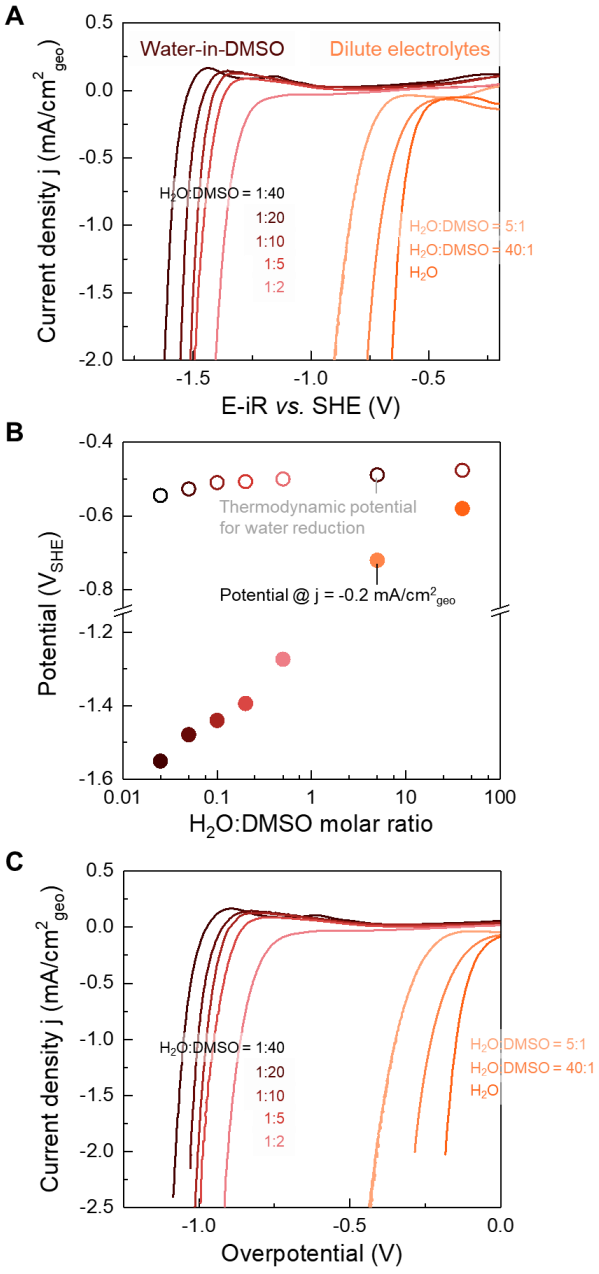

Fig. 6-13 HER current density for various water content in DMSO on Pt surface with Ar saturation, at rotation speed of 1600 rpm. (A) HER polarization curves in the SHE

scale. (B) Calculated thermodynamic potential for water reduction (open circles) and measured HER onset potential (filled circles) at different water content in DMSO. HER onset potentials were taken as the potential at which the current density reached -0.2 mA/cm^2_{geo}. (C) HER polarization curves with zero overpotentials shifted to the corresponding thermodynamic potentials for water reduction for each electrolyte. Electrolytes contained 0.1 m $NaClO_4$ as conducting ions.

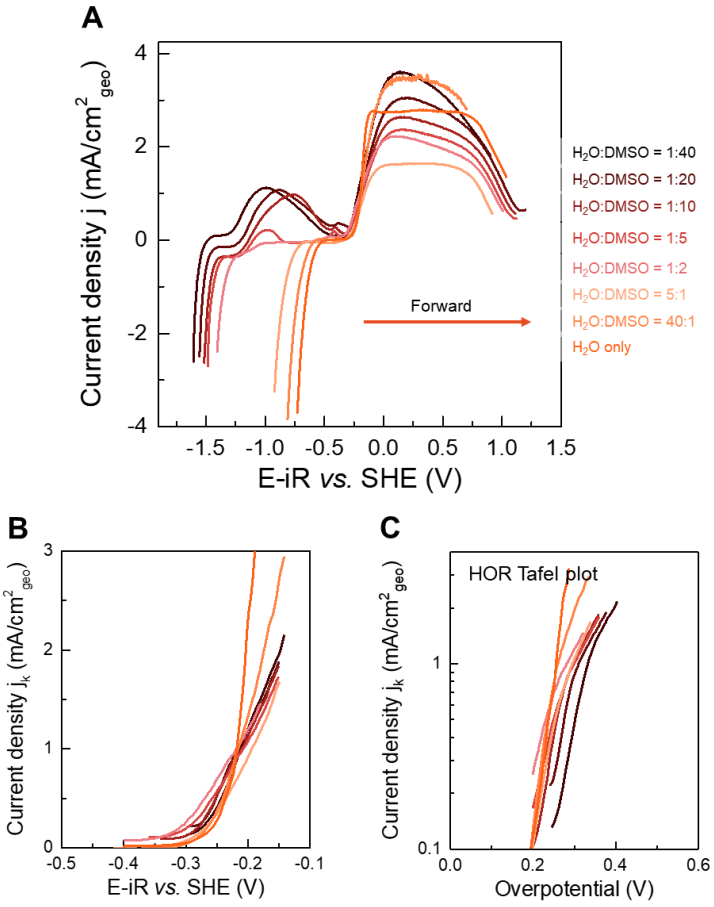

Fig. 6-14 HOR current density for various water content in DMSO on Pt surface with H_2 saturation. (A) HER/HOR polarization curves at rotation speed of 2500 rpm. (B) HOR kinetic current density extracted from measured current density at 2500 rpm to 400 rpm by the Koutechy-Levich equation. (C) HOR Tafel plots, with zero overpotentials shifted to the corresponding thermodynamic potentials calculated for each electrolyte. Electrolytes contained 0.1 m $NaClO_4$ as conducting ions.

To summarize the water-in-DMSO HER/HOR kinetics on Pt, the overall Tafel plots (Fig. 6-15A) for both HER and HOR kinetic current densities showed that HER had larger onset

overpotentials when water-to-DMSO ratio got smaller, while HOR kinetics did not change significantly. As we decreased the water content (Fig. 6-15B), pK_a of water increased according to the ^1H NMR shift, meanwhile the fraction of isolated water increased according to bulk FT-IR spectra. Water activity decreased at low water-to-DMSO ratios, indicated by the water reduction onset potential shift to more negative values (Fig. 6-15B).

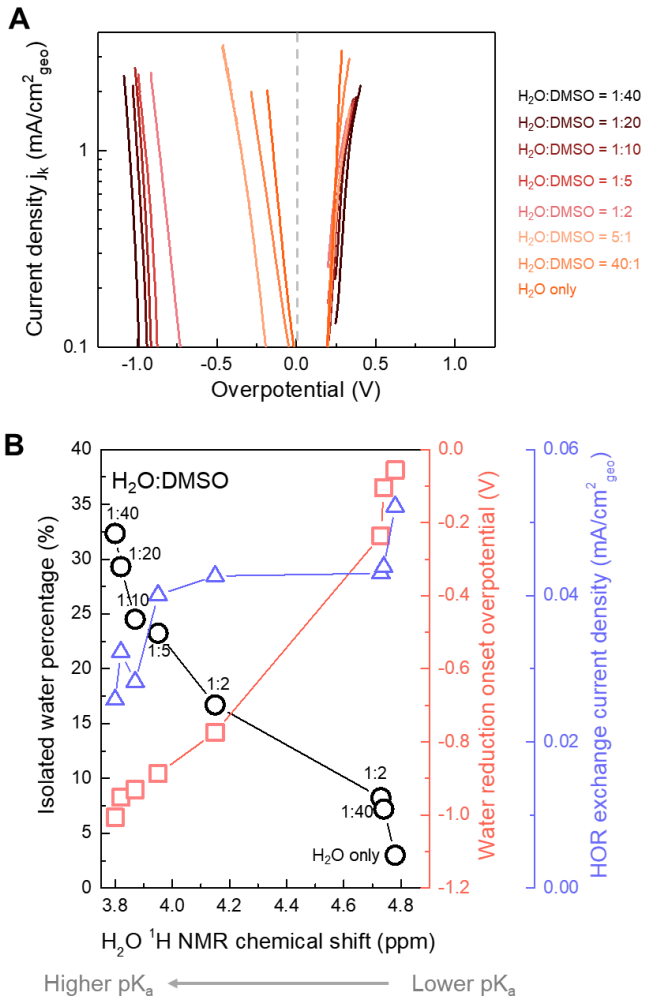

Fig. 6-15 HER/HOR summary plots for water-in-DMSO on Pt surface. (A) Tafel plots for both HER/HOR. The grey dotted line at the center marked the zero overpotential, and HER kinetic current densities were on the left, taken as the current densities measured in Ar. HOR kinetic current densities were on the right, calculated from the Koutechy-Levich equation. (B) Correlation between isolated water percentage in bulk electrolytes, water reduction onset potential in DMSO, and HOR exchange current densities with ^1H NMR shift.

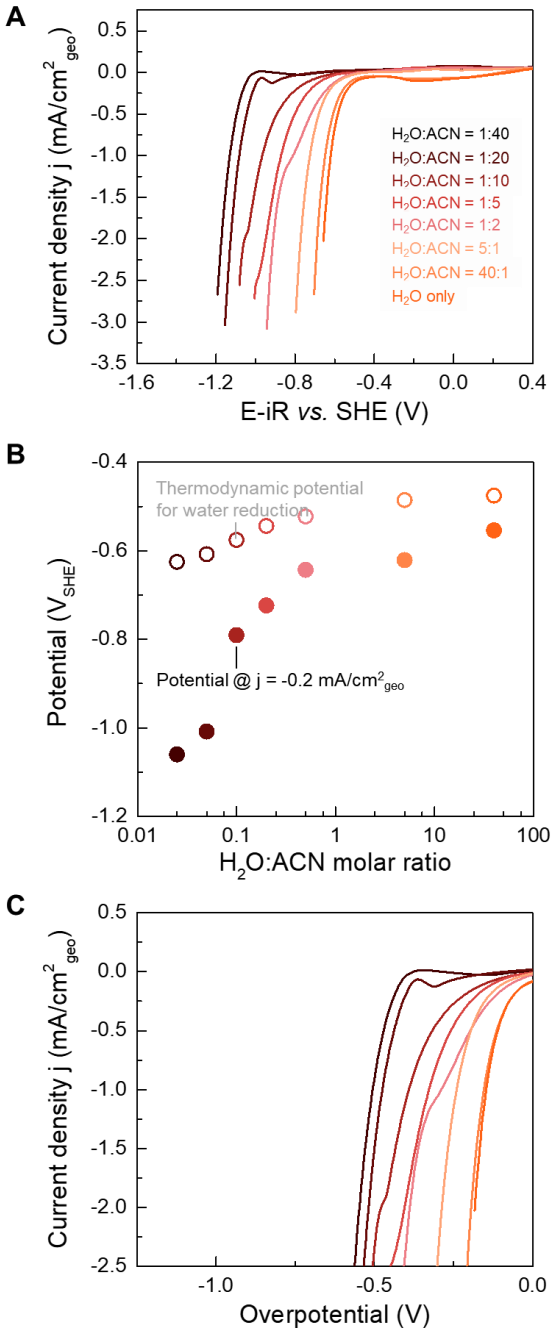

Fig. 6-16 HER current density for various water content in ACN on Pt surface with Ar saturation, at rotation speed of 1600 rpm. (A) HER polarization curves in the SHE scale. (B) Calculated thermodynamic potential for water reduction (open circles) and measured HER onset potential (filled circles) at different water content in ACN. HER onset potentials were taken as the potential at which the current density reached -0.2 mA/cm^2_{geo}. (C) HER polarization curves with zero overpotentials shifted to the corresponding

thermodynamic potentials for water reduction for each electrolyte. Electrolytes contained 0.1 m $NaClO_4$ as conducting ions.

We next explored the kinetics for water in ACN, the other solvent with much smaller DN than DMSO. Similarly, as we decreased water content, the HER polarization curves shifted to more negative (Fig. 6-16A). The HER onset potential (the potential at which the current density reached -0.2 mA/cm^2_{geo}) shifted from around -0.5 V_{SHE} for the pure aqueous electrolyte to around -1.1 V_{SHE} for the water-in-ACN (H_2O:ACN=1:40) electrolyte. Our results of HER for water-in-ACN were comparable to previous results reported[53], with similar onset potentials and current densities. We also calculated the thermodynamic equilibrium potential for HER/HOR, which shifted slightly from -0.45 V_{SHE} to -0.63 V_{SHE} across the concentration range (Fig. 6-16B). Shifting all the HER polarization curves with respect to the thermodynamic potentials also showed that HER was harder at low water-to-ACN ratios (Fig. 6-16C), but these overpotentials were much smaller than water-in-DMSO (Fig. 6-13C, Fig. 6-16C). For instance, H_2O:ACN = 1:40 had HER onset at -0.48 V in overpotential Fig. 6-16C, while H_2O:DMSO = 1:40 had HER onset at as high as -1 V as the overepotential (Fig. 6-13C).

Unlike DMSO, the HOR side for water-in-ACN had great difference when varying water content (Fig. 6-17A), and both the maximum HOR current densities and onset potential changed. At very low water content (H_2O:ACN = 1:40), HOR barely happened as shown from the very low current densities (Fig. 6-17A), despite the fact that H_2 gas had much larger solubility in ACN than in water[289,290]. Kinetic current densities were extracted from measurements at 4 rotation rates (2500 rpm, 1600 rpm, 900 rpm, and 400 rpm) using the

Koutechy-Levich equation (Fig. 6-17B), and Tafel plots for the HOR side (Fig. 6-17C) were generated based on the kinetic currents and the thermodynamic potentials calculated, both graphs further confirming that HOR activity got lower and onset potential increased as we decreased water content in ACN, in contract to the DMSO case (Fig. 6-14B-C). We presumed that the low HOR activity and late onset for low water content in ACN were most likely due to the poisoning and passivation effect of ACN on the Pt surface, as ACN was known to have strong adsorption on Pt[291–293] and led to abnormal behaviors in HOR[292]. Further support for the ACN poisoning effect came from the following phenomena observed in experiments. The HOR for H_2O:ACN=1:40 had large difference in the forward and backward scans (Fig. E-2A), while for DMSO the difference was small (Fig. E-2B). The forward scan showed much lower HOR current densities than the backward scans in H_2O:ACN=1:40 (Fig. E-2C-D), indicating that a large portion of the Pt surface was passivated by ACN during the forward scan, and recovered more after the potential went up to a high voltage and cleaned up the ACN on surface. Another evidence that ACN had more poisoning on Pt than DMSO was by changing the upper cutoff potentials in CV. While lowering the upper cutoff potential led to only a slight decrease in HER current densities for H_2O:DMSO=1:40 (Fig. E-3B), the decrease of HER current densities was much more obvious in the case of H_2O:DMSO=1:40 (Fig. E-5). These results indicated that ACN would adsorb and passivate the Pt surface more strongly than DMSO, especially when the CV did not scan to high potentials to desorb ACN and clean the surface.

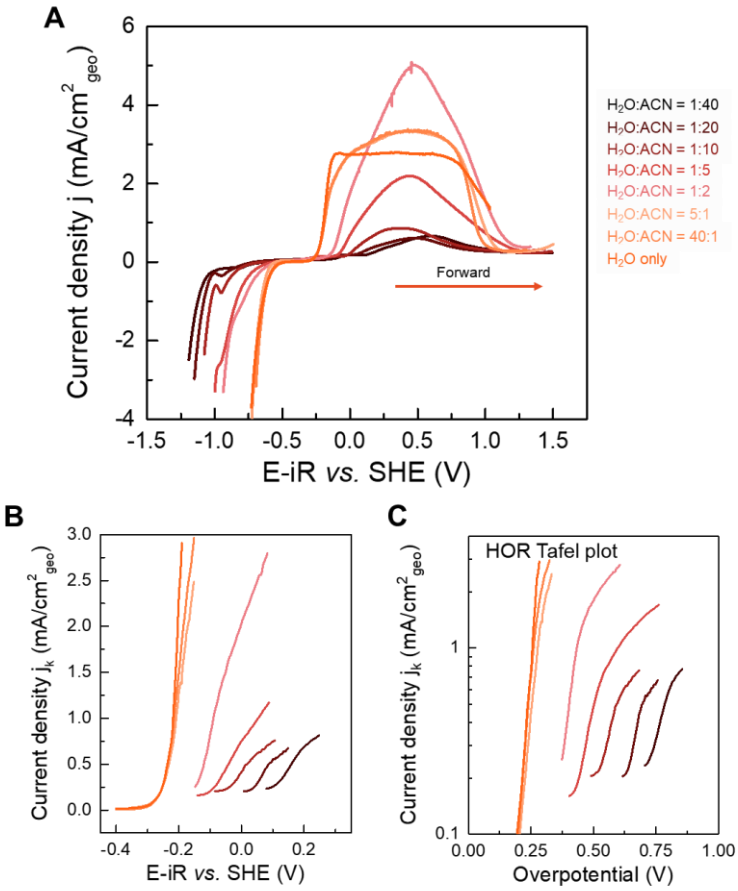

Fig. 6-17 HOR current density for various water content in ACN on Pt surface with H_2 saturation. (A) HER/HOR polarization curves at rotation speed of 2500 rpm. (B) HOR kinetic current density extracted from measured current density at 2500 rpm to 400 rpm by the Koutechy-Levich equation. (C) HOR Tafel plots, with zero overpotentials shifted to the corresponding thermodynamic potentials calculated for each electrolyte. Electrolytes contained 0.1 m $NaClO_4$ as conducting ions.

To sum up the trend for water in ACN and DMSO (Fig. E-6), water molecules become more isolated when decreasing the water-to-organic ratio in both cases, and the bulk structure of isolated water percentage directly correlated with the ^{1}H NMR chemical shift of water (Fig. 6-18), where ACN and DMSO followed a same trend line. The maximum change in pK_a was from 14 (for pure H_2O) to 16 (H_2O:ACN=1:40) (Fig. 6-18), where the pKa values were estimated from reported ^{1}H NMR of water at different temperatures[294]

and their pK_a values[295,296]. HER onset for water in both solvents shifted to a larger overpotential (Fig. 6-18), but the shifts in onset potentials were solvent-dependent. The HER polarization curves for DMSO-containing electrolytes were all at much larger overpotentials (Fig. E-6A) than ACN (Fig. E-6C) at same water-to-organics ratios. DMSO-containing electrolytes suppressed HER and lowered the onset potential more than ACN-containing electrolytes, and they followed different trend lines even with similar bulk pK_a values (Fig. 6-18).

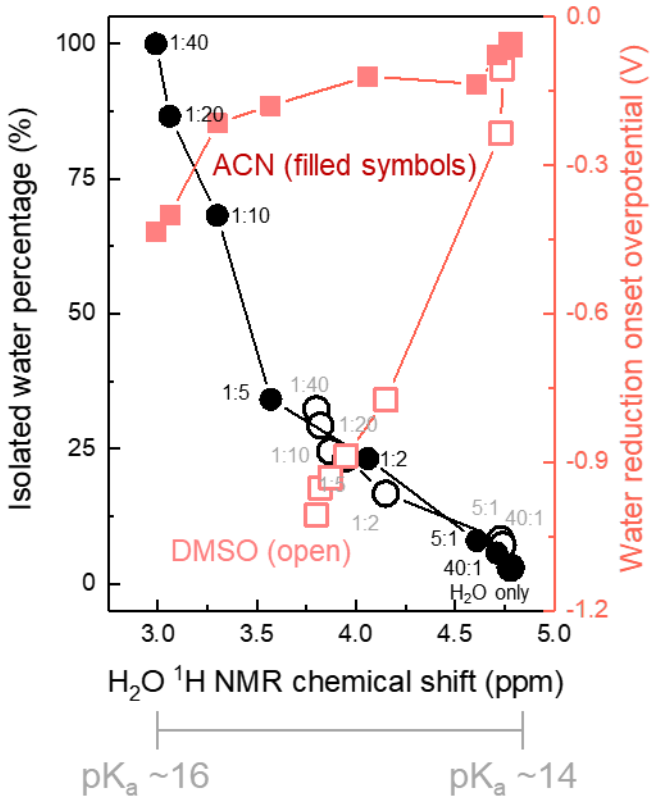

Fig. 6-18 Correlation between isolated water percentage in bulk electrolytes (black) and water reduction onset potential (red) in ACN (filled symbols) and DMSO (open symbols) with ^{1}H NMR chemical shift.

6.4 Solvent effects on HER/HOR

6.4.1 Quantifying organic poisoning effects

To develop a better understanding on how organic solvents changed the surface sites and affected the HER/HOR kinetics, we quantified the organics poisoning effects of ACN and DMSO from the changes in electrochemically active surface area (ECSA) of Pt before and after exposed to organics. The poisoning test was conducted in the following gmethod: after extensive polishing of the Pt disk electrode, we measured CV in a 0.1 M $HClO_4$ aqueous acid solution to obtain the ECSA for the pristine Pt electrode (Fig. 6-19). Then we took out the Pt and rinsed gently with dionized water (DI water) to remove the remaining acid on surface, then transferred it to water-in-solvent electrolyte (such as H_2O:organic = 40:1 with 1 m $NaClO_4$). After scanning CV in the organic mixture for 20 cycles at a fixed scan rate (50 mV/s), the surface had been contamination by organics. Finally we transferred the Pt electrode back to the 0.1 M $HClO_4$ acid solution after a gentle rinsing with DI water, and measured CV again in acid to obtain the ECSA after contamination. Within the whole process, Pt was not polished when switching electrolytes but only rinsed.

We found that for ACN-containing electrolytes, such as H_2O:ACN=40:1 where only tiny amount of ACN was in the mixture (Fig. 6-19A), the area of hydrogen underpotential deposition (H_{UPD}) region between 0 V_{RHE} to 0.3 V_{RHE} was much smaller after contamination than pristine Pt before contamination. While DMSO had similar suppression of HUPD after contamination for H_2O:DMSO=40:1 (Fig. 6-19B), the decrease was not as significant as ACN. At a low water content and high organics amount, such as

H_2O:organics=1:40 (Fig. 6-19C, D), the H_{UPD} region was even tinier, and might convoluted with the ACN adsorption peak around 0.5 V_{RHE} (Fig. 6-19C).

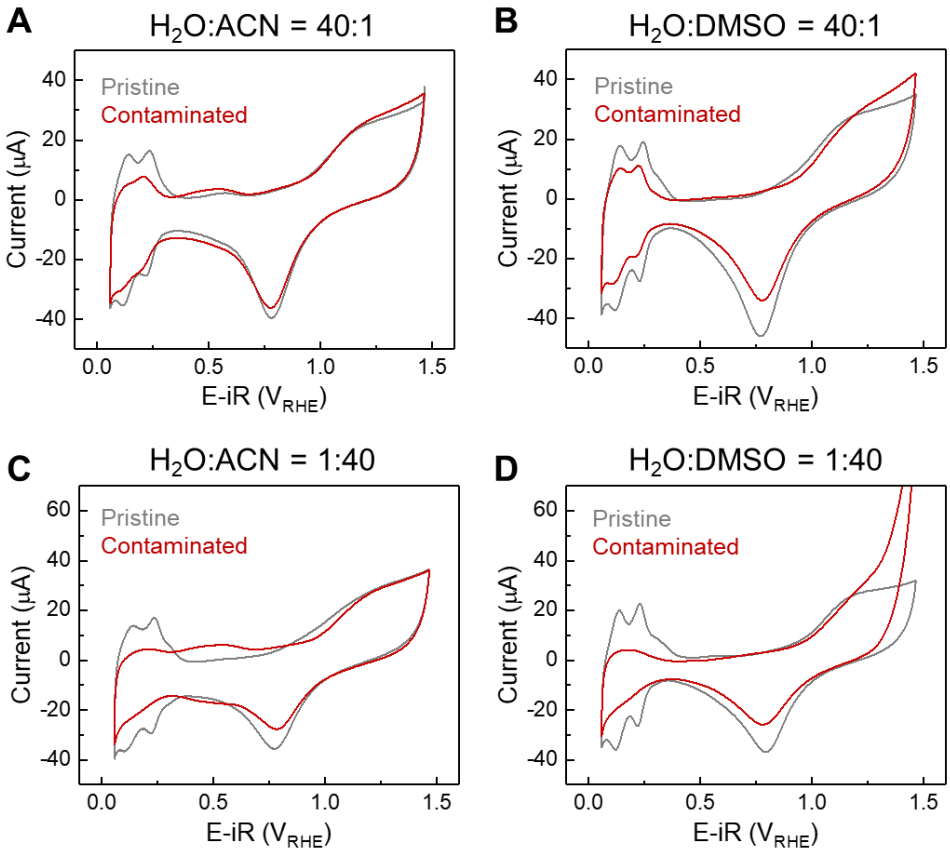

Fig. 6-19 CV for Pt in 0.1 M $HClO_4$ aqueous acid solution before (grey curves) and after (red curves) organic contaminations. Organic contamination in dilute cases (A) H_2O:ACN = 40:1 and (B) H_2O:DMSO = 40:1, and in low-water-content cases (C) H_2O:ACN=40:1 and (D) H_2O:DMSO=40:1. CV was measured in an Ar saturated environment.

ECSA was then estimated from the desorption of H_{UPD} features of CV. by calculating the net charge of hydrogen desorption region (around 0.05 V_{RHE} to 0.4V_{RHE}) with double layer correction, then divided by 210 μC/cm^2_{Pt}. The pristine Pt disk had ECSA around 0.3 cm^2_{Pt} (Fig. 6-20 A, B), while after exposure to small amount of ACN (H_2O:ACN=40:1), it decreased to 0.08 cm^2_{Pt} (Fig. 6-20A)[274]. ECSA further decreased to less than 0.03 cm^2_{Pt}

upon further decreasing water content to H_2O:ACN < 10. DMSO overall showed smaller extent of contamination to Pt, with ECSA decreased to 0.17 cm^2_{Pt} after exposure to H_2O:DMSO=40:1 (Fig. 6-20B), and stayed between 0.1 cm^2_{Pt} to 0.06 cm^2_{Pt} when further decreasing water content in DMSO (Fig. 6-20B). We further calculated the ratios of ECSA after contamination to ECSA before contamination (Fig. 6-20C) to quantify the extent of Pt passivation by organics. In ACN-containing electrolytes, only less than 10% of Pt sites were still active, while in DMSO-containing electrolytes, 30-40 % of Pt sites were active. These results that ACN had more poisoning effects on Pt than DMSO were consistent with our hypothesis and observed abnormal HOR behavior in ACN (Fig. 6-17, Fig. E-4, Fig. E-5), as well as previous literatures[291–293].

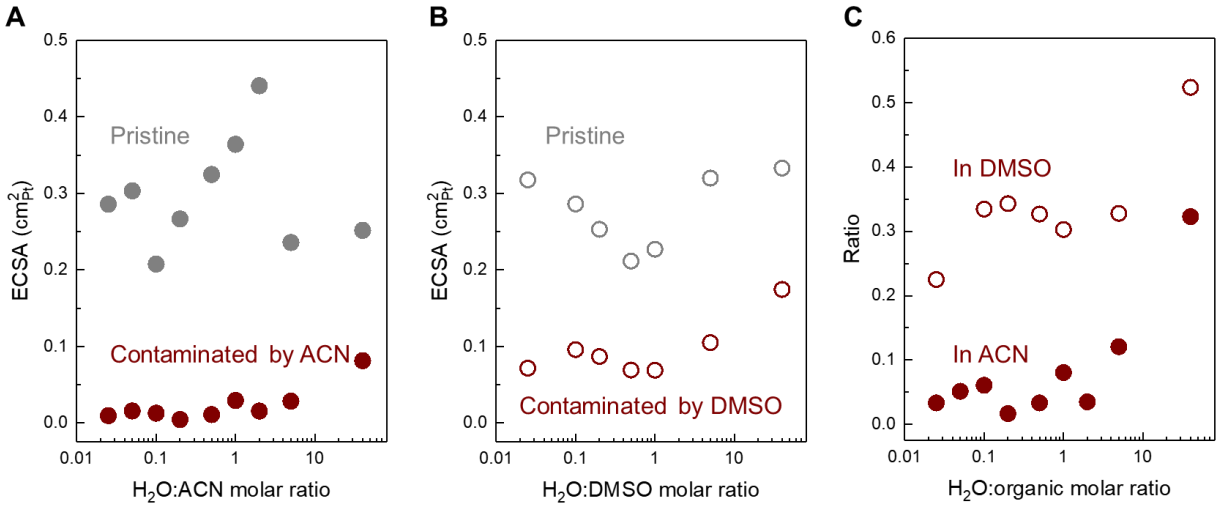

Fig. 6-20 Quantification of ECSA for Pt before (grey) and after (red) organic contaminations. ECSA of pristine Pt (A) before and after ACN contamination for each water/ACN mixtures, and (B) before and after DMSO contamination for each water/DMSO mixtures. (C) Ratios of ECSA after contamination to ECSA before contamination, in water/ACN mixtures (filled symbols) and water/DMSO mixtures (open symbols). ECSA was calculated from the CV in 0.1 M $HClO_4$ aqueous acid solutions.

Further support came from CV in organic mixtures (Fig. 6-21A-B). While the hydrogen desorption peaks were not as well-defined as in acid solutions, we could still try integrating the peaks, which ranged between -0.7 V_{SHE} to 0.2 V_{SHE}, and calculated ECSA after double layer correction. However, this method only served as a rough estimation for Pt ECSA due to the fact that the peak areas would possibly depend on the potential window scanned and hard to compare across different electrolytes with different CV potential cutoffs. Still, we could see a general trend that ACN-containing electrolytes had two to three times smaller ECSA than DMSO-containing electrolytes (Fig. 6-21C), in consistency with our results of acid CV (Fig. 6-20).

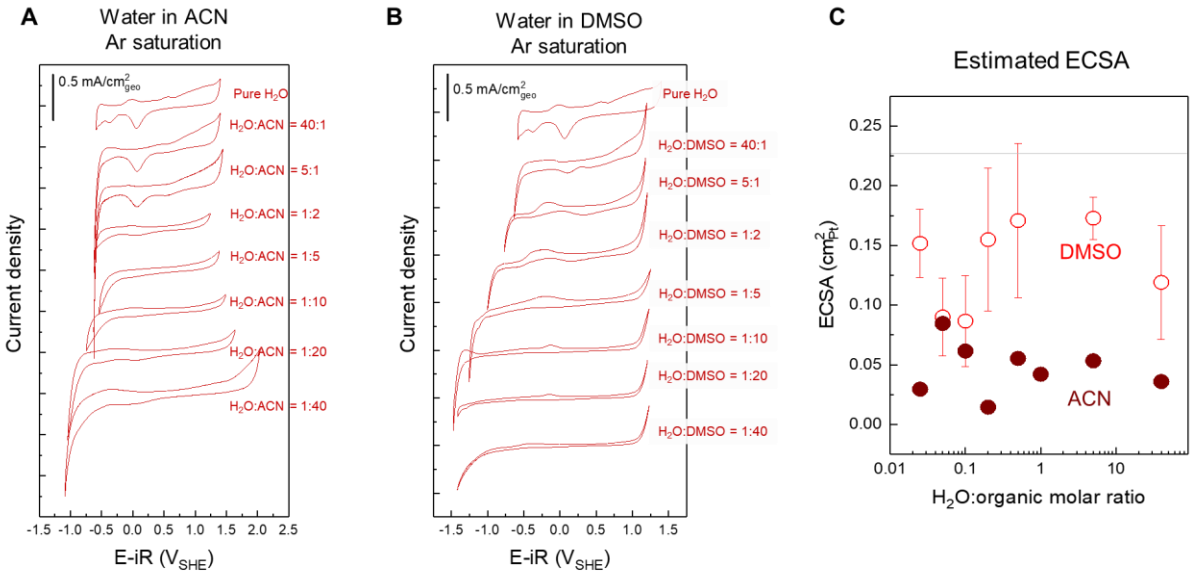

Fig. 6-21 Estimation of ECSA for Pt from CV in organic mixtures. CV of Pt in (A) water/ACN mixtures and (B) water/DMSO mixtures in an Ar-saturation environment. (C) Estimation of ECSA by integrating the hydrogen desorption peaks ranging between -0.7 V_{SHE} to 0.2 V_{SHE}, for water/ACN mixtures (filled symbols) and water/DMSO mixtures (open symbols). The grey line denotes ECSA for the case of pure water. All electrolytes contained 0.1 m $NaClO_4$ as conducting ions.

All these results suggested that ACN had more poisoning effects on Pt than DMSO, from the fact that ECSA in ACN was much smaller than DMSO. However, in the previous session we saw that DMSO suppressed HER much stronger than ACN, which could not be solely explained by poisoning effects where ACN should hinder more. Therefore, we believe water structure is playing a significant role in HER/HOR kinetics, and interfacial experiments and analysis will be needed. We next conducted *in situ* SEIRAS to probe the interfacial water structures.

6.4.2 Interfacial water structure from *in situ* SEIRAS

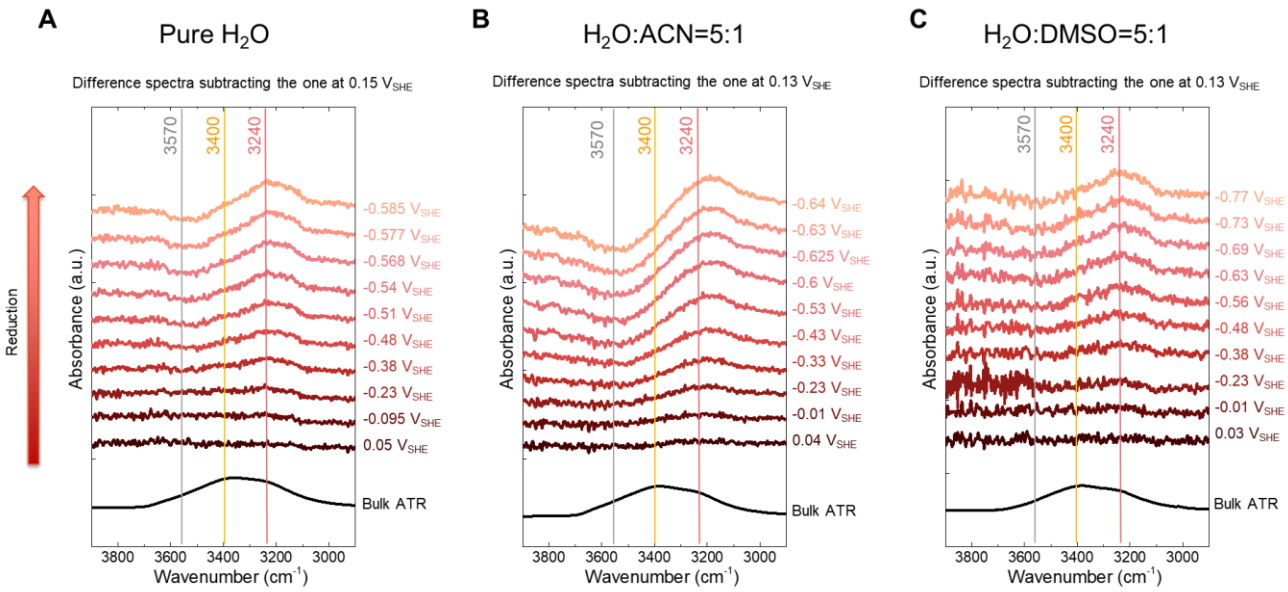

Fig. 6-22 *In situ* SEIRAS (O-H stretching region) for dilute electrolytes on Pt surfaces. *In situ* difference spectra (in red) for (A) pure water without organic solvents, (B) H_2O:ACN = 5:1, and (C) H_2O:DMSO = 5:1, and ATR spectra for the three electrolytes (in black). Electrolytes all contained 0.1 m $NaClO_4$ as conducting ions and under H_2 saturation. The spectra were subtracted with respect to the initial spectra collected at HOR potentials.

In situ SEIRAS revealed that ACN promoted hydrogen bonding between interfacial watre, while DMSO stabilized interfacial isolated water during HER on Pt. Firstly, for dilute cases

including pure water without organic solvents, H_2O:ACN = 5:1, and H_2O:DMSO = 5:1 (all with 0.1 m $NaClO_4$ as conducting ions), SEIRAS showed arising of peaks in the O-H stretching region (3000-3600 cm^{-1}) as potential moved from HOR to HER regions (Fig. 6-22). In pure water (Fig. 6-22A), symmetric H-bonded water at 3240 cm^{-1} increased in intensity, while isolated water at 3570 cm^{-1} slightly decreased as potential went down. The peak assignments were according to the bulk ATR spectra of the electrolyte (Fig. 6-22 black lines). For H_2O:ACN = 5:1 (Fig. 6-22B), similar growth of symmetric H-bonded water at 3240 cm^{-1} and decrease of isolated water at 3570 cm^{-1} was observed, and the decrease and increase were more significant than pure water. In H_2O:DMSO = 5:1 (Fig. 6-22C), while symmetric H-bonded water (3240 cm^{-1}) also increased as potential decreased, the decrease in isolated water at 3570 cm^{-1} was slight and not obvious.

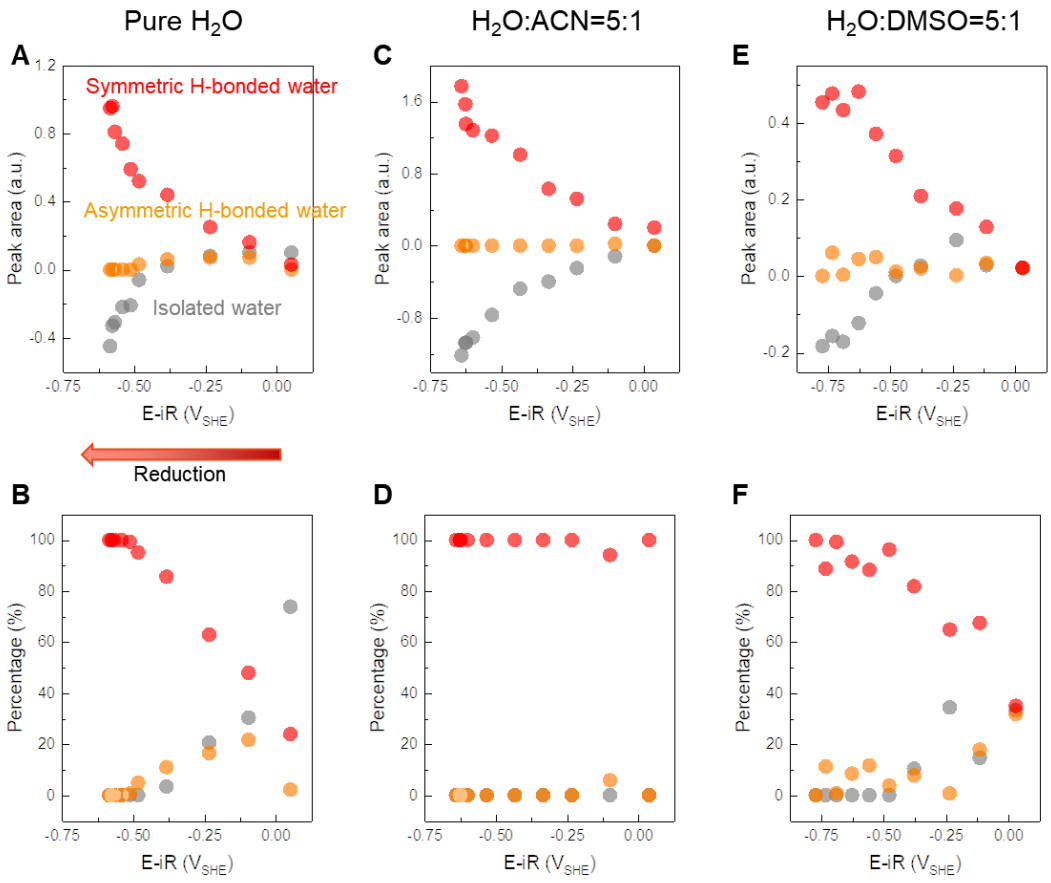

Fig. 6-23 Deconvolution of three types of water from *in situ* SEIRAS for dilute electrolytes. Deconvoluted peak areas of symmetric H-bonded water (red), asymmetric H-bonded water (orange), and isolated water (grey) for (A) pure water without organic solvents, (C) H_2O:ACN = 5:1, and (E) H_2O:DMSO = 5:1. Note that the y-axis has different scales in (A), (C), and (E). Relative peak percentage of the three types of water for (B) pure water without organic solvents, (D) H_2O:ACN = 5:1, and (F) H_2O:DMSO = 5:1.

Further support came from deconvolution of the spectra into the three types of water peaks (Fig. 6-23). As potential went down from HOR to HER region from right to left (Fig. 6-23 A, C, E), symmetric H-bonded water increased in peak areas as potential decreased for all three electrolytes, asymmetric H-bonded water only had small variations, and isolated water decreased in peak areas. Note that the y-axis has different scales in Fig. 6-23 A, C, E. The relative peak percentages of the three water species showed that for pure water (Fig. 6-23B) and H_2O:ACN = 5:1 (Fig. 6-23F), symmetric H-bonded water became more and more dominant in replacement of asymmetric H-bonded water as potential went down. For H_2O:ACN = 5:1 (Fig. 6-23D), symmetric H-bonded water was always the near 100% and even no asymmetric H-bonded water arose, indicating that ACN promoted symmetric hydrogen bonding between water molecules at the interface.

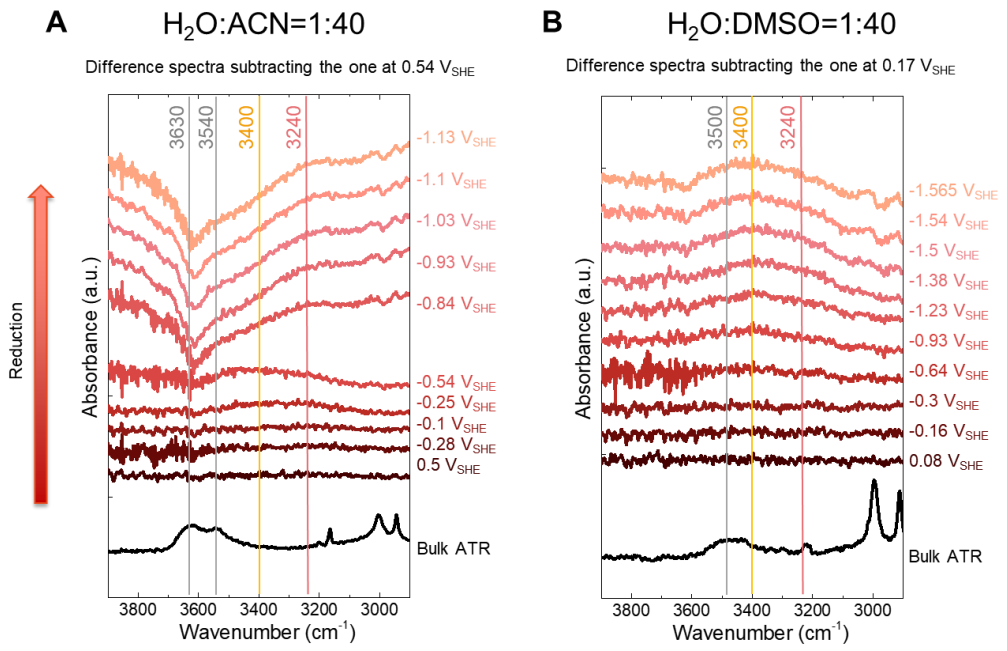

Fig. 6-24 *In situ* SEIRAS (O-H stretching region) for concentrated electrolytes with low water content on Pt surfaces. *In situ* difference spectra (in red) for (A) H_2O:ACN = 1:40 and (B) H_2O:DMSO = 1:40, and ATR spectra for the three electrolytes (in black). Electrolytes all contained 0.1 m $NaClO_4$ as conducting ions and under H_2 saturation. The spectra were subtracted with respect to the initial spectra collected at HOR potentials.

The effect of ACN in promoting symmetric H-bonded water at the interface was also supported by *in situ* SEIRAS of more electrolytes at medium and low water content. At low water content of H_2O:organic = 1:40 (Fig. 6-24), the spectra evolution of H_2O:ACN = 1:40 was drastically different from that of H_2O:DMSO = 1:40, more obvious than the difference between dilute cases (Fig. 6-22). H_2O:ACN = 1:40 showed huge decrease of isolated water at 3630 and 3540 cm^{-1} and asymmetric H-bonded water at 3400 cm^{-1} as the potential reduced to HER region (Fig. 6-24A). In contrast, H_2O:DMSO = 1:40 showed an increase in isolated and asymmetric H-bonded water instead of a decrease (Fig. 6-24B). These trends were confirmed upon deconvoluting the spectra, where peak areas of isolated water and asymmetric H-bonded water decreased significantly for H_2O:ACN = 1:40 (Fig.

6-25A) while increased for H_2O:DMSO = 1:40 (Fig. 6-25C). At low potentials when HER occurred, all water (100%) became symmetric H-bonded after -0.84 V_{SHE} for H_2O:ACN = 1:40 (Fig. 6-25B), whereas there was still over 50% of isolated water and asymmetric H-bonded water after -1.2 V_{SHE} for H_2O:DMSO = 1:40 (Fig. 6-25D), providing further support that that ACN suppressed isolated water and enhanced symmetric H-bonded water compared to DMSO.

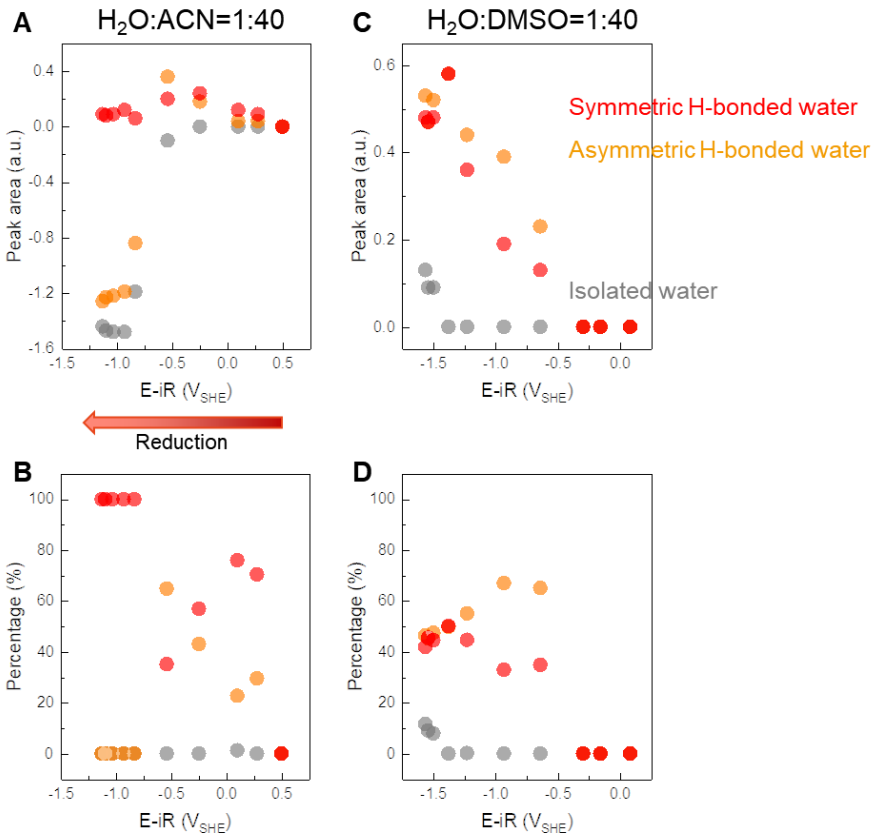

Fig. 6-25 Deconvolution of three types of water from *in situ* SEIRAS for concentrated electrolytes with low water content. Deconvoluted peak areas of symmetric H-bonded water (red), asymmetric H-bonded water (orange), and isolated water (grey) for (A) H_2O:ACN = 1:40 and (C) H_2O:DMSO = 1:40. Note that the y-axis has different scales. Relative peak percentage of the three types of water for (B) H_2O:ACN = 1:40 and (D) H_2O:DMSO = 1:40.

SEIRAS of electrolytes at intermediate water content H_2O:organic = 1:2 (Fig. 6-26) and the deconvolution (Fig. 6-27) also showed decreasing isolated and asymmetric H-bonded water for H_2O:ACN = 1:2, but increasing isolated and asymmetric H-bonded water for H_2O:DMSO = 1:2, in consistence with the trend for H_2O:organic = 1:40 electrolytes (Fig. 6-24 and Fig. 6-25) and further supporting that ACN suppressed isolated water and enhanced symmetric H-bonded water.

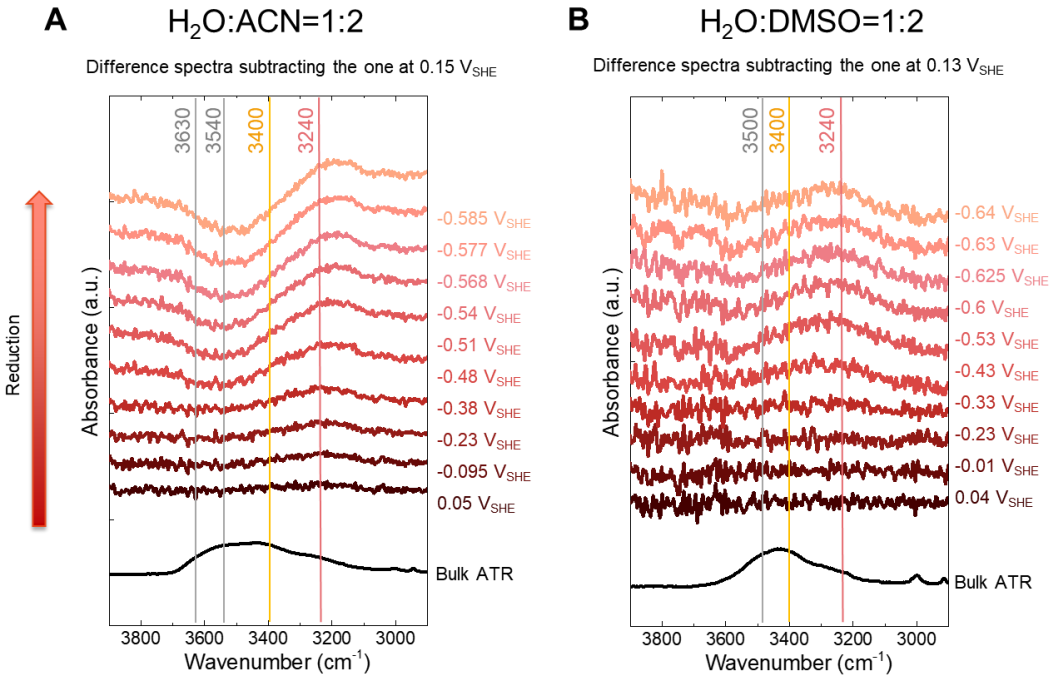

Fig. 6-26 *In situ* SEIRAS (O-H stretching region) for electrolytes with intermediate water content on Pt surfaces. *In situ* difference spectra (in red) for (A) H_2O:ACN = 1:2 and (B) H_2O:DMSO = 1:2, and ATR spectra for the three electrolytes (in black). Electrolytes all contained 0.1 m $NaClO_4$ as conducting ions and under H_2 saturation. The spectra were subtracted with respect to the initial spectra collected at HOR potentials.

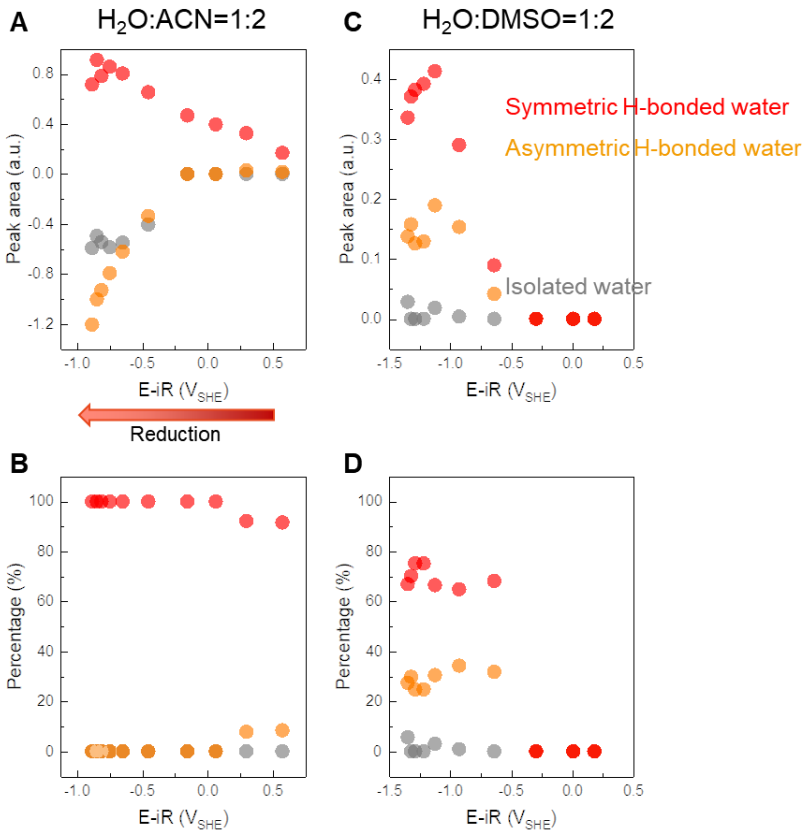

Fig. 6-27 Deconvolution of three types of water from *in situ* SEIRAS for electrolytes with intermediate water content. Deconvoluted peak areas of symmetric H-bonded water (red), asymmetric H-bonded water (orange), and isolated water (grey) for (A) H_2O:ACN = 1:2 and (C) H_2O:DMSO = 1:2. Note that the y-axis has different scales. Relative peak percentage of the three types of water for (B) H_2O:ACN = 1:2 and (D) H_2O:DMSO = 1:2.

6.4.3 Mechanistic discussion on the role of solvents

DMSO suppressed HER more significantly than ACN (Fig. 6-18), and we propose that it is because the DMSO stabilized interfacial isolated water and less H-bonded water at HER-relevant potentials, while ACN promoted symmetric H-bonded water. Firstly, we excluded the sole poisoning effect (Session 6.4.1) of solvents, as ACN had more poisoning according to lower ECSA while had less suppression on HER. Next, *in situ* SEIRAS on Pt showed that ACN significantly suppressed isolated water signals and enhanced symmetric H-

bonded water, while DMSO could still retain certain amount of isolated water and asymmetric H-bonded water at HER regions (Fig. 6-25, Fig. 6-27). The possible mechanism is that DMSO with a higher donor number has a stronger interaction with isolated water molecules (Fig. 6-10), therefore stabilizing these water molecules at the interface so that water molecules are prevented from aggregating and forming hydrogen bonding among themselves (Fig. 6-28B). This is supported by the observation that there was higher percentage of isolated water and asymmetric H-bonded water, and lower percentage of symmetric H-bonded water than ACN-containing electrolytes (Fig. 6-23, Fig. 6-25, and Fig. 6-27). The reduced hydrogen bonding network could lead to lower PCET kinetics and suppressed HER[198] for DMSO-containing electrolytes. In contrast, ACN has a lower donor number and weaker interaction with individual water molecules, having a minimal effect in disturbing the water hydrogen bonding network (Fig. 6-28A). Consequently, water molecules are able to form higher degree of hydrogen bonding networks among themselves at the interface, supported by the higher percentage of symmetric H-bonded water in SEIRAS measurements (Fig. 6-23, Fig. 6-25, and Fig. 6-27). The enhanced hydrogen bonding between water could facilitate PCET and HER[198] for ACN-containing electrolytes.

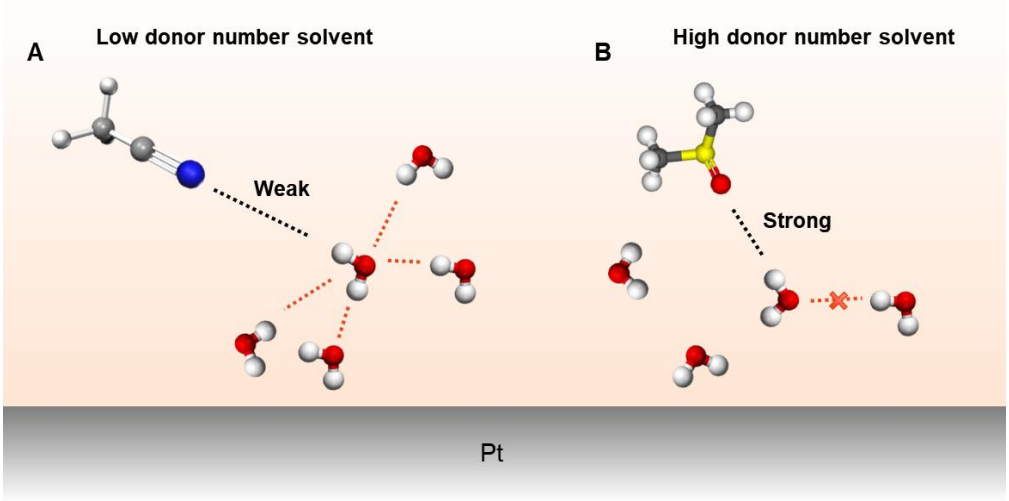

Fig. 6-28 Proposed physical picture of interfacial water structure during HER on Pt, with the presence of (A) ACN and (B) DMSO solvent.

6.5 Conclusions

In this study, we systematically investigated HER kinetics of water-in-solvent electrolytes, *i.e.* water confined in organic matrixes, including acetonitrile (ACN) and dimethyl sulfoxide (DMSO) as two representatives. *Ex situ* FT-IR and NMR measurements showed that water molecules became more isolated and had a larger pK_a when decreasing the water-to-organic ratio. FT-IR further revealed that lower-DN solvent like ACN had weaker interactions with isolated water. RDE experiments on Pt electrodes showed that water reduction shifted to a more negative potential when decreasing the water-to-organic ratio, and the shifts in onset potentials were solvent-dependent - DMSO-containing electrolytes suppressed HER and lowered the onset potential more significantly compared to ACN-containing electrolytes. The more suppression effect on HER with DMSO cannot be solely explained by solvent poisoning, as ECSA was found to be larger in DMSO-containing electrolytes than ACN-containing ones, in opposite trends to HER kinetics. *In situ* SEIRAS

instead revealed more isolated and asymmetric H-bonded water on Pt during HER in the presence of DMSO, while more symmetric H-bonded water in the presence of ACN, indicating that solvents altered interfacial water structures to tune HER. A mechanism was proposed that the suppression effect of HER with DMSO was attributed to its stabilization effect of isolated and weakly H-bonded water as a result of the high donor number of DMSO and strong interaction with isolated water, while the enhancement effect of HER with ACN was due to its low donor number and promotion of highly hydrogen-bonded water. These findings highlight the opportunities in modulating interfacial hydrogen bonding and HER kinetics through organic solvents with different donor numbers, which could contribute to broader applications in the decarbonization of sustainable fuels and chemical transformations, where HER and general PCET reactions play essential roles.

6.6 Material and Methods

Electrolyte preparation

The electrolyte was prepared from mixing organic solvents with Milli-Q water (18 MΩ•cm) and 0.1 molal (0.1 m = 0.1 mol/kg) $NaClO_4$ (> 98.0%, Sigma-Aldrich). Organic solvents in this work include acetonitrile (anhydrous, 99.8%, Sigma-Aldrich), dimethyl sulfoxide (anhydrous, >=99.9%, Sigma-Aldrich), 1,2-dimethoxyethane, anhydrous (99.5%, Sigma-Aldrich), n,n-dimethylacetamide (anhydrous, 99.8%, Sigma-Aldrich), n,n-dimethylformamide (anhydrous, 99.8%, Sigma-Aldrich), diethylene glycol dimethyl ether (anhydrous, 99.5%, Sigma-Aldrich), triethylene glycol dimethyl ether (99%, sigma-aldrich), and tetrahydrofuran (anhydrous, >=99.9%, Sigma-Aldrich). The solvents were dried with molecular sieves for 48 hr in the glovebox and kept inside to avoid moisture.

The residual water content in the electrolytes was measured by Karl Fischer titration and was less than 10 ppm before use.

Reference electrodes

Organic reference electrodes were adopted to measure the electrolytes with low water content (water-to-organics ratio < 1), and were regularly calibrated against ferrocene redox[297,298], while an aqueous Ag/AgCl reference electrode was used to measure dilute electrolytes. The organic reference electrodes consisted of a silver wire, and organic solvent (ACN or DMSO) with 0.01 M $AgNO_3$ and 0.1 M $NaClO_4$ (Fig. E-1A), using the MW-1085 Non-Aqueous Reference Electrode Kit from BASI.

The reference electrode based on Ag/Ag^+ (in ACN and DMSO) were calibrated regularly using ferrocene. The anodic and cathodic peak centers for ferrocene were averaged: for instance of DMSO, $E_{1/2}$ = 1/2 (Ep_a+Ep_c)= 0.162 V *vs.* Ag/0.01M Ag^+ (Fig. E-1B), which corresponded to 0.624 V *vs.* SHE[297,298]. Therefore, the potential of the Ag/0.01M Ag^+ reference electrode in DMSO is 0.462 V *vs.* SHE. Similarly, ACN organic reference electrodes were calibrated to 0.541 V *vs.* SHE.

Electrochemical characterization

All the electrochemical measurements were performed using Biologic SP-300 potentiostat with a three-electrode electrochemical system. The working electrode was Pt rotating disk electrode (RDE) (0.196 cm^2_{geo}, Pine instrument). Potentials were referenced to the organic reference electrodes or an aqueous Ag/AgCl reference electrode (Session 6.4.2).

The HER/HOR kinetics were examined by cyclic voltammetry (CV) at a scan rate of 50 mV/s under Ar or H_2 saturation (ultra-high-grade purity, Airgas), where current density was obtained base on geometric surface area of RDE (0.196 cm^2) and iR corrected. The kinetic current densities of HOR were extracted from rotation rate dependent CV at 2500, 1600, 900, and 400 rpm, using the Koutechy-Levich equation[287] for regions where $j_k/j_L < 0.1$ and $0.1 < j_k'/j_L < 1$.[198]

NMR measurements

^{1}H NMR was performed on a Bruker Avance Neo - 500 MHz nuclear magnetic resonance (NMR) spectrometer. Coaxial inserts containing D_2O were placed in NMR tubes that contained electrolyte samples, so that the electrolytes of interest were not diluted by D_2O.

***In situ* SEIRAS measurements**

Pt nanostructured film (~50 nm thick) was prepared by electroless deposition[272,273] on a Si prism (radius 22 mm, Pier optics) as the working electrode. The prism was then mounted to a three-electrode cell. The reference electrode was an aqueous Ag/AgCl reference electrode (for dilute electrolytes) or an organic reference electrode (for water-in-organic solvents) (see Session 6.4.2). The counter electrode was a platinum wire. SEIRAS spectra were collected on a FT-IR Vertex 70 (Bruker) FT-IR equipped with a MCT detector. The optical path was fully filled with nitrogen gas. The spectra were acquired in the attentuated total reflection (ATR) mode using a single-reflection ATR accessory (Pike Vee-Max II, Pike Technologies) at an incident angle of 68 degrees. The spectral resolution was 4 cm^{-1}

and the scan velocity was 7.5 kHz. Each spectrum was measured by superimposing 256 interferograms while applying potentiostatic potentials. H_2 was bubbled through the electrolyte All spectra were presented in the form of absorbance according to $\log(I_0/I)$, where I_0 and I are the spectra of reference background and at the potentiostatic potential, respectively.

Ex situ FT-IR measurements

For *ex situ* measurements on bulk electrolytes, the spectra were acquired in the ATR mode using a germanium (Ge) prism (radius 22 mm, Pier optics) at an incident angle of 50 degrees. Spectral settings were the same as *in situ* measurements.

Chapter 7. Summary and Perspectives

7.1 Thesis summary

In summary, the interfacial (electro)chemical reaction mechanisms in the molecular level and charge transfer kinetics at the electrified interfaces for energy storage and conversion systems are explored in this thesis. Specifically, the following questions for Li-ion batteries have been addressed: (1) what is the parasitic reaction on Ni-rich NMC positive electrodes in Li-ion batteries that lead to their capacity fading and degradation (Chapter 2), (2) how can we prevent the battery degradation through electrode and electrolyte engineering leveraging physical chemistry (Chapter 3), (3) what governs the power density and kinetic law for Li-ion batteries (Chapter 4). For the critical electrocatalytic reactions in fuel cells, I addressed the following questions: (1) how does interfacial hydrogen bonding enhance oxygen reduction reaction kinetics (Chapter 5), and (2) how can we tune hydrogen evolution reaction kinetics through interfacial hydrogen bonding (Chapter 6).

In Chapter 2 and 3, I developed an *in situ* FT-IR method and revealed oxidative dehydrogenation of carbonate solvents on composite NMC811 electrodes at voltages as low as 3.8 V_{Li}, in agreement with density functional theory (DFT) results. Dehydrogenation reactions were accompanied with huge growth in the charge transfer impedance measured from EIS, accounting for the capacity fading of Ni-rich positive electrodes. In order to enhance the cyclability of Li-ion batteries, it is desired to prevent electrolyte dehydrogenation. Leveraging the physical chemistry of electrodes, we demonstrated that decreasing surface oxygen reactivity, such as decreasing Ni-content or adding Al_2O_3 coatings, could effectively mitigate carbonate dehydrogenation and enhance the cycling

stability. Leveraging the physical chemistry of electrolytes, we showed that decreasing carbonate activity by increasing salt concentrations, adding sacrificial additives, or substituting with fluorinated solvents also prevented carbonate dehydrogenation and improved capacity retention. These electrode–electrolyte combinations without dehydrogenation further did not show significant impedance growth, in consistence with their enhanced cycling stability. These findings provide principles for rational design of long-living Li-ion batteries with Ni-rich positive electrodes.

In Chapter 4, we showed the current density of intercalation at each overpotential for Li_xCoO_2 and $Li_xNi_{1/3}Co_{1/3}Mn_{1/3}O_2$ was proportional to the Li^+ vacancy concentration $(1-x)$. The unique experimental evidence supports the proposed microscopic intercalation mechanism that the electron and Li^+ transfer in a concerted way, described by the theory of coupled ion-electron transfer. The mechanism predicts that the rate-dependent discharge capacity decreases linearly with increasing the discharge current under reaction-limited conditions, a trend validated for eight electrode materials. The proposed mechanism applies to a variety of intercalation materials, and governs the power density at low and moderate rates.

In Chapter 5 and 6, we extended the in situ FTIR characterization of electrified interfaces and kinetic studies to common electrocatalytic reactions, including ORR and HER, where we especially focused on leveraging physical chemistry of liquid electrolytes and non-covalent interactions to tune electrocatalytic activities. Protic ionic liquids as an interfacial layer on platinum and gold could enhance the ORR activity by up to fivefold, exhibiting a

volcano-shaped dependence on the pK_a of the ionic liquid. *In situ* SEIRAS showed that the enhanced ORR activity is attributed to strengthened hydrogen bonds between ORR products and ionic liquids with comparable pK_as, resulting in favourable PCET kinetics. HER of water confined in organic solvents was also found to strongly depend on the water content and type of organic solvents – decreasing water content significantly shifted HER onset to more negative overpotentials due to decreased hydrogen bonds between water. High-donor-number solvents such as DMSO also significantly suppressed HER by stabilizing isolated water and suppressing hydrogen-bonded water at the electrified interface, supported by *in situ* SEIRAS. These findings highlight opportunities for using non-covalent interactions and solvation environments at the electrified interface to tune the kinetics of general electrocatalytic reactions involving PECT.

This thesis has laid the foundation for the design of next-generation Li-ion batteries with higher energy density, higher power density, and better cyclability, as well as controllable electrocatalysis for fuel cells and broader applications. We next discuss some outlook on potential future directions following up this thesis work.

7.2 Perspectives

7.2.1 *In situ* FT-IR characterization of broader interfacial reactions

In Chapter 2 and 3, we successfully developed in situ FT-IR to probe the EEI formation on positive electrodes. It is also promising to apply the method to broader reactions, the most similar one being the solid-electrolyte interphase (SEI) on negative electrodes. The Fermi level of negative electrode materials such as graphite is higher than the LUMO level of

carbonate-based electrolytes, and therefore electrolytes are reduced on negative electrodes to form SEI, which is electronically insulating but lithium-ion conducting to enable reversible lithium intercalation. The chemical nature of SEI and its morphology directly affect the negative electrode performance and battery cycle life.[23,299,300] Although the well-known mosaic model of SEI on lithium and graphite is well accepted, it has not been fully experimentally established and fundamentally understood what and how organic and inorganic species are formed on the surface, and how applied potential and cycling influence SEI.[24] Further, recent advances in fluorinated electrolytes enabling Li metal anodes have shown much improved Columbic efficiencies (>99.5%) for Li metal batteries,[301,302] whereas it is unclear how fluorine affects SEI formation, lithium plating–stripping kinetics, and Li morphology.[303] It is essential to probe what and how surface species are formed in SEI and their dynamic changes upon cycling to better understand what determines the Coulombic efficiency, for which *in situ* techniques are required. Due to the sensitive nature of FT-IR to organic functional groups[91] in battery electrolytes, *in situ* FT-IR is promising to probe and reveal the chemical species and the dynamic changes during SEI formation, facilitating the understanding and development of new anodes and Li metal batteries. In addition, *in situ* SEIRAS has been widely used in electrocatalysis research to probe the surface intermediates and reaction pathways such as CO_2 reduction[304], and it is promising to further apply it to complex reactions to reveal novel mechanisms, such as electrochemical ammonia synthesis[305,306].

7.2.2 Ion transfer energetics during ion intercalation

In Chapter 4, we have shown experimental and theoretical evidence that ion intercalation occurs by coupled ion-electron transfer. While kinetics parameters including the current density prefactor i_r^* and the surface adsorption energy w^+ have been extracted from experimental results and they were found to be dependent on electrolytes and electrodes, it is not understood how electrolyte and electrode properties quantitatively determine these parameters. Specifically, i_r^* depends on the ion transfer energy ΔE_{IT}, for which it is unclear its quantitative trend and how to estimate it accurately from material properties. To deepen the understanding on ΔE_{IT} and even w^+, future DFT calculations and molecular dynamics (MD) simulations on the ion transfer process would help to quantify the terms and justify better their dependency on electrodes and electrolytes. Further experimental investigations on temperature-dependent measurements of Tafel plots would also be beneficial to quantify the ion transfer term, which could be obtained from the Arrhenius plot based on activation energies.

7.2.3 Solid-state batteries

Here I discuss the perspectives on potentially applying the methods and learning developed from liquid electrolytes in this thesis to studies on solid-state electrolytes. While conventional Li-ion batteries are based on liquid electrolytes, there is increasing interest nowadays in solid-state electrolytes and all-solid-state batteries[307], due to their non-flammable nature, safety, and higher mechanical strength compared to liquid electrolytes[308]. However, it has been challenging to incorporate these materials into high-performing batteries, one of the problem being the interfacial resistance and interface instability.[309,310] Current studies on interfacial stability and decomposition reactions of solid electrolytes are

predominately based on *ex situ* characterizations such as XPS[310]. While in situ FT-IR may not be directly applied to probe the inorganic species at the solid-solid interface, its complementary technique, *in situ* Raman spectroscopy, could be promising to capture the interfacial reactions and decomposition of solid electrolytes. The laser beam could come from the side of the battery and scatter off the solid electrolyte-electrode interface to probe the species. Further, the kinetics of Li-ion intercalation through solid-solid interfaces is largely unexplored. Similar Tafel kinetic analysis using the same experimental protocol and CIET models is feasible upon designing a reference electrode for 3-electrode solid-state cells. Alternatively, Li plating/stripping kinetics at solid-solid interfaces could be investigated in a Li-Li symmetric two-electrode cell and analyzed through the conventional MHC model.

7.2.4 Non-covalent interactions in electrolyte design for general electrocatalytic reactions

Chapter 5 and Chapter 6 leverage the physical chemistry of liquids to tune the hydrogen bonding at electrified interfaces and accordingly alter ORR and HER electrocatalytic activities. The strategy to utilize non-covalent interactions in electrolyte design is applicable to broader energy storage applications. For instance, in Chapter 6 we have found that DMSO with a high donor number is able to suppress HER significantly; it is possible that adding a small amount of DMSO to aqueous electrolytes could benefit CO_2 reduction in improving the selectivity of carbon-related products, since HER is in competition with CO_2 reduction. Similarly, it may be beneficial to nitrogen reduction where HER is the competitive reaction. Special cautions are needed though to prevent organics from poisoning the catalysts severely. For aqueous batteries where a large electrochemical

window is desired[49], confining water through non-covalent interactions is required, where the understanding developed in this thesis could be applied to select candidate spectators. For instance, it is possible that salt species with high donor numbers are good for enlarging the electrochemical window of "water-in-salt" electrolytes. Opportunities also lie in leveraging non-covalent interactions in electrolyte design in applications beyond electrocatalysis and batteries, such as PCET reactions in chemical and biological processes[311].

7.3 Closing remarks

Going beyond trial-and-error experimental exploration of better and new materials, it is essential to unravel the fundamentals behind the (electro)chemical processes, so that it is possible to derive science-guided design principles based on physical descriptors. The fundamental understanding would enable predictions of good material candidates and rational design effectively. Further, recent advances in machine learning and deep learning methods have motivated studies leveraging machine learning to accelerate material and system designs, while it needs special caution that the learning should be based on physical insights, where fundamental studies could be integrated and contribute to the high-throughput studies.

References

(1) Boden, T. A.; Marland, G.; Andres, R. J. Global, Regional, and National Fossil-Fuel CO2 Emissions. *Carbon Dioxide Inf. Anal. Cent. Oak Ridge Natl. Lab. US Dep. Energy Oak Ridge Tenn USA Doi* **2009**, *10*.

(2) United Nations Department of Economic and Social Affairs (UN DESA). *17 Goals to Transform Our World*. https://www.un.org/sustainabledevelopment/.

(3) Gielen, D.; Boshell, F.; Saygin, D.; Bazilian, M. D.; Wagner, N.; Gorini, R. The Role of Renewable Energy in the Global Energy Transformation. *Energy Strategy Rev.* **2019**, *24*, 38–50.

(4) Agreement, P. Paris Agreement. In *Report of the Conference of the Parties to the United Nations Framework Convention on Climate Change (21st Session, 2015: Paris). Retrived December*; HeinOnline, 2015; Vol. 4, p 2017.

(5) Tester, J. W.; Drake, E. M.; Driscoll, M. J.; Golay, M. W.; Peters, W. A. *Sustainable Energy: Choosing among Options*; MIT press, 2012.

(6) McCloskey, B. D. Expanding the Ragone Plot: Pushing the Limits of Energy Storage. *J. Phys. Chem. Lett.* **2015**, *6* (18), 3592–3593.

(7) The Batteries That Could Make Fossil Fuels Obsolete. *The batteries that could make fossil fuels obsolete*.

(8) Newkirk, M. What Is A Hybrid Solar System? *What Is A Hybrid Solar System?*, 2015.

(9) Electric Vehicle Benefits. *Electric Vehicle Benefits*.

(10) Etacheri, V.; Marom, R.; Elazari, R.; Salitra, G.; Aurbach, D. Challenges in the Development of Advanced Li-Ion Batteries: A Review. *Energy Environ. Sci.* **2011**, *4* (9), 3243–3262.

(11) Jung, R.; Metzger, M.; Maglia, F.; Stinner, C.; Gasteiger, H. A. Oxygen Release and Its Effect on the Cycling Stability of LiNixMnyCozO2 (NMC) Cathode Materials for Li-Ion Batteries. *J. Electrochem. Soc.* **2017**, *164* (7), A1361–A1377.

(12) Gasteiger, H. A.; Kocha, S. S.; Sompalli, B.; Wagner, F. T. Activity Benchmarks and Requirements for Pt, Pt-Alloy, and Non-Pt Oxygen Reduction Catalysts for PEMFCs. *Appl. Catal. B Environ.* **2005**, *56* (1–2), 9–35.

(13) Winter, M.; Brodd, R. J. What Are Batteries, Fuel Cells, and Supercapacitors? *Chem. Rev.* **2004**, *104* (10), 4245–4270.

(14) Simon, P.; Gogotsi, Y. Perspectives for Electrochemical Capacitors and Related Devices. *Nat. Mater.* **2020**, *19* (11), 1151–1163.

(15) Simon, P.; Gogotsi, Y. Materials for Electrochemical Capacitors. *Nat. Mater.* **2008**, *7* (11), 845–854.

(16) Goodenough, J. B.; Park, K.-S. The Li-Ion Rechargeable Battery: A Perspective. *J. Am. Chem. Soc.* **2013**, *135* (4), 1167–1176.

(17) Cutting Cobalt. *Nat. Energy* **2020**, *5*, 825. https://doi.org/10.1038/s41560-020-00731-3.

(18) Noh, H.-J.; Youn, S.; Yoon, C. S.; Sun, Y.-K. Comparison of the Structural and Electrochemical Properties of Layered Li [NixCoyMnz] O2 (X= 1/3, 0.5, 0.6, 0.7, 0.8 and 0.85) Cathode Material for Lithium-Ion Batteries. *J. Power Sources* **2013**, *233*, 121–130.

(19) Hwang, S.; Kim, S. Y.; Chung, K. Y.; Stach, E. A.; Kim, S. M.; Chang, W. Determination of the Mechanism and Extent of Surface Degradation in Ni-Based Cathode Materials after Repeated Electrochemical Cycling. *APL Mater.* **2016**, *4* (9), 096105.
(20) Myung, S.-T.; Maglia, F.; Park, K.-J.; Yoon, C. S.; Lamp, P.; Kim, S.-J.; Sun, Y.-K. Nickel-Rich Layered Cathode Materials for Automotive Lithium-Ion Batteries: Achievements and Perspectives. *ACS Energy Lett.* **2016**, *2* (1), 196–223.
(21) Hwang, S.; Kim, S. M.; Bak, S.-M.; Kim, S. Y.; Cho, B.-W.; Chung, K. Y.; Lee, J. Y.; Stach, E. A.; Chang, W. Using Real-Time Electron Microscopy To Explore the Effects of Transition-Metal Composition on the Local Thermal Stability in Charged Li x Ni y Mn z Co1–y–z O2 Cathode Materials. *Chem. Mater.* **2015**, *27* (11), 3927–3935.
(22) Sun, Y.-K.; Myung, S.-T.; Park, B.-C.; Prakash, J.; Belharouak, I.; Amine, K. High-Energy Cathode Material for Long-Life and Safe Lithium Batteries. *Nat. Mater.* **2009**, *8* (4), 320.
(23) Schranzhofer, H.; Bugajski, J.; Santner, H. J.; Korepp, C.; Möller, K.-C.; Besenhard, J. O.; Winter, M.; Sitte, W. Electrochemical Impedance Spectroscopy Study of the SEI Formation on Graphite and Metal Electrodes. *J. Power Sources* **2006**, *153* (2), 391–395.
(24) Gauthier, M.; Carney, T. J.; Grimaud, A.; Giordano, L.; Pour, N.; Chang, H.-H.; Fenning, D. P.; Lux, S. F.; Paschos, O.; Bauer, C. Electrode–Electrolyte Interface in Li-Ion Batteries: Current Understanding and New Insights. *J. Phys. Chem. Lett.* **2015**, *6* (22), 4653–4672.
(25) Butler, J. A. V. Studies in Heterogeneous Equilibria. Part I. Conditions at the Boundary Surface of Crystalline Solids and Liquids and the Application of Statistical Mechanics. *Trans. Faraday Soc.* **1924**, *19* (March), 659–665.
(26) Erdey-Grúz, T.; Volmer, M. Zur Theorie Der Wasserstoff Überspannung. *Z. Für Phys. Chem.* **1930**, *150* (1), 203–213.
(27) Doyle, M.; Fuller, T. F.; Newman, J. Modeling of Galvanostatic Charge and Discharge of the Lithium/Polymer/Insertion Cell. *J. Electrochem. Soc.* **1993**, *140* (6), 1526.
(28) Newman, J.; Thomas-Alyea, K. E. *Electrochemical Systems*; John Wiley & Sons, 2012.
(29) Ferguson, T. R.; Bazant, M. Z. Nonequilibrium Thermodynamics of Porous Electrodes. *J. Electrochem. Soc.* **2012**, *159* (12), A1967.
(30) Wang, L.; Zhao, J.; He, X.; Gao, J.; Li, J.; Wan, C.; Jiang, C. Electrochemical Impedance Spectroscopy (EIS) Study of LiNi1/3Co1/3Mn1/3O2 for Li-Ion Batteries. *Int J Electrochem Sci* **2012**, *7* (1), 345–353.
(31) Tatara, R.; Karayaylali, P.; Yu, Y.; Zhang, Y.; Giordano, L.; Maglia, F.; Jung, R.; Schmidt, J. P.; Lund, I.; Shao-Horn, Y. The Effect of Electrode-Electrolyte Interface on the Electrochemical Impedance Spectra for Positive Electrode in Li-Ion Battery. *J. Electrochem. Soc.* **2019**, *166* (3), A5090–A5098.
(32) Bouwman, P. J.; Boukamp, B. A.; Bouwmeester, H. J.; Notten, P. H. L. Influence of Diffusion Plane Orientation on Electrochemical Properties of Thin Film LiCoO2 Electrodes. *J. Electrochem. Soc.* **2002**, *149* (6), A699.

(33) Zhao, J.; Wang, L.; He, X.; Wan, C.; Jiang, C. Kinetic Investigation of LiCOO2 by Electrochemical Impedance Spectroscopy (EIS). *Int J Electrochem Sci* **2010**, *5* (4), 478–488.
(34) Nørskov, J. K.; Rossmeisl, J.; Logadottir, A.; Lindqvist, L.; Kitchin, J. R.; Bligaard, T.; Jonsson, H. Origin of the Overpotential for Oxygen Reduction at a Fuel-Cell Cathode. *J. Phys. Chem. B* **2004**, *108* (46), 17886–17892.
(35) Wu, G.; More, K. L.; Johnston, C. M.; Zelenay, P. High-Performance Electrocatalysts for Oxygen Reduction Derived from Polyaniline, Iron, and Cobalt. *Science* **2011**, *332* (6028), 443–447.
(36) Bernt, M.; Gasteiger, H. A. Influence of Ionomer Content in IrO2/TiO2 Electrodes on PEM Water Electrolyzer Performance. *J. Electrochem. Soc.* **2016**, *163* (11), F3179.
(37) Wei, C.; Rao, R. R.; Peng, J.; Huang, B.; Stephens, I. E.; Risch, M.; Xu, Z. J.; Shao-Horn, Y. Recommended Practices and Benchmark Activity for Hydrogen and Oxygen Electrocatalysis in Water Splitting and Fuel Cells. *Adv. Mater.* **2019**, *31* (31), 1806296.
(38) Stamenkovic, V.; Mun, B. S.; Mayrhofer, K. J.; Ross, P. N.; Markovic, N. M.; Rossmeisl, J.; Greeley, J.; Nørskov, J. K. Changing the Activity of Electrocatalysts for Oxygen Reduction by Tuning the Surface Electronic Structure. *Angew. Chem.* **2006**, *118* (18), 2963–2967.
(39) Seh, Z. W.; Kibsgaard, J.; Dickens, C. F.; Chorkendorff, I. B.; Nørskov, J. K.; Jaramillo, T. F. Combining Theory and Experiment in Electrocatalysis: Insights into Materials Design. *Science* **2017**, *355* (6321), eaad4998.
(40) Chen, C.; Kang, Y.; Huo, Z.; Zhu, Z.; Huang, W.; Xin, H. L.; Snyder, J. D.; Li, D.; Herron, J. A.; Mavrikakis, M. Highly Crystalline Multimetallic Nanoframes with Three-Dimensional Electrocatalytic Surfaces. *Science* **2014**, *343* (6177), 1339–1343.
(41) Wang, C.; Chi, M.; Li, D.; Strmcnik, D.; Van der Vliet, D.; Wang, G.; Komanicky, V.; Chang, K.-C.; Paulikas, A. P.; Tripkovic, D. Design and Synthesis of Bimetallic Electrocatalyst with Multilayered Pt-Skin Surfaces. *J. Am. Chem. Soc.* **2011**, *133* (36), 14396–14403.
(42) Escudero-Escribano, M.; Verdaguer-Casadevall, A.; Malacrida, P.; Grønbjerg, U.; Knudsen, B. P.; Jepsen, A. K.; Rossmeisl, J.; Stephens, I. E.; Chorkendorff, I. Pt5Gd as a Highly Active and Stable Catalyst for Oxygen Electroreduction. *J. Am. Chem. Soc.* **2012**, *134* (40), 16476–16479.
(43) Greeley, J.; Stephens, I. E. L.; Bondarenko, A. S.; Johansson, T. P.; Hansen, H. A.; Jaramillo, T. F.; Rossmeisl, J.; Chorkendorff, I.; Nørskov, J. K. Alloys of Platinum and Early Transition Metals as Oxygen Reduction Electrocatalysts. *Nat. Chem.* **2009**, *1* (7), 552–556.
(44) Escudero-Escribano, M.; Malacrida, P.; Hansen, M. H.; Vej-Hansen, U. G.; Velázquez-Palenzuela, A.; Tripkovic, V.; Schiøtz, J.; Rossmeisl, J.; Stephens, I. E.; Chorkendorff, I. Tuning the Activity of Pt Alloy Electrocatalysts by Means of the Lanthanide Contraction. *Science* **2016**, *352* (6281), 73–76.
(45) Strmcnik, D.; Kodama, K.; van der Vliet, D.; Greeley, J.; Stamenkovic, V. R.; Marković, N. M. The Role of Non-Covalent Interactions in Electrocatalytic Fuel-Cell Reactions on Platinum. *Nat. Chem.* **2009**, *1* (6), 466–472.

(46) Mei, D.; Da He, Z.; Zheng, Y. L.; Jiang, D. C.; Chen, Y.-X. Mechanistic and Kinetic Implications on the ORR on a Au (100) Electrode: PH, Temperature and H–D Kinetic Isotope Effects. *Phys. Chem. Chem. Phys.* **2014**, *16* (27), 13762–13773.
(47) Koper, M. Volcano Activity Relationships for Proton-Coupled Electron Transfer Reactions in Electrocatalysis. *Top. Catal.* **2015**, *58* (18), 1153–1158.
(48) Strmcnik, D.; Lopes, P. P.; Genorio, B.; Stamenkovic, V. R.; Markovic, N. M. Design Principles for Hydrogen Evolution Reaction Catalyst Materials. *Nano Energy* **2016**, *29*, 29–36.
(49) Suo, L.; Borodin, O.; Gao, T.; Olguin, M.; Ho, J.; Fan, X.; Luo, C.; Wang, C.; Xu, K. "Water-in-Salt" Electrolyte Enables High-Voltage Aqueous Lithium-Ion Chemistries. *Science* **2015**, *350* (6263), 938–943.
(50) Zhang, Y.-J.; Sethuraman, V.; Michalsky, R.; Peterson, A. A. Competition between CO2 Reduction and H2 Evolution on Transition-Metal Electrocatalysts. *Acs Catal.* **2014**, *4* (10), 3742–3748.
(51) Ooka, H.; Figueiredo, M. C.; Koper, M. T. Competition between Hydrogen Evolution and Carbon Dioxide Reduction on Copper Electrodes in Mildly Acidic Media. *Langmuir* **2017**, *33* (37), 9307–9313.
(52) Choi, C.; Gu, G. H.; Noh, J.; Park, H. S.; Jung, Y. Understanding Potential-Dependent Competition between Electrocatalytic Dinitrogen and Proton Reduction Reactions. *Nat. Commun.* **2021**, *12* (1), 1–11.
(53) Dubouis, N.; Serva, A.; Berthin, R.; Jeanmairet, G.; Porcheron, B.; Salager, E.; Salanne, M.; Grimaud, A. Tuning Water Reduction through Controlled Nanoconfinement within an Organic Liquid Matrix. *Nat. Catal.* **2020**, *3* (8), 656–663.
(54) Menkin, S.; Golodnitsky, D.; Peled, E. Artificial Solid-Electrolyte Interphase (SEI) for Improved Cycleability and Safety of Lithium–Ion Cells for EV Applications. *Electrochem. Commun.* **2009**, *11* (9), 1789–1791.
(55) Smith, A.; Burns, J.; Trussler, S.; Dahn, J. Precision Measurements of the Coulombic Efficiency of Lithium-Ion Batteries and of Electrode Materials for Lithium-Ion Batteries. *J. Electrochem. Soc.* **2010**, *157* (2), A196–A202.
(56) Attia, P. M.; Das, S.; Harris, S. J.; Bazant, M. Z.; Chueh, W. C. Electrochemical Kinetics of SEI Growth on Carbon Black: Part I. Experiments. *J. Electrochem. Soc.* **2019**, *166* (4), E97–E106.
(57) Das, S.; Attia, P. M.; Chueh, W. C.; Bazant, M. Z. Electrochemical Kinetics of SEI Growth on Carbon Black: Part II. Modeling. *J. Electrochem. Soc.* **2019**, *166* (4), E107–E118.
(58) Jung, R.; Metzger, M.; Maglia, F.; Stinner, C.; Gasteiger, H. A. Chemical versus Electrochemical Electrolyte Oxidation on NMC111, NMC622, NMC811, LNMO, and Conductive Carbon. *J. Phys. Chem. Lett.* **2017**, *8* (19), 4820–4825. https://doi.org/10.1021/acs.jpclett.7b01927.
(59) Giordano, L.; Karayaylali, P.; Yu, Y.; Katayama, Y.; Maglia, F.; Lux, S.; Shao-Horn, Y. Chemical Reactivity Descriptor for the Oxide-Electrolyte Interface in Li-Ion Batteries. *J. Phys. Chem. Lett.* **2017**, *8* (16), 3881–3887.
(60) Yu, Y.; Karayaylali, P.; Katayama, Y.; Giordano, L.; Gauthier, M.; Maglia, F.; Jung, R.; Lund, I.; Shao-Horn, Y. Coupled LiPF6 Decomposition and Carbonate

Dehydrogenation Enhanced by Highly Covalent Metal Oxides in High-Energy Li-Ion Batteries. *J. Phys. Chem. C* **2018**, *122* (48), 27368–27382.
(61) Gauthier, M.; Karayaylali, P.; Giordano, L.; Feng, S.; Lux, S. F.; Maglia, F.; Lamp, P.; Shao-Horn, Y. Probing Surface Chemistry Changes Using LiCoO2-Only Electrodes in Li-Ion Batteries. *J. Electrochem. Soc.* **2018**, *165* (7), A1377–A1387.
(62) Han, B.; Paulauskas, T.; Key, B.; Peebles, C.; Park, J. S.; Klie, R. F.; Vaughey, J. T.; Dogan, F. Understanding the Role of Temperature and Cathode Composition on Interface and Bulk: Optimizing Aluminum Oxide Coatings for Li-Ion Cathodes. *ACS Appl. Mater. Interfaces* **2017**, *9* (17), 14769–14778.
(63) Wise, A. M.; Ban, C.; Weker, J. N.; Misra, S.; Cavanagh, A. S.; Wu, Z.; Li, Z.; Whittingham, M. S.; Xu, K.; George, S. M. Effect of Al2O3 Coating on Stabilizing LiNi0. 4Mn0. 4Co0. 2O2 Cathodes. *Chem. Mater.* **2015**, *27* (17), 6146–6154.
(64) Cho, J.; Kim, T.-G.; Kim, C.; Lee, J.-G.; Kim, Y.-W.; Park, B. Comparison of Al2O3-and AlPO4-Coated LiCoO2 Cathode Materials for a Li-Ion Cell. *J. Power Sources* **2005**, *146* (1–2), 58–64.
(65) Zhang, X.; Belharouak, I.; Li, L.; Lei, Y.; Elam, J. W.; Nie, A.; Chen, X.; Yassar, R. S.; Axelbaum, R. L. Structural and Electrochemical Study of Al2O3 and TiO2 Coated Li1. 2Ni0. 13Mn0. 54Co0. 13O2 Cathode Material Using ALD. *Adv. Energy Mater.* **2013**, *3* (10), 1299–1307.
(66) Cheng, H.-M.; Wang, F.-M.; Chu, J. P.; Santhanam, R.; Rick, J.; Lo, S.-C. Enhanced Cycleabity in Lithium Ion Batteries: Resulting from Atomic Layer Depostion of Al2O3 or TiO2 on LiCoO2 Electrodes. *J. Phys. Chem. C* **2012**, *116* (14), 7629–7637.
(67) Sun, Y.-K.; Lee, B.-R.; Noh, H.-J.; Wu, H.; Myung, S.-T.; Amine, K. A Novel Concentration-Gradient Li [Ni 0.83 Co 0.07 Mn 0.10] O 2 Cathode Material for High-Energy Lithium-Ion Batteries. *J. Mater. Chem.* **2011**, *21* (27), 10108–10112.
(68) Hua, C.; Du, K.; Tan, C.; Peng, Z.; Cao, Y.; Hu, G. Study of Full Concentration-Gradient Li (Ni0. 8Co0. 1Mn0. 1) O2 Cathode Material for Lithium Ion Batteries. *J. Alloys Compd.* **2014**, *614*, 264–270.
(69) Yoon, C. S.; Kim, S. J.; Kim, U.-H.; Park, K.-J.; Ryu, H.-H.; Kim, H.-S.; Sun, Y.-K. Microstructure Evolution of Concentration Gradient Li [Ni0. 75Co0. 10Mn0. 15] O2 Cathode for Lithium-Ion Batteries. *Adv. Funct. Mater.* **2018**, 1802090.
(70) Sun, Y.-K.; Kim, D.-H.; Jung, H.-G.; Myung, S.-T.; Amine, K. High-Voltage Performance of Concentration-Gradient Li [Ni0. 67Co0. 15Mn0. 18] O2 Cathode Material for Lithium-Ion Batteries. *Electrochimica Acta* **2010**, *55* (28), 8621–8627.
(71) Haregewoin, A. M.; Wotango, A. S.; Hwang, B.-J. Electrolyte Additives for Lithium Ion Battery Electrodes: Progress and Perspectives. *Energy Environ. Sci.* **2016**, *9* (6), 1955–1988.
(72) Kim, G.-Y.; Dahn, J. The Effect of Some Nitriles as Electrolyte Additives in Li-Ion Batteries. *J. Electrochem. Soc.* **2015**, *162* (3), A437–A447.
(73) Petibon, R.; Rotermund, L.; Dahn, J. Evaluation of Phenyl Carbonates as Electrolyte Additives in Lithium-Ion Batteries. *J. Power Sources* **2015**, *287*, 184–195.
(74) Ma, L.; Ellis, L.; Glazier, S. L.; Ma, X.; Dahn, J. R. Combinations of LiPO2F2 and Other Electrolyte Additives in Li [Ni0. 5Mn0. 3Co0. 2] O2/Graphite Pouch Cells. *J. Electrochem. Soc.* **2018**, *165* (9), A1718–A1724.
(75) Li, J.; Liu, H.; Xia, J.; Cameron, A. R.; Nie, M.; Botton, G. A.; Dahn, J. The Impact of Electrolyte Additives and Upper Cut-off Voltage on the Formation of a Rocksalt

Surface Layer in LiNi0. 8Mn0. 1Co0. 1O2 Electrodes. *J. Electrochem. Soc.* **2017**, *164* (4), A655–A665.
(76) Xu, C.; Renault, S.; Ebadi, M.; Wang, Z.; Björklund, E.; Guyomard, D.; Brandell, D.; Edström, K.; Gustafsson, T. LiTDI: A Highly Efficient Additive for Electrolyte Stabilization in Lithium-Ion Batteries. *Chem. Mater.* **2017**, *29* (5), 2254–2263.
(77) Aurbach, D.; Markovsky, B.; Rodkin, A.; Levi, E.; Cohen, Y. S.; Kim, H.-J.; Schmidt, M. On the Capacity Fading of LiCoO2 Intercalation Electrodes:: The Effect of Cycling, Storage, Temperature, and Surface Film Forming Additives. *Electrochimica Acta* **2002**, *47* (27), 4291–4306.
(78) Aurbach, D.; Gamolsky, K.; Markovsky, B.; Salitra, G.; Gofer, Y.; Heider, U.; Oesten, R.; Schmidt, M. The Study of Surface Phenomena Related to Electrochemical Lithium Intercalation into Li x MO y Host Materials (M= Ni, Mn). *J. Electrochem. Soc.* **2000**, *147* (4), 1322–1331.
(79) Feng, S.; Huang, M.; Lamb, J. R.; Zhang, W.; Tatara, R.; Zhang, Y.; Zhu, Y. G.; Perkinson, C. F.; Johnson, J. A.; Shao-Horn, Y. Molecular Design of Stable Sulfamide-and Sulfonamide-Based Electrolytes for Aprotic Li-O2 Batteries. *Chem* **2019**.
(80) Leung, K. First-Principles Modeling of the Initial Stages of Organic Solvent Decomposition on Li x Mn2O4 (100) Surfaces. *J. Phys. Chem. C* **2012**, *116* (18), 9852–9861.
(81) Xu, S.; Luo, G.; Jacobs, R.; Fang, S.; Mahanthappa, M. K.; Hamers, R. J.; Morgan, D. Ab Initio Modeling of Electrolyte Molecule Ethylene Carbonate Decomposition Reaction on Li (Ni, Mn, Co) O2 Cathode Surface. *ACS Appl. Mater. Interfaces* **2017**, *9* (24), 20545–20553.
(82) Borodin, O.; Olguin, M.; Spear, C. E.; Leiter, K. W.; Knap, J. Towards High Throughput Screening of Electrochemical Stability of Battery Electrolytes. *Nanotechnology* **2015**, *26* (35), 354003.
(83) Kumar, N.; Leung, K.; Siegel, D. J. Crystal Surface and State of Charge Dependencies of Electrolyte Decomposition on LiMn2O4 Cathode. *J. Electrochem. Soc.* **2014**, *161* (8), E3059–E3065.
(84) La Mantia, F.; Rosciano, F.; Tran, N.; Novák, P. Direct Evidence of Oxygen Evolution from Li 1+ x (Ni 1/3 Mn 1/3 Co 1/3) 1− x O 2 at High Potentials. *J. Appl. Electrochem.* **2008**, *38* (7), 893–896.
(85) Xiong, D. J.; Ellis, L. D.; Li, J.; Li, H.; Hynes, T.; Allen, J. P.; Xia, J.; Hall, D. S.; Hill, I. G.; Dahn, J. R. Measuring Oxygen Release from Delithiated LiNixMnyCo1-x-yO2 and Its Effects on the Performance of High Voltage Li-Ion Cells. *J. Electrochem. Soc.* **2017**, *164* (13), A3025–A3037.
(86) Goodenough, J. B.; Kim, Y. Challenges for Rechargeable Li Batteries. *Chem. Mater.* **2009**, *22* (3), 587–603.
(87) Guéguen, A.; Streich, D.; He, M.; Mendez, M.; Chesneau, F. F.; Novák, P.; Berg, E. J. Decomposition of LiPF6 in High Energy Lithium-Ion Batteries Studied with Online Electrochemical Mass Spectrometry. *J. Electrochem. Soc.* **2016**, *163* (6), A1095–A1100.
(88) Dedryvère, R.; Martinez, H.; Leroy, S.; Lemordant, D.; Bonhomme, F.; Biensan, P.; Gonbeau, D. Surface Film Formation on Electrodes in a LiCoO2/Graphite Cell: A Step by Step XPS Study. *J. Power Sources* **2007**, *174* (2), 462–468.

(89) Edström, K.; Gustafsson, T.; Thomas, J. O. The Cathode–Electrolyte Interface in the Li-Ion Battery. *Electrochimica Acta* **2004**, *50* (2–3), 397–403.
(90) Harks, P.; Mulder, F. M.; Notten, P. H. L. In Situ Methods for Li-Ion Battery Research: A Review of Recent Developments. *J. Power Sources* **2015**, *288*, 92–105.
(91) Stuart, B. Infrared Spectroscopy. *Kirk-Othmer Encycl. Chem. Technol.* **2000**, 1–18.
(92) Goren, E.; Chusid, O.; Aurbach, D. The Application of in Situ FTIR Spectroscopy to the Study of Surface Films Formed on Lithium and Noble Metals at Low Potentials in Li Battery Electrolytes. *J. Electrochem. Soc.* **1991**, *138* (5), L6–L9.
(93) Zhuang, G. V.; Yang, H.; Blizanac, B.; Ross, P. N. A Study of Electrochemical Reduction of Ethylene and Propylene Carbonate Electrolytes on Graphite Using ATR-FTIR Spectroscopy. *Electrochem. Solid-State Lett.* **2005**, *8* (9), A441–A445.
(94) Hongyou, K.; Hattori, T.; Nagai, Y.; Tanaka, T.; Nii, H.; Shoda, K. Dynamic in Situ Fourier Transform Infrared Measurements of Chemical Bonds of Electrolyte Solvents during the Initial Charging Process in a Li Ion Battery. *J. Power Sources* **2013**, *243*, 72–77.
(95) Moshkovich, M.; Cojocaru, M.; Gottlieb, H. E.; Aurbach, D. The Study of the Anodic Stability of Alkyl Carbonate Solutions by in Situ FTIR Spectroscopy, EQCM, NMR and MS. *J. Electroanal. Chem.* **2001**, *497* (1–2), 84–96.
(96) Kanamura, K.; Toriyama, S.; Shiraishi, S.; Ohashi, M.; Takehara, Z. Studies on Electrochemical Oxidation of Non-Aqueous Electrolyte on the LiCoO2 Thin Film Electrode. *J. Electroanal. Chem.* **1996**, *419* (1), 77–84.
(97) Akita, Y.; Segawa, M.; Munakata, H.; Kanamura, K. In-Situ Fourier Transform Infrared Spectroscopic Analysis on Dynamic Behavior of Electrolyte Solution on LiFePO4 Cathode. *J. Power Sources* **2013**, *239*, 175–180.
(98) Kanamura, K.; Umegaki, T.; Ohashi, M.; Toriyama, S.; Shiraishi, S.; Takehara, Z. Oxidation of Propylene Carbonate Containing LiBF4 or LiPF6 on LiCoO2 Thin Film Electrode for Lithium Batteries. *Electrochimica Acta* **2001**, *47* (3), 433–439.
(99) Matsui, M.; Dokko, K.; Akita, Y.; Munakata, H.; Kanamura, K. Surface Layer Formation of LiCoO2 Thin Film Electrodes in Non-Aqueous Electrolyte Containing Lithium Bis (Oxalate) Borate. *J. Power Sources* **2012**, *210*, 60–66.
(100) Sharabi, R.; Markevich, E.; Borgel, V.; Salitra, G.; Aurbach, D.; Semrau, G.; Schmidt, M. A. In Situ FTIR Spectroscopy Study of Li/LiNi0. 8Co0. 15Al0. 05O2 Cells with Ionic Liquid-Based Electrolytes in Overcharge Condition. *Electrochem. Solid-State Lett.* **2010**, *13* (4), A32–A35.
(101) Phillip, N. D.; Ruther, R. E.; Sang, X.; Wang, Y.; Unocic, R. R.; Westover, A. S.; Daniel, C.; Veith, G. M. Synthesis of Ni-Rich Thin-Film Cathode as Model System for Lithium Ion Batteries. *ACS Appl. Energy Mater.* **2019**, *2* (2), 1405–1412.
(102) Teshager, M. A.; Lin, S. D.; Hwang, B.-J.; Wang, F.-M.; Hy, S.; Haregewoin, A. M. In Situ DRIFTS Analysis of Solid-Electrolyte Interphase Formation on Li-Rich Li1. 2Ni0. 2Mn0. 6O2 and LiCoO2 Cathodes during Oxidative Electrolyte Decomposition. *ChemElectroChem* **2016**, *3* (2), 337–345.
(103) Hy, S.; Felix, F.; Rick, J.; Su, W.-N.; Hwang, B. J. Direct In Situ Observation of Li2O Evolution on Li-Rich High-Capacity Cathode Material, Li [Ni x Li (1–2 x)/3Mn (2–x)/3] O2 (0≤ X≤ 0.5). *J. Am. Chem. Soc.* **2014**, *136* (3), 999–1007.

(104) Zhang, X.; Pugh, J. K.; Ross, P. N. Computation of Thermodynamic Oxidation Potentials of Organic Solvents Using Density Functional Theory. *J. Electrochem. Soc.* **2001**, *148* (5), E183–E188.
(105) Xing, L.; Borodin, O.; Smith, G. D.; Li, W. Density Functional Theory Study of the Role of Anions on the Oxidative Decomposition Reaction of Propylene Carbonate. *J. Phys. Chem. A* **2011**, *115* (47), 13896–13905.
(106) Borodin, O.; Jow, T. R. Quantum Chemistry Studies of the Oxidative Stability of Carbonate, Sulfone and Sulfonate-Based Electrolytes Doped with BF4-, Pf6-Anions. *ECS Trans.* **2011**, *33* (28), 77–84.
(107) Ue, M.; Takeda, M.; Takehara, M.; Mori, S. Electrochemical Properties of Quaternary Ammonium Salts for Electrochemical Capacitors. *J. Electrochem. Soc.* **1997**, *144* (8), 2684–2688.
(108) Egashira, M.; Takahashi, H.; Okada, S.; Yamaki, J. Measurement of the Electrochemical Oxidation of Organic Electrolytes Used in Lithium Batteries by Microelectrode. *J. Power Sources* **2001**, *92* (1–2), 267–271.
(109) Xu, K.; Ding, S. P.; Jow, T. R. Toward Reliable Values of Electrochemical Stability Limits for Electrolytes. *J. Electrochem. Soc.* **1999**, *146* (11), 4172–4178.
(110) Lee, J.-C.; Litt, M. H. Ring-Opening Polymerization of Ethylene Carbonate and Depolymerization of Poly (Ethylene Oxide-Co-Ethylene Carbonate). *Macromolecules* **2000**, *33* (5), 1618–1627.
(111) Sloop, S. E.; Kerr, J. B.; Kinoshita, K. The Role of Li-Ion Battery Electrolyte Reactivity in Performance Decline and Self-Discharge. *J. Power Sources* **2003**, *119*, 330–337.
(112) Xing, L.; Li, W.; Wang, C.; Gu, F.; Xu, M.; Tan, C.; Yi, J. Theoretical Investigations on Oxidative Stability of Solvents and Oxidative Decomposition Mechanism of Ethylene Carbonate for Lithium Ion Battery Use. *J. Phys. Chem. B* **2009**, *113* (52), 16596–16602.
(113) Xu, K. Electrolytes and Interphases in Li-Ion Batteries and Beyond. *Chem. Rev.* **2014**, *114* (23), 11503–11618.
(114) Yu, L.; Liu, H.; Wang, Y.; Kuwata, N.; Osawa, M.; Kawamura, J.; Ye, S. Preferential Adsorption of Solvents on the Cathode Surface of Lithium Ion Batteries. *Angew. Chem.* **2013**, *125* (22), 5865–5868.
(115) Logan, E. R.; Tonita, E. M.; Gering, K. L.; Li, J.; Ma, X.; Beaulieu, L. Y.; Dahn, J. R. A Study of the Physical Properties of Li-Ion Battery Electrolytes Containing Esters. *J. Electrochem. Soc.* **2018**, *165* (2), A21–A30.
(116) Day, R. P.; Xia, J.; Petibon, R.; Rucska, J.; Wang, H.; Wright, A. T. B.; Dahn, J. R. Differential Thermal Analysis of Li-Ion Cells as an Effective Probe of Liquid Electrolyte Evolution during Aging. *J. Electrochem. Soc.* **2015**, *162* (14), A2577–A2581.
(117) Freiberg, A. T.; Roos, M. K.; Wandt, J.; de Vivie-Riedle, R.; Gasteiger, H. A. Singlet Oxygen Reactivity with Carbonate Solvents Used for Li-Ion Battery Electrolytes. *J. Phys. Chem. A* **2018**, *122* (45), 8828–8839.
(118) Hong, W. T.; Stoerzinger, K. A.; Lee, Y.-L.; Giordano, L.; Grimaud, A.; Johnson, A. M.; Hwang, J.; Crumlin, E. J.; Yang, W.; Shao-Horn, Y. Charge-Transfer-Energy-Dependent Oxygen Evolution Reaction Mechanisms for Perovskite Oxides. *Energy Environ. Sci.* **2017**, *10* (10), 2190–2200.

(119) Giordano, L.; Østergaard, T. M.; Muy, S.; Yu, Y.; Charles, N.; Kim, S.; Zhang, Y.; Maglia, F.; Jung, R.; Lund, I. Ligand-Dependent Energetics for Dehydrogenation: Implications in Li-Ion Battery Electrolyte Stability and Selective Oxidation Catalysis of Hydrogen-Containing Molecules. *Chem. Mater.* **2019**.
(120) Giordano, L.; Karayaylali, P.; Yu, Y.; Katayama, Y.; Maglia, F.; Lux, S.; Shao-Horn, Y. Chemical Reactivity Descriptor for the Oxide-Electrolyte Interface in Li-Ion Batteries. *J. Phys. Chem. Lett.* **2017**, *8* (16), 3881–3887.
(121) Østergaard, T. M.; Giordano, L.; Castelli, I. E.; Maglia, F.; Antonopoulos, B. K.; Shao-Horn, Y.; Rossmeisl, J. Oxidation of Ethylene Carbonate on Li Metal Oxide Surfaces. *J. Phys. Chem. C* **2018**, *122* (19), 10442–10449.
(122) Leung, K.; Qi, Y.; Zavadil, K. R.; Jung, Y. S.; Dillon, A. C.; Cavanagh, A. S.; Lee, S.-H.; George, S. M. Using Atomic Layer Deposition to Hinder Solvent Decomposition in Lithium Ion Batteries: First-Principles Modeling and Experimental Studies. *J. Am. Chem. Soc.* **2011**, *133* (37), 14741–14754.
(123) Lu, Y.-C.; Mansour, A. N.; Yabuuchi, N.; Shao-Horn, Y. Probing the Origin of Enhanced Stability of "AlPO4" Nanoparticle Coated LiCoO2 during Cycling to High Voltages: Combined XRD and XPS Studies. *Chem. Mater.* **2009**, *21* (19), 4408–4424.
(124) Verdier, S.; El Ouatani, L.; Dedryvere, R.; Bonhomme, F.; Biensan, P.; Gonbeau, D. XPS Study on Al2O3-and AlPO4-Coated LiCoO2 Cathode Material for High-Capacity Li Ion Batteries. *J. Electrochem. Soc.* **2007**, *154* (12), A1088–A1099.
(125) Cho, J.; Kim, Y. J.; Park, B. Novel LiCoO2 Cathode Material with Al2O3 Coating for a Li Ion Cell. *Chem. Mater.* **2000**, *12* (12), 3788–3791.
(126) Hu, S.-K.; Cheng, G.-H.; Cheng, M.-Y.; Hwang, B.-J.; Santhanam, R. Cycle Life Improvement of ZrO2-Coated Spherical LiNi1/3Co1/3Mn1/3O2 Cathode Material for Lithium Ion Batteries. *J. Power Sources* **2009**, *188* (2), 564–569.
(127) Yesibolati, N.; Shahid, M.; Chen, W.; Hedhili, M. N.; Reuter, M. C.; Ross, F. M.; Alshareef, H. N. SnO2 Anode Surface Passivation by Atomic Layer Deposited HfO2 Improves Li-Ion Battery Performance. *Small* **2014**, *10* (14), 2849–2858.
(128) Nohira, H.; Tsai, W.; Besling, W.; Young, E.; Pétry, J.; Conard, T.; Vandervorst, W.; De Gendt, S.; Heyns, M.; Maes, J. Characterization of ALCVD-Al2O3 and ZrO2 Layer Using X-Ray Photoelectron Spectroscopy. *J. Non-Cryst. Solids* **2002**, *303* (1), 83–87.
(129) Karayaylali, P.; Tatara, R.; Zhang, Y.; Chan, K.-L.; Yu, Y.; Giordano, L.; Maglia, F.; Jung, R.; Lund, I.; Shao-Horn, Y. Coating-Dependent Electrode-Electrolyte Interface for Ni-Rich Positive Electrodes in Li-Ion Batteries. *J. Electrochem. Soc.* **2019**, *166* (6), A1022–A1030.
(130) Yamada, Y.; Yamada, A. Superconcentrated Electrolytes for Lithium Batteries. *J. Electrochem. Soc.* **2015**, *162* (14), A2406–A2423.
(131) Yamada, Y.; Yamada, A. Superconcentrated Electrolytes to Create New Interfacial Chemistry in Non-Aqueous and Aqueous Rechargeable Batteries. *Chem. Lett.* **2017**, *46* (8), 1056–1064.
(132) Yoshida, K.; Nakamura, M.; Kazue, Y.; Tachikawa, N.; Tsuzuki, S.; Seki, S.; Dokko, K.; Watanabe, M. Oxidative-Stability Enhancement and Charge Transport Mechanism in Glyme–Lithium Salt Equimolar Complexes. *J. Am. Chem. Soc.* **2011**, *133* (33), 13121–13129.

(133) Tatara, R.; Yu, Y.; Karayaylali, P.; Chan, A. K.; Zhang, Y.; Jung, R.; Maglia, F.; Giordano, L.; Shao-Horn, Y. Enhanced Cycling Performance of Ni-Rich Positive Electrodes (NMC) in Li-Ion Batteries by Reducing Electrolyte Free-Solvent Activity. *ACS Appl. Mater. Interfaces* **2019**, *11* (38), 34973–34988.
(134) Han, S.-D.; Yun, S.-H.; Borodin, O.; Seo, D. M.; Sommer, R. D.; Young Jr, V. G.; Henderson, W. A. Solvate Structures and Computational/Spectroscopic Characterization of LiPF6 Electrolytes. *J. Phys. Chem. C* **2015**, *119* (16), 8492–8500.
(135) Chan, A. K.; Tatara, R.; Feng, S.; Karayaylali, P.; Lopez, J.; Stephens, I. E.; Shao-Horn, Y. Concentrated Electrolytes for Enhanced Stability of Al-Alloy Negative Electrodes in Li-Ion Batteries. *J. Electrochem. Soc.* **2019**, *166* (10), A1867–A1874.
(136) Tatara, R.; Kwabi, D. G.; Batcho, T. P.; Tulodziecki, M.; Watanabe, K.; Kwon, H.-M.; Thomas, M. L.; Ueno, K.; Thompson, C. V.; Dokko, K. Oxygen Reduction Reaction in Highly Concentrated Electrolyte Solutions of Lithium Bis (Trifluoromethanesulfonyl) Amide/Dimethyl Sulfoxide. *J. Phys. Chem. C* **2017**, *121* (17), 9162–9172.
(137) Terada, S.; Ikeda, K.; Ueno, K.; Dokko, K.; Watanabe, M. Liquid Structures and Transport Properties of Lithium Bis (Fluorosulfonyl) Amide/Glyme Solvate Ionic Liquids for Lithium Batteries. *Aust. J. Chem.* **2019**, *72* (2), 70–80.
(138) Ueno, K.; Tatara, R.; Tsuzuki, S.; Saito, S.; Doi, H.; Yoshida, K.; Mandai, T.; Matsugami, M.; Umebayashi, Y.; Dokko, K. Li+ Solvation in Glyme–Li Salt Solvate Ionic Liquids. *Phys. Chem. Chem. Phys.* **2015**, *17* (12), 8248–8257.
(139) Cao, Z.; Hashinokuchi, M.; Doi, T.; Inaba, M. Improved Cycle Performance of LiNi0. 8Co0. 1Mn0. 1O2 Positive Electrode Material in Highly Concentrated LiBF4/DMC. *J. Electrochem. Soc.* **2019**, *166* (2), A82–A88.
(140) Doi, T.; Shimizu, Y.; Hashinokuchi, M.; Inaba, M. LiBF4-Based Concentrated Electrolyte Solutions for Suppression of Electrolyte Decomposition and Rapid Lithium-Ion Transfer at LiNi0. 5Mn1. 5O4/Electrolyte Interface. *J. Electrochem. Soc.* **2016**, *163* (10), A2211–A2215.
(141) Doi, T.; Hashinokuchi, M.; Inaba, M. Solvation-Controlled Ester-Based Concentrated Electrolyte Solutions for High-Voltage Lithium-Ion Batteries. *Curr. Opin. Electrochem.* **2018**, *9*, 49–55.
(142) Aiken, C. P.; Harlow, J.; Thompson, L.; Bauer, M.; Hynes, T.; Ma, X.; Dahn, J. R. Using Varied Salt Concentration and High Charging Potential to Study "Rollover" Failure Mechanisms in Li-Ion Cells. In *Meeting Abstracts*; The Electrochemical Society, 2019; pp 223–223.
(143) Petibon, R.; Madec, L.; Abarbanel, D. W.; Dahn, J. R. Effect of LiPF6 Concentration in Li [Ni0. 4Mn0. 4Co0. 2] O2/Graphite Pouch Cells Operated at 4.5 V. *J. Power Sources* **2015**, *300*, 419–429.
(144) Ma, X.; Harlow, J.; Keefe, A. S.; Li, J.; Glazier, S.; Ma, L.; Hall, D. S.; Aiken, C. P.; Genovese, M.; Cormier, M. Studies of Rollover Failure in Lithium-Ion Cells. In *Meeting Abstracts*; The Electrochemical Society, 2019; pp 210–210.
(145) Chen, Z.; Qin, Y.; Amine, K.; Sun, Y.-K. Role of Surface Coating on Cathode Materials for Lithium-Ion Batteries. *J. Mater. Chem.* **2010**, *20* (36), 7606. https://doi.org/10.1039/c0jm00154f.
(146) Zhang, S. S. A Review on Electrolyte Additives for Lithium-Ion Batteries. *J. Power Sources* **2006**, *162* (2), 1379–1394.

(147) Zhao, H.; Yu, X.; Li, J.; Li, B.; Shao, H.; Li, L.; Deng, Y. Film-Forming Electrolyte Additives for Rechargeable Lithium Ion Batteries: Progress and Outlooks. *J. Mater. Chem. A* **2019**.
(148) Xue, W.; Huang, M.; Li, Y.; Zhu, Y. G.; Gao, R.; Xiao, X.; Zhang, W.; Li, S.; Xu, G.; Yu, Y. Ultra-High-Voltage Ni-Rich Layered Cathodes in Practical Li Metal Batteries Enabled by a Sulfonamide-Based Electrolyte. *Nat. Energy* **2021**, *6* (5), 495–505.
(149) Qiu, W.; Xia, J.; Chen, L.; Dahn, J. A Study of Methyl Phenyl Carbonate and Diphenyl Carbonate as Electrolyte Additives for High Voltage LiNi0. 8Mn0. 1Co0. 1O2/Graphite Pouch Cells. *J. Power Sources* **2016**, *318*, 228–234.
(150) Kim, G.-Y.; Petibon, R.; Dahn, J. Effects of Succinonitrile (SN) as an Electrolyte Additive on the Impedance of LiCoO2/Graphite Pouch Cells during Cycling. *J. Electrochem. Soc.* **2014**, *161* (4), A506–A512.
(151) Ma, L.; Xia, J.; Dahn, J. Improving the High Voltage Cycling of Li [Ni0. 42Mn0. 42Co0. 16] O2 (NMC442)/Graphite Pouch Cells Using Electrolyte Additives. *J. Electrochem. Soc.* **2014**, *161* (14), A2250–A2254.
(152) Li, J.; Downie, L. E.; Ma, L.; Qiu, W.; Dahn, J. Study of the Failure Mechanisms of LiNi0. 8Mn0. 1Co0. 1O2 Cathode Material for Lithium Ion Batteries. *J. Electrochem. Soc.* **2015**, *162* (7), A1401–A1408.
(153) Arumugam, R. S.; Ma, L.; Li, J.; Xia, X.; Paulsen, J.; Dahn, J. Special Synergy between Electrolyte Additives and Positive Electrode Surface Coating to Enhance the Performance of Li [Ni0. 6Mn0. 2Co0. 2] O2/Graphite Cells. *J. Electrochem. Soc.* **2016**, *163* (13), A2531–A2538.
(154) Burns, J.; Petibon, R.; Nelson, K.; Sinha, N.; Kassam, A.; Way, B.; Dahn, J. Studies of the Effect of Varying Vinylene Carbonate (VC) Content in Lithium Ion Cells on Cycling Performance and Cell Impedance. *J. Electrochem. Soc.* **2013**, *160* (10), A1668–A1674.
(155) Abe, K.; Ushigoe, Y.; Yoshitake, H.; Yoshio, M. Functional Electrolytes: Novel Type Additives for Cathode Materials, Providing High Cycleability Performance. *J. Power Sources* **2006**, *153* (2), 328–335.
(156) Karayaylali, P.; Zhang, Y.; Giordano, L.; Katayama, Y.; Tatara, R.; Yu, Y.; Maglia, F.; Jung, R.; Shao-Horn, Y. The Role of Diphenyl Carbonate Additive on the Interfacial Reactivity of Positive Electrodes in Li-Ion Batteries. *J. Electrochem. Soc.* **2020**, *167* (4), 040522.
(157) Zhang, Y.; Katayama, Y.; Tatara, R.; Giordano, L.; Yu, Y.; Fraggedakis, D.; Sun, J. G.; Maglia, F.; Jung, R.; Bazant, M. Z. Revealing Electrolyte Oxidation via Carbonate Dehydrogenation on Ni-Based Oxides in Li-Ion Batteries by in Situ Fourier Transform Infrared Spectroscopy. *Energy Environ. Sci.* **2020**, *13* (1), 183–199.
(158) Zuo, X.; Zhao, M.; Ma, X.; Xiao, X.; Liu, J.; Nan, J. Effect of Diphenyl Disulfide as an Additive on the Electrochemical Performance of Li1. 2Mn0. 54Ni0. 13Co0. 13O2/Graphite Batteries at Elevated Temperature. *Electrochimica Acta* **2017**, *245*, 705–714.
(159) Lee, J.-N.; Han, G.-B.; Ryou, M.-H.; Lee, D. J.; Song, J.; Choi, J. W.; Park, J.-K. N-(Triphenylphosphoranylidene) Aniline as a Novel Electrolyte Additive for High

Voltage LiCoO2 Operations in Lithium Ion Batteries. *Electrochimica Acta* **2011**, *56* (14), 5195–5200.
(160) Kubota, T.; Ihara, M.; Katayama, S.; Nakai, H.; Ichikawa, J. 1, 1-Difluoro-1-Alkenes as New Electrolyte Additives for Lithium Ion Batteries. *J. Power Sources* **2012**, *207*, 141–149.
(161) Xue, W.; Gao, R.; Shi, Z.; Xiao, X.; Zhang, W.; Zhang, Y.; Zhu, Y. G.; Waluyo, I.; Li, Y.; Hill, M. R. Stabilizing Electrode–Electrolyte Interfaces to Realize High-Voltage Li|| LiCoO 2 Batteries by a Sulfonamide-Based Electrolyte. *Energy Environ. Sci.* **2021**, *14* (11), 6030–6040.
(162) Shyamsunder, A.; Beichel, W.; Klose, P.; Pang, Q.; Scherer, H.; Hoffmann, A.; Murphy, G. K.; Krossing, I.; Nazar, L. F. Inhibiting Polysulfide Shuttle in Lithium–Sulfur Batteries through Low-ion-pairing Salts and a Triflamide Solvent. *Angew. Chem.* **2017**, *129* (22), 6288–6293.
(163) Sood, A.; Poletayev, A. D.; Cogswell, D. A.; Csernica, P. M.; Mefford, J. T.; Fraggedakis, D.; Toney, M. F.; Lindenberg, A. M.; Bazant, M. Z.; Chueh, W. C. Electrochemical Ion Insertion from the Atomic to the Device Scale. *Nat. Rev. Mater.* **2021**, 1–21.
(164) Delmas, C. Sodium and Sodium-ion Batteries: 50 Years of Research. *Adv. Energy Mater.* **2018**, *8* (17), 1703137.
(165) Wang, H.; Xu, S.; Tsai, C.; Li, Y.; Liu, C.; Zhao, J.; Liu, Y.; Yuan, H.; Abild-Pedersen, F.; Prinz, F. B. Direct and Continuous Strain Control of Catalysts with Tunable Battery Electrode Materials. *Science* **2016**, *354* (6315), 1031–1036.
(166) Rauh, R. D. Electrochromic Windows: An Overview. *Electrochimica Acta* **1999**, *44* (18), 3165–3176.
(167) Alkhadra, M. Electrochemical Methods for Water Purification, Ion Separations, and Energy Conversion. *Chemical Reviews* **2022**.
(168) Gonzalez-Rosillo, J. C.; Balaish, M.; Hood, Z. D.; Nadkarni, N.; Fraggedakis, D.; Kim, K. J.; Mullin, K. M.; Pfenninger, R.; Bazant, M. Z.; Rupp, J. L. Lithium-Battery Anode Gains Additional Functionality for Neuromorphic Computing through Metal–Insulator Phase Separation. *Adv. Mater.* **2020**, *32* (9), 1907465.
(169) Urban, A.; Seo, D.-H.; Ceder, G. Computational Understanding of Li-Ion Batteries. *Npj Comput. Mater.* **2016**, *2* (1), 1–13.
(170) Bazant, M. Z. Theory of Chemical Kinetics and Charge Transfer Based on Nonequilibrium Thermodynamics. *Acc. Chem. Res.* **2013**, *46* (5), 1144–1160.
(171) Berliner, M. D.; Zhao, H.; Das, S.; Forsuelo, M.; Jiang, B.; Chueh, W. H.; Bazant, M. Z.; Braatz, R. D. Nonlinear Identifiability Analysis of the Porous Electrode Theory Model of Lithium-Ion Batteries. *J. Electrochem. Soc.* **2021**, *168* (9), 090546.
(172) Bai, P.; Bazant, M. Z. Charge Transfer Kinetics at the Solid–Solid Interface in Porous Electrodes. *Nat. Commun.* **2014**, *5* (1), 1–7.
(173) Marcus, R. A. Electron Transfer Reactions in Chemistry. Theory and Experiment. *Rev. Mod. Phys.* **1993**, *65* (3), 599.
(174) Marcus, R. A. On the Theory of Oxidation-reduction Reactions Involving Electron Transfer. I. *J. Chem. Phys.* **1956**, *24* (5), 966–978.
(175) Kuznetsov, A. M.; Ulstrup, J. *Electron Transfer in Chemistry and Biology: An Introduction to the Theory*; John Wiley & Sons Ltd, 1999.

(176) Hush, N. S. Homogeneous and Heterogeneous Optical and Thermal Electron Transfer. *Electrochimica Acta* **1968**, *13* (5), 1005–1023.
(177) Chidsey, C. E. Free Energy and Temperature Dependence of Electron Transfer at the Metal-Electrolyte Interface. *Science* **1991**, *251* (4996), 919–922.
(178) Marcus, R. A. On the Theory of Electron-transfer Reactions. VI. Unified Treatment for Homogeneous and Electrode Reactions. *J. Chem. Phys.* **1965**, *43* (2), 679–701.
(179) Bai, P.; Tian, G. Statistical Kinetics of Phase-Transforming Nanoparticles in LiFePO4 Porous Electrodes. *Electrochimica Acta* **2013**, *89*, 644–651.
(180) Heubner, C.; Schneider, M.; Michaelis, A. Investigation of Charge Transfer Kinetics of Li-Intercalation in LiFePO4. *J. Power Sources* **2015**, *288*, 115–120.
(181) Bazant, M. Z. Thermodynamic Stability of Driven Open Systems and Control of Phase Separation by Electro-Autocatalysis. *Faraday Discuss.* **2017**, *199*, 423–463.
(182) Lim, J.; Li, Y.; Alsem, D. H.; So, H.; Lee, S. C.; Bai, P.; Cogswell, D. A.; Liu, X.; Jin, N.; Yu, Y. Origin and Hysteresis of Lithium Compositional Spatiodynamics within Battery Primary Particles. *Science* **2016**, *353* (6299), 566–571.
(183) Park, J.; Zhao, H.; Kang, S. D.; Lim, K.; Chen, C.-C.; Yu, Y.-S.; Braatz, R. D.; Shapiro, D. A.; Hong, J.; Toney, M. F. Fictitious Phase Separation in Li Layered Oxides Driven by Electro-Autocatalysis. *Nat. Mater.* **2021**, 1–9.
(184) Zhao, H.; Deng, H. D.; Cohen, A. E.; Lim, J.; Li, Y.; Fraggedakis, D.; Jiang, B.; Storey, B. D.; Chueh, W. C.; Braatz, R. D.; Bazant, M. Z. Learning Heterogeneous Reaction Kinetics of Nanoparticles from Images. 2022.
(185) Fraggedakis, D.; McEldrew, M.; Smith, R. B.; Krishnan, Y.; Zhang, Y.; Bai, P.; Chueh, W. C.; Shao-Horn, Y.; Bazant, M. Z. Theory of Coupled Ion-Electron Transfer Kinetics. *Electrochimica Acta* **2021**, *367*, 137432.
(186) Cukier, R. I.; Nocera, D. G. Proton-Coupled Electron Transfer. *Annu. Rev. Phys. Chem.* **1998**, *49* (1), 337–369.
(187) Koper, M. T. Theory of the Transition from Sequential to Concerted Electrochemical Proton–Electron Transfer. *Phys. Chem. Chem. Phys.* **2013**, *15* (5), 1399–1407.
(188) Hammes-Schiffer, S. Controlling Electrons and Protons through Theory: Molecular Electrocatalysts to Nanoparticles. *Acc. Chem. Res.* **2018**, *51* (9), 1975–1983.
(189) Smith, R. B.; Bazant, M. Z. Multiphase Porous Electrode Theory. *J. Electrochem. Soc.* **2017**, *164* (11), E3291.
(190) Zeng, Y.; Smith, R. B.; Bai, P.; Bazant, M. Z. Simple Formula for Marcus–Hush–Chidsey Kinetics. *J. Electroanal. Chem.* **2014**, *735*, 77–83.
(191) Nitzan, A. *Chemical Dynamics in Condensed Phases: Relaxation, Transfer and Reactions in Condensed Molecular Systems*; Oxford university press, 2006.
(192) Shirodkar, S. N.; Kaxiras, E. Li Intercalation at Graphene/Hexagonal Boron Nitride Interfaces. *Phys. Rev. B* **2016**, *93* (24), 245438.
(193) Holzwarth, N. A. W.; Louie, S. G.; Rabii, S. Lithium-Intercalated Graphite: Self-Consistent Electronic Structure for Stages One, Two, and Three. *Phys. Rev. B* **1983**, *28* (2), 1013.
(194) Biesheuvel, P. M.; Van Soestbergen, M.; Bazant, M. Z. Imposed Currents in Galvanic Cells. *Electrochimica Acta* **2009**, *54* (21), 4857–4871.
(195) Schmickler, W.; Santos, E. *Interfacial Electrochemistry*; Springer Science & Business Media, 2010.

(196) Milewska, A.; Świerczek, K.; Tobola, J.; Boudoire, F.; Hu, Y.; Bora, D. K.; Mun, B. S.; Braun, A.; Molenda, J. The Nature of the Nonmetal–Metal Transition in LixCoO2 Oxide. *Solid State Ion.* **2014**, *263*, 110–118.
(197) Huang, B.; Myint, K. H.; Wang, Y.; Zhang, Y.; Rao, R. R.; Sun, J.; Muy, S.; Katayama, Y.; Corchado Garcia, J.; Fraggedakis, D. Cation-Dependent Interfacial Structures and Kinetics for Outer-Sphere Electron-Transfer Reactions. *J. Phys. Chem. C* **2021**, *125* (8), 4397–4411.
(198) Huang, B.; Rao, R. R.; You, S.; Hpone Myint, K.; Song, Y.; Wang, Y.; Ding, W.; Giordano, L.; Zhang, Y.; Wang, T. Cation-and PH-Dependent Hydrogen Evolution and Oxidation Reaction Kinetics. *JACS Au* **2021**, *1* (10), 1674–1687.
(199) Park, K.-S.; Xiao, P.; Kim, S.-Y.; Dylla, A.; Choi, Y.-M.; Henkelman, G.; Stevenson, K. J.; Goodenough, J. B. Enhanced Charge-Transfer Kinetics by Anion Surface Modification of LiFePO4. *Chem. Mater.* **2012**, *24* (16), 3212–3218.
(200) Heubner, C.; Schneider, M.; Michaelis, A. Detailed Study of Heat Generation in Porous LiCoO2 Electrodes. *J. Power Sources* **2016**, *307*, 199–207.
(201) Tsai, P.-C.; Wen, B.; Wolfman, M.; Choe, M.-J.; Pan, M. S.; Su, L.; Thornton, K.; Cabana, J.; Chiang, Y.-M. Single-Particle Measurements of Electrochemical Kinetics in NMC and NCA Cathodes for Li-Ion Batteries. *Energy Environ. Sci.* **2018**, *11* (4), 860–871.
(202) Chapman, N.; Borodin, O.; Yoon, T.; Nguyen, C. C.; Lucht, B. L. Spectroscopic and Density Functional Theory Characterization of Common Lithium Salt Solvates in Carbonate Electrolytes for Lithium Batteries. *J. Phys. Chem. C* **2017**, *121* (4), 2135–2148.
(203) Ashassi-Sorkhabi, H.; Kazempour, A.; Salehi-Abar, P. On the First Coordination Shell of Lithium Ion in Linear Carbonate Solvents as Electrolyte Model for Lithium-Ion Batteries: A Computational Study. *Ionics* **2019**, *25* (8), 3705–3713.
(204) Kameda, Y.; Saito, S.; Umebayashi, Y.; Fujii, K.; Amo, Y.; Usuki, T. Local Structure of Li+ in Concentrated LiPF6–Dimethyl Carbonate Solutions. *J. Mol. Liq.* **2016**, *217*, 17–22.
(205) Feng, Z.; Higa, K.; Han, K. S.; Srinivasan, V. Evaluating Transport Properties and Ionic Dissociation of LiPF6 in Concentrated Electrolyte. *J. Electrochem. Soc.* **2017**, *164* (12), A2434.
(206) Wang, C.; Kakwan, I.; Appleby, A. J.; Little, F. E. In Situ Investigation of Electrochemical Lithium Intercalation into Graphite Powder. *J. Electroanal. Chem.* **2000**, *489* (1–2), 55–67.
(207) Wang, X.; Feng, Z.; Huang, J.; Deng, W.; Li, X.; Zhang, H.; Wen, Z. Graphene-Decorated Carbon-Coated LiFePO4 Nanospheres as a High-Performance Cathode Material for Lithium-Ion Batteries. *Carbon* **2018**, *127*, 149–157.
(208) Wang, J.; Gu, Y.-J.; Kong, W.-L.; Liu, H.-Q.; Chen, Y.-B.; Liu, W. Effect of Carbon Coating on the Crystal Orientation and Electrochemical Performance of Nanocrystalline LiFePO4. *Solid State Ion.* **2018**, *327*, 11–17.
(209) Zhang, S.; Ding, M. S.; Xu, K.; Allen, J.; Jow, T. R. Understanding Solid Electrolyte Interface Film Formation on Graphite Electrodes. *Electrochem. Solid-State Lett.* **2001**, *4* (12), A206.

(210) Xu, B.; Qian, D.; Wang, Z.; Meng, Y. S. Recent Progress in Cathode Materials Research for Advanced Lithium Ion Batteries. *Mater. Sci. Eng. R Rep.* **2012**, *73* (5–6), 51–65.
(211) Gao, T.; Han, Y.; Fraggedakis, D.; Das, S.; Zhou, T.; Yeh, C.-N.; Xu, S.; Chueh, W. C.; Li, J.; Bazant, M. Z. Interplay of Lithium Intercalation and Plating on a Single Graphite Particle. *Joule* **2021**.
(212) West, W. C.; Soler, J.; Smart, M. C.; Ratnakumar, B. V.; Firdosy, S.; Ravi, V.; Anderson, M. S.; Hrbacek, J.; Lee, E. S.; Manthiram, A. Electrochemical Behavior of Layered Solid Solution Li2MnO3− LiMO2 (M= Ni, Mn, Co) Li-Ion Cathodes with and without Alumina Coatings. *J. Electrochem. Soc.* **2011**, *158* (8), A883–A889.
(213) Munakata, H.; Takemura, B.; Saito, T.; Kanamura, K. Evaluation of Real Performance of LiFePO4 by Using Single Particle Technique. *J. Power Sources* **2012**, *217*, 444–448.
(214) Nocedal, J.; Wright, S. *Numerical Optimization*; Springer Science & Business Media, 2006.
(215) Griewank, A. On Automatic Differentiation. *Math. Program. Recent Dev. Appl.* **1989**, *6* (6), 83–107.
(216) Landesfeind, J.; Gasteiger, H. A. Temperature and Concentration Dependence of the Ionic Transport Properties of Lithium-Ion Battery Electrolytes. *J. Electrochem. Soc.* **2019**, *166* (14), A3079.
(217) Benkovic, S. J.; Hammes-Schiffer, S. A Perspective on Enzyme Catalysis. *Science* **2003**, *301* (5637), 1196–1202.
(218) Hammes-Schiffer, S.; Stuchebrukhov, A. A. Theory of Coupled Electron and Proton Transfer Reactions. *Chem. Rev.* **2010**, *110* (12), 6939–6960.
(219) Horvath, S.; Fernandez, L. E.; Soudackov, A. V.; Hammes-Schiffer, S. Insights into Proton-Coupled Electron Transfer Mechanisms of Electrocatalytic H2 Oxidation and Production. *Proc. Natl. Acad. Sci.* **2012**, *109* (39), 15663–15668.
(220) Mayer, J. M. Proton-Coupled Electron Transfer: A Reaction Chemist's View. *Annu. Rev. Phys. Chem.* **2004**, *55*, 363.
(221) Koper, M. T. Theory of Multiple Proton–Electron Transfer Reactions and Its Implications for Electrocatalysis. *Chem. Sci.* **2013**, *4* (7), 2710–2723.
(222) Morris, A. J.; Meyer, G. J.; Fujita, E. Molecular Approaches to the Photocatalytic Reduction of Carbon Dioxide for Solar Fuels. *Acc. Chem. Res.* **2009**, *42* (12), 1983–1994.
(223) Meyer, T. J.; Huynh, M. H. V.; Thorp, H. H. The Possible Role of Proton-coupled Electron Transfer (PCET) in Water Oxidation by Photosystem II. *Angew. Chem. Int. Ed.* **2007**, *46* (28), 5284–5304.
(224) Viswanathan, V.; Hansen, H. A.; Rossmeisl, J.; Nørskov, J. K. Unifying the 2e–and 4e–Reduction of Oxygen on Metal Surfaces. *J. Phys. Chem. Lett.* **2012**, *3* (20), 2948–2951.
(225) Ohta, N.; Nomura, K.; Yagi, I. Adsorption and Electroreduction of Oxygen on Gold in Acidic Media: In Situ Spectroscopic Identification of Adsorbed Molecular Oxygen and Hydrogen Superoxide. *J. Phys. Chem. C* **2012**, *116* (27), 14390–14400.
(226) Dong, J.-C.; Zhang, X.-G.; Briega-Martos, V.; Jin, X.; Yang, J.; Chen, S.; Yang, Z.-L.; Wu, D.-Y.; Feliu, J. M.; Williams, C. T. In Situ Raman Spectroscopic Evidence

for Oxygen Reduction Reaction Intermediates at Platinum Single-Crystal Surfaces. *Nat. Energy* **2019**, *4* (1), 60–67.
(227) Kulkarni, A.; Siahrostami, S.; Patel, A.; Nørskov, J. K. Understanding Catalytic Activity Trends in the Oxygen Reduction Reaction. *Chem. Rev.* **2018**, *118* (5), 2302–2312.
(228) Mavrikakis, M.; Hammer, B.; Nørskov, J. K. Effect of Strain on the Reactivity of Metal Surfaces. *Phys. Rev. Lett.* **1998**, *81* (13), 2819.
(229) Strasser, P.; Koh, S.; Anniyev, T.; Greeley, J.; More, K.; Yu, C.; Liu, Z.; Kaya, S.; Nordlund, D.; Ogasawara, H. Lattice-Strain Control of the Activity in Dealloyed Core–Shell Fuel Cell Catalysts. *Nat. Chem.* **2010**, *2* (6), 454–460.
(230) Kitchin, J. R.; Nørskov, J. K.; Barteau, M. A.; Chen, J. G. Modification of the Surface Electronic and Chemical Properties of Pt (111) by Subsurface 3d Transition Metals. *J. Chem. Phys.* **2004**, *120* (21), 10240–10246.
(231) Bligaard, T.; Nørskov, J. K. Ligand Effects in Heterogeneous Catalysis and Electrochemistry. *Electrochimica Acta* **2007**, *52* (18), 5512–5516.
(232) Li, D.; Wang, C.; Strmcnik, D. S.; Tripkovic, D. V.; Sun, X.; Kang, Y.; Chi, M.; Snyder, J. D.; van der Vliet, D.; Tsai, Y. Functional Links between Pt Single Crystal Morphology and Nanoparticles with Different Size and Shape: The Oxygen Reduction Reaction Case. *Energy Environ. Sci.* **2014**, *7* (12), 4061–4069.
(233) Calle-Vallejo, F.; Tymoczko, J.; Colic, V.; Vu, Q. H.; Pohl, M. D.; Morgenstern, K.; Loffreda, D.; Sautet, P.; Schuhmann, W.; Bandarenka, A. S. Finding Optimal Surface Sites on Heterogeneous Catalysts by Counting Nearest Neighbors. *Science* **2015**, *350* (6257), 185–189.
(234) Tian, N.; Zhou, Z.-Y.; Sun, S.-G.; Ding, Y.; Wang, Z. L. Synthesis of Tetrahexahedral Platinum Nanocrystals with High-Index Facets and High Electro-Oxidation Activity. *science* **2007**, *316* (5825), 732–735.
(235) Stamenkovic, V. R.; Fowler, B.; Mun, B. S.; Wang, G.; Ross, P. N.; Lucas, C. A.; Markovic, N. M. Improved Oxygen Reduction Activity on Pt3Ni (111) via Increased Surface Site Availability. *science* **2007**, *315* (5811), 493–497.
(236) Strmcnik, D.; Escudero-Escribano, M.; Kodama, K.; Stamenkovic, V. R.; Cuesta, A.; Marković, N. M. Enhanced Electrocatalysis of the Oxygen Reduction Reaction Based on Patterning of Platinum Surfaces with Cyanide. *Nat. Chem.* **2010**, *2* (10), 880–885.
(237) Snyder, J.; Fujita, T.; Chen, M. W.; Erlebacher, J. Oxygen Reduction in Nanoporous Metal–Ionic Liquid Composite Electrocatalysts. *Nat. Mater.* **2010**, *9* (11), 904–907.
(238) Blizanac, B. B.; Ross, P. N.; Markovic, N. M. Oxygen Electroreduction on Ag (1 1 1): The PH Effect. *Electrochimica Acta* **2007**, *52* (6), 2264–2271.
(239) Strmcnik, D.; Van Der Vliet, D. F.; Chang, K.-C.; Komanicky, V.; Kodama, K.; You, H.; Stamenkovic, V. R.; Markovic, N. M. Effects of Li+, K+, and Ba2+ Cations on the ORR at Model and High Surface Area Pt and Au Surfaces in Alkaline Solutions. *J. Phys. Chem. Lett.* **2011**, *2* (21), 2733–2736.
(240) Zheng, J.; Sheng, W.; Zhuang, Z.; Xu, B.; Yan, Y. Universal Dependence of Hydrogen Oxidation and Evolution Reaction Activity of Platinum-Group Metals on PH and Hydrogen Binding Energy. *Sci. Adv.* **2016**, *2* (3), e1501602.

(241) Sheng, W.; Zhuang, Z.; Gao, M.; Zheng, J.; Chen, J. G.; Yan, Y. Correlating Hydrogen Oxidation and Evolution Activity on Platinum at Different PH with Measured Hydrogen Binding Energy. *Nat. Commun.* **2015**, *6* (1), 1–6.
(242) Ledezma-Yanez, I.; Wallace, W. D. Z.; Sebastián-Pascual, P.; Climent, V.; Feliu, J. M.; Koper, M. Interfacial Water Reorganization as a PH-Dependent Descriptor of the Hydrogen Evolution Rate on Platinum Electrodes. *Nat. Energy* **2017**, *2* (4), 1–7.
(243) Li, M. F.; Liao, L. W.; Yuan, D. F.; Mei, D.; Chen, Y.-X. PH Effect on Oxygen Reduction Reaction at Pt (1 1 1) Electrode. *Electrochimica Acta* **2013**, *110*, 780–789.
(244) Zhang, G.-R.; Munoz, M.; Etzold, B. J. Accelerating Oxygen-Reduction Catalysts through Preventing Poisoning with Non-Reactive Species by Using Hydrophobic Ionic Liquids. *Angew. Chem. Int. Ed.* **2016**, *55* (6), 2257–2261.
(245) Miran, M. S.; Yasuda, T.; Susan, M. A. B. H.; Dokko, K.; Watanabe, M. Electrochemical Properties of Protic Ionic Liquids: Correlation between Open Circuit Potential for H 2/O 2 Cells under Non-Humidified Conditions and Δp K a. *RSC Adv.* **2013**, *3* (13), 4141–4144.
(246) Higgins, E. M.; Sherwood, J. A.; Lindsay, A. G.; Armstrong, J.; Massey, R. S.; Alder, R. W.; O'Donoghue, A. C. P K as of the Conjugate Acids of N-Heterocyclic Carbenes in Water. *Chem. Commun.* **2011**, *47* (5), 1559–1561.
(247) Kaupmees, K.; Trummal, A.; Leito, I. Basicities of Strong Bases in Water: A Computational Study. *Croat. Chem. Acta* **2014**, *87* (4), 385–395.
(248) Otake, Y.; Nakamura, H.; Fuse, S. Rapid and Mild Synthesis of Amino Acid N-Carboxy Anhydrides: Basic-to-Acidic Flash Switching in a Microflow Reactor. *Angew. Chem. Int. Ed.* **2018**, *57* (35), 11389–11393.
(249) Spialter, L.; Moshier, R. W. Amines. IV. The Base Strengths of Tetramethylated 1, 2-Ethanediamines1. *J. Am. Chem. Soc.* **1957**, *79* (22), 5955–5957.
(250) Tehan, B. G.; Lloyd, E. J.; Wong, M. G.; Pitt, W. R.; Gancia, E.; Manallack, D. T. Estimation of PKa Using Semiempirical Molecular Orbital Methods. Part 2: Application to Amines, Anilines and Various Nitrogen Containing Heterocyclic Compounds. *Quant. Struct. Relatsh.* **2002**, *21* (5), 473–485.
(251) Blizanac, B. B.; Lucas, C. A.; Gallagher, M. E.; Arenz, M.; Ross, P. N.; Marković, N. M. Anion Adsorption, CO Oxidation, and Oxygen Reduction Reaction on a Au (100) Surface: The PH Effect. *J. Phys. Chem. B* **2004**, *108* (2), 625–634.
(252) Wang, J. X.; Markovic, a N.; Adzic, R. R. Kinetic Analysis of Oxygen Reduction on Pt (111) in Acid Solutions: Intrinsic Kinetic Parameters and Anion Adsorption Effects. *J. Phys. Chem. B* **2004**, *108* (13), 4127–4133.
(253) Shinozaki, K.; Zack, J. W.; Richards, R. M.; Pivovar, B. S.; Kocha, S. S. Oxygen Reduction Reaction Measurements on Platinum Electrocatalysts Utilizing Rotating Disk Electrode Technique: I. Impact of Impurities, Measurement Protocols and Applied Corrections. *J. Electrochem. Soc.* **2015**, *162* (10), F1144.
(254) Garsany, Y.; Baturina, O. A.; Swider-Lyons, K. E.; Kocha, S. S. *Experimental Methods for Quantifying the Activity of Platinum Electrocatalysts for the Oxygen Reduction Reaction*; ACS Publications, 2010.
(255) Mayrhofer, K. J. J.; Strmcnik, D.; Blizanac, B. B.; Stamenkovic, V.; Arenz, M.; Markovic, N. M. Measurement of Oxygen Reduction Activities via the Rotating

Disc Electrode Method: From Pt Model Surfaces to Carbon-Supported High Surface Area Catalysts. *Electrochimica Acta* **2008**, *53* (7), 3181–3188.
(256) Sheng, W.; Chen, S.; Vescovo, E.; Shao-Horn, Y. Size Influence on the Oxygen Reduction Reaction Activity and Instability of Supported Pt Nanoparticles. *J. Electrochem. Soc.* **2011**, *159* (2), B96.
(257) Warren, J. J.; Tronic, T. A.; Mayer, J. M. Thermochemistry of Proton-Coupled Electron Transfer Reagents and Its Implications. *Chem. Rev.* **2010**, *110* (12), 6961–7001.
(258) Ford, D. C.; Nilekar, A. U.; Xu, Y.; Mavrikakis, M. Partial and Complete Reduction of O2 by Hydrogen on Transition Metal Surfaces. *Surf. Sci.* **2010**, *604* (19–20), 1565–1575.
(259) Chevalet, J.; Rouelle, F.; Gierst, L.; Lambert, J.-P. Electrogeneration and Some Properties of the Superoxide Ion in Aqueous Solutions. *J. Electroanal. Chem. Interfacial Electrochem.* **1972**, *39* (1), 201–216.
(260) Costentin, C.; Evans, D. H.; Robert, M.; Savéant, J.-M.; Singh, P. S. Electrochemical Approach to Concerted Proton and Electron Transfers. Reduction of the Water− Superoxide Ion Complex. *J. Am. Chem. Soc.* **2005**, *127* (36), 12490–12491.
(261) Li, X.; Gewirth, A. A. Oxygen Electroreduction through a Superoxide Intermediate on Bi-Modified Au Surfaces. *J. Am. Chem. Soc.* **2005**, *127* (14), 5252–5260.
(262) Casalongue, H. S.; Kaya, S.; Viswanathan, V.; Miller, D. J.; Friebel, D.; Hansen, H. A.; Nørskov, J. K.; Nilsson, A.; Ogasawara, H. Direct Observation of the Oxygenated Species during Oxygen Reduction on a Platinum Fuel Cell Cathode. *Nat. Commun.* **2013**, *4* (1), 1–6.
(263) Edwards, S. J.; Soudackov, A. V.; Hammes-Schiffer, S. Driving Force Dependence of Rates for Nonadiabatic Proton and Proton-Coupled Electron Transfer: Conditions for Inverted Region Behavior. *J. Phys. Chem. B* **2009**, *113* (44), 14545–14548.
(264) Brzezinski, B.; Zundel, G. Formation of Hydrogen-Bonded Chains between Strong N-Base and N H Acids—a FTIR Study. *J. Mol. Struct.* **1998**, *446* (3), 199–207.
(265) Moschovi, A. M.; Ntais, S.; Dracopoulos, V.; Nikolakis, V. Vibrational Spectroscopic Study of the Protic Ionic Liquid 1-H-3-Methylimidazolium Bis (Trifluoromethanesulfonyl) Imide. *Vib. Spectrosc.* **2012**, *63*, 350–359.
(266) Bégué, D.; Qiao, G. G.; Wentrup, C. Nitrile Imines: Matrix Isolation, IR Spectra, Structures, and Rearrangement to Carbodiimides. *J. Am. Chem. Soc.* **2012**, *134* (11), 5339–5350.
(267) Nakamoto, K.; Margoshes, M.; Rundle, R. E. Stretching Frequencies as a Function of Distances in Hydrogen Bonds. *J. Am. Chem. Soc.* **1955**, *77* (24), 6480–6486.
(268) Steiner, T. The Hydrogen Bond in the Solid State. *Angew. Chem. Int. Ed.* **2002**, *41* (1), 48–76.
(269) Gilli, P.; Pretto, L.; Bertolasi, V.; Gilli, G. Predicting Hydrogen-Bond Strengths from Acid− Base Molecular Properties. The p K a Slide Rule: Toward the Solution of a Long-Lasting Problem. *Acc. Chem. Res.* **2009**, *42* (1), 33–44.
(270) Jusys, Z.; Schnaidt, J.; Behm, R. J. O2 Reduction on a Au Film Electrode in an Ionic Liquid in the Absence and Presence of Mg2+ Ions: Product Formation and Adlayer Dynamics. *J. Chem. Phys.* **2019**, *150* (4), 041724.
(271) Cheng, H.-W.; Stock, P.; Moeremans, B.; Baimpos, T.; Banquy, X.; Renner, F. U.; Valtiner, M. Characterizing the Influence of Water on Charging and Layering at

Electrified Ionic-liquid/Solid Interfaces. *Adv. Mater. Interfaces* **2015**, *2* (12), 1500159.
(272) Miki, A.; Ye, S.; Osawa, M. Surface-Enhanced IR Absorption on Platinum Nanoparticles: An Application to Real-Time Monitoring of Electrocatalytic Reactions. *Chem. Commun.* **2002**, No. 14, 1500–1501.
(273) Miyake, H.; Ye, S.; Osawa, M. Electroless Deposition of Gold Thin Films on Silicon for Surface-Enhanced Infrared Spectroelectrochemistry. *Electrochem. Commun.* **2002**, *4* (12), 973–977.
(274) Wang, T.; Zhang, Y.; Huang, B.; Cai, B.; Rao, R. R.; Giordano, L.; Sun, S.-G.; Shao-Horn, Y. Enhancing Oxygen Reduction Electrocatalysis by Tuning Interfacial Hydrogen Bonds. *Nat. Catal.* **2021**, *4* (9), 753–762.
(275) Frisch, M. J.; Trucks, G. W.; Schlegel, H. B.; Scuseria, G. E.; Robb, M. A.; Cheeseman, J. R.; Scalmani, G.; Barone, V.; Mennucci, B.; Petersson, G. A. Gaussian 09, Revision A. 02; Gaussian, Inc: Wallingford, CT, 2009. *There No Corresp. Rec. This Ref.* **2015**.
(276) Laury, M. L.; Carlson, M. J.; Wilson, A. K. Vibrational Frequency Scale Factors for Density Functional Theory and the Polarization Consistent Basis Sets. *J. Comput. Chem.* **2012**, *33* (30), 2380–2387.
(277) Suntivich, J.; May, K. J.; Gasteiger, H. A.; Goodenough, J. B.; Shao-Horn, Y. A Perovskite Oxide Optimized for Oxygen Evolution Catalysis from Molecular Orbital Principles. *Science* **2011**, *334* (6061), 1383–1385.
(278) Skúlason, E.; Tripkovic, V.; Björketun, M. E.; Gudmundsdóttir, S.; Karlberg, G.; Rossmeisl, J.; Bligaard, T.; Jónsson, H.; Nørskov, J. K. Modeling the Electrochemical Hydrogen Oxidation and Evolution Reactions on the Basis of Density Functional Theory Calculations. *J. Phys. Chem. C* **2010**, *114* (42), 18182–18197.
(279) McCrum, I. T.; Koper, M. The Role of Adsorbed Hydroxide in Hydrogen Evolution Reaction Kinetics on Modified Platinum. *Nat. Energy* **2020**, *5* (11), 891–899.
(280) Dubouis, N.; Serva, A.; Salager, E.; Deschamps, M.; Salanne, M.; Grimaud, A. The Fate of Water at the Electrochemical Interfaces: Electrochemical Behavior of Free Water versus Coordinating Water. *J. Phys. Chem. Lett.* **2018**, *9* (23), 6683–6688.
(281) Ataka, K.; Yotsuyanagi, T.; Osawa, M. Potential-Dependent Reorientation of Water Molecules at an Electrode/Electrolyte Interface Studied by Surface-Enhanced Infrared Absorption Spectroscopy. *J. Phys. Chem.* **1996**, *100* (25), 10664–10672.
(282) Yamakata, A.; Osawa, M. Destruction of the Water Layer on a Hydrophobic Surface Induced by the Forced Approach of Hydrophilic and Hydrophobic Cations. *J. Phys. Chem. Lett.* **2010**, *1* (9), 1487–1491.
(283) van de Voort, F. R.; Sedman, J.; Cocciardi, R.; Juneau, S. An Automated FTIR Method for the Routine Quantitative Determination of Moisture in Lubricants: An Alternative to Karl Fischer Titration. *Talanta* **2007**, *72* (1), 289–295.
(284) Harris, R. K.; Becker, E. D.; De Menezes, S. M. C.; Granger, P.; Hoffman, R. E.; Zilm, K. W. Further Conventions for NMR Shielding and Chemical Shifts (IUPAC Recommendations 2008). *Pure Appl. Chem.* **2008**, *80* (1), 59–84.
(285) Tułodziecki, M.; Leverick, G. M.; Amanchukwu, C. V.; Katayama, Y.; Kwabi, D. G.; Barde, F.; Hammond, P. T.; Shao-Horn, Y. The Role of Iodide in the Formation

of Lithium Hydroxide in Lithium–Oxygen Batteries. *Energy Environ. Sci.* **2017**, *10* (8), 1828–1842.
(286) Sheng, W.; Gasteiger, H. A.; Shao-Horn, Y. Hydrogen Oxidation and Evolution Reaction Kinetics on Platinum: Acid vs Alkaline Electrolytes. *J. Electrochem. Soc.* **2010**, *157* (11), B1529–B1536. https://doi.org/10.1149/1.3483106.
(287) Bard, A. J.; Faulkner, L. R. *ELECTROCHEMICAL METHODS Fundamentals and Applications*, 2nd ed.; John Wiley & Sons, INC: New York.
(288) Symons, E. A. Hydrogen Gas Solubility in the Dimethyl Sulfoxide–Water System: A Further Clue to Solvent Structure in These Media. *Can. J. Chem.* **1971**, *49* (24), 3940–3947.
(289) Purwanto, P.; Deshpande, R. M.; Chaudhari, R. V.; Delmas, H. Solubility of Hydrogen, Carbon Monoxide, and 1-Octene in Various Solvents and Solvent Mixtures. *J. Chem. Eng. Data* **1996**, *41* (6), 1414–1417.
(290) Brunner, E. Solubility of Hydrogen in 10 Organic Solvents at 298.15, 323.15, and 373.15 K. *J. Chem. Eng. Data* **1985**, *30* (3), 269–273.
(291) Szklarczyk, M.; Sobkowski, J. The Behaviour of High Polar Organic Solvents at Platinum Electrode—II. Adsorption and Electrode Reactions of Acetonitrile. *Electrochimica Acta* **1980**, *25* (12), 1597–1601.
(292) Barrette, W. C.; Sawyer, D. T. Determination of Dissolved Hydrogen and Effects of Media and Electrode Materials on the Electrochemical Oxidation of Molecular Hydrogen. *Anal. Chem.* **1984**, *56* (4), 653–657.
(293) Rudnev, A. V.; Molodkina, E. B.; Danilov, A. I.; Polukarov, Y. M.; Berna, A.; Feliu, J. M. Adsorption Behavior of Acetonitrile on Platinum and Gold Electrodes of Various Structures in Solution of 0.5 M H2SO4. *Electrochimica Acta* **2009**, *54* (14), 3692–3699.
(294) Pfrommer, B. G.; Mauri, F.; Louie, S. G. NMR Chemical Shifts of Ice and Liquid Water: The Effects of Condensation. *J. Am. Chem. Soc.* **2000**, *122* (1), 123–129.
(295) Marshall, W. L.; Franck, E. U. Ion Product of Water Substance, 0–1000 C, 1–10,000 Bars New International Formulation and Its Background. *J. Phys. Chem. Ref. Data* **1981**, *10* (2), 295–304.
(296) Bandura, A. V.; Lvov, S. N. The Ionization Constant of Water over Wide Ranges of Temperature and Density. *J. Phys. Chem. Ref. Data* **2006**, *35* (1), 15–30.
(297) Rosen, B. A.; Salehi-Khojin, A.; Thorson, M. R.; Zhu, W.; Whipple, D. T.; Kenis, P. J.; Masel, R. I. Ionic Liquid–Mediated Selective Conversion of CO2 to CO at Low Overpotentials. *Science* **2011**, *334* (6056), 643–644.
(298) Pavlishchuk, V. V.; Addison, A. W. Conversion Constants for Redox Potentials Measured versus Different Reference Electrodes in Acetonitrile Solutions at 25 C. *Inorganica Chim. Acta* **2000**, *298* (1), 97–102.
(299) Aurbach, D.; Zinigrad, E.; Teller, H.; Dan, P. Factors Which Limit the Cycle Life of Rechargeable Lithium (Metal) Batteries. *J. Electrochem. Soc.* **2000**, *147* (4), 1274.
(300) Vetter, J.; Novák, P.; Wagner, M. R.; Veit, C.; Möller, K.-C.; Besenhard, J. O.; Winter, M.; Wohlfahrt-Mehrens, M.; Vogler, C.; Hammouche, A. Ageing Mechanisms in Lithium-Ion Batteries. *J. Power Sources* **2005**, *147* (1–2), 269–281.
(301) Suo, L.; Xue, W.; Gobet, M.; Greenbaum, S. G.; Wang, C.; Chen, Y.; Yang, W.; Li, Y.; Li, J. Fluorine-Donating Electrolytes Enable Highly Reversible 5-V-Class Li Metal Batteries. *Proc. Natl. Acad. Sci.* **2018**, *115* (6), 1156–1161.

(302) Yang, Y.; Davies, D. M.; Yin, Y.; Borodin, O.; Lee, J. Z.; Fang, C.; Olguin, M.; Zhang, Y.; Sablina, E. S.; Wang, X. High-Efficiency Lithium-Metal Anode Enabled by Liquefied Gas Electrolytes. *Joule* **2019**, *3* (8), 1986–2000.
(303) Hobold, G. M.; Lopez, J.; Guo, R.; Minafra, N.; Banerjee, A.; Shirley Meng, Y.; Shao-Horn, Y.; Gallant, B. M. Moving beyond 99.9% Coulombic Efficiency for Lithium Anodes in Liquid Electrolytes. *Nat. Energy* **2021**, *6* (10), 951–960.
(304) Katayama, Y.; Nattino, F.; Giordano, L.; Hwang, J.; Rao, R. R.; Andreussi, O.; Marzari, N.; Shao-Horn, Y. An in Situ Surface-Enhanced Infrared Absorption Spectroscopy Study of Electrochemical CO2 Reduction: Selectivity Dependence on Surface C-Bound and O-Bound Reaction Intermediates. *J. Phys. Chem. C* **2018**, *123* (10), 5951–5963.
(305) Andersen, S. Z.; Čolić, V.; Yang, S.; Schwalbe, J. A.; Nielander, A. C.; McEnaney, J. M.; Enemark-Rasmussen, K.; Baker, J. G.; Singh, A. R.; Rohr, B. A. A Rigorous Electrochemical Ammonia Synthesis Protocol with Quantitative Isotope Measurements. *Nature* **2019**, *570* (7762), 504–508.
(306) Tsuneto, A.; Kudo, A.; Sakata, T. Lithium-Mediated Electrochemical Reduction of High Pressure N2 to NH3. *J. Electroanal. Chem.* **1994**, *367* (1–2), 183–188.
(307) Zhou, L.; Minafra, N.; Zeier, W. G.; Nazar, L. F. Innovative Approaches to Li-Argyrodite Solid Electrolytes for All-Solid-State Lithium Batteries. *Acc. Chem. Res.* **2021**, *54* (12), 2717–2728.
(308) Manthiram, A.; Yu, X.; Wang, S. Lithium Battery Chemistries Enabled by Solid-State Electrolytes. *Nat. Rev. Mater.* **2017**, *2* (4), 1–16.
(309) Richards, W. D.; Miara, L. J.; Wang, Y.; Kim, J. C.; Ceder, G. Interface Stability in Solid-State Batteries. *Chem. Mater.* **2016**, *28* (1), 266–273.
(310) Yoshinari, T.; Koerver, R.; Hofmann, P.; Uchimoto, Y.; Zeier, W. G.; Janek, J. Interfacial Stability of Phosphate-NASICON Solid Electrolytes in Ni-Rich NCM Cathode-Based Solid-State Batteries. *ACS Appl. Mater. Interfaces* **2019**, *11* (26), 23244–23253.
(311) Hammes-Schiffer, S.; Soudackov, A. V. Proton-Coupled Electron Transfer in Solution, Proteins, and Electrochemistry. *J. Phys. Chem. B* **2008**, *112* (45), 14108–14123.
(312) Ender, M.; Illig, J.; Ivers-Tiffée, E. Three-Electrode Setups for Lithium-Ion Batteries I. Fem-Simulation of Different Reference Electrode Designs and Their Implications for Half-Cell Impedance Spectra. *J. Electrochem. Soc.* **2017**, *164* (2), A71–A79.
(313) Costard, J.; Ender, M.; Weiss, M.; Ivers-Tiffée, E. Three-Electrode Setups for Lithium-Ion Batteries II. Experimental Study of Different Reference Electrode Designs and Their Implications for Half-Cell Impedance Spectra. *J. Electrochem. Soc.* **2017**, *164* (2), A80–A87.
(314) Osaka, T.; Mukoyama, D.; Nara, H. Development of Diagnostic Process for Commercially Available Batteries, Especially Lithium Ion Battery, by Electrochemical Impedance Spectroscopy. *J. Electrochem. Soc.* **2015**, *162* (14), A2529–A2537.
(315) Hoshi, Y.; Narita, Y.; Honda, K.; Ohtaki, T.; Shitanda, I.; Itagaki, M. Optimization of Reference Electrode Position in a Three-Electrode Cell for Impedance

Measurements in Lithium-Ion Rechargeable Battery by Finite Element Method. *J. Power Sources* **2015**, *288*, 168–175.
(316) Fedorov, M. V.; Kornyshev, A. A. Ionic Liquids at Electrified Interfaces. *Chem. Rev.* **2014**, *114* (5), 2978–3036.
(317) Allen, J. B.; Larry, R. F. *Electrochemical Methods Fundamentals and Applications*; John Wiley & Sons, 2001.
(318) Fraggedakis, D.; Bazant, M. Z. Tuning the Stability of Electrochemical Interfaces by Electron Transfer Reactions. *J. Chem. Phys.* **2020**, *152* (18), 184703.
(319) Neath, A. A.; Cavanaugh, J. E. The Bayesian Information Criterion: Background, Derivation, and Applications. *Wiley Interdiscip. Rev. Comput. Stat.* **2012**, *4* (2), 199–203.
(320) Brown, S. M.; Orella, M.; Hsiao, Y. W.; Román-Leshkov, Y.; Surendranath, Y.; Bazant, M. Z.; Brushett, F. Electron Transfer Limitation in Carbon Dioxide Reduction Revealed by Data-Driven Tafel Analysis. **2020**.
(321) Andriyevsky, B.; Doll, K.; Jacob, T. Electronic and Transport Properties of LiCoO 2. *Phys. Chem. Chem. Phys.* **2014**, *16* (42), 23412–23420.
(322) Swiderska-Mocek, A.; Lewandowski, A. Kinetics of Li-Ion Transfer Reaction at LiMn 2 O 4, LiCoO 2, and LiFePO 4 Cathodes. *J. Solid State Electrochem.* **2017**, *21* (5), 1365–1372.
(323) Heubner, C.; Schneider, M.; Michaelis, A. SoC Dependent Kinetic Parameters of Insertion Electrodes from Staircase—GITT. *J. Electroanal. Chem.* **2016**, *767*, 18–23.
(324) Garcia, B.; Farcy, J.; Pereira-Ramos, J. P.; Baffier, N. Electrochemical Properties of Low Temperature Crystallized LiCoO2. *J. Electrochem. Soc.* **1997**, *144* (4), 1179.
(325) Nishikawa, K.; Zettsu, N.; Teshima, K.; Kanamura, K. Intrinsic Electrochemical Characteristics in the Individual Needle-like LiCoO2 Crystals Synthesized by Flux Growth. *Electrochemistry* **2017**, *85* (2), 72–76.
(326) Greenleaf, M.; Li, H.; Zheng, J. P. Application of Physical Electric Circuit Modeling to Characterize Li-Ion Battery Electrochemical Processes. *J. Power Sources* **2014**, *270*, 113–120.
(327) Wen, B.; Deng, Z.; Tsai, P.-C.; Lebens-Higgins, Z. W.; Piper, L. F.; Ong, S. P.; Chiang, Y.-M. Ultrafast Ion Transport at a Cathode–Electrolyte Interface and Its Strong Dependence on Salt Solvation. *Nat. Energy* **2020**, *5* (8), 578–586.
(328) Csomós, B.; Fodor, D.; Vajda, I. Estimation of Battery Separator Area, Cell Thickness and Diffusion Coefficient Based on Non-Ideal Liquid-Phase Diffusion Modeling. *Energies* **2020**, *13* (23), 6238.
(329) Zhang, Q.; White, R. E. Moving Boundary Model for the Discharge of a LiCoO2 Electrode. *J. Electrochem. Soc.* **2007**, *154* (6), A587.
(330) Renganathan, S.; Sikha, G.; Santhanagopalan, S.; White, R. E. Theoretical Analysis of Stresses in a Lithium Ion Cell. *J. Electrochem. Soc.* **2009**, *157* (2), A155.
(331) Kumaresan, K.; Sikha, G.; White, R. E. Thermal Model for a Li-Ion Cell. *J. Electrochem. Soc.* **2007**, *155* (2), A164.
(332) Sikha, G.; White, R. E.; Popov, B. N. A Mathematical Model for a Lithium-Ion Battery/Electrochemical Capacitor Hybrid System. *J. Electrochem. Soc.* **2005**, *152* (8), A1682.

(333) Zhang, Q.; Guo, Q.; White, R. E. Semi-Empirical Modeling of Charge and Discharge Profiles for a LiCoO2 Electrode. *J. Power Sources* **2007**, *165* (1), 427–435.
(334) Yan, B.; Lim, C.; Yin, L.; Zhu, L. Three Dimensional Simulation of Galvanostatic Discharge of LiCoO2 Cathode Based on X-Ray Nano-CT Images. *J. Electrochem. Soc.* **2012**, *159* (10), A1604.
(335) Varini, M.; Ko, J. Y.; Svens, P.; Mattinen, U.; Klett, M.; Ekström, H.; Lindbergh, G. On Resistance and Capacity of LiNi1/3Mn1/3Co1/3O2 under High Voltage Operation. *J. Energy Storage* **2020**, *31*, 101616.
(336) Ko, J. Y.; Varini, M.; Klett, M.; Ekström, H.; Lindbergh, G. Porous Electrode Model with Particle Stress Effects for Li (Ni1/3Co1/3Mn1/3) O2 Electrode. *J. Electrochem. Soc.* **2019**, *166* (13), A2939.
(337) Xu, M.; Reichman, B.; Wang, X. Modeling the Effect of Electrode Thickness on the Performance of Lithium-Ion Batteries with Experimental Validation. *Energy* **2019**, *186*, 115864.
(338) El-Bana, M. S.; El Radaf, I. M.; Fouad, S. S.; Sakr, G. B. Structural and Optoelectrical Properties of Nanostructured LiNiO2 Thin Films Grown by Spray Pyrolysis Technique. *J. Alloys Compd.* **2017**, *705*, 333–339.
(339) Petousis, I.; Mrdjenovich, D.; Ballouz, E.; Liu, M.; Winston, D.; Chen, W.; Graf, T.; Schladt, T. D.; Persson, K. A.; Prinz, F. B. High-Throughput Screening of Inorganic Compounds for the Discovery of Novel Dielectric and Optical Materials. *Sci. Data* **2017**, *4* (1), 1–12.
(340) Islam, M. S.; Driscoll, D. J.; Fisher, C. A.; Slater, P. R. Atomic-Scale Investigation of Defects, Dopants, and Lithium Transport in the LiFePO4 Olivine-Type Battery Material. *Chem. Mater.* **2005**, *17* (20), 5085–5092.
(341) Johnson, L. G.; Dresselhaus, G. Optical Properies of Graphite. *Phys. Rev. B* **1973**, *7* (6), 2275.
(342) Fraggedakis, D.; Nadkarni, N.; Gao, T.; Zhou, T.; Zhang, Y.; Han, Y.; Stephens, R. M.; Shao-Horn, Y.; Bazant, M. Z. A Scaling Law to Determine Phase Morphologies during Ion Intercalation. *Energy Environ. Sci.* **2020**, *13* (7), 2142–2152.
(343) Bai, P.; Cogswell, D. A.; Bazant, M. Z. Suppression of Phase Separation in LiFePO4 Nanoparticles during Battery Discharge. *Nano Lett.* **2011**, *11* (11), 4890–4896.
(344) Hess, M.; Sasaki, T.; Villevieille, C.; Novák, P. Combined Operando X-Ray Diffraction–Electrochemical Impedance Spectroscopy Detecting Solid Solution Reactions of LiFePO4 in Batteries. *Nat. Commun.* **2015**, *6* (1), 1–9.
(345) Dreyer, W.; Jamnik, J.; Guhlke, C.; Huth, R.; Moškon, J.; Gaberšček, M. The Thermodynamic Origin of Hysteresis in Insertion Batteries. *Nat. Mater.* **2010**, *9* (5), 448–453.
(346) Peng, S.; Lee, Y.; Wang, C.; Yin, H.; Dai, S.; Sun, S. A Facile Synthesis of Monodisperse Au Nanoparticles and Their Catalysis of CO Oxidation. *Nano Res.* **2008**, *1* (3), 229–234.
(347) Huddleston, J. G.; Visser, A. E.; Reichert, W. M.; Willauer, H. D.; Broker, G. A.; Rogers, R. D. Characterization and Comparison of Hydrophilic and Hydrophobic Room Temperature Ionic Liquids Incorporating the Imidazolium Cation. *Green Chem.* **2001**, *3* (4), 156–164.

(348) Wakisaka, M.; Suzuki, H.; Mitsui, S.; Uchida, H.; Watanabe, M. Increased Oxygen Coverage at Pt− Fe Alloy Cathode for the Enhanced Oxygen Reduction Reaction Studied by EC− XPS. *J. Phys. Chem. C* **2008**, *112* (7), 2750–2755.
(349) Weingaertner, H. The Static Dielectric Permittivity of Ionic Liquids. *J. Mol. Liq.* **2014**, *192*, 185–190.
(350) Wakai, C.; Oleinikova, A.; Ott, M.; Weingärtner, H. How Polar Are Ionic Liquids? Determination of the Static Dielectric Constant of an Imidazolium-Based Ionic Liquid by Microwave Dielectric Spectroscopy. *J. Phys. Chem. B* **2005**, *109* (36), 17028–17030.
(351) Uematsu, M.; Frank, E. U. Static Dielectric Constant of Water and Steam. *J. Phys. Chem. Ref. Data* **1980**, *9* (4), 1291–1306.
(352) Bolton, J. R.; Archer, M. D. Basic Electron-Transfer Theory. In *Electron Transfer in Inorganic, Organic, and Biological Systems*; Advances in Chemistry; American Chemical Society, 1991; Vol. 228, pp 7–23. https://doi.org/10.1021/ba-1991-0228.ch002.
(353) Newton, M. D.; Sutin, N. Electron Transfer Reactions in Condensed Phases. *Annu. Rev. Phys. Chem.* **1984**, *35* (1), 437–480. https://doi.org/10.1146/annurev.pc.35.100184.002253.

Appendix A: Supplementary Data for Chapter 2

Methods

Electrode preparation

The composite electrode for *in situ* FT-IR was composed of NMC (85 wt%, from Ecopro and Umicore) as the active material, carbon black (5 wt % KS6 and 2 wt% Super P, both from Timcal) as an electrically conductive carbon, and poly(vinylidene fluoride) (8 wt%, PVDF, Kynar) as the binder. These materials were mixed thoroughly with N-methylpyrrolidone (NMP, Aldrich) in a 1:15 mass ratio, using a planetary centrifugal mixer (THINKY AR-100). The obtained slurry was drop-casted onto glassy fiber substrates (Whatman 934-AH, 10 mm in diameter) and dried at 100 ^{o}C. Then the composite composites were compressed at 0.5 T/cm^2 using a hydraulic press to improve electrical conductivity. Finally the electrodes were completely dried at 120 ^{o}C under vacuum for 24h. The active material loading was ~6.5 mg/cm^2, but it is noted here that the effective loading is smaller because some particles could permeate into the glassy fiber and not all of the loading is on the top surface.

The positive electrode for EIS experiments was composed of 85 wt% of NMC, carbon black (5 wt % KS6 and 2 wt% Super P, both from Timcal), and poly(vinylidene fluoride) (8 wt%, PVDF, Kynar. The mesh reference electrode was also composed of 80 wt% of $Li_4Ti_5O_{12}$ (Itasco, >99.5 %), 10 wt% of acetylene black (C-55, Chevron) and 10 wt% of PVDF. These materials were mixed together and thoroughly agitated in NMP. The obtained slurry was applied with a blade applicator onto aluminum foil (for NMC, 16 μm thickness) or 316 stainless-steel mesh (for $Li_4Ti_5O_{12}$, 325x325 mesh, opening size 0.0017”),

and resulting sheet/mesh were dried at 70 ^{o}C. Next, each electrode was punched with a 1/2 inch diameter (1.27 cmϕ) for NMC and 18 mm diameter for $Li_4Ti_5O_{12}$ mesh reference. The NMC composite were compressed at 6.3 T/cm^2 using a hydraulic press. All of the electrodes were further dried in vacuum at 120 ^{o}C prior to cell assembling. The active material loading was ~2.7 mg/cm^2 for NMC and ~1 mg/cm^2 for $Li_4Ti_5O_{12}$ respectively. Particle size of NMC111, NMC622 and NMC811 was examined with a scanning electron microscope (JEOL 5910, with secondary electron detector at accelerating voltage of 15 kV) and shown in Figure S23 (d = 5~10 μm).

In this study, the electrolytes include 1 M $LiPF_6$ in a 3:7 wt:wt ethylene carbonate (EC): ethyl methyl carbonate (EMC) (LP57, battery-grade, BASF), 1.5 M $LiPF_6$ (>99.99%, battery-grade, Aldrich) in EC (battery-grade, BASF), and 1 M $LiPF_6$ in EMC (battery-grade, BASF). For $LiPF_6$ / EC electrolyte, the salt concentration was 1.5 M rather than 1 M so that the electrolyte was in liquid phase at room temperature. The electrolytes (except for LP57) were prepared by simple mixing of $LiPF_6$ and EC or EMC in the glove box. The residual water content in the electrolytes was measured by Karl Fischer titration and was less than 20 ppm.

Electrochemistry tests

After assembly, the cell was first rested for 6 hours. Next, galvanostatic charge were performed using BCS-COM (Biologic) and VMP3 (Biologic). Electrochemical behavior of the electrodes in the *in situ* FT-IR cell was confirmed by galvanostatic measurements above (27.5 mA/g). The actual or effective loading which could be charged might be

smaller than measured: during electrode preparation (dropcasting) some particles could permeate through the glassy fiber substrate and stay on the other side of the substrate, and they may not be charged actually. Fig. A-3 summarizes the charging time to reach 4.8 V_{Li} during the first cycle for different electrode-electrolyte combinations in this paper, which shows comparable SOCs (8.2 hours on average with same charging rate at 27.5 mA/g, variance within 20%, so the SOC reaches around 82%). For the measurements without oxides, sputtered Pt was the positive electrode and linear sweep voltammetry was performed.

EIS was measured using a three-electrode cell. The three-electrode cell was assembled in an argon-filled glove box with a Li metal foil (15 mmϕ), 2 pieces of Celgard 2325 (19 mmϕ) as the separators, $Li_4Ti_5O_{12}$ mesh reference electrode (18 mmϕ), 2 pieces of Celgard 2325 (19 mmϕ) again, and NMC composite electrode (1/2 inchϕ) from bottom to top, where a mesh $Li_4Ti_5O_{12}$ reference electrode was placed between positive and negative electrode with two separators. Detail cell configuration can be found in previous paper.[31] 200 μL of electrolyte was added to the cell. For the test with 1.5 M $LiPF_6$/EC solution, 1 piece of Whatman GF/A (19 mmϕ, dried at 150 ^oC in vacuum overnight prior to use) was used as separator instead of 2 pieces of Celgard 2325 due to wettability problem. Mesh reference electrode was used to avoid inhomogeneous electric field during EIS measurement, which is known to cause artifactual EIS response (*ex.* "spiral" behavior on Nyquist plots with Li rod reference electrode).[31,312–315] Galvanostatic and potentiostatic charge and EIS tests were performed using VMP3 (potentiostat with frequency response analyzer, Biologic) with thermally equilibrated by thermostat chamber (SU-241, Espec) at 25 ^oC. After cell

assembly, $Li_4Ti_5O_{12}$ mesh reference electrode was electrochemically lithiated (negatively polarized at constant current of 500 μA against Li metal counter electrode with cut-off voltage of 1.3 V_{Li}) and got stable reference electrode potential at 1.56 V_{Li}.[313] Then NMC working electrode was charged with different end-of-charge potential (3.9-4.6 V_{Li}) at 27.5 mA/g (0.1C rate based on theoretical capacity of 275 mAh/g, which corresponds to full lithium deintercalation: $LiNi_xMn_yCo_{1-x-y}O_2 \rightarrow Li^+ + e^- + Ni_xMn_yCo_{1-x-y}O_2$, 27.5 mA/g corresponds to ~70 μA/cm^2 for average loading density of ~2.7 mg/cm^2), hold end-of-charge potential for 1 hour, and relax for 1 hour. After relax, EIS measurements were carried out at open circuit potential with 10 mV amplitude and frequency range from ~10^{-1} to 10^6 Hz. Obtained EIS data (excluded very high frequency region > 100 kHz if needed) were analyzed using ZView2 (Scribner).

Supplementary figures for Chapter 2

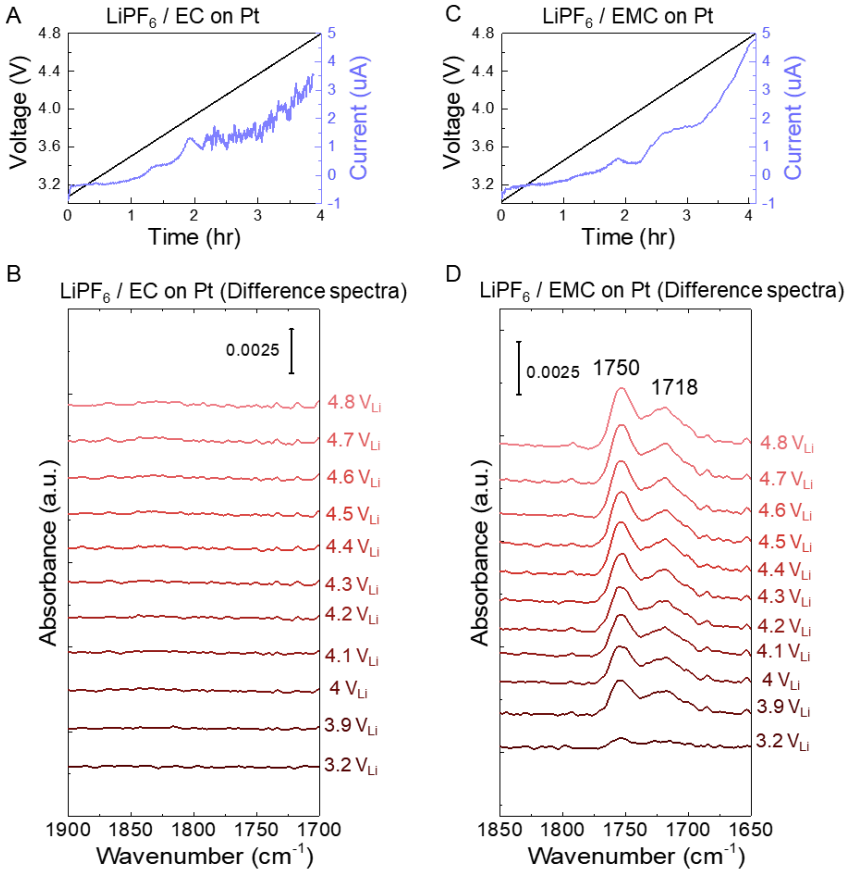

Fig. A-1 CV on Pt and *in situ* FT-IR difference spectra on Pt. (A) CV and (B) difference spectra for EC with 1.5 M $LiPF_6$ on a Pt electrode. (C) CV and (D) difference spectra for EMC with 1 M $LiPF_6$ on a Pt electrode.

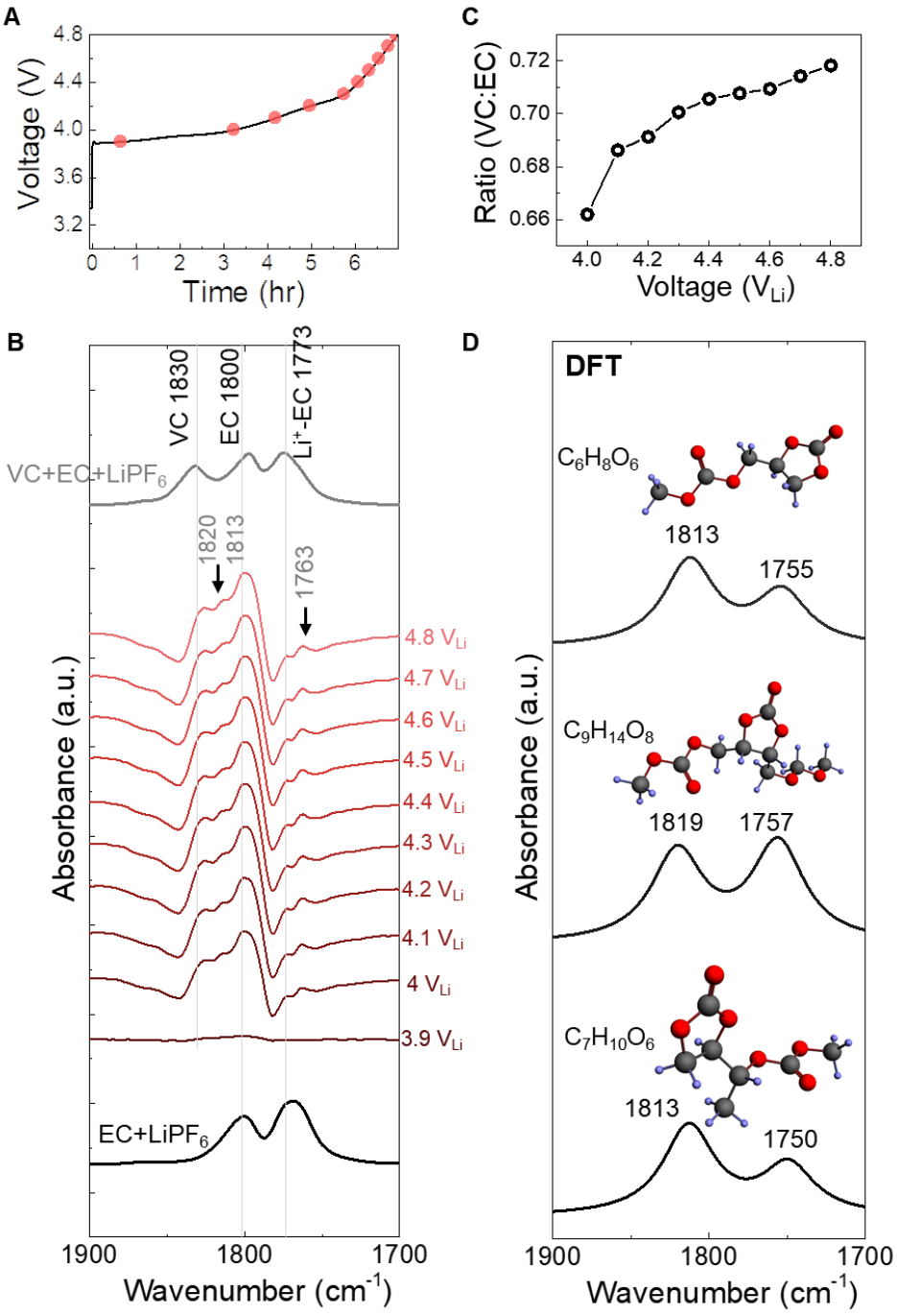

Fig. A-2 In-situ FTIR spectra on NMC811 surface during charging in 1.5 M $LiPF_6$ / EC from OCV (3.3 V_{Li}) to 4.8 V_{Li}. In situ cell was galvanostatically charged at 27.5 mA/g. (A) Voltage profile during NMC811 charging in 1.5 M $LiPF_6$ / EC, with voltage up to 4.8 V_{Li}. (B) In-situ FTIR difference spectra for C=O stretching region (in red) on NMC811 surface during charging in 1.5 M $LiPF_6$ / EC electrolyte, and ATR spectra for 1.5 M $LiPF_6$ in EC and 1.5 M $LiPF_6$ in EC/VC (1:1) electrolyte solution (in black). (C) Peak ratio of

VC to EC, which continues to increase during charging. (D) DFT computed spectra for EC-derived oligomers with EC-like rings intact (C=O stretching region).

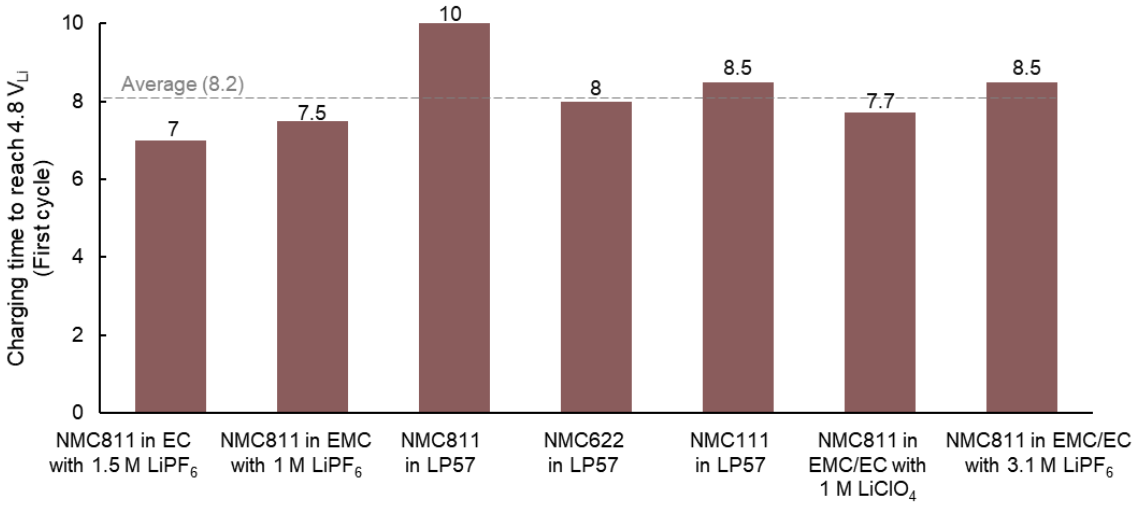

Fig. A-3 Summary of charging time to reach 4.8 V_{Li} during first cycle for *in situ* cells. The electrode loadings were all around 6.5 mg/cm^2, with areas all 78.5 mm^2 (10 mm in diameter). *In situ* FT-IR cells were galvanostatically charged at 27.5 mA/g, with voltage cutoffs all 4.8 V_{Li}. 10 hours of charging corresponds to 100% SOC (based on charge capacity of 275 mAh/g).

Appendix B: Supplementary Data for Chapter 3

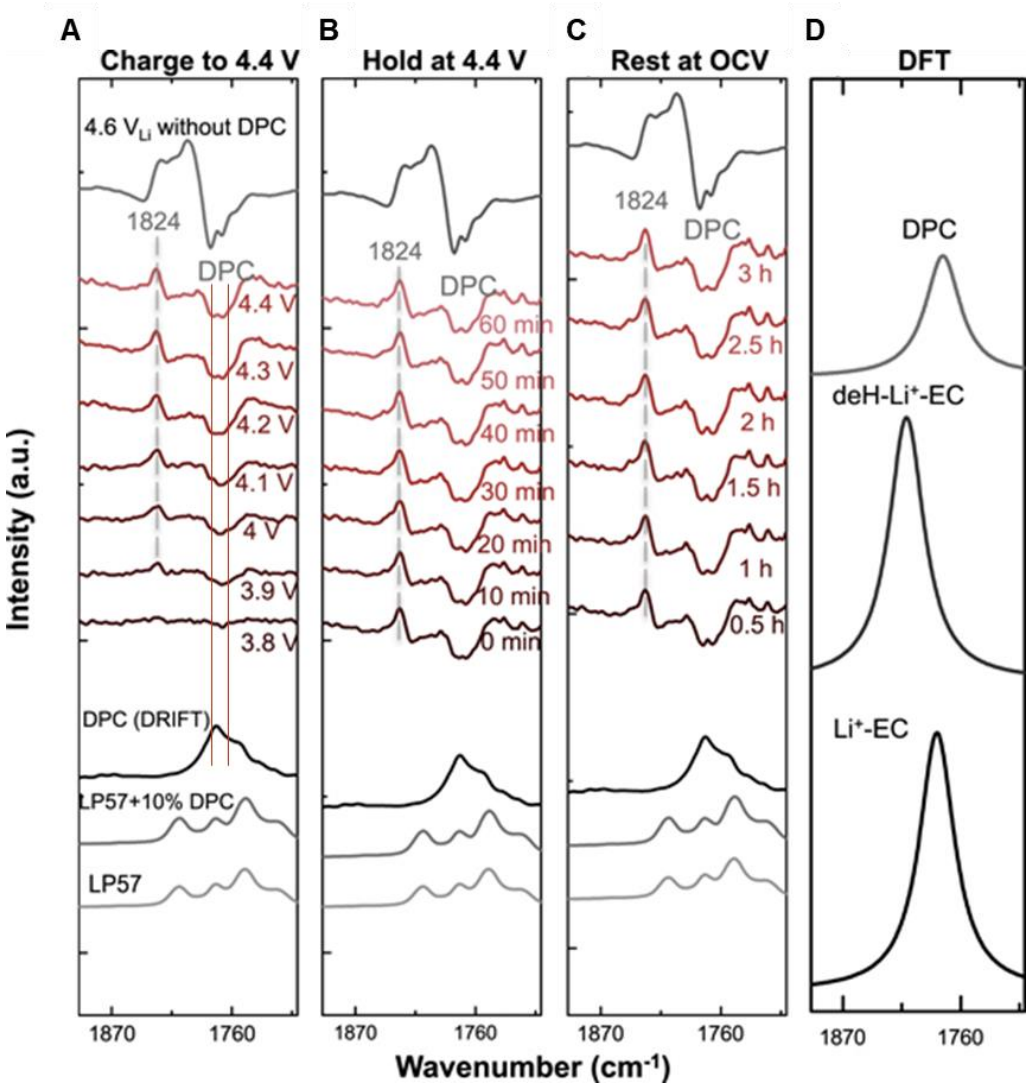

Fig. B-1 In-situ FTIR difference spectra (C=O stretching region) on NMC811 surface during (A) charging to 4.4 V_{Li}, (B) potentiostatic holding at 4.4 V_{Li}, and (C) resting at OCV in LP57 with 1 wt% DPC. NMC811 was galvanostatically charged to 4.4 $V_{Li,}$ potentiostatically holding at 4.4 V_{Li}, and resting at OCV, in LP57 with 1 wt% DPC, with the in situ FTIR cell, at a current of 27.5 mA g^{-1}. (D) The ATR spectra of LP57 electrolyte, LP57 electrolyte with 10% DPC additive, DRIFT spectra of DPC and in situ IR spectra of NMC811 electrode charged to 4.6 V_{Li} without DPC additive (LP57 electrolyte only) were added as references.

Appendix C: Supplementary Data for Chapter 4

Supplementary notes

Supplementary Note 1. Electronic and ionic aspects of the theory

The electronic part of the theory, which was based on the celebrated Marcus theory, predicts the existence of reaction-limited current at large values of the applied overpotential η, but it is the novel coupling with the ionic part that explains how the limiting current changes as a function of Li^+ fractional concentration x in the intercalation material. The introduced ion intercalation mechanism connects the current density i and/or the voltage with the microscopic physics of the process and the materials used.

First, the electron transfer part allows for the description of: (i) the nature of the electron donor through its electronic density of states $\rho(\epsilon)$ and (ii) the reorganization energy λ of the intercalation material. The value of λ includes all the contributions from the long- (electrostatic) and short-range (phonon-e^- coupling) interactions of the electrons with the intercalation medium. Therefore, the dielectric permittivity ε_s, as well as the phonon density of states are reflected in λ.

Second, the ion transfer part allows for the description of: (i) configurational entropy of intercalated ions; (ii) ion-interface interactions; (iii) (de-)solvation of ions from the electrolyte (from)into the intercalation material. Configurational entropy leads to excluded volume interactions in the transition state, which requires an ionic vacancy for the reaction to proceed and contributes a rate pre-factor *(1-x).* Ion-interface interactions determine the probability of finding an ion in the proximity of the interface, and includes the effects from

the formed double layers, as well as long-range interaction of the solvated ions with the atoms of the interface. These effects are described through $e^{-\alpha_{IT}\Delta E_{IT}/k_BT}$, which is included in the current density prefactor i_r^*. ΔE_{IT} corresponds to the energy barrier required for moving an ion nearby the intercalation material interface in order to initiate ion insertion[316]. The w_+ term describes the effects of dielectric mismatch between the electrolyte and the intercalation material.

Finally, the coupling between the ion and electron transfer introduces the short-range interaction between the ions and electrons when they are inside the intercalation material. Although several material parameters are included in the model, most of them are lumped in the current density prefactor i_r^* leading to only two three model parameters, e.g. , i_r^*, and w_+.

The expanded full formula for Eq. 1 in the main text is

$$i = \frac{i_r^*(1-x)}{\sqrt{4\pi\lambda k_B T}} \int_{-\infty}^{\infty} \left[\tilde{c}_+ \, n_e(\varepsilon) \exp\left[-\frac{(\lambda + e\eta_f - \varepsilon)^2}{4\lambda k_B T} \right] - x\left(1 - n_e(\varepsilon)\right) \exp\left[-\frac{(\lambda - e\eta_f + \varepsilon)^2}{4\lambda k_B T} \right] \right] \rho(\varepsilon) d\varepsilon \qquad \text{(Eq. S1)}$$

where $\tilde{c}_+ = \frac{\tilde{c}\, e^{-\tilde{w}_+}}{1 + \tilde{c}\, e^{-\tilde{w}_+}}$ (Eq. 4)

$i_r^* = (e k_0 H_{DA}^2 / \hbar v_{\ddagger}) e^{-\alpha_{IT}\Delta E_{IT}/k_BT}$ (Eq. S2)

The expanded formula for the asymptotic approximation Eq. 5 is

$$i(\eta, x, \tilde{c}_+) \approx i_r^* (1-x)\left(\frac{\tilde{c}_+}{1+e^{\frac{e\eta}{k_BT}+\ln\left(\frac{\tilde{c}_+}{x}\right)}} - \frac{x}{1+e^{-\left(\frac{e\eta}{k_BT}+\ln\left(\frac{\tilde{c}_+}{x}\right)\right)}}\right)\operatorname{erfc}\left[\frac{\lambda/k_BT - \sqrt{1+\sqrt{\lambda/k_BT}+\left(\frac{e\eta}{k_BT}+\ln\left(\frac{\tilde{c}_+}{x}\right)\right)^2}}{2\sqrt{\lambda/k_BT}}\right] \quad \text{(Eq. S3)}$$

where $\tilde{c}$ is the molar concentration of the Li^+ in the bulk electrolyte; $\eta_f = \eta + \frac{k_BT}{e}\ln\left(\frac{\tilde{c}_+}{x}\right) + i\,R_c$ (Eq. 3); $n_e(\varepsilon) = 1/(1+e^{\varepsilon/k_BT})$ is the Fermi distribution; $\rho(\varepsilon)$ is the electronic density of states (band structure) of the electrode.

Supplementary Note 2. Exchange current density

The exchange current density is defined for any electrochemical kinetics model when the overpotential tends to zero[185,317]. Following the uniformly valid approximation as described in Eq. S3, the approximate form of the exchange current density reads,

$$i_0 \simeq \lim_{\eta\to 0}\frac{i(\eta,x,\tilde{c}_+)}{(e\eta} = \lim_{\eta\to 0} i_r^*(1-x)\left(\frac{\tilde{c}_+}{1+e^{\frac{e\eta}{k_BT}+\ln\left(\frac{\tilde{c}_+}{x}\right)}}\right)\operatorname{erfc}\left[\frac{\frac{\lambda}{k_BT} - \sqrt{1+\sqrt{\frac{\lambda}{k_BT}}+\left(\frac{e\eta}{k_BT}+\ln\left(\frac{\tilde{c}_+}{x}\right)\right)^2}}{2\sqrt{\frac{\lambda}{k_BT}}}\right]$$

$$= i_r^*(1-x)x\left(\frac{\tilde{c}_+}{x+\tilde{c}_+}\right)\operatorname{erfc}\left[\frac{\frac{\lambda}{k_BT} - \sqrt{1+\sqrt{\frac{\lambda}{k_BT}}+\ln^2\left(\frac{\tilde{c}_+}{x}\right)}}{2\sqrt{\frac{\lambda}{k_BT}}}\right] \quad \text{(Eq. S4)}$$

which shows that increasing λ decreases the resulting exchange current density of the material. Additionally, the form demonstrates the asymmetric exchange current density with respect to x, resulting in the autocatalytic phenomenon that leads to suppression of phase separation in open-driven systems [181,318].

Supplementary Note 3. Bayesian model selection

We made statistical comparison of the different models by computing the Bayesian information criterion (BIC) for each model. BIC is an asymptotic approximation to the negative natural logarithm of the Bayesian posterior probability of a model [319], and it compares models with different numbers of fitting parameters to determine the relative likelihood that a certain model describes the observed data.[320] The observed data is usually a deviation between the model-predicted current density and the experimentally-measured current density under the same overpotentials. Here in Tafel plots, we assume that these errors are normally distributed on the log-scale, such that as the magnitude of the current increases, so does the magnitude of the error.[320] If k is the number of parameters in the model, N is the number of data points, and θ^* are the best fit parameters for a model ($\theta^* \in \mathbb{R}^k$), the residuals for a given model m ($e_m \in \mathbb{R}^N$) are therefore defined as the difference of the log of the current:

$$e_m(\theta^*) = \log_{10}\left(i_{predicted}(\eta;\theta^*)\right) - \log_{10}(i_{measured}(\eta)) \qquad \text{(Eq. S5)}$$

where $i_{measured}$ and $i_{predicted} \in \mathbb{R}^N$ are the vector of experimentally-measured current densities and model-predicted current densities using the set of fitting parameters θ^*, respectively, at the corresponding experimental overpotentials, $\eta \in \mathbb{R}^N$.

Under the assumption that the model residuals are independent and identically distributed (I.I.D.) according to a normal distribution (Gaussian distribution with zero mean, as verified in Fig. C-16A), and that the sample size N is much larger than the number of parameters k. BIC for model m becomes

$$BIC = N\ ln(\ Var(e_m)\ )\ +\ k\ ln\ N \qquad \text{(Eq. S6)}$$

BIC penalizes the complexity of the model where complexity refers to the number of parameters in the model. The most likely model will therefore have the lowest (most negative) BIC which corresponds to the largest Bayesian posterior probability, while models with larger BIC either fail to fit the experimental data (large $Var(e_m)$) or overfit the data with too many parameters (large k).

Here we examined and compared 5 different models on datasets of LCO and NMC111 (Fig. C-16): BV, BV+film, BV+film with fixed α=0.5, and CIET with and without film resistance. For BV kinetics described as

$$i = i_0[e^{-\alpha\frac{e\eta}{k_BT}} - e^{(1-\alpha)\frac{e\eta}{k_BT}}] \qquad \text{(Eq. S7)}$$

the fitting parameter is i_0 (assuming α=0.5), and the total number of parameters for *n* Tafel curves is *n*.

For BV+film described as

$$i = i_0[e^{-\alpha\frac{e(\eta+iR_{film})}{k_BT}} - e^{(1-\alpha)\frac{e(\eta+iR_{film})}{k_BT}}] \qquad \text{(Eq. S8)}$$

the fitting parameters are i_0, α, and R_{film}, and therefore the number of parameters is 3*n*. If assuming α=0.5, the number of parameters is 2*n*.

For CIET (without film resistance), the number of parameters is 3 when λ, i_r^*, and w^+ are independent on x. For cases with film resistances or with varied w^+, all additional number of parameters will be counted in.

Supplementary Note 4. Marcus outer sphere reorganization energy

Marcus outer sphere reorganization energy [172,175,317] is the Born energy to create a sphere of charge near an electrode, as well as its image at distance 2d, minus the attraction energy between the ion and its image, described by the following relation

$$\lambda = \frac{e^2}{8\pi\varepsilon_0 k_B T}\left(\frac{1}{a_0} - \frac{1}{2d}\right)\left(\frac{1}{\varepsilon_{op}} - \frac{1}{\varepsilon_s}\right) \qquad \text{(Eq. S9)}$$

where ε_0 is the permittivity of free space, a_0 the effective radius of the reactant, d the distance from the center of the reactant to the surface of the electrode, ε_{op} the optical dielectric constant and ε_s the static dielectric constant. For $LiCoO_2$, we use the length of Co-O bond as the radius a_0, which is roughly 0.19 nm [196]. We use the dielectric permittivities from ab-initio calculations[321], $\varepsilon_s = 13.02$ and $\varepsilon_{op} = 8.1$, for the static and optical values, respectively. Additionally, we assume $d = a_0$.[172] We get $\lambda = 3.44\ \mathrm{k_B T} = 88.4$ meV for $LiCoO_2$.

Supplementary Note 5. Estimation of the ΔE_{IT} term in i_r^* based on electrostatics

The prefactor i_r^* can be approximated as $i_r^* = (ek_0 H_{DA}^2/\hbar\nu_{\ddagger})e^{-\alpha_{IT}\Delta E_{IT}/k_B T}$ (Eq. S2), which is related to ΔE_{IT}, the energy required to move the ion from the oxidized state when it is adsorbed at the interface in the liquid electrolyte, to the position it will occupy. ΔE_{IT} is split into two contributions [185]: 1) the energy to separate the electron and ion pairs, which

can be estimated by the electrostatic interaction between the ion and the electron E_C, 2) the energy to move the ion between two dielectric media from liquid to solid $\Delta G_{l\to s}$.

E_C is estimated as the Coulomb potential [185]

$$E_c = \frac{e^2}{4\pi\varepsilon_0\varepsilon_s r} \qquad \text{(Eq. S10)}$$

where ε_0 and ε_s are the permittivities of vacuum and the solid, and r the distance between the localized electron (transition metal) and Li^+ in the solid electrode. Screened Coulomb potential may also apply in some cases, but here we only use Eq. S10 as a rough estimation.

$\Delta G_{l\to s}$ is estimated in the following form

$$\Delta G_{l\to s} = \frac{e^2}{8\pi\varepsilon_0 a_{Li}}\left[\left(\frac{1}{\varepsilon_s}-\frac{1}{\varepsilon_l}\right)+\frac{1}{2}\left(\frac{\varepsilon_s-\varepsilon_l}{\varepsilon_s+\varepsilon_l}\right)\left(\frac{a_{Li}}{\varepsilon_s d_s}+\frac{a_{Li}}{\varepsilon_l d_l}\right)\right] \qquad \text{(Eq. S11)}$$

where a_{Li} stands for the Li-ion radius, ε_l is the permittivity of the liquid, d_s and d_l are the distances from the Li-ion to the interface in solid and liquid, respectively.

To summarize, we have the formula for ΔE_{IT} below:

$$\Delta E_{IT} = E_c + \Delta G_{l\to s} = \frac{e^2}{4\pi\varepsilon_0\varepsilon_s r} + \frac{e^2}{8\pi\varepsilon_0 a_{Li}}\left[\left(\frac{1}{\varepsilon_s}-\frac{1}{\varepsilon_l}\right)+\frac{1}{2}\left(\frac{\varepsilon_s-\varepsilon_l}{\varepsilon_s+\varepsilon_l}\right)\left(\frac{a_{Li}}{\varepsilon_s d_s}+\frac{a_{Li}}{\varepsilon_l d_l}\right)\right] \qquad \text{(Eq. S12)}$$

Now we use Eq. S12 to justify the difference of i_r^* between LCO and LFP. The constants are ε_0 = 8.854× 10^{-12} F/m, $a_{Li} = 76\times10^{-12}m$. For LCO in EMC/EC/1 M $LiClO_4$, using the following values ($\varepsilon_s = 13.02, \varepsilon_l = 22.8, r = 2.87\times10^{-10}m$) we get $E_{c,LCO} = 0.233\ eV$, $\Delta G_{l\to s,LCO} = 0.234\ eV$, and $\Delta E_{IT,LCO} = 0.467\ eV$. For LFP in EMC/EC/1 M $LiClO_4$, plugging in the known values ($\varepsilon_s = 11.58, \varepsilon_l = 22.8, r = 3.32\times10^{-10}m$) we get

$E_{c,LFP} = 0.227\ eV$, $\Delta G_{l\to s,LFP} = 0.301\ eV$, and $\Delta E_{IT,LFP} = 0.528\ eV$ which is 0.06 eV higher than LCO. The ratio of i_r^* from these estimations is therefore (assuming $\alpha_{IT} = 1$, and H_{DA}^2 and $\nu_{\ddagger}$ are not changing among materials)

$$\frac{i_{r,LCO}^*}{i_{r,LFP}^*} \sim \frac{e^{-\alpha_{IT}\Delta E_{IT,LCO}/k_BT}}{e^{-\alpha_{IT}\Delta E_{IT,LFP}/k_BT}} \sim \frac{e^{-\Delta E_{IT,LCO}/k_BT}}{e^{-\Delta E_{IT,LFP}/k_BT}} = 11 \qquad \text{(Eq. S13)}$$

Experimentally the ratio of i_r^* between LCO and LFP is 40 from the Tafel kinetic measurements, which could be qualitatively explained by the larger ΔE_{IT} for LFP.

The formula (Eq. S12), however, fails to capture the electrolyte dependency of i_r^*. Future studies from first-principle calculations or molecular dynamic simulations with explicit chemical structures will be needed to understand and better estimate the value of ΔE_{IT}.

Supplementary Note 6. Non-linear region in rate capability plot

In the rate capability measurement (Fig. 4-5), some experimental points deviated from the linear trend at large applied currents and followed an exponential decrease. The linear region has been discussed in the main text based on CIET. Here we use many-particle PET simulation to provide physical origin to the exponential region, which is related to inhomogeneous particle size distribution and mixed contributions to overpotentials.

Using many-particle simulations with a constant macroscopic applied current *i*, we observe similar linear and exponential regions in the rate capability behavior (Fig. C-31). At a small applied current i/i_r^*=0.02 (Fig. C-31B), the smallest particle takes up the current and gets lithiated first due to high area-to-volume ratio until fully lithiated. The smallest particle

mostly determines the overpotential and hits the cutoff voltage. At a high applied current $i/i_r^* = 0.83$ (Fig. C-31C), however, all particles start to lithiate at the same time and contribute to overpotentials. The overpotential and cutoff voltage are a mixed results of all particles of different sizes, and the maximum capacity diverges from the linear trend.

Supplementary tables for Chapter 4

Table C-1. Exchange current densities measured in literature. Current density is with respect to the specific surface area of oxides unless otherwise specified.

Electrode material	Electrolyte	Exchange current density	Reference
Li_xCoO_2 thin film from pulsed laser deposition	1 M $LiClO_4$ in EC:DEC 1:1	0.1-0.17 $\mu A/cm^2$	Reference [32]
$LiCoO_2$ powders	1 M $LiPF_6$ in EC:DMC 1:1	0.0094 mA/cm^2	Reference [322]
Li_xCoO_2 thin film from RF sputtering	1 M $LiClO_4$ in EC:DEC 1:1	0.01-0.03 mA/cm^2	Reference [32]
Li_xCoO_2 powders	1 M $LiPF_6$ in EC:DEC 1:1	0.01-0.04 mA/cm^2	Reference [200]
Li_xCoO_2 powders	1 M $LiPF_6$ in EC: DEC 1:1	0.05-0.1 mA/cm^2	Reference [323]
Li_xCoO_2 powders	0.2-1 mM $LiClO_4$ in PC	0.3-2.5 $mA/cm^2_{(geo)}$	Reference [324]
$Li_{0.2}CoO_2$ powders	1 M $LiPF_6$ in EC:PC 1:1, v/v	1.83 $mA/cm^2_{(geo)}$	Reference [325]
Li_xCoO_2 powders	1 M $LiPF_6$ in EC:EMC:DMC 1:1:1, v/v	2-5 $mA/cm^2_{(geo)}$	Reference [33]
Li_xCoO_2 powders	Unknown	8-10 mA/cm^2	Reference [326]
Li_xCoO_2 powders	1 M $LiClO_4$ in EC:EMC 3:7	0.03-0.07 mA/cm^2	This work
Li_xCoO_2 powders	1 M $LiPF_6$ in EC:EMC 3:7	0.007-0.02 mA/cm^2	This work
$Li_xNi_{1/3}Co_{1/3}Mn_{1/3}O_2$ single particle	1 M $LiPF_6$ in EC:DMC 1:1	0.002-0.3 mA/cm^2	Reference [201]
$Li_xNi_{1/3}Co_{1/3}Mn_{1/3}O_2$ powders	1 M $LiPF_6$ in DMC	0.01-2 mA/cm^2	Reference [327]
$Li_xNi_{1/3}Co_{1/3}Mn_{1/3}O_2$ powders	Unknown	0.054 mA/cm^2	Reference [328]
$Li_xNi_{1/3}Co_{1/3}Mn_{1/3}O_2$ powders	1 M $LiPF_6$ in EC:EMC:DMC 1:1:1, v/v	8-16 mA/cm^2	Reference [30]
$Li_xNi_{1/3}Co_{1/3}Mn_{1/3}O_2$ powders	1 M $LiClO_4$ in EC:EMC 3:7	0.02-0.05 mA/cm^2	This work
$Li_xNi_{1/3}Co_{1/3}Mn_{1/3}O_2$ powders	1 M $LiPF_6$ in EC:EMC 3:7	0.005-0.012 mA/cm^2	This work

Table C-2. Exchange current densities i_0 used in literature modelling

Electrode	Electrolyte	Exchange current density	Reference
$Li_{0.5}CoO_2$	1 M $LiPF_6$ in EC/PC/EMC/DEC	0.8142 mA/cm^2	Reference [329]
$Li_{0.5}CoO_2$	1 M $LiPF_6$ in EC/PC/EMC/DEC	10.028 mA/cm^2	Reference [330]
$Li_{0.5}CoO_2$	1 M $LiPF_6$ in EC/PC/EMC/DEC	50.2 mA/cm^2	Reference [331]
$Li_{0.5}CoO_2$	1 M $LiPF_6$ in EC/DMC 1:2	100.93 mA/cm^2	Reference [332]
$Li_{0.5}CoO_2$	1 M $LiPF_6$ in EC/PC/EMC/DEC	~350 mA/cm^2	Reference [333]
$Li_{0.5}CoO_2$	1 M $LiPF_6$ in EC/PC/EMC/DEC	380.6 mA/cm^2	Reference [334]
$Li_{0.5}Ni_{1/3}Co_{1/3}Mn_{1/3}O_2$	1 M $LiPF_6$ in EC/DEC 1:1	8 mA/cm^2	Reference [335]
$Li_{0.5}Ni_{1/3}Co_{1/3}Mn_{1/3}O_2$	1 M $LiPF_6$ in EC:DEC 1:1	44.8 mA/cm^2	Reference [336]
$Li_{0.5}Ni_{1/3}Co_{1/3}Mn_{1/3}O_2$	1 M $LiPF_6$ in EC/PC/DMC	~56000 mA/cm^2	Reference [337]

Table C-3. Electrode information for electrochemical response tests in Fig. 4-2, Fig. 4-4, Fig. C-7, Figs. 4-17 to 4-22, and Fig. C-26.

Materials	Electrolyte	Loading of active material (mg)	Electrode geometric area (cm^2)	Real surface area (cm^2)
LCO	1 M $LiClO_4$ in EMC:EC 7:3	1.67	1.27	7.4
LCO	1 M $LiPF_6$ in EMC:EC 7:3	1.11	1.27	4.9
LCO	1 M $LiPF_6$ in EMC	2.19	1.27	9.7
LCO	2 M $LiPF_6$ in EMC:EC 7:3	1.03	1.27	4.5
LCO	0.1 M $LiPF_6$ in EMC:EC 7:3	1.07	1.27	4.7
LCO	0.02 M $LiPF_6$ in EMC:EC 7:3	1.02	1.27	4.5
LCO	1 M $LiClO_4$ in EMC:EC 7:3 (temperature dependent measurement)	2.10	1.27	9.2
NMC111	1 M $LiClO_4$ in EMC:EC 7:3	2.03	1.27	7.9
NMC111	1 M $LiPF_6$ in EMC:EC 7:3	1.96	1.27	7.6
NMC811	1 M $LiClO_4$ in EMC:EC 7:3	0.82	1.27	2.8
LFP	1 M $LiClO_4$ in EMC:EC 7:3	1.24	1.27	145
Graphite	1 M $LiClO_4$ in EMC:EC 7:3	1.87	1.27	69

Table C-4. Measured reorganization energy and calculated Marcus outer sphere reorganization energy according to Supplementary Note 2. Available dielectric data from literature for NMC111 was not found.

Materials	LCO	NMC111	NMC811	LFP	Graphite
ε_{op}	8.1	--	6.57 (for $LiNiO_2$)	4.74	5
ε_s	13.02	--	14.56 (for $LiNiO_2$)	11.85	8.9
a_0 and d (nm)	0.19	--	0.2 (for $LiNiO_2$)	0.21	0.14
λ calculated from Marcus outer sphere reorganization energy (k_BT)	3.5	--	5.84	8.43	8.76
λ calculated from Marcus outer sphere reorganization energy (meV)	90	--	150.2	216	225
λ measured (meV)	104	116	124	147	184
Reference	[321]	--	[338,339]	[340]	[341]

Table C-5. Electrode information for rate capability tests in Fig. 4-5

Materials	Graphite	LCO	LMO	LTO	NCA	NMC532	NMC111	LFP
Loading of active material (mg)	1.04	1.6	1.12	1.36	2.16	1.28	0.8	0.88

Electrode geometric area (cm^2)	1.27	1.27	1.27	1.27	1.27	1.27	1.27	1.27
Real surface area (cm^2)	38.48	6.4	7.84	81.6	10.8	3.84	2.4	103
Porosity	79.20%	54.80%	84.70%	76.70%	60.60%	80.40%	87.70%	83.80%

Supplementary figures for Chapter 4

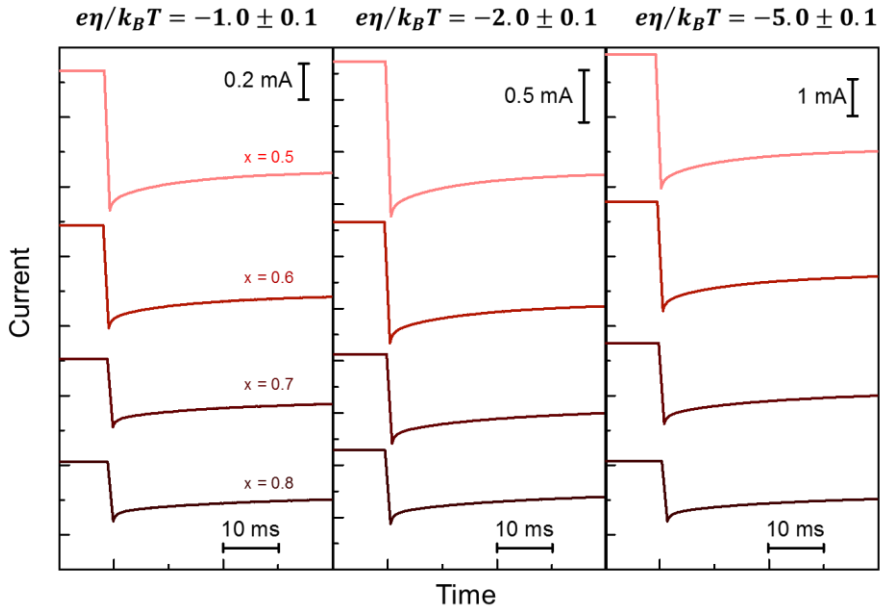

Fig. C-1. Current response for Li_xCoO_2 during potentiostatic discharging (intercalation) within the first 50 ms, for three representative overpotentials (left: $e\eta/k_BT = -1.0$, middle: $e\eta/k_BT = -2.0$, right: $e\eta/k_BT = -5.0$). Note that the y-axis have different scales. Electrolyte is EMC:EC (7:3) with 1 M $LiClO_4$. Loading of Li_xCoO_2 in the positive electrode is 1.32 mg/cm^2_{geo}.

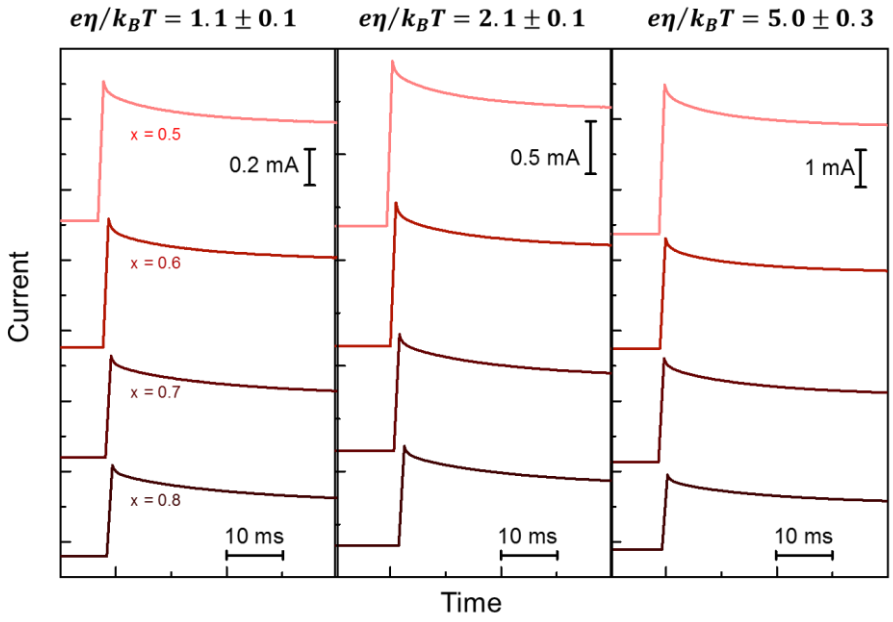

Fig. C-2. Current response for Li_xCoO_2 during potentiostatic charging (deintercalation) within the first 50 ms, for three representative overpotentials (left: $e\eta/k_BT = +1.1$, middle: $e\eta/k_BT = +2.1$, right: $e\eta/k_BT = +5.0$). Note that the y-axis have different scales. Electrolyte is EMC:EC (7:3) with 1 M $LiClO_4$. Loading of Li_xCoO_2 in the positive electrode is 1.32 mg/cm^2_{geo}.

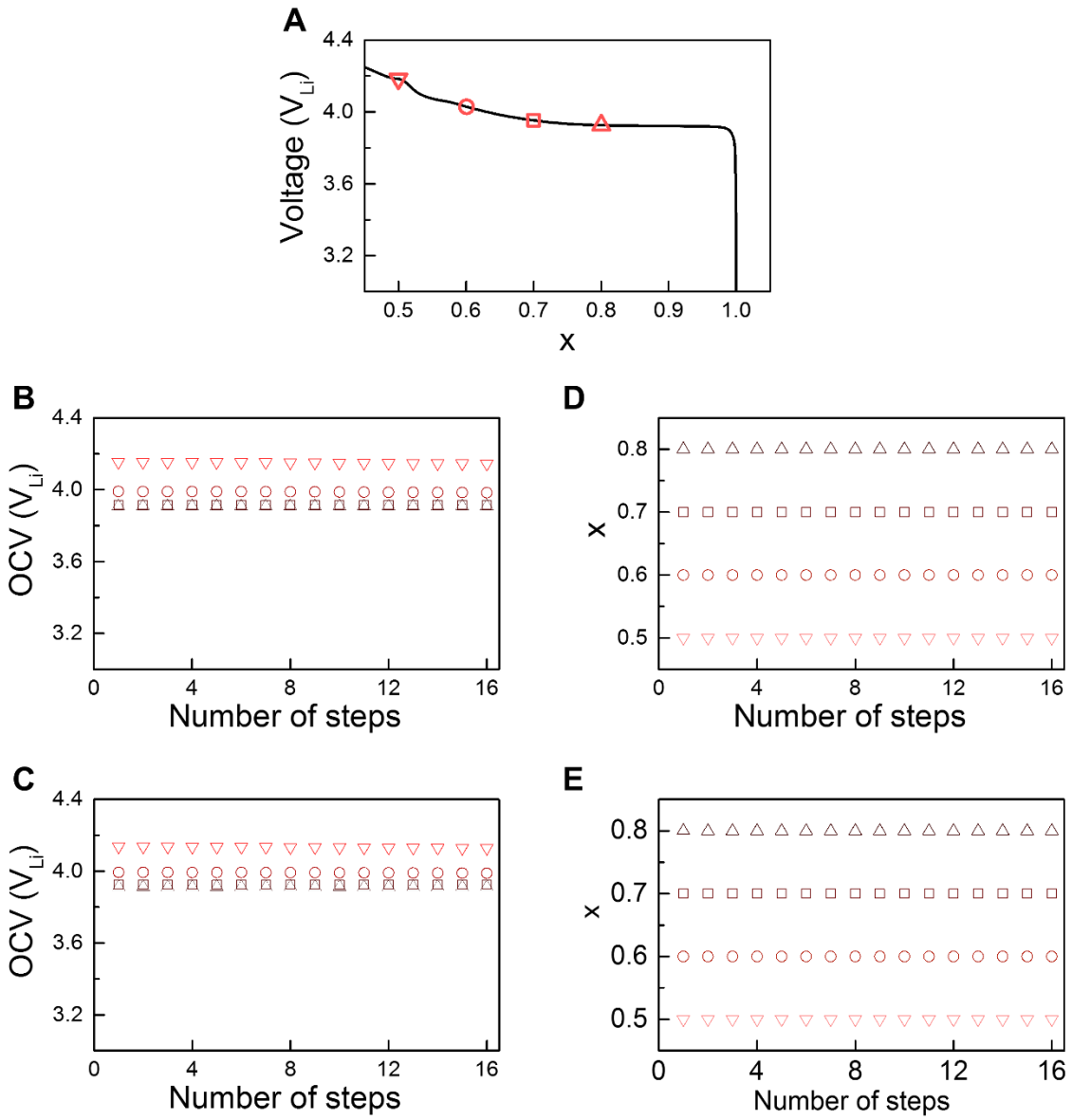

Fig. C-3. Voltage profile, open circuit voltage (OCV), and x values for Li_xCoO_2. (A) Typical charging profile at ~28 mA/g (black line), and cutoff voltage (red marks) for later kinetic measurements. Open circuit voltage during concentration-dependent current-voltage response measurements for (B) intercalation and (C) de-intercalation at x = 0.5 to 0.8. ∇ for x=0.5; ○ for x=0.6; □ for x=0.7; △ for x=0.8. Values of x for Li_xCoO_2 when the reported current was collected, for (D) intercalation and (E) de-intercalation. The timescale for which the currents were taken is smaller than 0.5 s, and the change in x during this time is negligible with $\Delta x < 0.0001$. Electrolyte is EMC:EC (7:3) with 1 M $LiClO_4$.

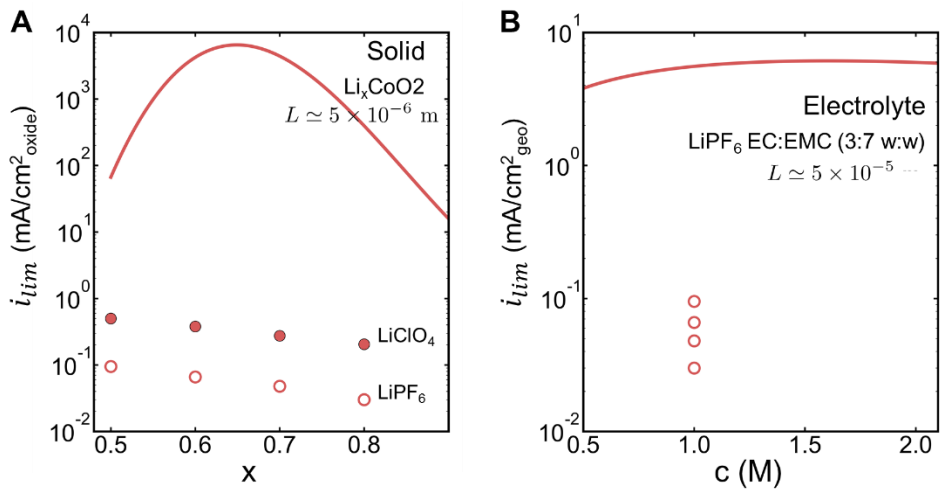

Fig. C-4. Diffusion limiting current $i_{lim} = DFc_{ref}/L$, where L is a characteristic length, D is the Li^+ diffusivity in the solid or liquid phase, and c_{ref} is the characteristic concentration. (A) Limiting current (blue line) for a solid $LiCoO_2$ particle of radius $L \simeq 5 \times 10^{-6}$ m as a function of the intercalated Li ions, and c_{ref} is the maximum concentration of Li^+ in the solid. The x-dependent diffusivity is taken from literature [342]. Experimental current densities at around $|e\eta/k_BT| = 6$ in EMC:EC (7:3) with 1 M $LiClO_4$ or $LiPF_6$ are marked in blue circles. (B) Limiting current for $LiPF_6$ liquid electrolyte in EMC:EC (7:3) as a function of the salt concentration c. The concentration-dependent diffusivity is taken from literature [216], while the distance between the positive and negative electrodes is $L \simeq 5 \times 10^{-5}$ m.

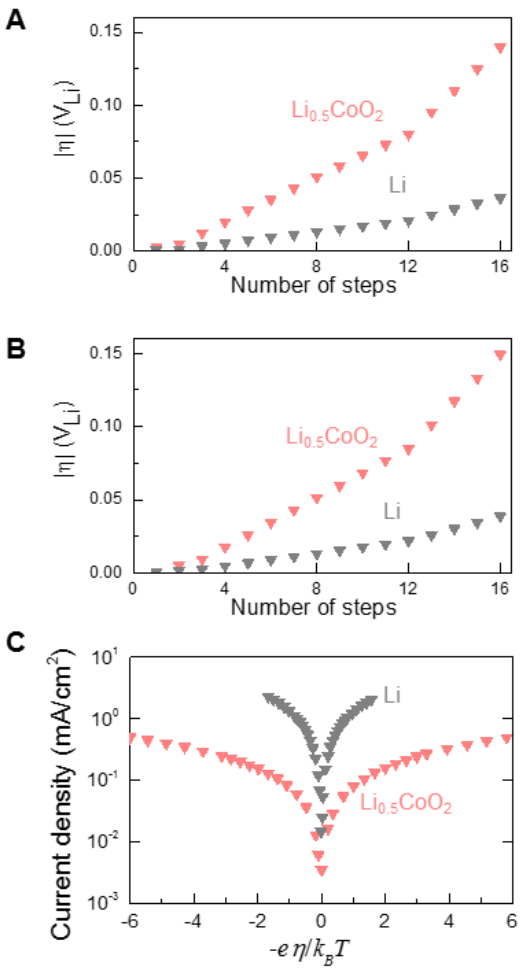

Fig. C-5. Comparison of the overpotentials and kinetics of $Li_{0.5}CoO_2$ and Li. Overpotentials of positive electrode $Li_{0.5}CoO_2$ and negative electrode Li in a same cell during (A) intercalation and (B) deintercalation. At each voltage step, the current on $Li_{0.5}CoO_2$ and Li are the same magnitude, while $Li_{0.5}CoO_2$ experiences more overpotentials than Li. (C) Kinetics $Li_{0.5}CoO_2$ and Li. Li has faster kinetics than $Li_{0.5}CoO_2$, and therefore is not the rate limiting electrode. Electrolyte is EMC:EC (7:3) with 1 M $LiClO_4$. Loading of Li_xCoO_2 in the positive electrode is 1.32 mg/cm$^2_{geo}$. The current density is calculated by the oxide surface area for the porous $Li_{0.5}CoO_2$ electrode (7.348 cm$^2_{oxide}$) and the by the geometric surface area for the planar Li electrode (1.767 cm$^2_{planar}$). All overpotentials have been iR corrected.

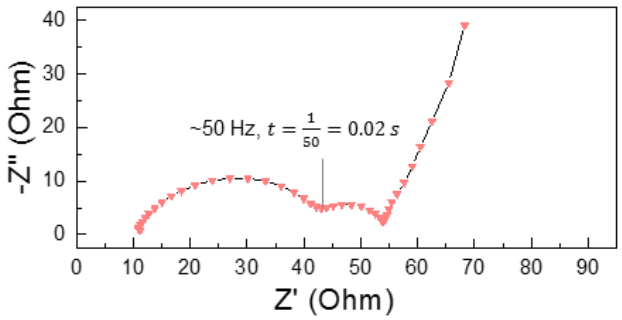

Fig. C-6. EIS for $Li_{0.5}CoO_2$. The high-frequency semicircle ends at around 50 Hz, and the timescale for charge transfer is 1/50 = 0.02 s. Current values at around 20 ms in Fig. C-1 and C-2 were taken as the current responses for the corresponding overpotentials. Electrolytes are EMC:EC (7:3) with 1 M $LiClO_4$. Loading of Li_xCoO_2 in the positive electrode is 1.32 mg/cm^2_{geo}.

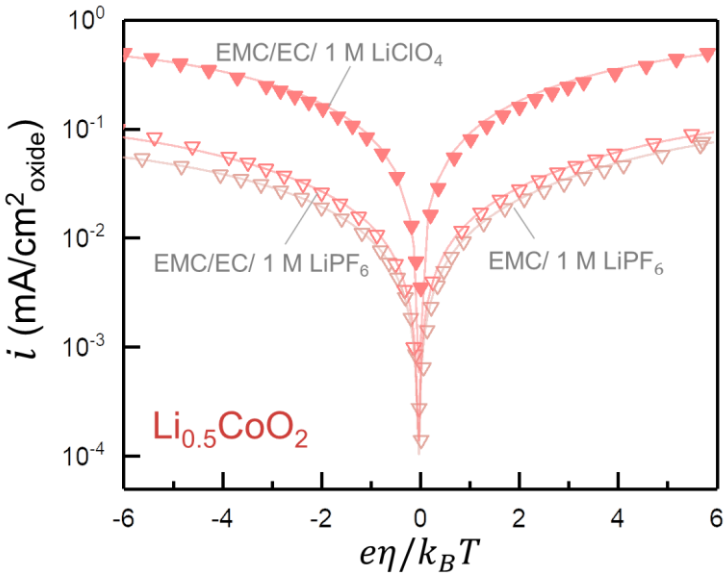

Fig. C-7. Experimental Tafel plots and CIET fitting for $Li_{0.5}CoO_2$ measured in in three electrolytes with different salts or solvents, including EMC:EC (7:3) with 1 M $LiClO_4$, EMC:EC (7:3) with 1 M $LiPF_6$, and EMC-only electrolytes with 1 M $LiPF_6$. LCO loadings are 1-2 mg_{active}/cm^2_{geo} (Table C-3).

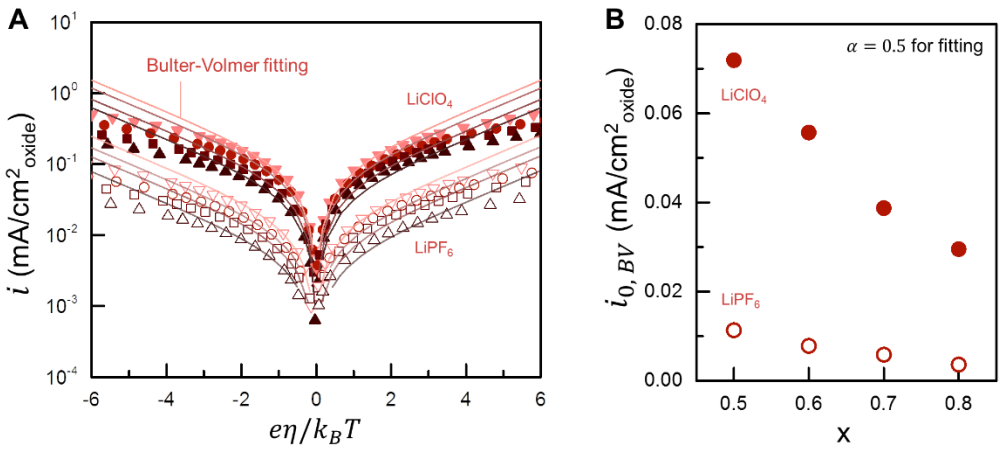

Fig. C-8. Fitting experimental Tafel plots with Bulter-Volmer (BV) kinetics for Li_xCoO_2. (A) Experimental results (points, ▽ for x=0.5; ○ for x=0.6; □ for x=0.7; △ for x=0.8) and Bulter-Volmer fittings (lines) with $\boldsymbol{\alpha = 0.5}$. (B) Fitted exchange current density from Bulter-Volmer kinetics. Electrolytes are EMC:EC (7:3) with 1 M $LiClO_4$ (filled symbols) or $LiPF_6$ (open symbols).

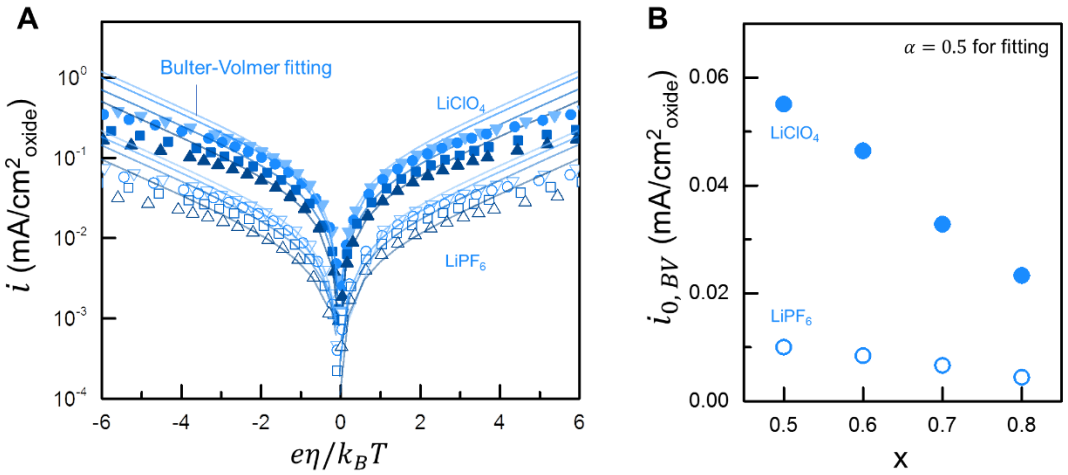

Fig. C-9. Fitting experimental Tafel plots with BV kinetics for NMC111. (A) Experimental results (points, ▽ for x=0.5; ○ for x=0.6; □ for x=0.7; △ for x=0.8) and BV fittings (lines) with $\boldsymbol{\alpha = 0.5}$. (B) Fitted exchange current density from BV kinetics. Electrolytes are EMC:EC (7:3) with 1 M $LiClO_4$ (filled symbols) or $LiPF_6$ (open symbols).

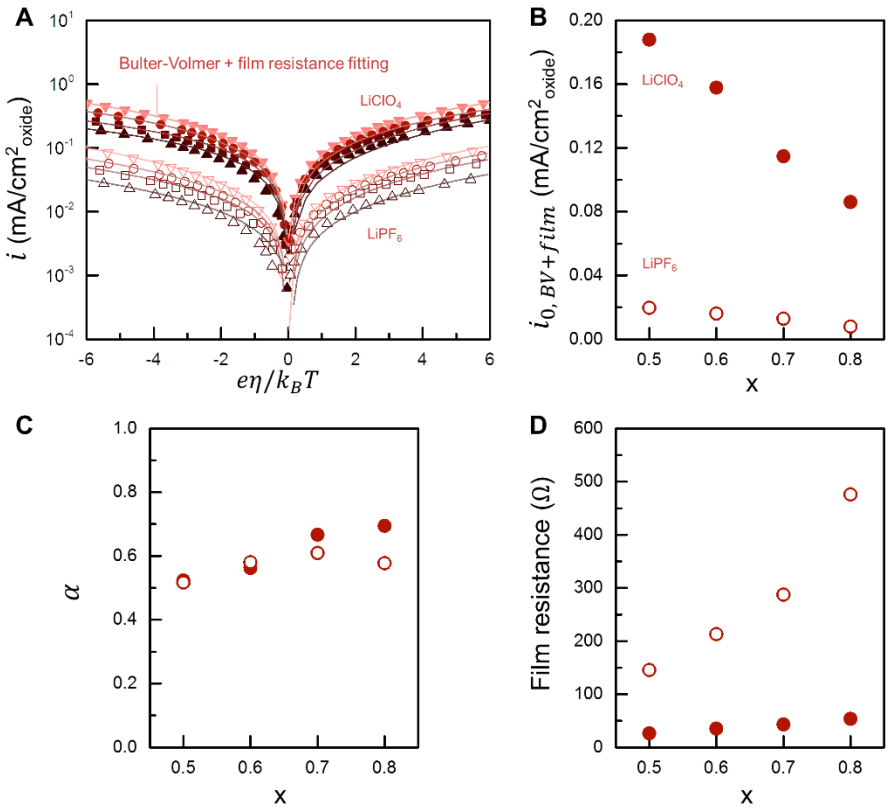

Fig. C-10. Fitting experimental Tafel plots with BV plus film resistance for Li_xCoO_2. (A) Experimental results (points, ▽ for x=0.5; ○ for x=0.6; □ for x=0.7; △ for x=0.8) and fittings (lines). Fitted exchange current density (B), $\boldsymbol{\alpha}$ (C), and film resistance (D) from the BV + film model. Electrolytes are EMC:EC (7:3) with 1 M $LiClO_4$ (filled symbols) or $LiPF_6$ (open symbols). It is noted that the film resistance varies with x so as to fit the experiments.

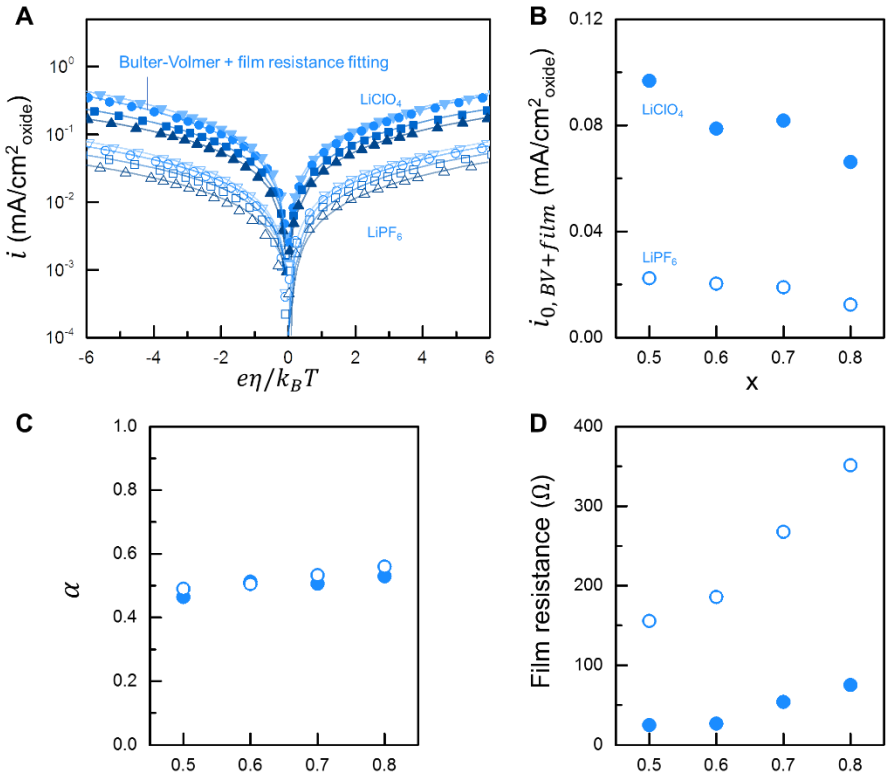

Fig. C-11. Fitting experimental Tafel plots with BV plus film resistance for NMC111. (A) Experimental results (points, ▽ for x=0.5; ○ for x=0.6; □ for x=0.7; △ for x=0.8) and fitting (lines). Fitted exchange current density (B), $\boldsymbol{\alpha}$ (C), and film resistance (D) from the BV + film model. Electrolytes are EMC:EC (7:3) with 1 M $LiClO_4$ (filled symbols) or $LiPF_6$ (open symbols).

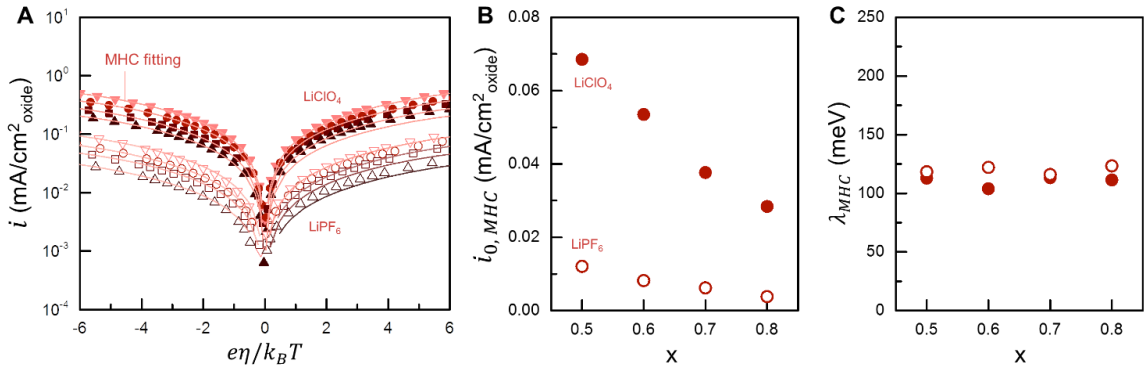

Fig. C-12. Fitting experimental Tafel plots with MHC kinetics. (A) Experimental results (points, ▽ for x=0.5; ○ for x=0.6; □ for x=0.7; △ for x=0.8) for Li_xCoO_2 and MHC fittings (lines). Fitted exchange current density (B) and reorganization energy (C) from MHC kinetics. Electrolytes are EMC:EC (7:3) with 1 M $LiClO_4$ (filled symbols) or $LiPF_6$ (open symbols).

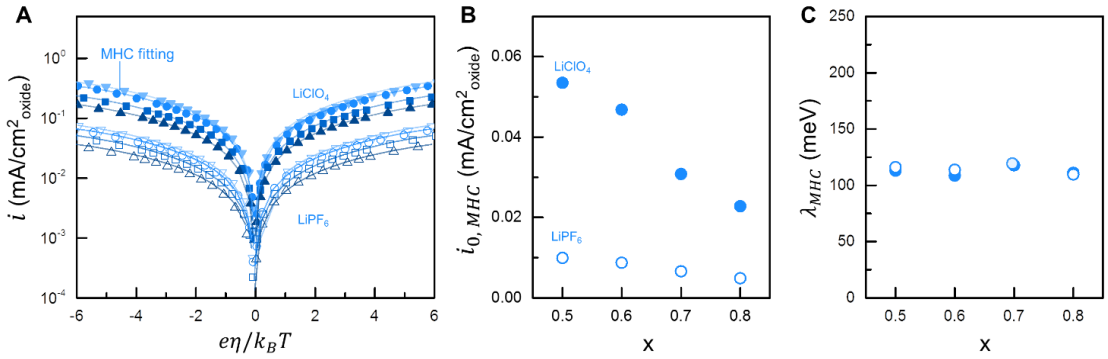

Fig. C-13. Fitting experimental Tafel plots with MHC kinetics. (A) Experimental results (points, ▽ for x=0.5; ○ for x=0.6; □ for x=0.7; △ for x=0.8) for NMC111 and MHC fittings (lines). Fitted exchange current density (B) and reorganization energy (C) from MHC kinetics. Electrolytes are EMC:EC (7:3) with 1 M $LiClO_4$ (filled symbols) or $LiPF_6$ (open symbols).

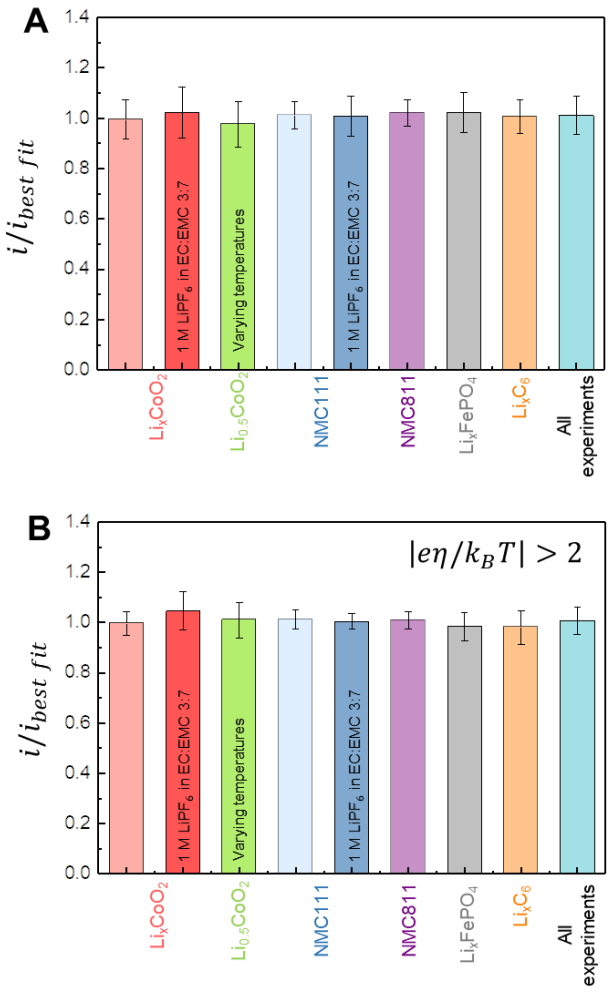

Fig. C-14. Goodness of fit for the CIET fittings in Fig. 4-2, Figs. C-17, C-18, and C-21. Goodness of fit is examined by the ratio of experimental current densities and the best-fitted current densities from CIET. Color codes follow those in Fig. 4-4D. Electrolytes are EMC:EC (7:3) with 1 M $LiClO_4$ unless specified otherwise. (A) Average values of $\boldsymbol{i/i_{best\ fit}}$ for all data sets and overpotentials, where standard deviations are all within 0.11 for each group. The total standard deviation for all experiments is 0.078. (B) Average values of $\boldsymbol{i/i_{best\ fit}}$ for only $\boldsymbol{|e\eta/k_BT| > 2}$ to eliminate errors at small overpotentials below thermal fluctuations, where the small value of current densities amplifies errors in the ratio. Standard deviations are all within 0.075 for each group. The total standard deviation for all experiments is 0.055.

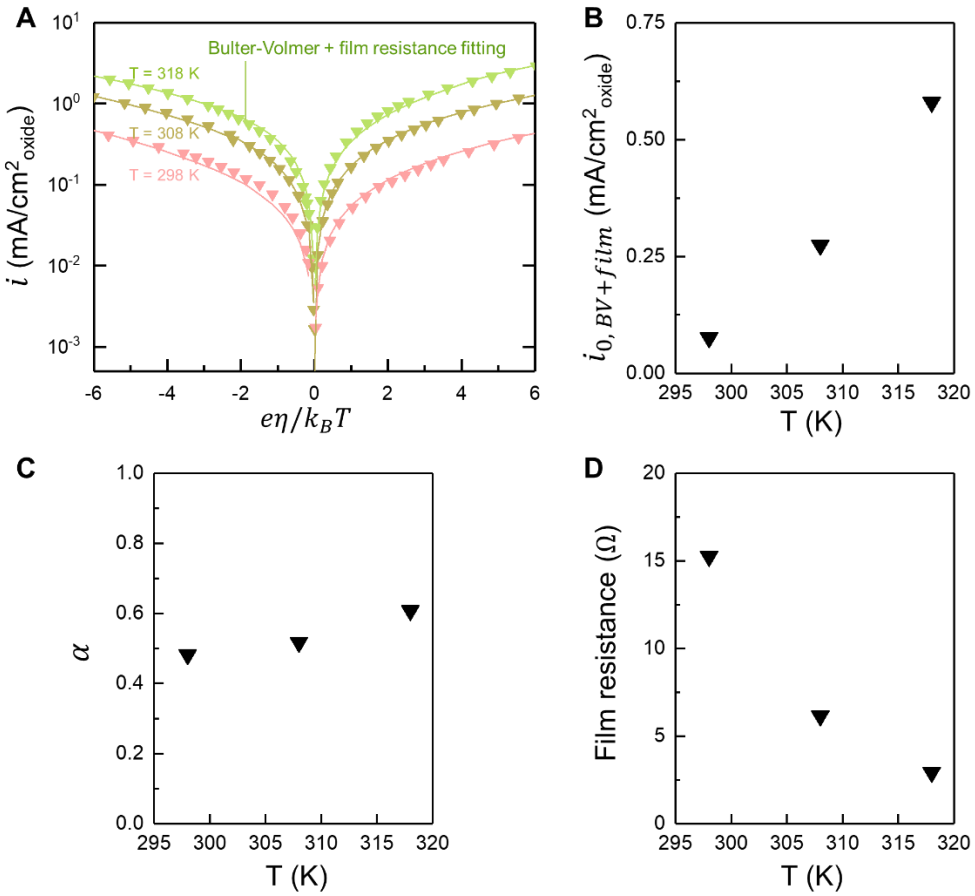

Fig. C-15. BV plus film resistance fitting for $Li_{0.5}CoO_2$ at three different temperatures. (A) Experimental results (points) and fittings (lines). Fitted exchange current density (B), $\boldsymbol{\alpha}$ (C), and film resistance (D) from the BV + film model. Electrolytes are EMC:EC (7:3) with 1 M $LiClO_4$. It is noted that the film resistance varies with the temperature so as to fit the experiments.

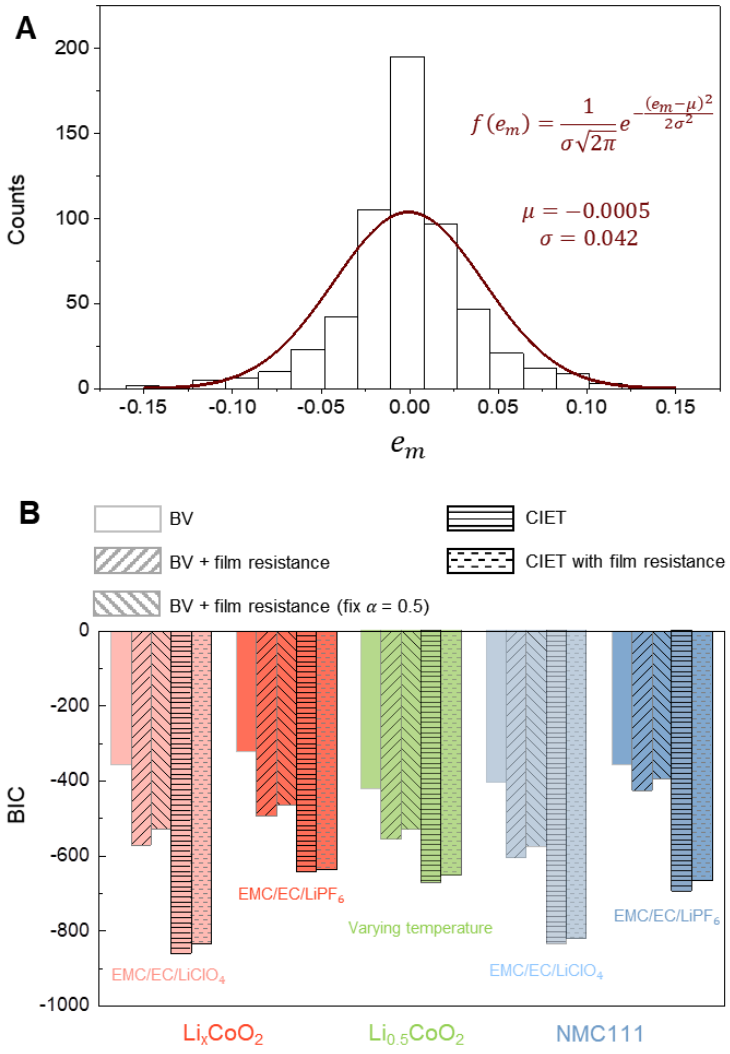

Fig. C-16. Distribution of CIET fitting errors and computed BIC for multiple models. (A) Distribution of CIET fitting errors $\boldsymbol{e_m}$ defined as the difference of log currents in Eq. S5. Data set is all the data for LCO and NMC111 presented in Fig. 4-2. $\boldsymbol{e_m}$ follows a Gaussian distribution with mean around zero and standard deviation of 0.042. (B) Computed BIC for each of the data sets presented for LCO and NMC111 in Fig. 4-2, comparing the different models (BV, BV + film resistance, BV + film resistance with fixed α = 0.5, and CIET with/without film resistance), for the entire overpotential range. A lower (more negative) BIC corresponds to a higher model veracity. CIET has the lowest BIC values and is considerably better, especially without film resistance.

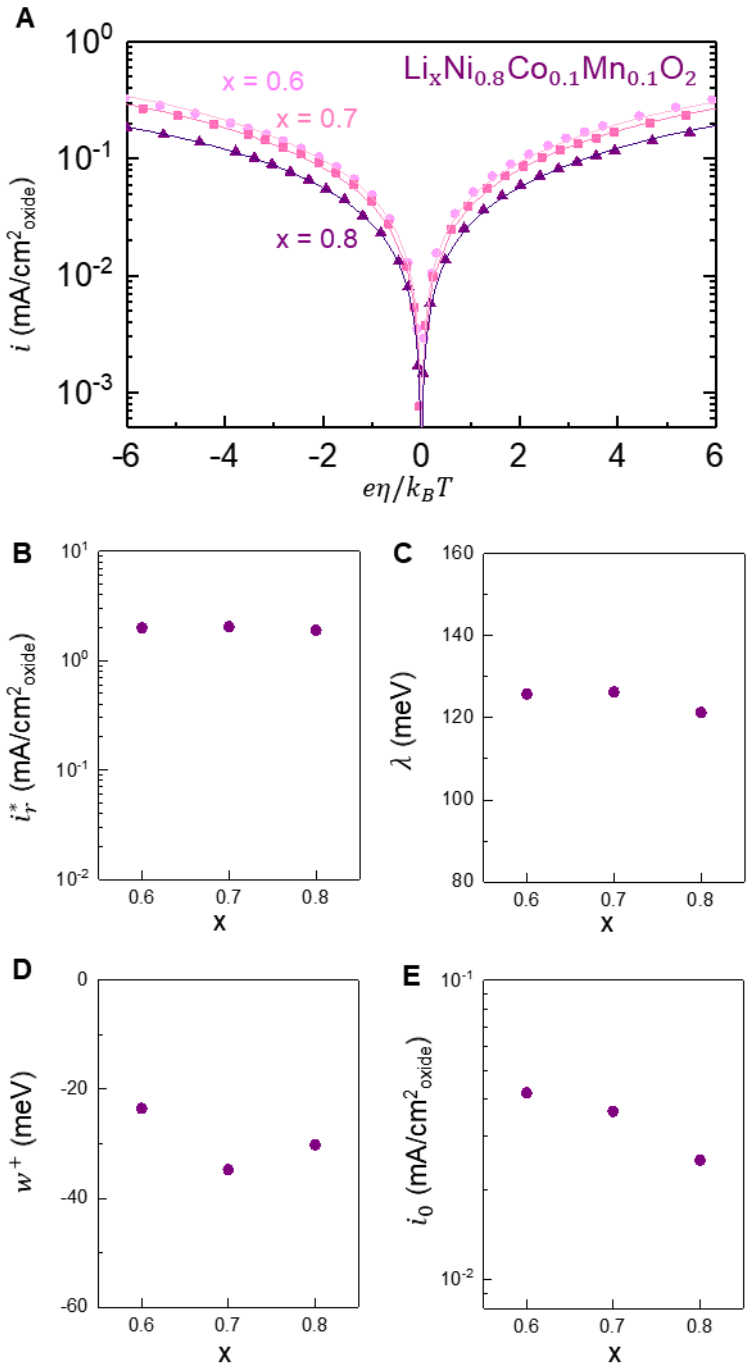

Fig. C-17. Experimental Tafel plots and fitted CIET parameters for $\mathbf{Li_xNi_{0.8}Co_{0.1}Mn_{0.1}O_2}$. (A) Experimental results (○ for x=0.6; □ for x=0.7; △ for x=0.8). (B) $\boldsymbol{i_r^*}$, (C) reorganization energy $\boldsymbol{\lambda}$, and (D) energy of Li^+ surface adsorption $\boldsymbol{w_+}$ fitted from CIET kinetics. (E) exchange current density from CIET kinetics. Electrolytes are EMC:EC (7:3) with 1 M $LiClO_4$. Loading of $\mathbf{Li_xNi_{0.8}Co_{0.1}Mn_{0.1}O_2}$ in the positive electrode is 0.65 mg/cm$^2_{geo}$.

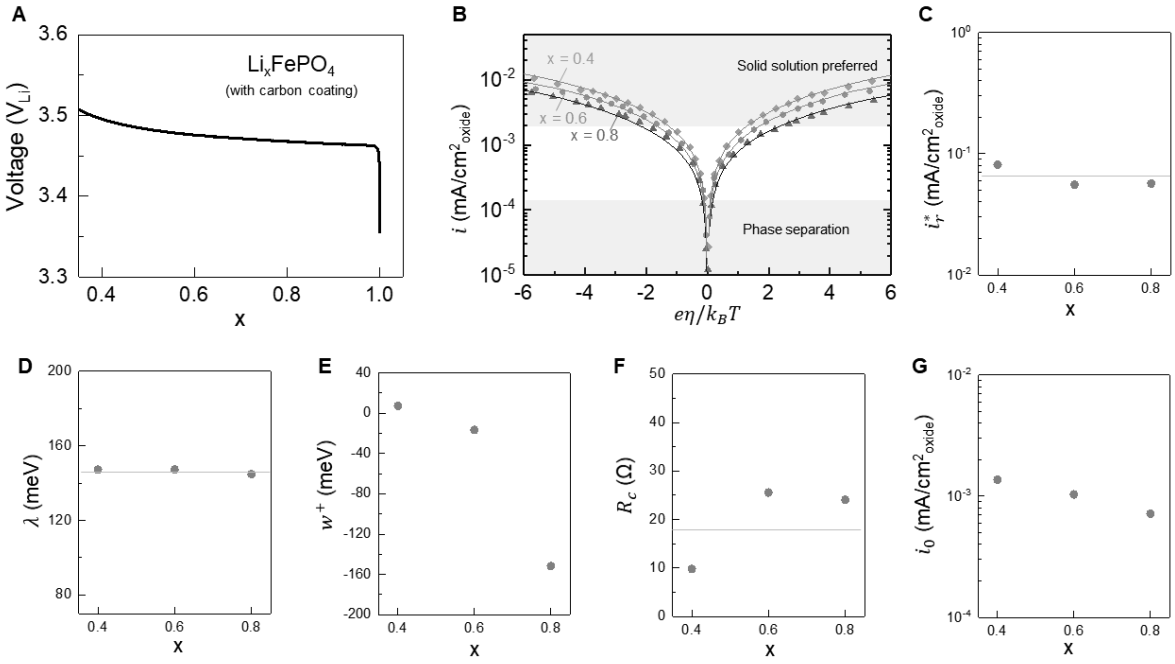

Fig. C-18. Experimental Tafel plots and fitted CIET parameters for Li_xFePO_4, where fitting was performed with considering surface coating R_c. (A) Typical charging profile at ~17 mA/g. (B) Experimental results (♦ for x=0.4, ■ for x=0.6 and ▲ for x=0.8). Shaded areas correspond to phase separation region ($i < 10^{-4}$ mA/cm$^2_{oxide}$) [343,344], and regions where solid solution phase is preferred (white, $i > 2 \times 10^{-3}$ mA/cm$^2_{oxide}$) [343–345]. In between is a quasi-solid solution phase [343,344], Fitted parameters including (C) i_r^*, (D) reorganization energy λ, (E) energy of Li^+ surface adsorption w_+, and (F) ionic resistance of surface coating R_c. The grey straight lines indicate the average values for the fitting parameters which are regarded as unchanged across x. (G) Exchange current density extracted from CIET kinetics. Electrolytes are EMC:EC (7:3) with 1 M $LiClO_4$. Loading of Li_xFePO_4 in the positive electrode is 0.98 mg/cm$^2_{geo}$.

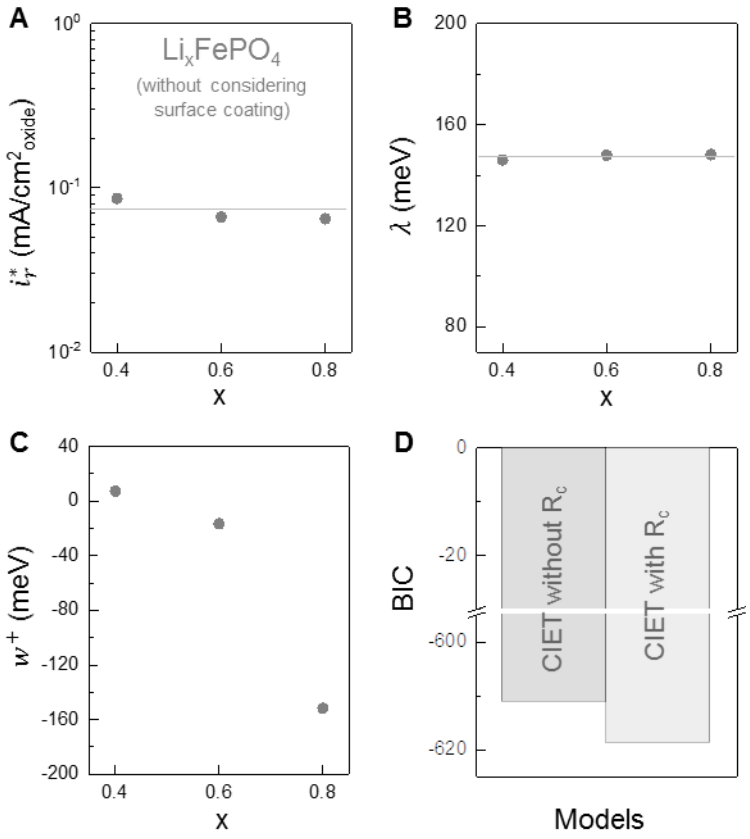

Fig. C-19. CIET fitting parameters for Li_xFePO_4, without considering surface coating R_c. Experimental data are the same ones as Fig. C-18B. Fitted values for (A) i_r^*, (B) reorganization energy λ, and (C) energy of Li^+ surface adsorption w_+. The grey straight lines indicate the average values for the fitting parameters which are regarded as unchanged across x. (D) Computed BIC values for CIET fitting with and without considering R_c. The values of k in Eq. S6 (total numbers of parameters) used to calculate BIC are 6 for CIET without R_c (constant i_r^* and λ, three different w_+), and 6 for CIET with R_c (constant i_r^*, λ, and R_c, three different w_+).

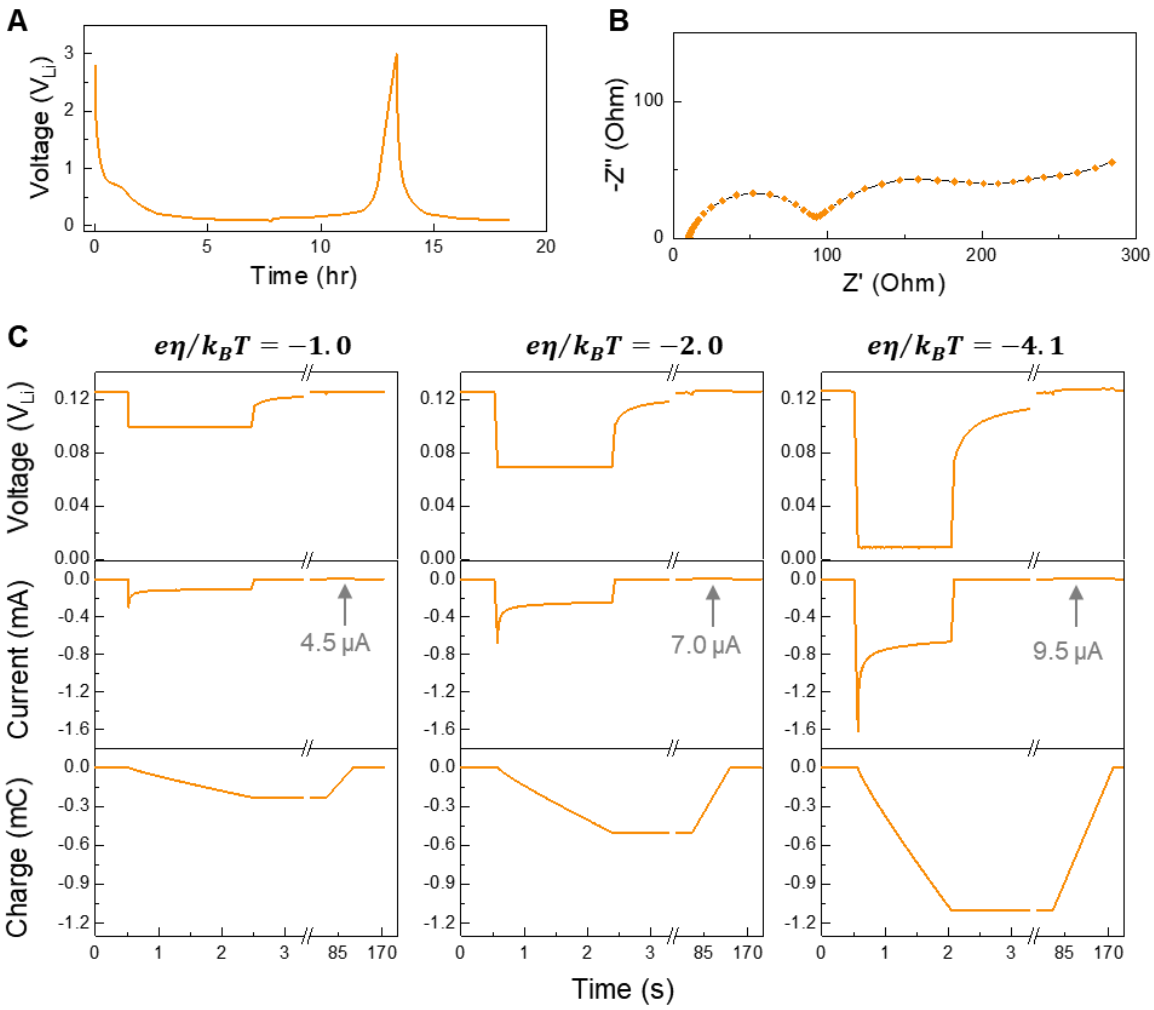

Fig. C-20. Voltage profile, EIS, and schematics for three representative charge-adjusted voltage steps at a fixed Li^+-concentration for for Li_xC_6. (A) A formation cycle between 3 V_{Li} and 0.09 V_{Li} and the following lithiation of graphite to $Li_{0.4}C_6$. Current density is around 37 mA/g_{active}. (B) EIS for $Li_{0.4}C_6$. (C) Schematics for three representative charge-adjusted voltage steps at $Li_{0.4}CoO_2$, corresponding to a fixed equilibrium voltage of around 0.125 V. Note the different time scales on the x-axis. Loading of graphite in the negative electrode is 1.48 mg/cm^2_{geo}, and the electrolyte is EMC:EC (7:3) with 1 M $LiClO_4$ salt.

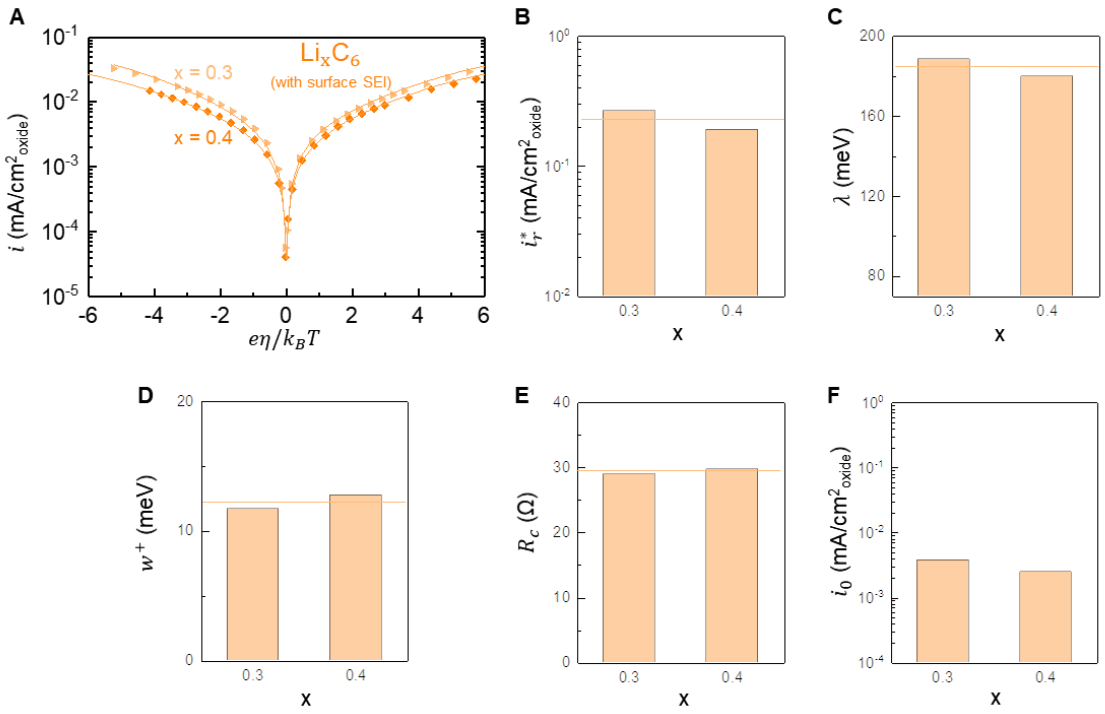

Fig. C-21. Experimental Tafel plots and fitted CIET parameters for Li_xC_6, where fitting was performed with considering surface R_c originated from solid-electrolyte interphase. (A) Experimental results (‣ for x=0.3 and ♦ for x=0.4). (B) i_r^*, (C) reorganization energy λ, (D) energy of Li^+ surface adsorption w_+, and (E) surface ionic resistance R_c fitted from CIET kinetics. The orange straight lines indicate the average values for the fitting parameters which are regarded as unchanged across x. Note that Li_xC_6 is also phase separating and the nominal x cannot reflect the real concentrations of two phases and different particles. (F) Exchange current density extracted from CIET kinetics. Electrolytes are EMC:EC (7:3) with 1 M $LiClO_4$. Loading of Li_xC_6 in the electrode is 1.47 mg/cm$^2_{geo}$. For x=0.4, the applied potential for intercalation is kept above 0 V_{Li} ($e\eta/k_BT > -4$) to avoid Li plating.

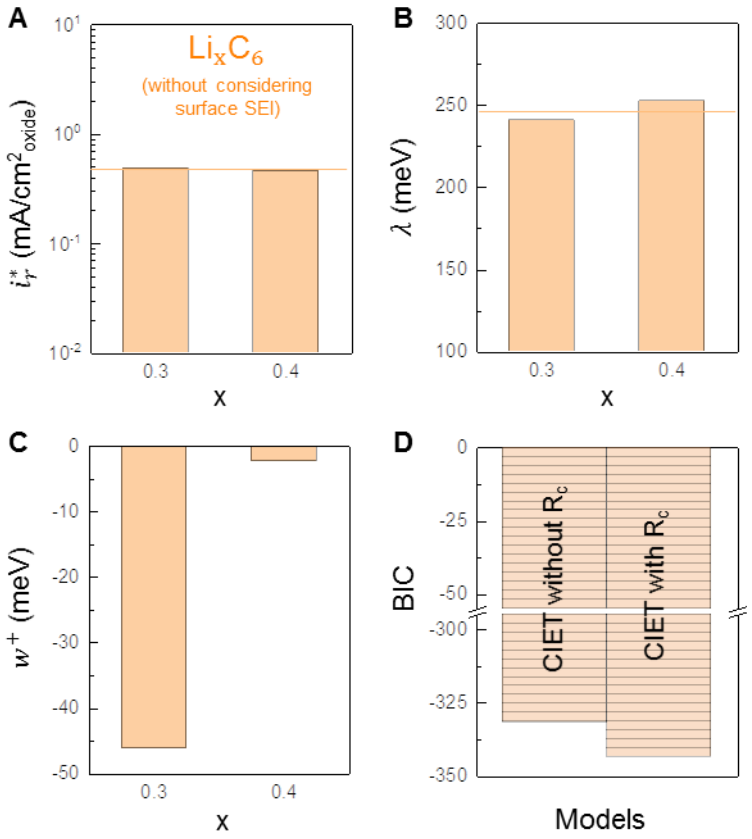

Fig. C-22. CIET fitting parameters for Li_xC_6, without considering surface R_c. Experimental data are the same ones as Fig. C-21A. Fitted values for (A) i_r^*, (B) reorganization energy λ, and (C) energy of Li^+ surface adsorption w_+. The orange straight lines indicate the average values for the fitting parameters which are regarded as unchanged across x. (D) Computed BIC values for CIET fitting with and without considering R_c. The values of k in Eq. S6 (total numbers of parameters) used to calculate BIC are 4 for CIET with R_c (constant i_r^*, λ, w_+, and R_c), 4 for CIET without R_c (constant i_r^* and λ, two different w_+).

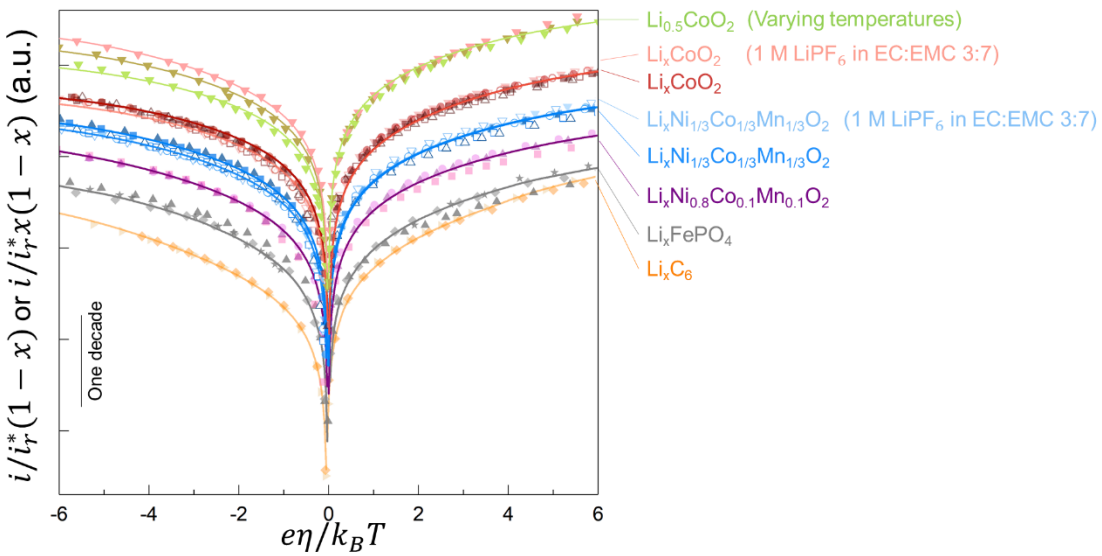

Fig. C-23. Overlay with offsets of normalized current densities. Normalizing the current densities with the fitted $\boldsymbol{i_r^*}$ times (1-x) for Li^+ insertion or x(1-x) for Li^+ extraction, with constant and arbitrary offsets between each dataset to show the collapse of each electrode/electrolyte combinations with same $\boldsymbol{i_r^*}$, $\boldsymbol{\lambda}$, and $\boldsymbol{w_+}$. Symbols for $\mathbf{Li_xCoO_2}$ (red), NMC111 (blue), NMC811 (purple), $\mathbf{Li_xFePO_4}$ (grey), and $\mathbf{Li_xC_6}$ (yellow) $\mathbf{Li_xCoO_2}$, NMC111, NMC811, and $\mathbf{Li_xC_6}$ at different Li content *x*, and $\mathbf{Li_{0.5}CoO_2}$ at three different temperatures (green) follow those of Figs. 4-2 A-C and Figs. C-17 to C-22. Electrolytes are EMC:EC (7:3) with 1 M $LiClO_4$ unless specified otherwise. Varying temperatures also varies $\boldsymbol{w_+}$, and therefore the three temperatures each has its own line.

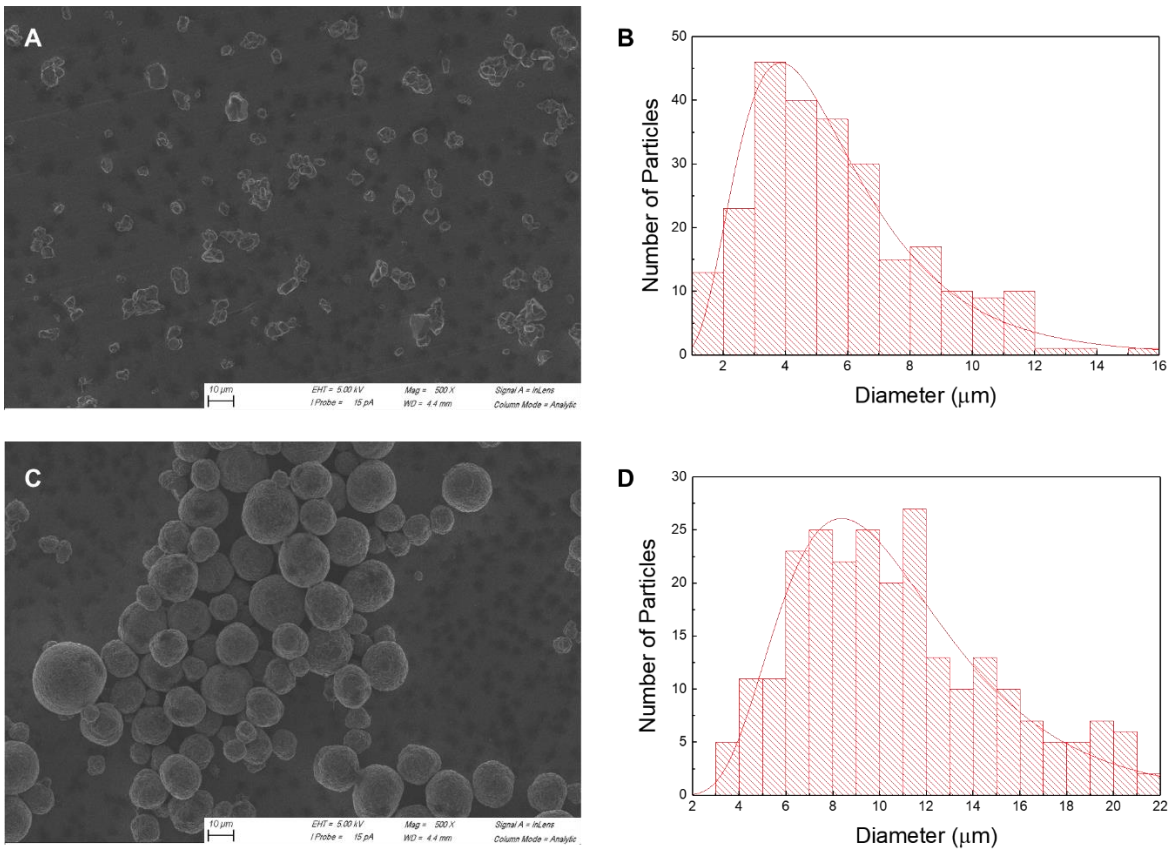

Fig. C-24. SEM images and particle size distributions for LCO and NMC111 used in Tafel kinetic measurements. Representative SEM images for (A) LCO and (C) NMC111. Histogram of particles for (B) LCO and (D) NMC111. The histogram of particles is obtained from 250 randomly selected spherical particles in SEM micrographs.

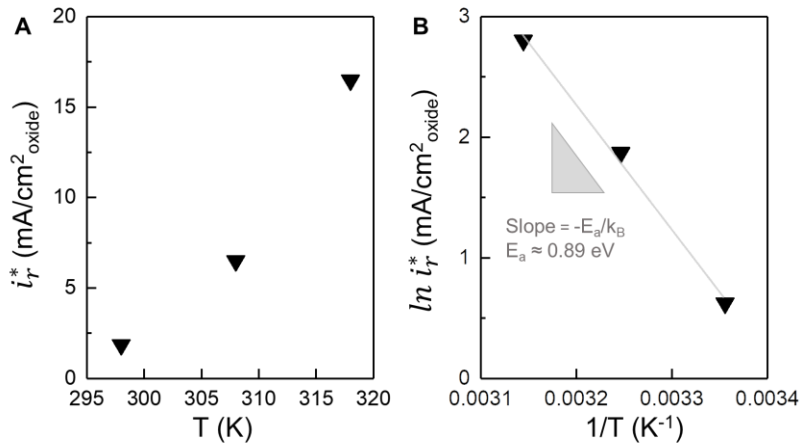

Fig. C-25. Temperature-dependent current density prefactor. (A) $\boldsymbol{i_r^*}$ at 298, 308 and 318 K fitted by CIET for $\mathbf{Li_{0.5}CoO_2}$. (B) Arrhenius plot. From the slopes of the Arrhenius plot, the activation energy for the total reaction was obtained as $E_a \approx 0.89$ eV. E_a is a convoluted activation energy for all the processes described in $\boldsymbol{i_r^*}$ (Eq. S2), including the electronic coupling process described by $\boldsymbol{H_{DA}^2}$ and the electrostatic coupling of the transferring ion with its environment $\boldsymbol{\Delta E_{IT}}$. Electrolyte is EMC:EC (7:3) with 1 M $LiClO_4$.

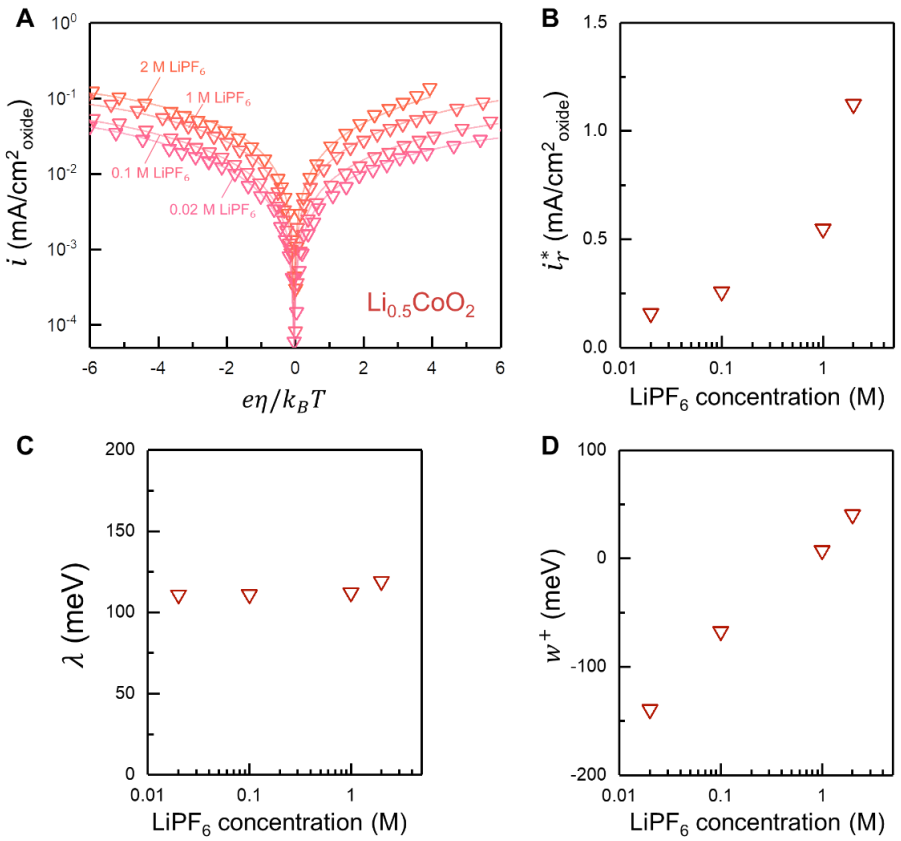

Fig. C-26. Experimental Tafel plots and CIET fitting for $\mathbf{Li_{0.5}CoO_2}$ measured in four electrolytes with different $\mathbf{LiPF_6}$ concentrations. (A) Experimental results (points) and fittings (lines). Fitted values for (A) $\boldsymbol{i_r^*}$, (B) reorganization energy $\boldsymbol{\lambda}$, and (C) energy of Li^+ surface adsorption $\boldsymbol{w_+}$ from the CIET model. Electrolytes are EMC:EC (7:3) with 2 M, 1 M, 0.1 M, and 0.02 M $LiPF_6$ respectively.

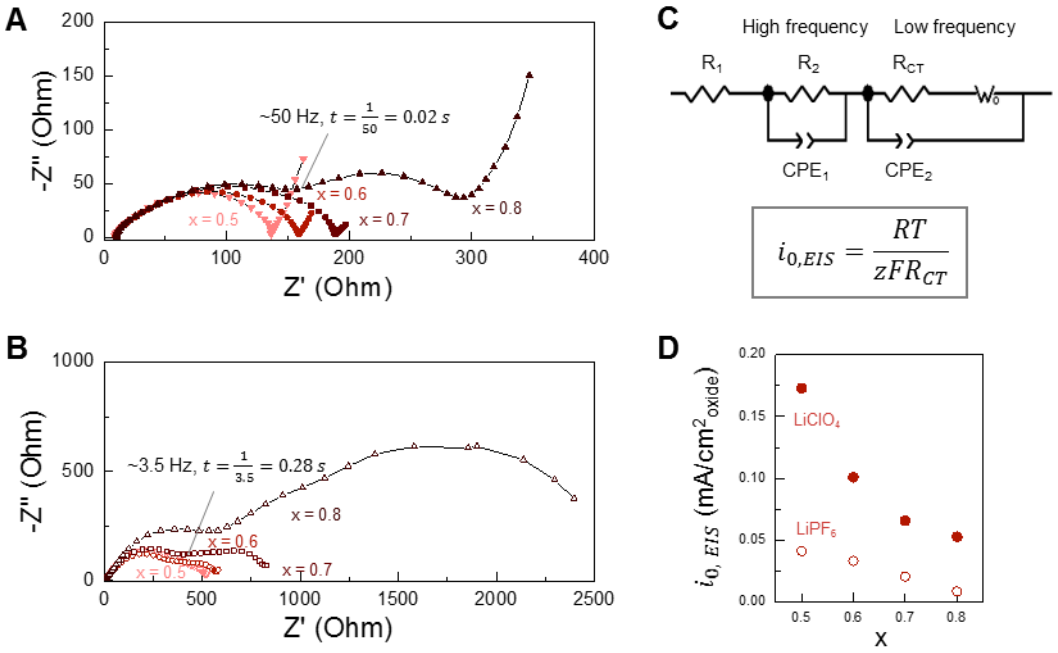

Fig. C-27. EIS and fitted exchange current density from approximation form of Bulter-Volmer kinetics $i_{0,EIS} = \frac{RT}{zFR_{CT}}$, for Li_xCoO_2. EIS for Li_xCoO_2 at x=0.5, 0.6, 0.7 and 0.8, with electrolytes (A) EMC:EC (7:3) with 1 M $LiClO_4$ and (B) EMC:EC (7:3) with 1 M $LiPF_6$. (C) Electrical circuit to fit EIS and extract charge transfer resistance R_{CT}, and formlula to extract exchange current density. (D) Extracted exchange current density from EIS. Loading of Li_xCoO_2 in the positive electrode is 0.84 mg/cm$^2_{geo}$ (for $LiClO_4$ case) and 0.88 mg/cm$^2_{geo}$ (for $LiPF_6$ case), respectively.

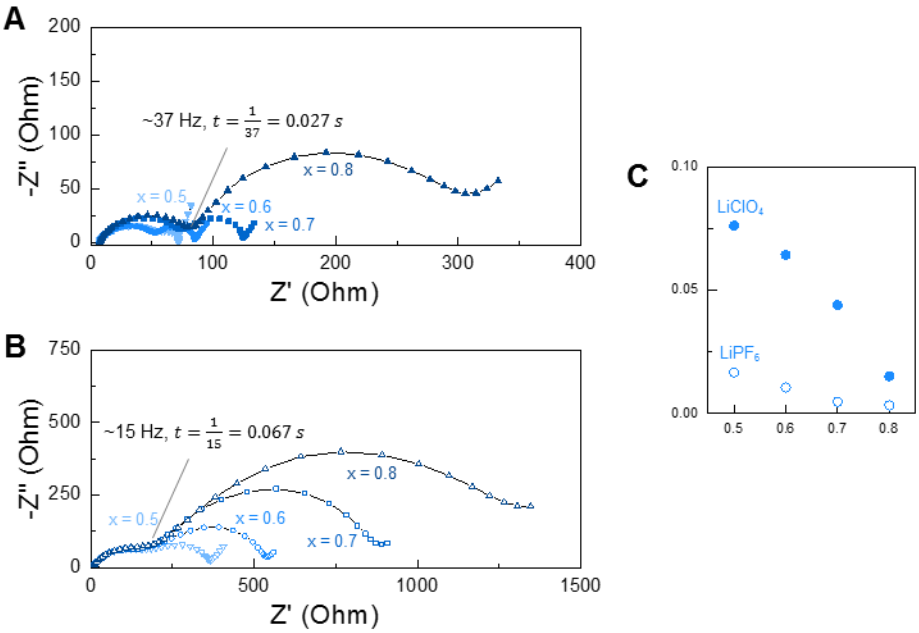

Fig. C-28. EIS and fitted exchange current density from approximation form of Bulter-Volmer kinetics $i_{0,EIS} = \frac{RT}{zFR_{CT}}$, for $Li_x Ni_{1/3} Co_{1/3} Mn_{1/3} O_2$. EIS for $Li_xNi_{1/3}Co_{1/3}Mn_{1/3}O_2$ at x=0.5, 0.6, 0.7 and 0.8, with electrolytes (A) EMC:EC (7:3) with 1 M $LiClO_4$ and (B) EMC:EC (7:3) with 1 M $LiPF_6$. (C) Extracted exchange current density from EIS. Loading of $Li_xNi_{1/3}Co_{1/3}Mn_{1/3}O_2$ in the positive electrode is 1.6 mg/cm$^2_{geo}$ (for $LiClO_4$ case) and 1.54 mg/cm$^2_{geo}$ (for $LiPF_6$ case), respectively.

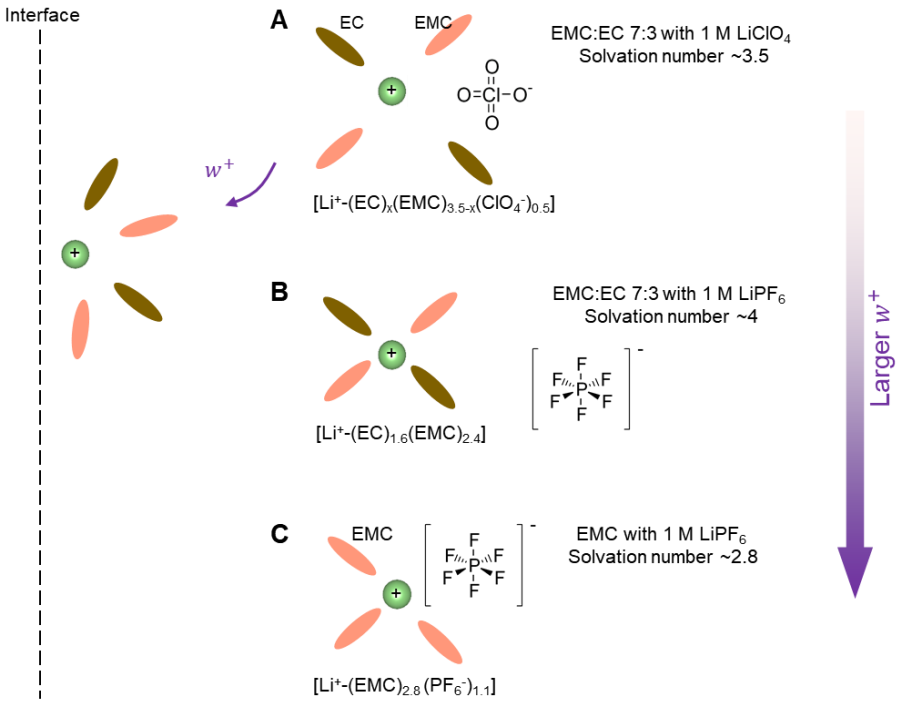

Fig. C-29. Solvation structure for three electrolytes. (A) For EMC:EC 7:3 with 1 M $LiClO_4$, Li^+ is solvated by ~3.5 solvent molecules [202], denoted as $[Li^+\text{-}(EC)_x(EMC)_{3.5-x}(ClO_4^-)_{0.5}]$. The ClO_4^- anion comes into the solvation shell because $LiClO_4$ is less dissociate than $LiPF_6$ (fully dissociative). (B) For EMC:EC 7:3 with 1 M $LiPF_6$, Li^+ is solvated by ~4 solvent molecules, denoted as $[Li^+\text{-}(EC)_{1.6}(EMC)_{2.4}]$ [133,202]. $LiPF_6$ fully dissociates and thus does not enter the Li^+ solvation shell. (C) For EMC with 1 M $LiPF_6$, Li^+ is solvated by ~2.8 solvent molecules, denoted as $[Li^+\text{-}(EMC)_{2.8}(PF_6^-)_{1.1}]$ [202–204]. Due to the low dielectric constant of EMC, $LiPF_6$ cannot fully dissociate and the PF_6^- anion enters the Li^+ solvation shell. The stronger Li^+-solvent/anion interactions result in higher energy $\mathbf{w}^+$ to bring the Li ions at their adsorbed state (in the order of EMC with 1 M $LiPF_6$ > EMC:EC 7:3 with 1 M $LiPF_6$ > EMC:EC 7:3 with 1 M $LiClO_4$), leading to lower i_r^*.

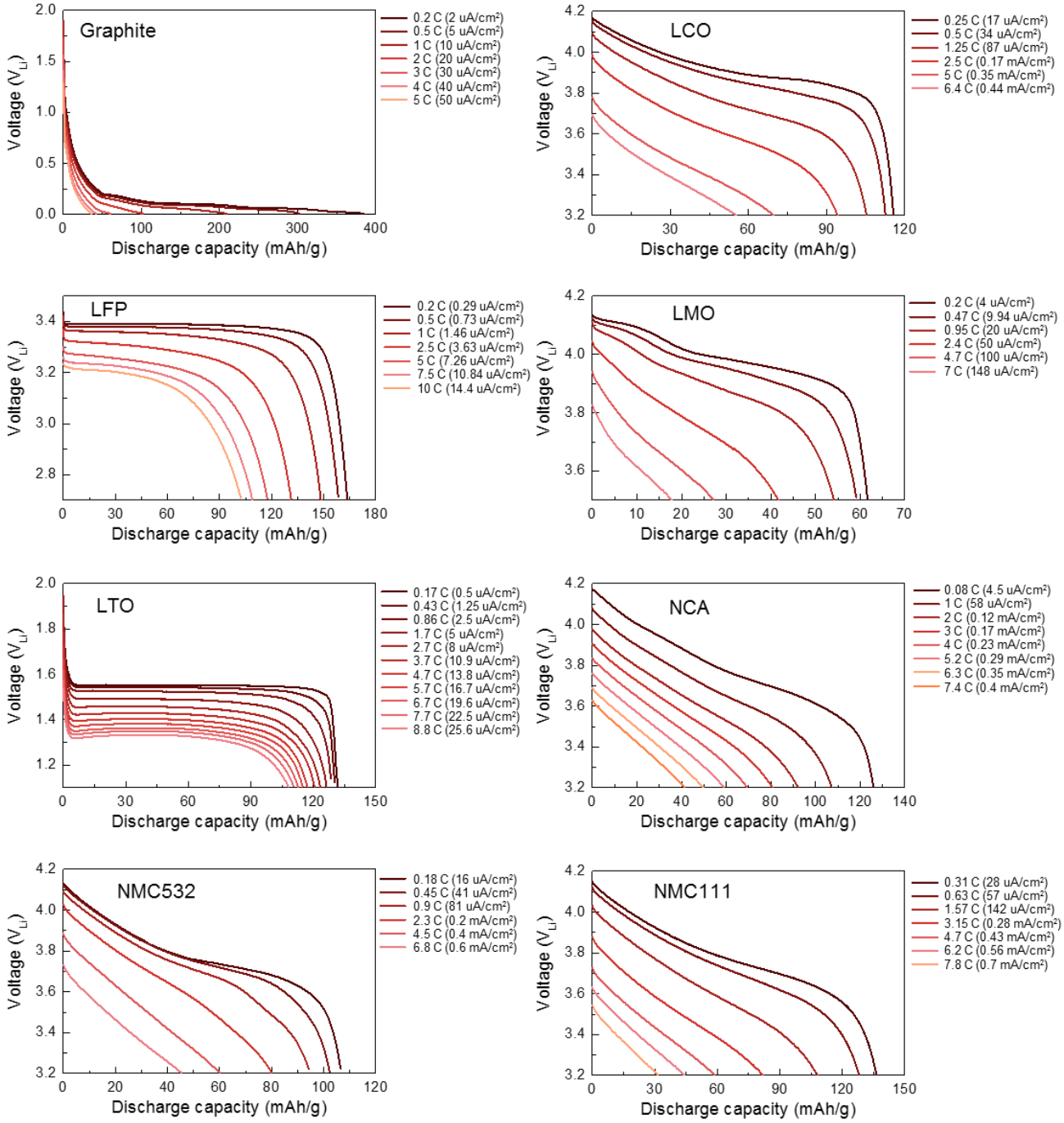

Fig. C-30. Rate capability tests for eight battery materials: graphite, LCO, LFP, LMO, LTO, NCA, NMC532, and NMC111. The C-rates are calculated with respect to the theoretical capacity for each material. Loadings and surface areas of the electrodes are listed in Table C-5.

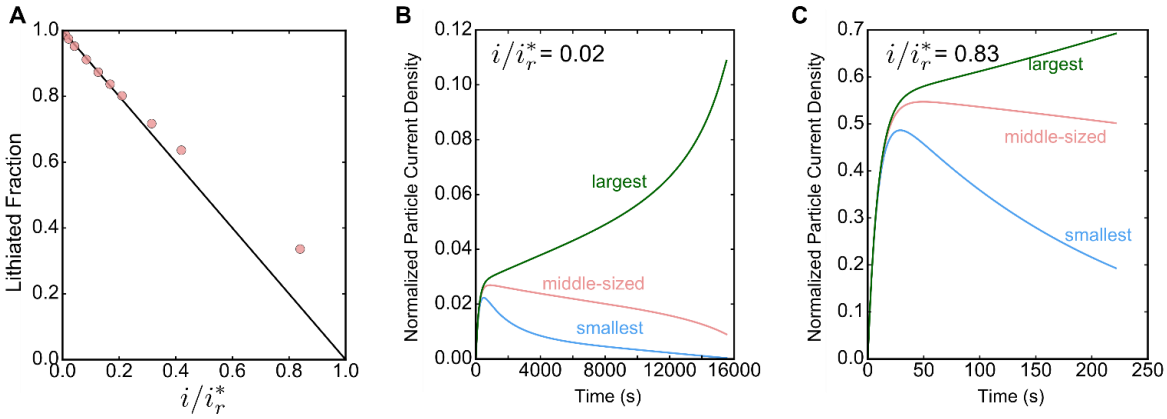

Fig. C-31. Simulated result for rate capability with a many-particle model. (A) Simulated maximum capacity as a function of macroscopic applied current *i* (normalized by $\boldsymbol{i_r^*}$). Particle-level microscopic currents for (B) a small macroscopic current $\boldsymbol{i/i_r^*}$=0.02, and (C) a large macroscopic current $\boldsymbol{i/i_r^*}$=0.83.

Appendix D: Supplementary Data for Chapter 5

Materials

Pt/C and Au/C and Ag/C catalysts:

Pt/C catalysts was supplied by Tanaka Kikinzoku (TKK TEC10E20A), with weight fraction 19%. The Au nanoparticles were synthesized following a reported approach[346] and synthesis the Au/C catalysts is discussed elsewhere.[274]

Synthesis of ionic liquids and ionic-liquid-modified catalysts

The $[C_4C_1im][NTf_2]$(1-butyl-3-methylimidazolium bis(trifluoromethanesulfonyl)imide CAS No: 174899-83-3) was purchased from Sigma Aldrich. [TMPim][NTf2] 1,3-Bis(2,4,6-trimethylphenyl)imidazolium bis(trifluoromethanesulfonyl)imide was synthesized by the reported anion exchange reaction[347] and discussed elsewhere.[274] $[MTBD][NTf_2]$(1,3,4,6,7,8-Hexahydro-1-methyl-2H-pyrimido[1,2-a]pyrimidinebis(trifluoromethanesulfonyl)imide), $[DBU][NTf_2]$(2,3,4,6,7,8,9,10-Octahydropyrimidol[1,2-a]azepine bis(trifluoromethanesulfonyl)imide), [DEMA][NTf2](N,N-diethylmethylamine bis(trifluoromethanesulfonyl)imide, $[TEMEDA][NTf_2]$ (N,N,N′,N′-tetramethylethylenediamine bis(trifluoromethanesulfonyl)imide), $[C_4Him][NTf_2]$ (1-butyl-imidazolium bis(trifluoromethanesulfonyl)imide) were prepared through neutralization reactions.[274] The ionic-liquid-modified catalysts were synthesized by a reported protocol[244], by mixing M/C with iso-propyl alcohol solution containing IL, followed by ultrasonic treatments, solvent evaporation and drying under vacuum (details in Ref. [274]).

Supplementary figures for Chapter 5

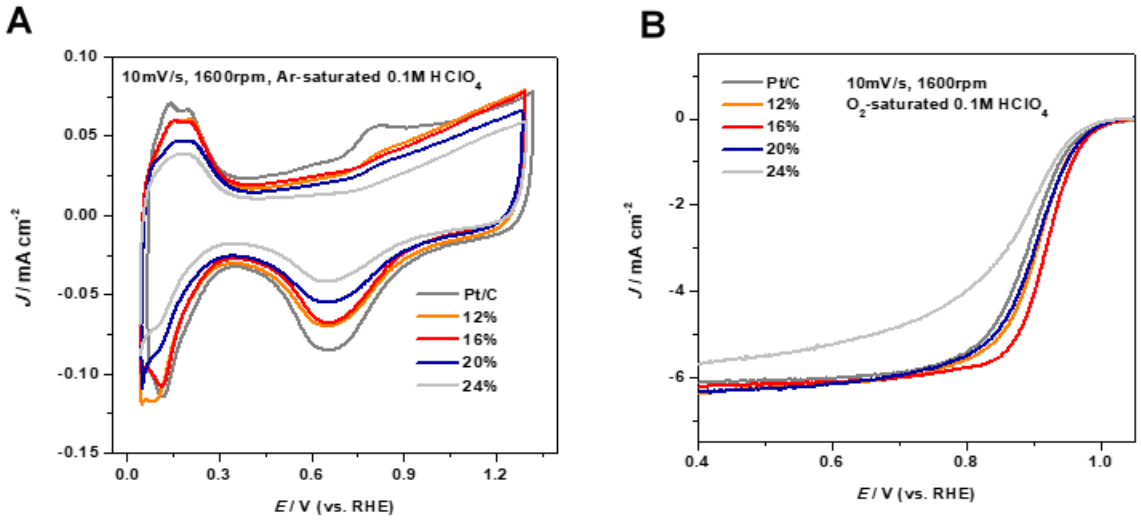

Fig. D-1 IL loading dependent experiments. (A) CV curves of Pt/C modified with different loading of $[C_4C_1im][NTf_2]$ measured in Ar saturated 0.1 M $HClO_4$, rotation speed is 1600 rpm and the scan rate is 10 mV s^{-1}. The counter electrode is Pt wire electrode. The reference electrode is $Hg/HgSO_4$, which was converted to RHE scale by calibrating of HER/HOR polarization test. The average thickness of ionic liquids on Pt/C were estimated to be 0.6 nm for 12% loading, 0.9 nm for 16% loading, 1.1 nm for 20% loading and 1.4 nm for 24% loading, with assumption that the specific surface area of carbon support is 200 $m^2 \cdot g^{-1}$ and the specific surface area of 2nm Pt nanoparticles is 70 $m^2 \cdot g^{-1}$. (B) Background and *iR* corrected ORR polarization curves measured in O_2 saturated 0.1 M $HClO_4$, rotation speed is 1600 rpm, and the scan rate is 10 mV s^{-1}. The loading of Pt was controlled at 20 $\mu g \cdot cm^{-2}$. 0.05 wt% Nafion was added to the catalytic layer. The results suggested 16% is the best loading.

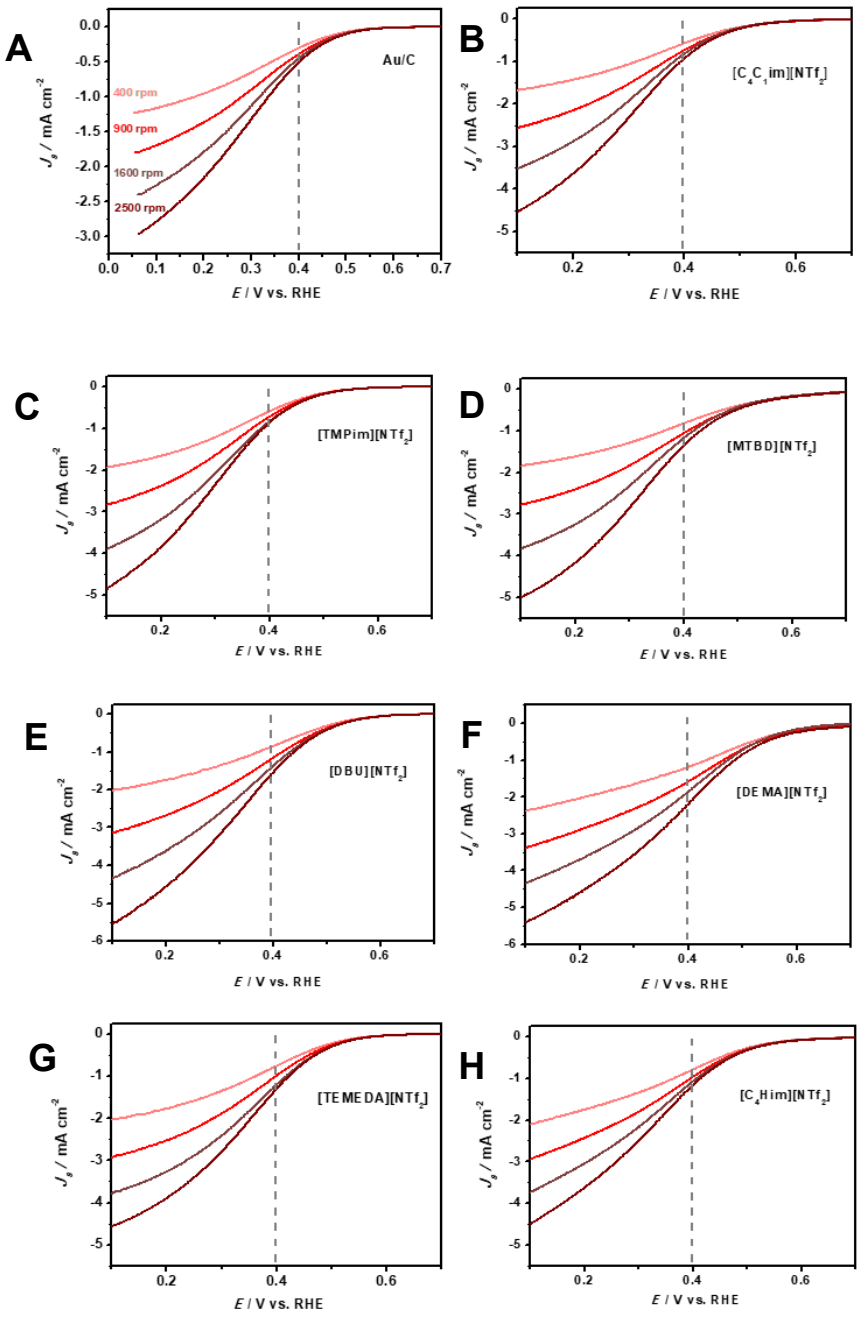

Fig. D-2 Rotation dependent background and *iR* corrected ORR polarization curves of ionic liquids modified Au/C, measured in O_2-saturated 0.1 M $HClO_4$. The rotation speed is controlled at 400 rpm, 900 rpm, 1600 rpm and 2500 rpm, and the scan rate is 10 mV s^{-1}. The counter electrode is graphite electrode. The reference electrode is $Hg/HgSO_4$, which was converted to RHE scale by calibrating of HER/HOR polarization test. The loading of Au was controlled at 40 μg·cm^{-2}, the ionic liquid loading is 16 wt%. 0.05 wt% Nafion was added to the catalytic layer.

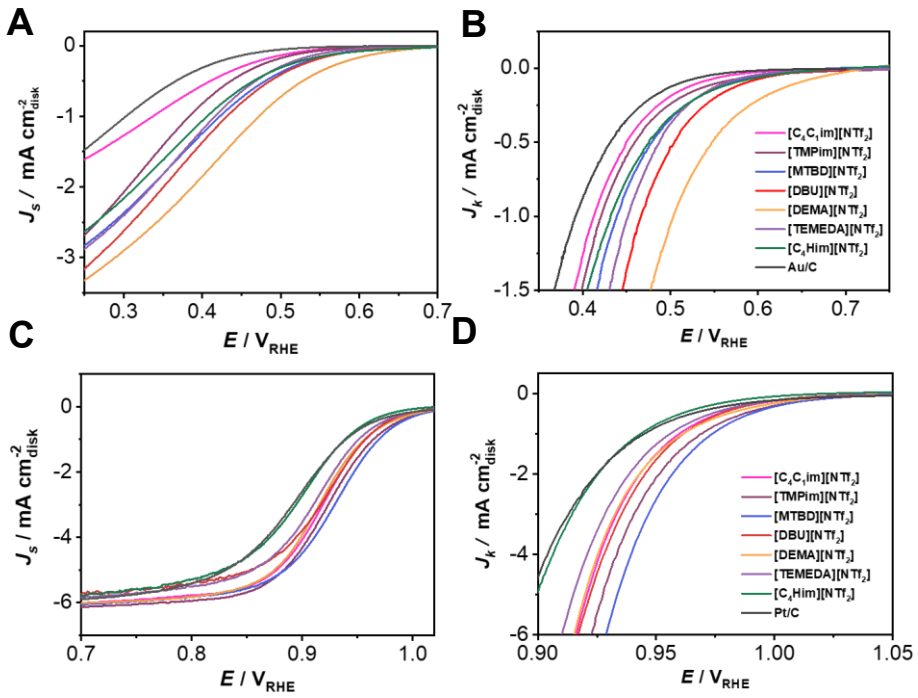

Fig. D-3 (A, C) Background and *iR* corrected ORR polarization curves of ionic-liquid-modified Au/C (A) and Pt/C (C). The polarization curves were measured in O_2-saturated 0.1 M $HClO_4$, with a scan rate of 10 mV/s and the rotation speed is 1600 rpm. The counter electrode is graphite electrode for measurements of Au/C, and is Pt wire electrode for measurements of Pt/C. The reference electrode is $Hg/HgSO_4$, which was converted to RHE scale by calibrating of HER/HOR polarization test. The loading of Au was controlled at 40 μg·cm^{-2} and Pt was controlled at 20 μg·cm^{-2}. 0.05 wt% Nafion was added to the catalytic layer. (B, D) The kinetic currents of Au/C (B) and Pt/C (D) were extracted from polarization curves. Typically, the Koutecký–Levich plot were generated to extract the kinetic currents of Au/C. The inverse of ORR current (i_m^{-1}) measured with 400rpm, 900rpm, 1600rpm and 2500 rpm (Fig. D-2) were plot against the $\omega^{-1/2}$, ω is the rotation speed. The inverse of the kinetic current (i_k^{-1}) was obtained by extracting the intercept of the fitting line. Besides, the kinetic currents of Pt/C were extracted by Koutecký–Levich equation directly. The specific method of determination of kinetic current was depicted in Supplementary methods. The kinetic current densities (J_k) were obtained by normalizing kinetic current (i_k) by the area of working electrode.

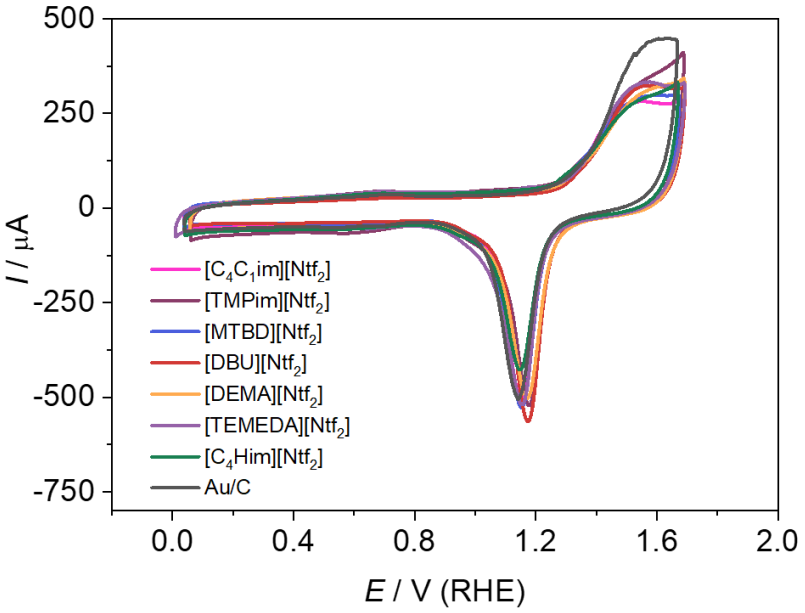

Fig. D-4 CV curves of ionic-liquid-modified Au/C measured in Ar-0.1 M $HClO_4$, rotation speed is 1600 rpm and the scan rate is 50 mV s^{-1}. The counter electrode is graphite electrode. The reference electrode is $Hg/HgSO_4$, which was converted to RHE scale by calibrating of HER/HOR polarization test. The loading of Au was controlled at 40 $\mu g \cdot cm^{-2}$, the ionic liquid loading is 16 wt%. 0.05 wt% Nafion was added to the catalytic layer.

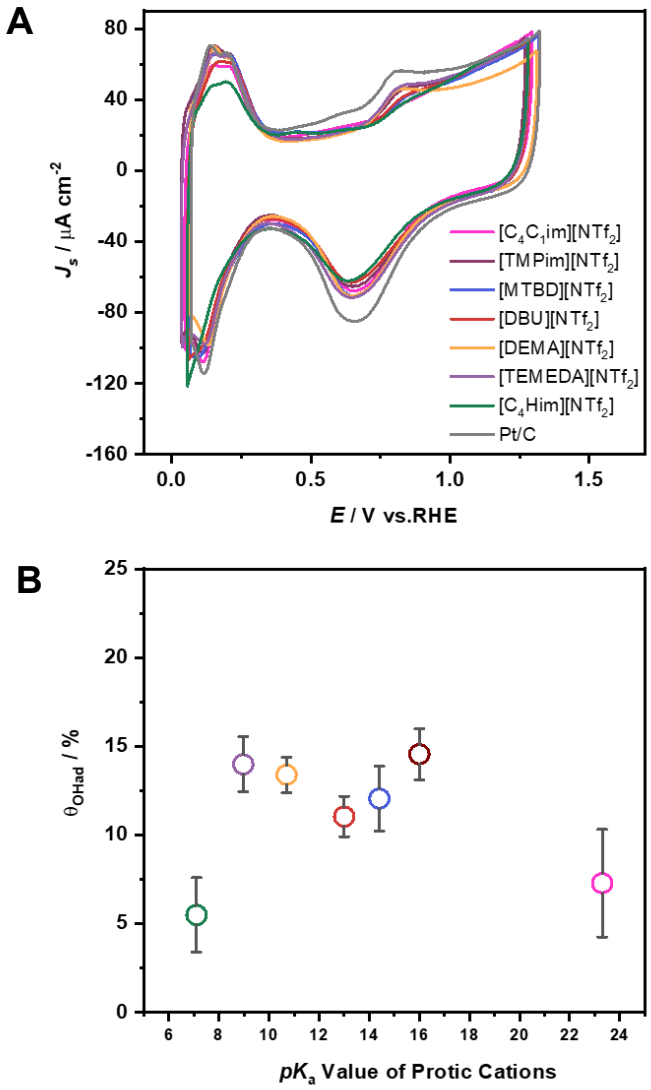

Fig. D-5 Cation dependent CV curves. (A) CV curves of ionic-liquid-modified Pt/C at 10 mV s^{-1} in Ar-saturated 0.1 M $HClO_4$. The counter electrode is Pt wire electrode. The reference electrode is $Hg/HgSO_4$, which was converted to RHE scale by calibrating of HER/HOR polarization test. The loading of Pt was controlled at 20 μg·cm^{-2}. 0.05 wt% Nafion was added to the catalytic layer. (B) the relationship between OH coverage and the pK_a value of cations. Error bars represent standard deviations (SDs) of at least three independent measurements.

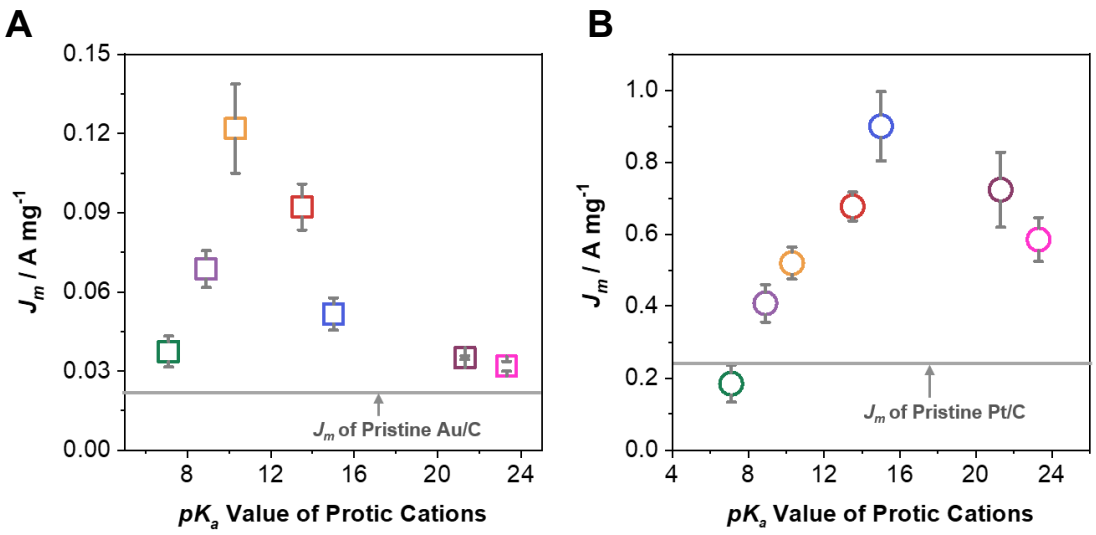

Fig. D-6. The relationship between the mass-normalized kinetic current densities of ionic-liquid-modified Au/C (A), Pt/C (B) as a function of pK_a value of protic cations in ionic liquids. The mass-normalized kinetic current densities were obtained by normalizing kinetic current (i_k) (Fig. D-3) by the mass of Au and Pt deposited on working electrode. Error bars represent SDs of at least three independent measurements.

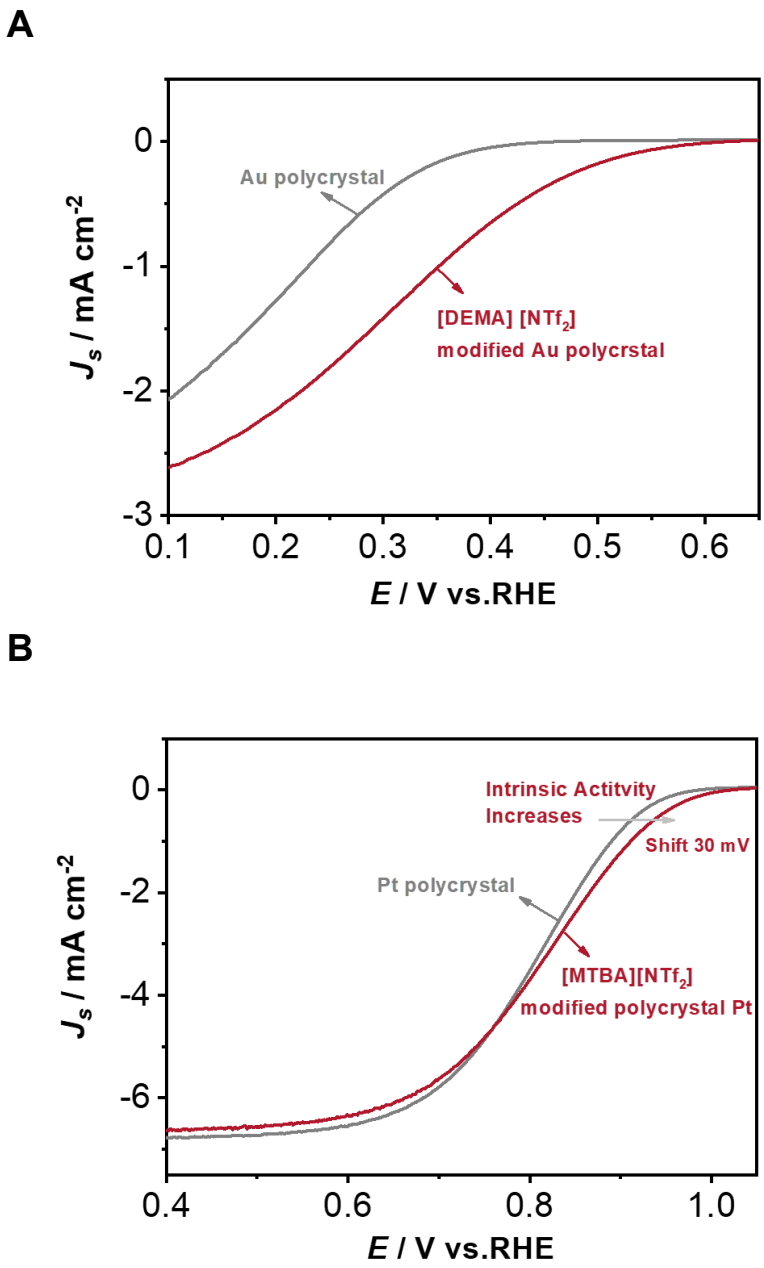

Fig. D-7 Ionic liquid enhancement for bulk electrode. (a) background and *iR*-corrected ORR polarization curves of polycrystal Au electrode and [DEMA][NTf_2]-modified polycrystal Au electrode. (b) Background and *iR*-corrected ORR polarization curves of polycrystal Pt electrode and [MTBD][NTf_2]-modified polycrystal Pt electrode. The experiments were measured at 10 mV s^{-1} and 1600 rpm in O_2-saturated 0.1 M $HClO_4$. 2μL ionic liquids were deposit on working electrode, resulting in 100 μm ionic liquid layer, which is much thicker than ionic liquid modified nanomaterials.

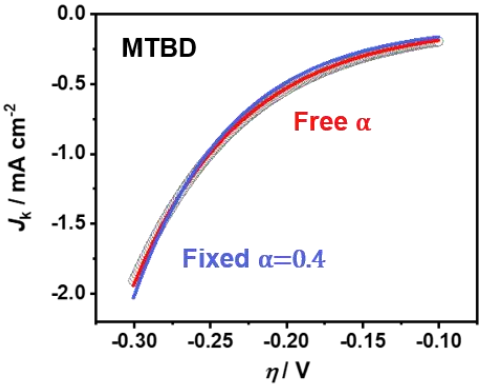

α	j_0 / mA cm^{-2}	$j_{0,s}$ / mA cm$_{Au}^{-2}$
0.3626	0.02667	$1.46*10^{-3}$
0.4	0.01802	$9.84*10^{-4}$

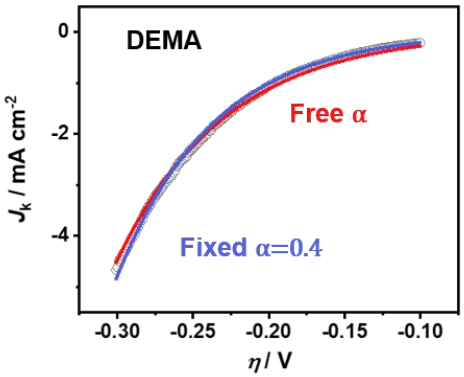

α	j_0 / mA cm^{-2}	$j_{0,s}$ / mA cm$_{Au}^{-2}$
0.3563	0.06952	$3.38*10^{-3}$
0.4	0.04474	$2.18*10^{-3}$

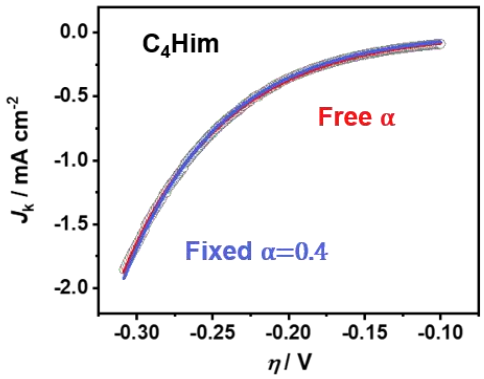

α	j_0 / mA cm^{-2}	$j_{0,s}$ / mA cm$_{Au}^{-2}$
0.3848	0.01843	$1.09*10^{-3}$
0.4	0.01575	$9.34*10^{-4}$

Fig. D-8 ORR kinetic current density of Au/C measured in oxygen saturated 0.1M $HClO_4$ (Fig. D-3B) is plotted against overpotential (η) and fitted to the Butler-Volmer equation with faraday constant F=96485 C mol^{-1}, idea gas constant R=8.314 J mol^{-1} K^{-1} and temperature T=293.15K. Charge coefficient α was found in the range of 0.35-0.4 when it free to vary. To simplify comparison, we then fixed α at 0.4 to extract the exchange current density (J_0). The specific exchange current density ($J_{0,s}$) was extracted by normalizing j_0 with electrochemically surface area of Au. The equilibrium potential of ORR on Au was defined as the equilibrium potential of oxygen reducing to H_2O_2 (O_2 + $2H^+ + 2e^- \rightarrow H_2O_2$, 0.68 V_{RHE})

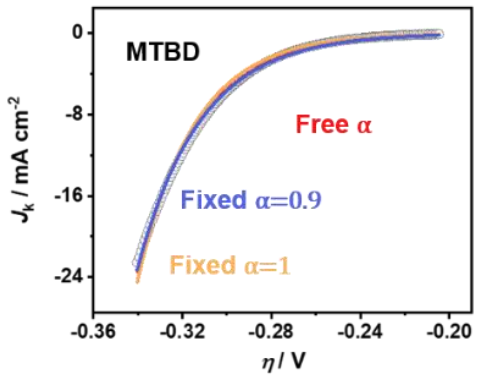

α	J_0 / mA cm^{-2}	$J_{0,s}$ / mA cm$_{Pt}^{-2}$
0.9106	1.34*10^{-4}	5.28*10^{-6}
0.9	1.53*10^{-4}	6.02*10^{-6}
1	4.29*10^{-5}	1.68*10^{-6}

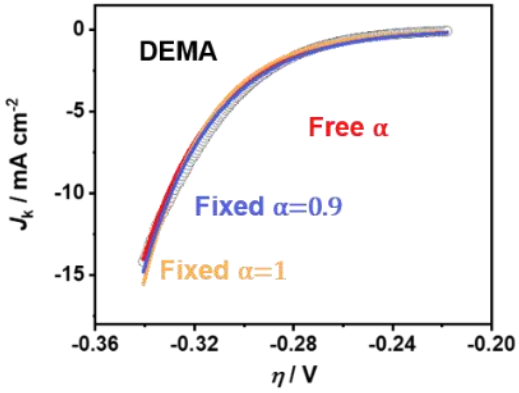

α	J_0 / mA cm^{-2}	$J_{0,s}$ / mA cm$_{Pt}^{-2}$
0.8921	1.01*10^{-4}	3.98*10^{-6}
0.9	9.63*10^{-5}	3.79*10^{-6}
1	2.69*10^{-5}	1.06*10^{-6}

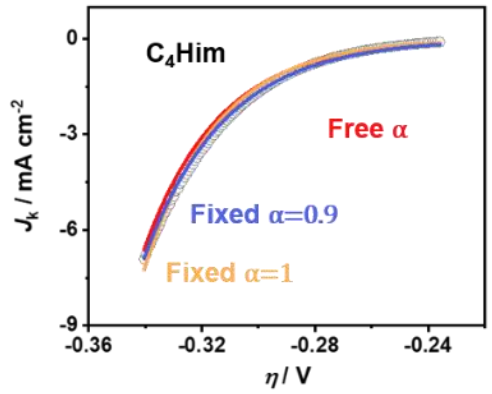

α	J_0 / mA cm^{-2}	$J_{0,s}$ / mA cm$_{Pt}^{-2}$
0.9582	2.16*10^{-5}	1.23*10^{-6}
0.9	4.53*10^{-5}	2.59*10^{-6}
1	1.26*10^{-5}	7.20*10^{-7}

Fig. D-9 ORR kinetic current density of Pt/C measured in oxygen saturated 0.1M $HClO_4$ (Fig. D-3D) is plotted against overpotential (η) and fitted to the Butler-Volmer equation with faraday constant F=96485 C mol^{-1}, idea gas constant R=8.314 J mol^{-1} K^{-1} and temperature T=293.15K. Charge coefficient α was found in the range of 0.9-1 when it free to vary. To simplify comparison, we then fixed α at 0.9 and 1 to extract the exchange current density (J_0). The specific exchange current density ($J_{0,s}$) was extracted by normalizing J_0 with electrochemically surface area of Pt. The equilibrium potential of ORR

on Pt was defined as the equilibrium potential of oxygen reducing to H_2O ($O_2 + 4H^+ + 4e^- \rightarrow H_2O$, 1.23 V_{RHE}).

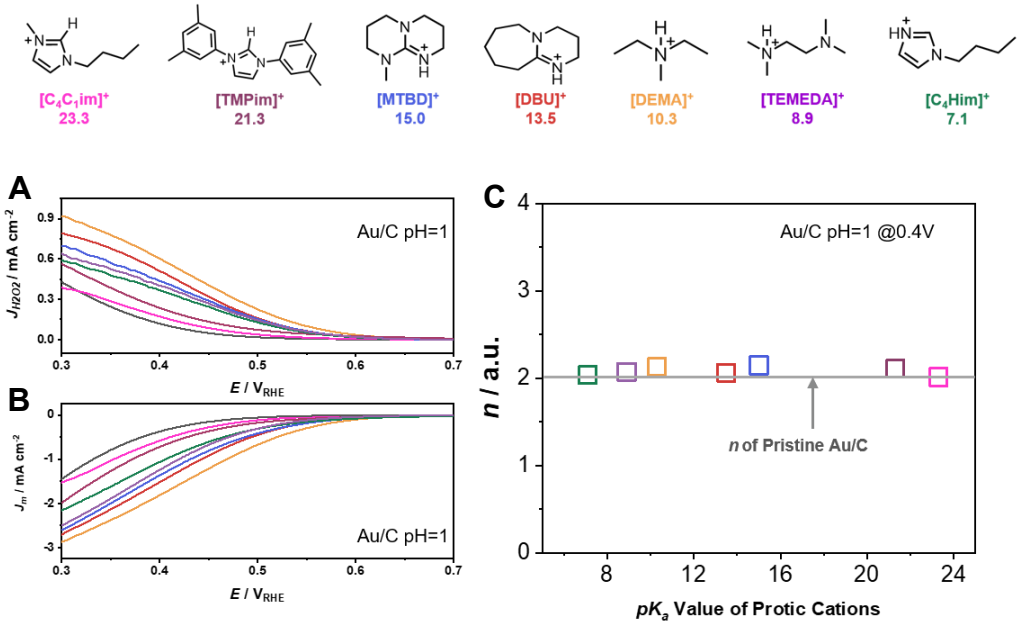

Fig. D-10. pK_a-dependent ORR activity on Au/C measured in O_2-saturated 0.1 M $HClO_4$, with a scan rate of 10 mV/s and the rotation speed is 1600 rpm. (A) The H_2O_2 production in ORR process (denoted as *n*) measured on ionic-liquids-modified Au/C by RRDE; (B) Background and *IR* corrected ORR polarization curves of ionic-liquids-modified Au/C; (C) The number of electrons transferred in ORR process (denoted as *n*) was extracted from J_m and J_{H2O2} following the equation that $\boldsymbol{n = 4 \times \frac{J_m}{J_m + \frac{J_{H_2O_2}}{N_c}}}$, N_c is the collection efficiency of RRDE which is 0.37 here. The loading of Au was controlled at 40 μg·cm^{-2}. 0.05wt% Nafion was added to the catalytic layer.

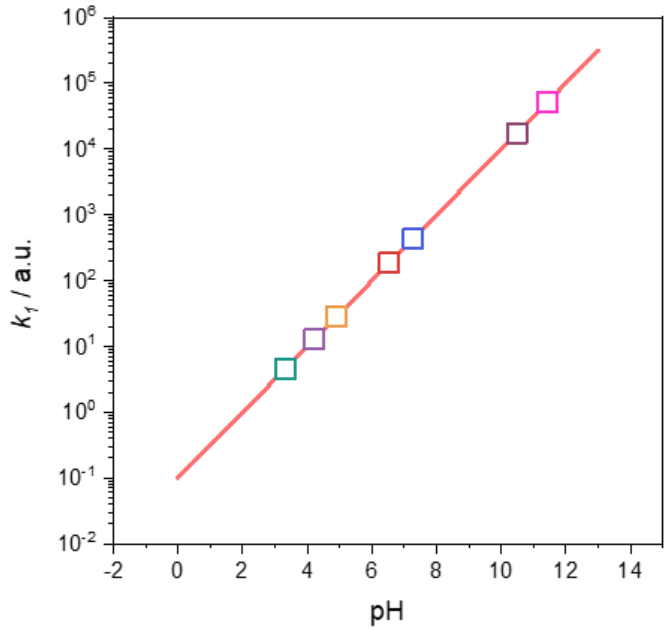

Fig. D-11 The pH effect on the first step of ORR on Au in ionic liquids (O_2 + e^- + N-H^+ => OOH + N) was estimated using Koper's model[187], the detailed method was depicted in Supplementary methods. The local pH of ionic liquids is calculated from pK_a value of them. As shown in Fig. D-11, the apparent rate constant (k_1) of first ORR step on Au in ionic liquids can increase by two to six orders of magnitude compared to the reaction carried out in acid solution when pH=0. Although, the rate constant of the first step (O_2 + e^- + H^+ => OOH) has been suggested to be slightly slower than the second step (OOH + e^- + H^+ => HOOH) in acid aqueous solution, the difference is estimated to be less than 2 orders of magnitude[258]. Because the second step is coupled PCET step, which isn't affected by pH[221], k_1 would become much higher than k_2 in ionic liquids, which would make the second step play a more important role in overall kinetics. This suggestion agrees with the previous works in studying oxygen reduction in organic solvent, where the first ET step[259] is about 3 orders of magnitude faster than the second PCET step[260].

Table D-1. Summary of estimated size and coverage of cations. The predicted and measured enhancement of ORR on Au and Pt were also depicted. The coverage of intermediates (O_{Pt} and OH_{Pt} on Pt) is about 20-30% at ORR relevant potentials[262,348] and that of cations was estimated to be 17-30% on Pt and 18-32% on Au, we suggested the coverage of cations is comparative with the coverage of ORR intermediates when we consider the ORR intermediates on the surface grabbing proton from ionic liquids. Further, the predict enhancement in intrinsic activity of RDS is higher than measured enhancement in overall reaction rate, indicating the ionic liquids can afford the enhancement observed

experimentally, even though the coverage of $[MTBD]^+$ and $[DEMA]^+$ is lower than $[C_4Him]^+$.

Cation	Length / Å	Width / Å	Coverage on Pt	Coverage on Au	Predicted enhancement on Pt (j_0)	Measured enhancement on Pt (j_0)	Predicted enhancement on Au (j_0)	Measured enhancement on Au (j_0)
$[MTBD]^+$	9.1	5.1	17%	18%	5.88	2.33	1.09	1.05
$[DEMA]^+$	8.5	5.1	18%	19%	1.62	1.47	4.07	2.33
$[C_4Him]^+$	6.3	4.1	30%	32%	1	1	1	1

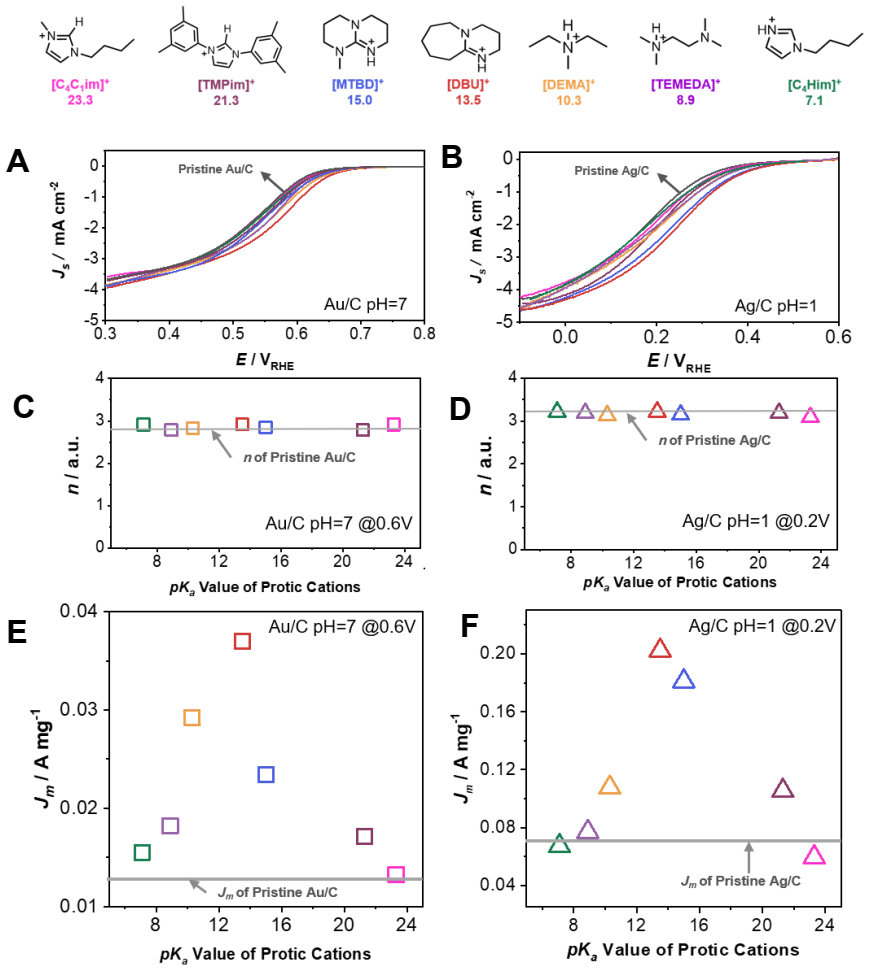

Fig. D-12. pK_a-dependent ORR activity on Au/C measured in O_2-saturated 0.1 M $NaClO_4$ and Ag/C measured in O_2-saturated 0.1 M $HClO_4$, with a scan rate of 10 mV/s

and the rotation speed is 1600 rpm. (A and B) Background and *IR* corrected ORR polarization curves of ionic-liquids-modified Au/C (A) and Ag/C (B); (c and d) The number of electrons transferred in ORR process (denoted as *n*) was measured on Au/C (C) and Ag/C (D) by RRDE. *n* was extracted from J_m and J_{H2O2} following the equation that $\boldsymbol{n = 4 \times \frac{J_m}{J_m + \frac{J_{H_2O_2}}{N_c}}}$, N_c is the collection efficiency of RRDE, which is 0.37 in these measurements; (E and F) The relationship between the enhancement in ORR mass specific kinetic currents on ionic-liquids-modified Au/C (E), Ag/C (F) as a function of the pK_a value of protic cations in ionic liquids. The loading of Au and Ag was controlled at 40 μg·cm^{-2}. 0.05wt% Nafion was added to the catalytic layer.

The ORR polarization curves of ionic-liquid-modified Au/C in 0.1M $NaClO_4$ are depicted in Fig. D-13 (A). ORR activity was found depend on pK_a value of cations. The number of electrons transferred in ORR (*n*) is depicted in Fig. D-13 (C), showing that *n* of Au/C and ionic-liquid-modified Au/C is within 2.7-2.9, which reveals that Au/C in the natural electrolyte catalyse ORR via both two-electron and four-electron pathway. The relationship between pK_a value of cations and ORR enhancement of Au/C is depicted in Fig. D-13 E. The maximum ORR activity enhancement for Au/C at pH=7 was found for [DBU][NTf_2] with pK_a of 13.5, of which the pK_a is higher than [DEMA][NTf_2] (pK_a=10.3) for two-electron pathway and lower than [MTBD][NTf_2] (pK_a=15.0) for four-electron pathway. Besides, the max enhancement for ionic liquid modified Au/C (Fig. D-13 E) was found around 2.6 time, which is slightly lower than the max enhancement of Au/C measured at pH=1 depicted in Fig. 5-1 (about 5 times). The reason for the decrease in maximum enhancement might be originated from the compromising enhancement of [DBU][NTf_2] for both two-electron and four-electron pathway.

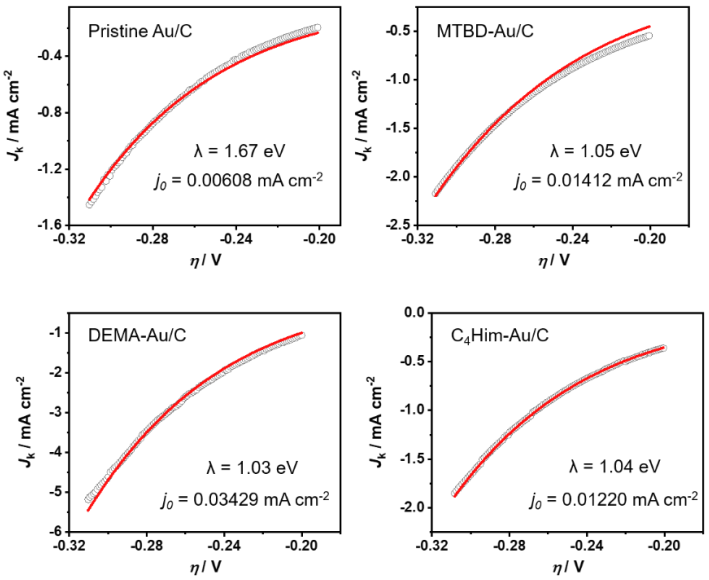

Fig. D-13 ORR kinetic current density of Au/C measured in oxygen saturated 0.1M $HClO_4$ (Fig. D-3B) is plotted against overpotential (η) and fitted to the MHC equation. The reorganization energy extracted from MHC equation is depicted in figures. The details of analysis were depicted in supplementary methods. The equilibrium potential of ORR on Au was defined as the equilibrium potential of oxygen reducing to H_2O_2 ($O_2 + 2H^+ + 2e^- \rightarrow H_2O_2$, 0.68 V_{RHE}). The results show that the reorganization energy in aqueous solution is 1.67 eV and in ionic liquids are around 1 eV. Therefore, the hydrophobic environment created by ionic liquids (static dielectric constant is around 12-15 in bulk[349,350]) actually reduce the dielectric constant of catalysts' surface compared with aqueous environment (static dielectric constant is 78.5 in bulk[351]) and, consequently, reduce the reorganization energy for ORR and increase ORR activity. Moreover, the reorganization energy for different ionic liquids is similar, since the dielectric constant is similar for the ionic liquids we studied, of which the anion is TFSI[349,350]. Therefore, our discussion in manuscript focused on the effect of hydrogen bonding structure on the pre-exponential factor and exchange current density of ORR by comparing PCET kinetics of different ionic liquids.

Besides, we could extract the dielectric constant in local reaction environment by Born model from reorganization energy, $\boldsymbol{\lambda_o = \frac{e^2}{8\pi\varepsilon_0 k_B T}\left(\frac{1}{a_0} - \frac{1}{2d}\right)\left(\frac{1}{\varepsilon_{op}} - \frac{1}{\varepsilon_s}\right)}$, where $\boldsymbol{\varepsilon_0}$ is the permittivity of free space, $\boldsymbol{a_0}$ as the effective radius of the reactant, $\boldsymbol{d}$ as the distance from the redox center to the surface of the electrode, $\boldsymbol{\varepsilon_{op}}$ the optical dielectric constant and $\boldsymbol{\varepsilon_s}$ as the static dielectric constant of the electrolyte near the electrified interface. The radius of H_2O_2 molecule (1.3 Å) was adopted as the radius of redox species for $\boldsymbol{a_0}$, the distance *d* between redox and the Au electrode was found to be 3.0 Å in previous work[18], the optical dielectric constant is 1.8 for water and around 2.0 for ionic liquids. It is also need to mention that the reorganization energy we extracted from MHC theory ($\boldsymbol{\lambda}$) is compose of inner and outer components, $\boldsymbol{\lambda = \lambda_i + \lambda_o}$, and we need to obtain $\boldsymbol{\lambda_o}$ for fitting Born Model by subtracting $\boldsymbol{\lambda_i}$ from $\boldsymbol{\lambda}$. The inner component of reorganization energy for ORR on Au can be estimated by the George-Griffith model[352,353], where $\boldsymbol{\lambda_i = 2n\left[\frac{f_z f_{z+1}}{f_z + f_{z+1}}(\Delta r)^2\right]}$ having $\boldsymbol{f_i}$ as force constant described by $\boldsymbol{4\pi^2 m_L C^2 \omega_i^2 / \mathcal{N}_A}$, $\boldsymbol{\Delta r}$ is the change in bond length between oxidized and reduced forms, n is the number of ligands, $\boldsymbol{m_L}$ is the molar mass of the ligand, $\boldsymbol{C}$ is the speed of light in vacuum and $\boldsymbol{\mathcal{N}_A}$ is the Avogadro constant. The change in O-H bond length ($\boldsymbol{\Delta r}$) could be measured in DFT models of oxidized species (HOO···H-N, ~2 Å) and reduced species (HOO-H···N, ~1 Å), the inner reorganization energy was calculated to be 0.38 - 0.43 eV for three different cations and 0.45 eV for water. Consequently, we can estimate that the dielectric constants of ionic liquid on Au surface is around 2.5 - 2.6, which is evident lower than that of water on Au (~3.6) under ORR condition. Therefore, we can further confirm that the increasing hydrophobicity of ionic liquids can reduce the dielectric constant in local reaction environment and consequently reduce the reorganization energy of ORR.

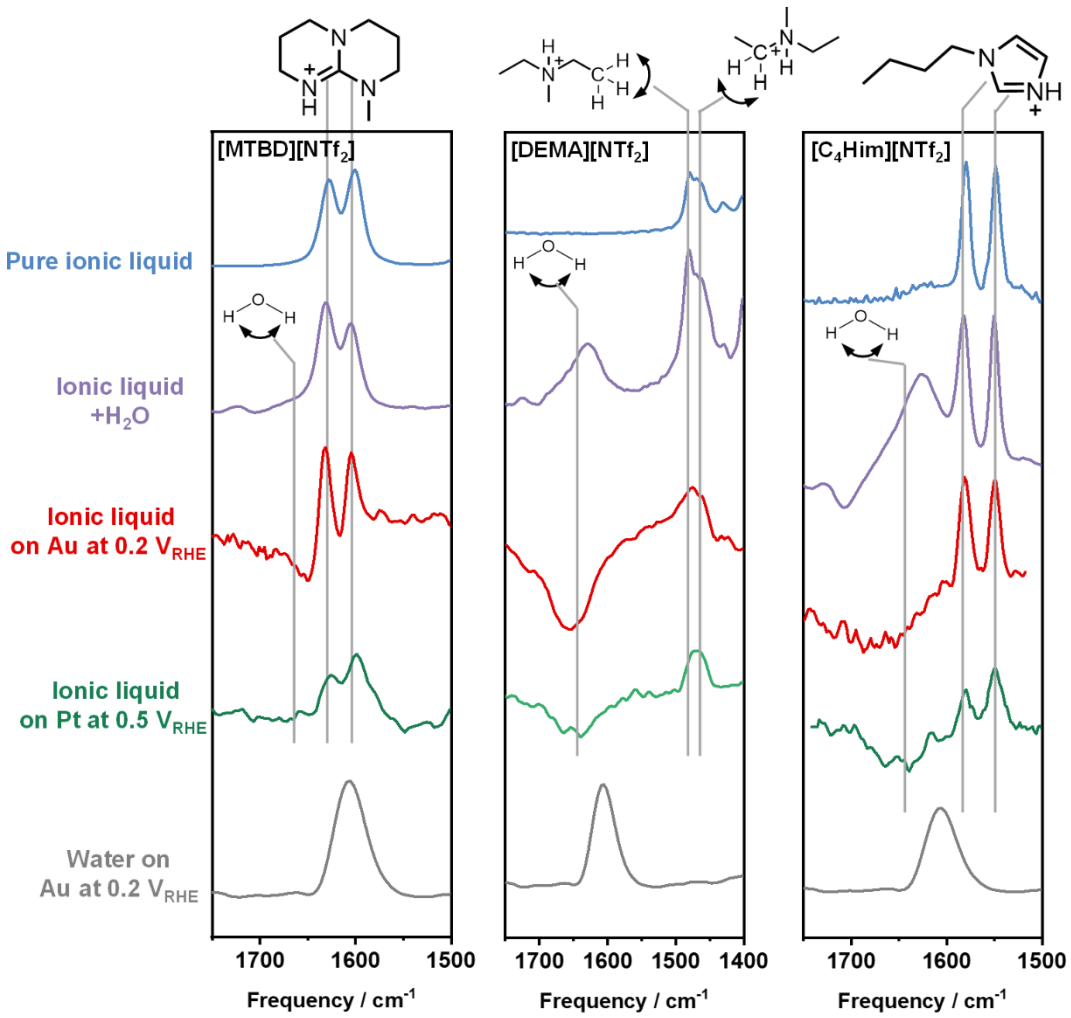

Fig. D-14 The HOH bending signal of water and the signal of cations for pristine ionic liquid (blue), ionic liquid with 0.5 M water (purple), ORR on ionic-liquid-modified Au at 0.2 V_{RHE} (red), ORR on ionic liquid modified Pt at 0.5 V_{RHE} (green) and the HOH bending signal of water on bare Au surface at 0.2 V_{RHE} (gray). The cumulative number of 256 was used at a 4 cm^{-1} resolution. Spectra were subtracted with respect to a reference spectrum obtained at OCV in 0.1 M $HClO_4$.

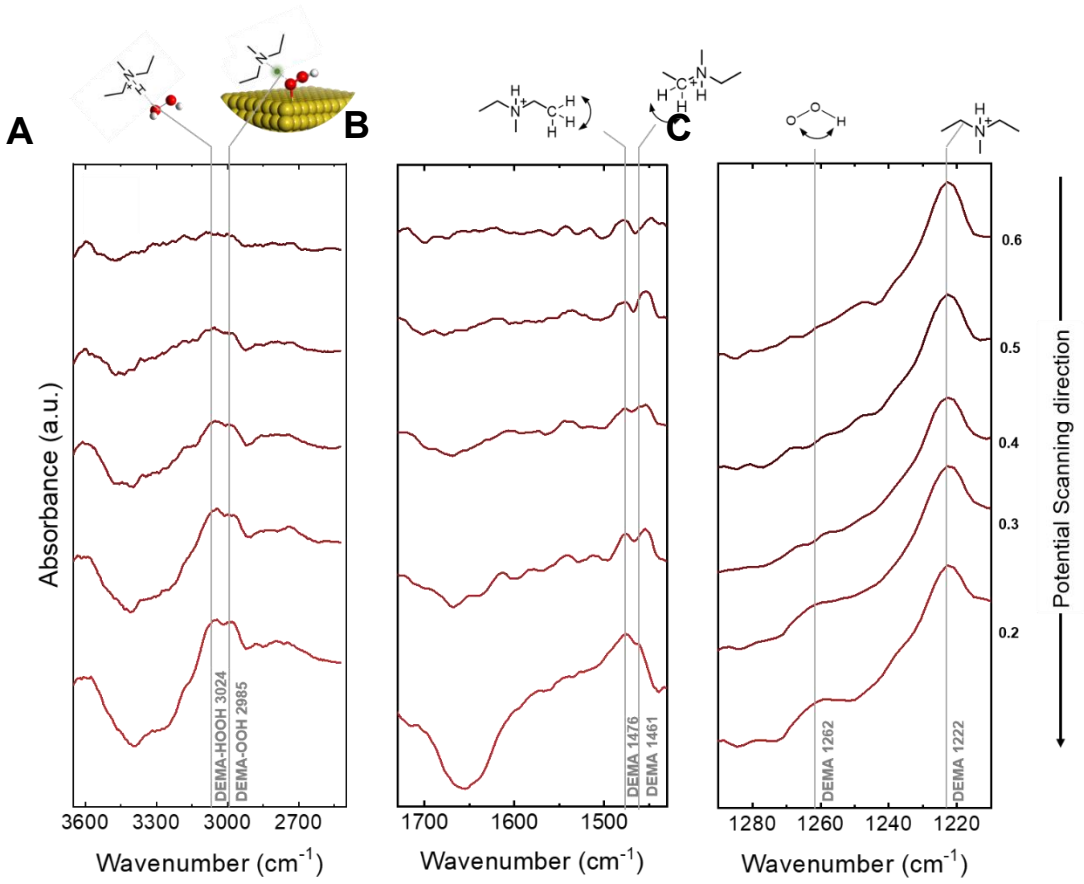

Fig. D-15 *In-situ* ATR-SEIRAS measurement on a [DEMA][NTf_2]-modified Au electrode in oxygen-saturated 0.1 M $HClO_4$. (A) X-H (X=N, O) stretching region, the molecular schematic represents the H-bond specie formed between $[DEMA]^+$ and OOH; (B) H-C-H bending region and (C) O-O-H bending region were obtained during potential steps swept from 0.2 V_{RHE} to 0.6 V_{RHE} in 0.1 M $HClO_4$. The cumulative number of 256 was used at a 4 cm^{-1} resolution. Spectra were subtracted with respect to a reference spectrum obtained at OCV in 0.1 M $HClO_4$.

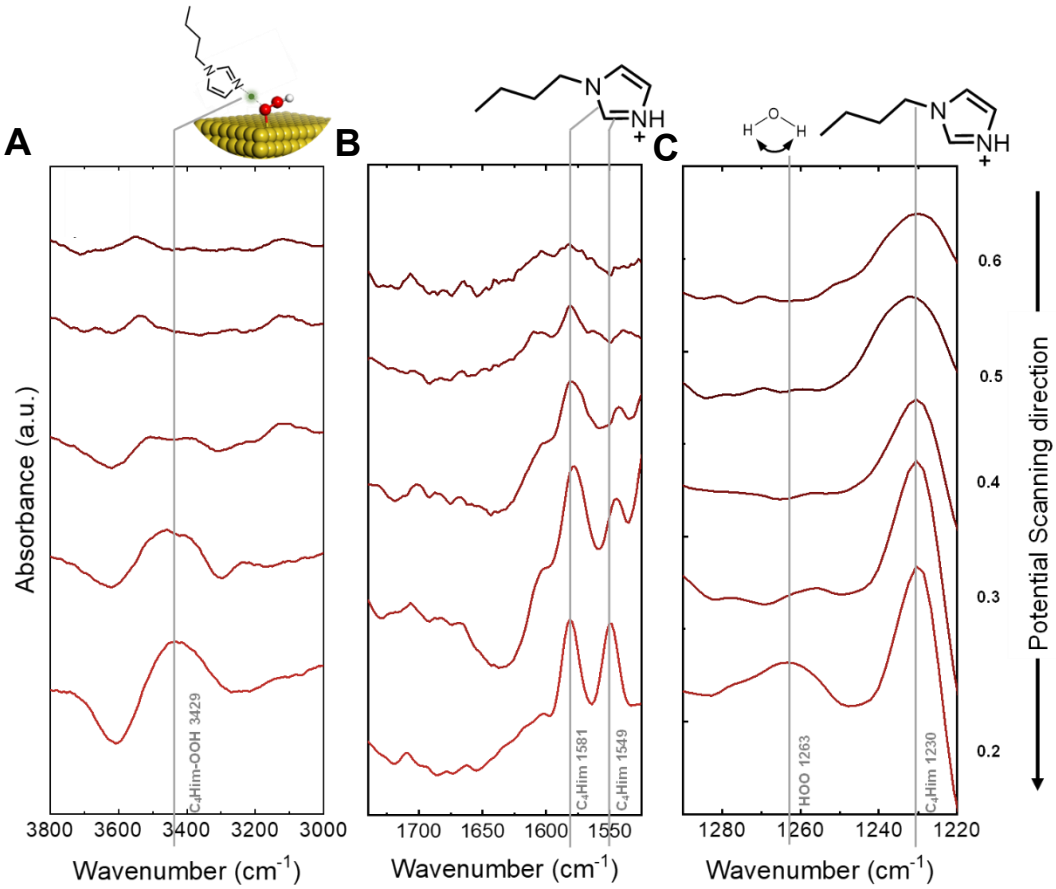

Fig. D-16 *In-situ* ATR-SEIRAS measurement on a [C_4Him][NTf_2]-modified Au electrode in oxygen-saturated 0.1 M $HClO_4$. (A) X-H (X=N, O) stretching region, the molecular schematic represents the H-bond specie formed between $[C_4Him]^+$ and OOH; (B) C=N stretching region and (C) O-O-H bending region were obtained during potential steps swept from 0.2 V_{RHE} to 0.6 V_{RHE} in 0.1 M $HClO_4$. The cumulative number of 256 was used at a 4 cm^{-1} resolution. Spectra were subtracted with respect to a reference spectrum obtained at OCV in 0.1 M $HClO_4$.

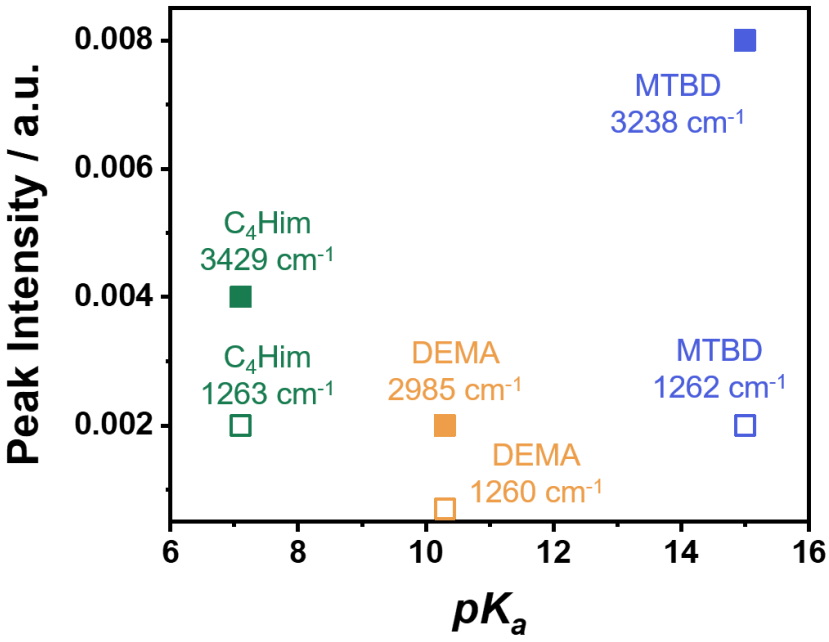

Fig. D-17 The peak intensity of N-H stretching (solid square) and O-O-H bending (open square) of [MTBD][NTf_2]-modified (blue, Fig. 5-2B, C), [DEMA][NTf_2]-modified (yellow, Fig. D-15) and [C_4Him][NTf_2]-modified (green, Fig. D-16) Au electrode at 0.2V_{RHE} in 0.1M $HClO_4$. The cumulative number of 256 was used at a 4 cm^{-1} resolution.

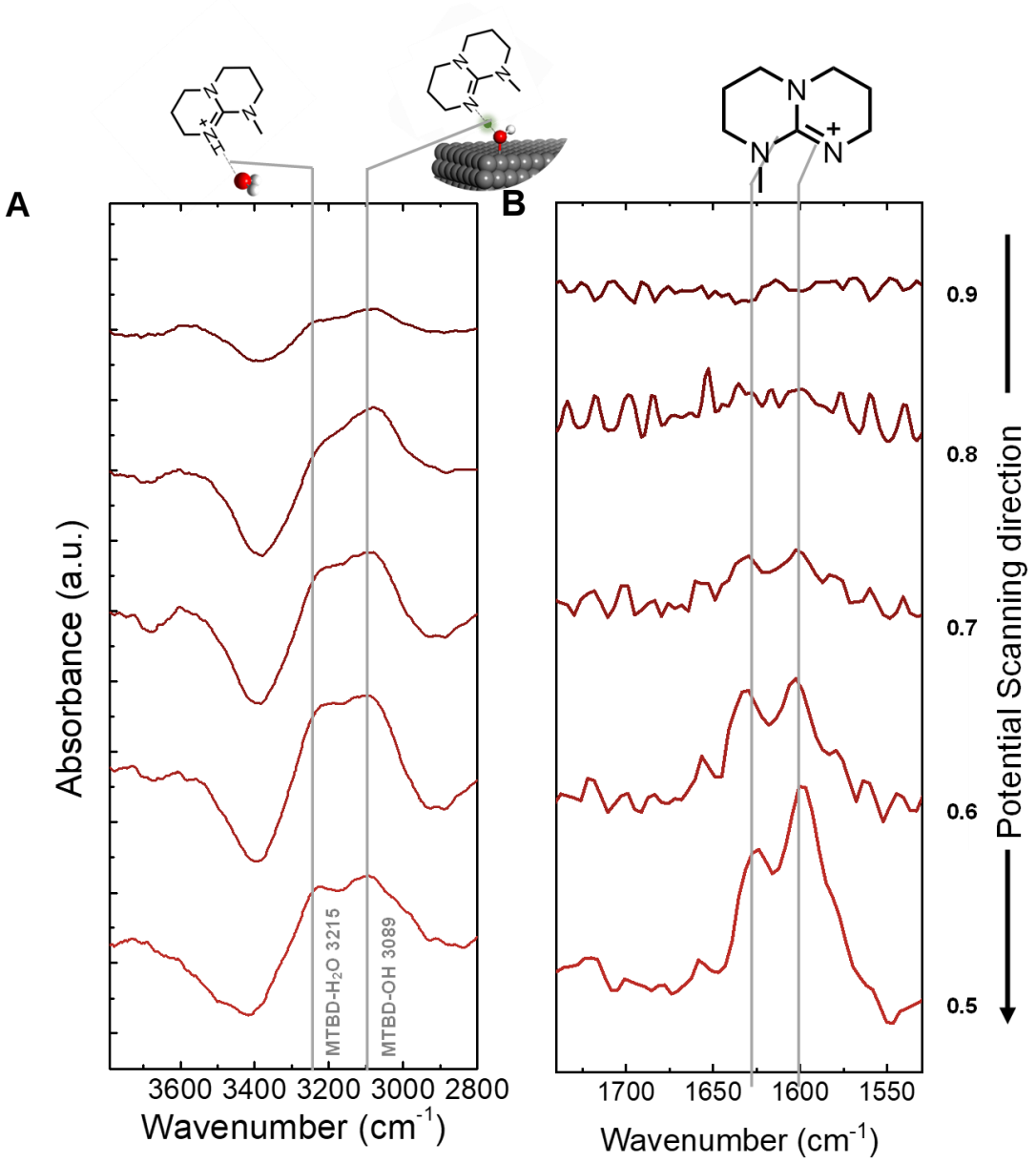

Fig. D-18 *In-situ* ATR-SEIRAS measurement on a [MTBD][NTf_2]-modified Pt electrode modified by [MTBD][NTf_2] in oxygen-saturated 0.1 M $HClO_4$. (A) X-H (X=N, O) stretching region, the molecular schematic represents the H-bond specie formed between $[MTBD]^+$ and OH; (B) C=N stretching region were obtained during potential steps swept from 0.5 V_{RHE} to 0.9 V_{RHE} in 0.1 M $HClO_4$. The cumulative number of 256 was used at a 4 cm^{-1} resolution. Spectra were subtracted with respect to a reference spectrum obtained at OCV in 0.1 M $HClO_4$.

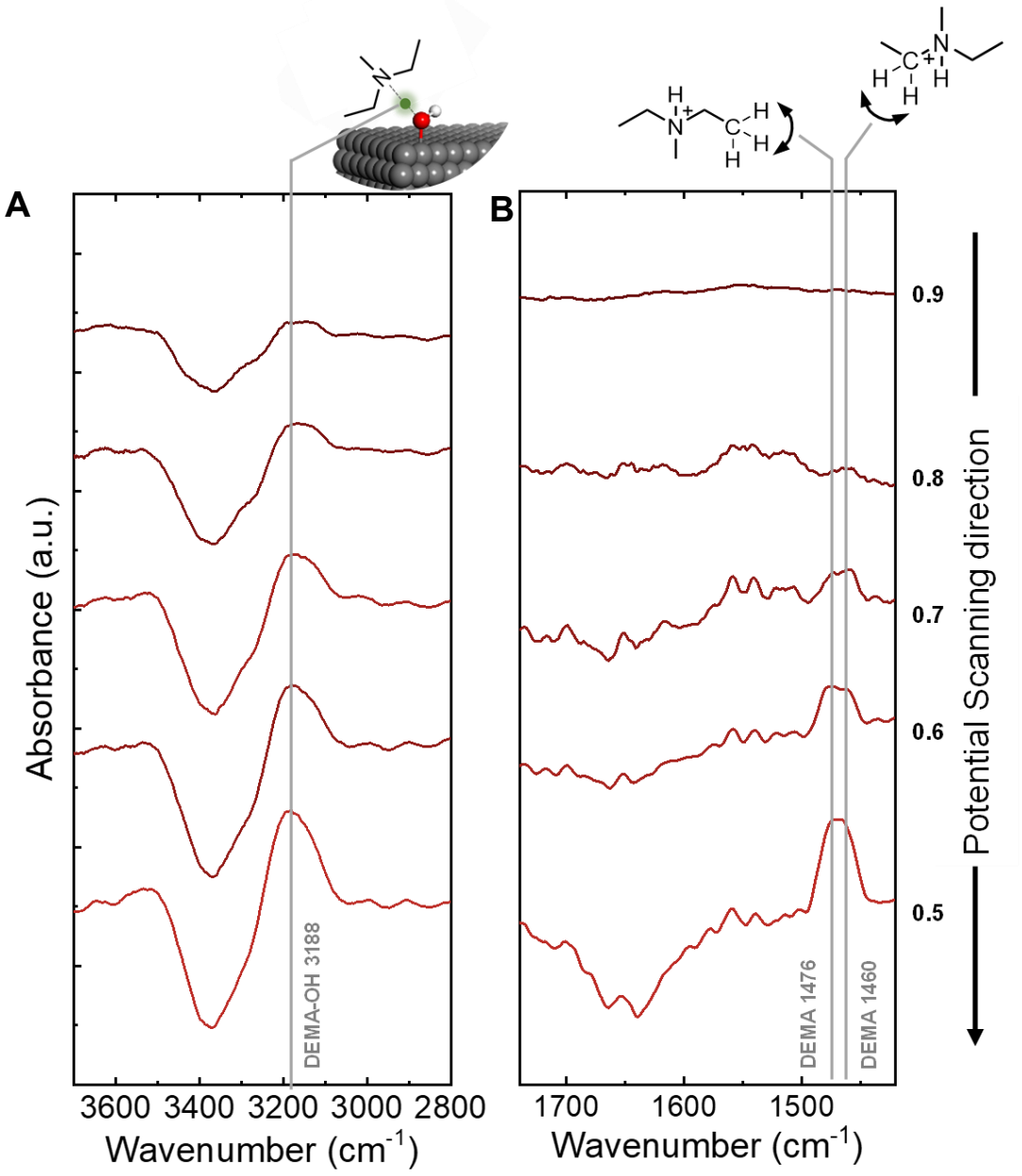

Fig. D-19 *In-situ* ATR-SEIRAS measurement on a [DEMA][NTf_2]-modified Pt electrode in oxygen-saturated 0.1 M $HClO_4$. (A) X-H (X=N, O) stretching region, the molecular schematic represents the H-bond specie formed between $[DEMA]^+$ and OH (B) H-C-H bending region were obtained during potential steps swept from 0.5 V_{RHE} to 0.9 V_{RHE} in 0.1 M $HClO_4$. The cumulative number of 256 was used at a 4 cm^{-1} resolution. Spectra were subtracted with respect to a reference spectrum obtained at OCV in 0.1 M $HClO_4$.

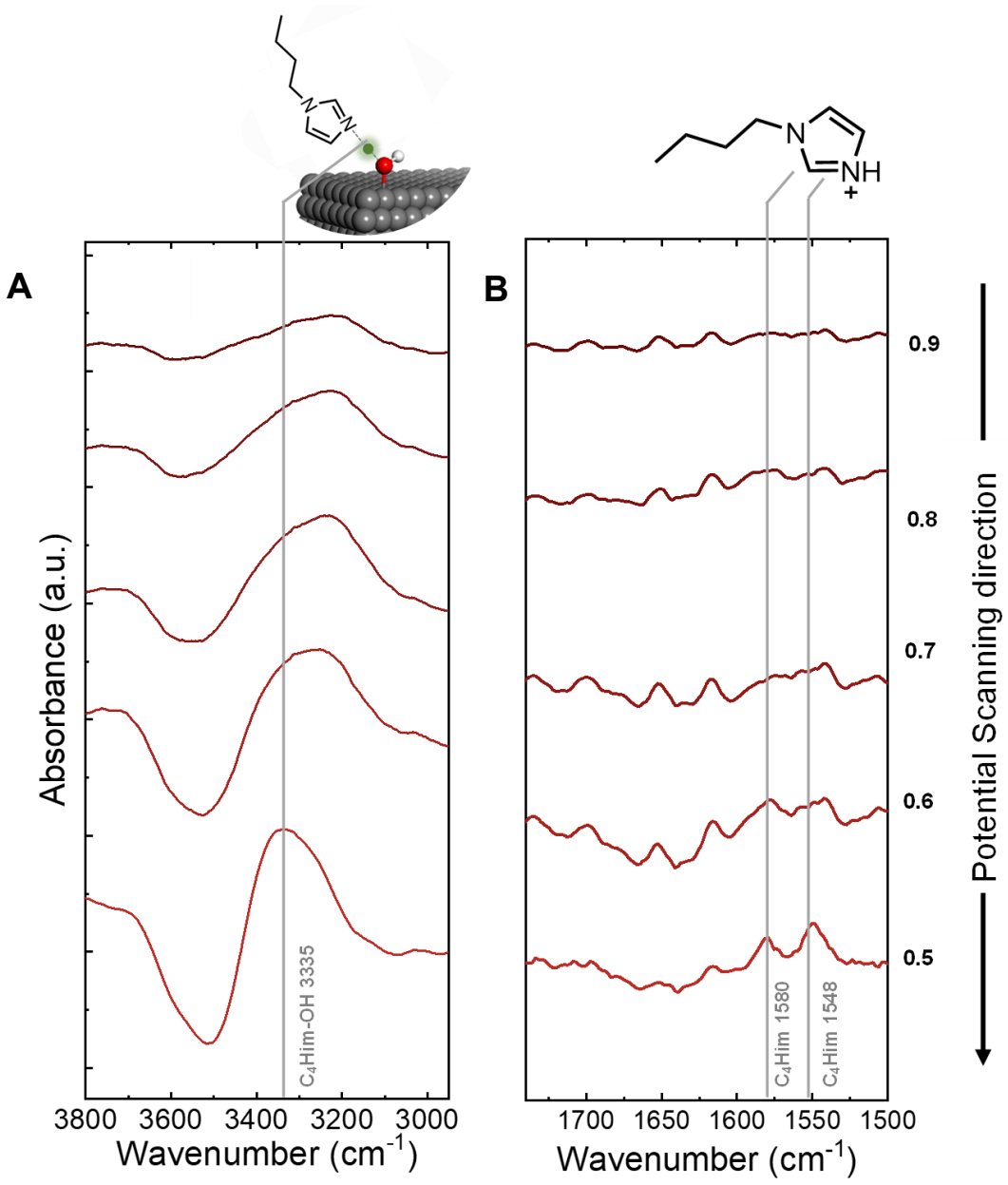

Fig. D-20 *In-situ* ATR-SEIRAS measurement on a [C_4Him][NTf_2]-modified Pt electrode in oxygen-saturated 0.1 M $HClO_4$. (A) X-H (X=N, O) stretching region, the molecular schematic represents the H-bond specie formed between $[C_4Him]^+$ and OH; (B) C=N stretching region were obtained during potential steps swept from 0.5 V_{RHE} to 0.9 V_{RHE} in 0.1 M $HClO_4$. The cumulative number of 256 was used at a 4 cm^{-1} resolution. Spectra were subtracted with respect to a reference spectrum obtained at OCV in 0.1 M $HClO_4$.

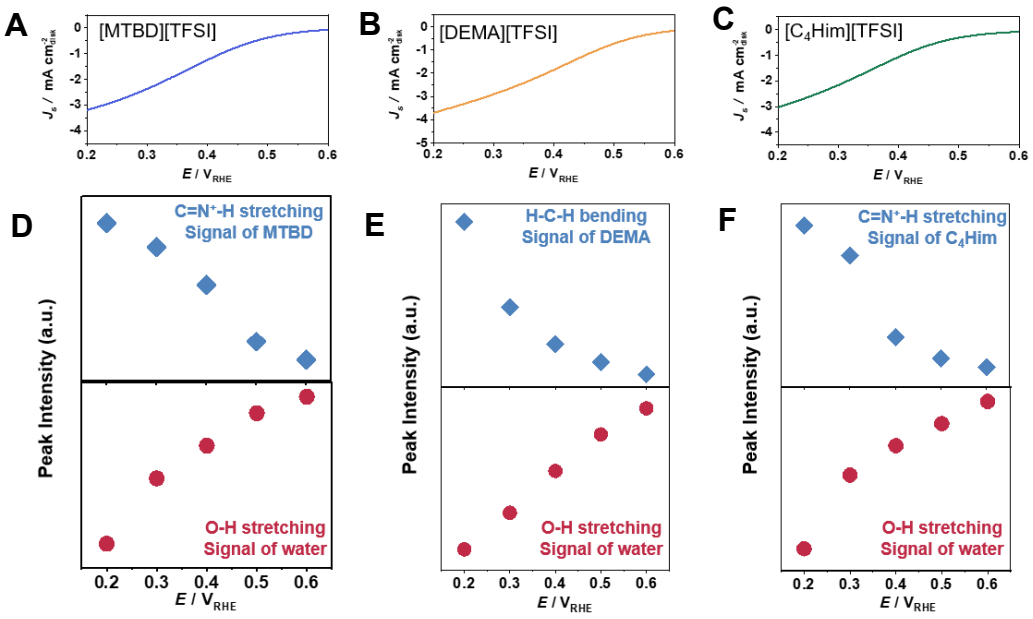

Fig. D-21. (A-C) ORR polarization curves of [MTBD][TFSI], [DEMA][TFSI] and [C_4Him][TFSI] measured in O_2-saturated 0.1 M $HClO_4$, with a scan rate of 10 mV/s and the rotation speed is 1600 rpm; **(D-F)** the IR peak intensity of cations (blue) and water (red) at ORR relevant potentials. The cumulative number of 256 was used at a 4 cm^{-1} resolution. Spectra were subtracted with respect to a reference spectrum obtained at OCV in 0.1 M $HClO_4$.

Table D-2. The simulated and experimental stretching frequency for H-bonded species formed between protic cations ($[MTBD]^+$, $[DEMA]^+$ and $[C_4Him]^+$) and ORR intermediates/products. The spectra of X-H (X=N, O) stretching region of [MTBD][NTf_2]-modified Au, [DEMA][NTf_2]-modified Au, [C_4Him][NTf_2]-modified Au, [MTBD][NTf_2]-modified Pt, [DEMA][NTf_2]-modified Pt and [C_4Him][NTf_2]-modified Pt were depicted in Fig. 5-3. *In situ* ATR-SEIRA measurement on an ionic-liquid-modified Au and a Pt electrode in 0.1 M $HClO_4$. The spectra were acquired at 0.2 V_{RHE} for Au and 0.5V_{RHE} for Pt. The cumulative number of 256 was used at a 4 cm^{-1} resolution.

Au-IL	Frequency/cm^{-1} (Simulated)	Frequency/cm^{-1} (Experimental)
$[MTBD]^+$-OOH	3267	3240
$[DEMA]^+$-OOH	3110	2985
$[DEMA]^+$-HOOH	3204	3024
$[C_4Him]^+$-OOH	3371	3429

Pt-IL	Frequency/cm^{-1} (Simulated)	Frequency/cm^{-1} (Experimental)
$[MTBD]^+$-OH	3198	3089
$[MTBD]^+$-H_2O	3277	3215
$[DEMA]^+$-OH	3253	3188
$[C_4Him]^+$-OH	3332	3335

Table D-3. Summary of water solubility of different ionic liquids and corresponding ORR activity on Au/C and Pt/C. The water solubility was measured by Karl Fischer titration. Error bars represent standard deviations (SDs) of at least three independent measurements.

Cations	C_4C_1im	TMPim	MTBD	DBU	DEMA	TEMEDA	C_4Him
Water solubility (M)	0.49±0.02	0.45±0.03	1.29±0.03	1.25±0.02	1.19±0.02	0.78±0.03	0.59±0.02
ORR Activity on Au (mA cm^{-2})	0.074±0.005	0.078±0.002	0.113±0.013	0.200±0.019	0.237±0.033	0.150±0.015	0.089±0.012
ORR Activity on Pt (mA cm^{-2})	0.426±0.036	0.554±0.045	0.649±0.052	0.508±0.038	0.362±0.033	0.270±0.028	0.177±0.013

Appendix E: Supplementary Data for Chapter 6

Supplementary figures for Chapter 6

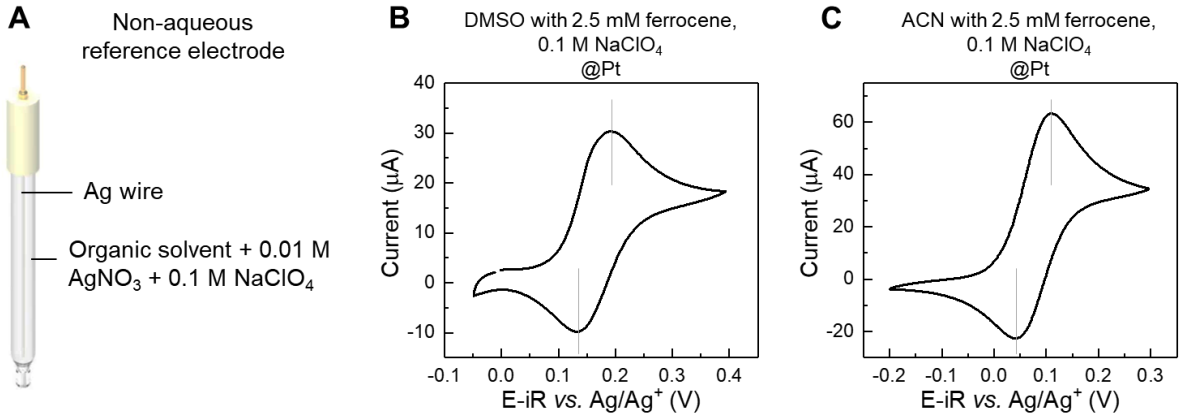

Fig. E-1 Organic reference electrodes and calibration. (A) Non-aqueous reference electrodes consisting of a Ag wire and filling solutions of the organic solvent (ACN or DMSO) with 0.01 M $AgNO_3$ and 0.1 M $NaClO_4$. Calibration of (B) DMSO-based and (C) ACN-based reference electrode using 2.5 mM ferrocene.

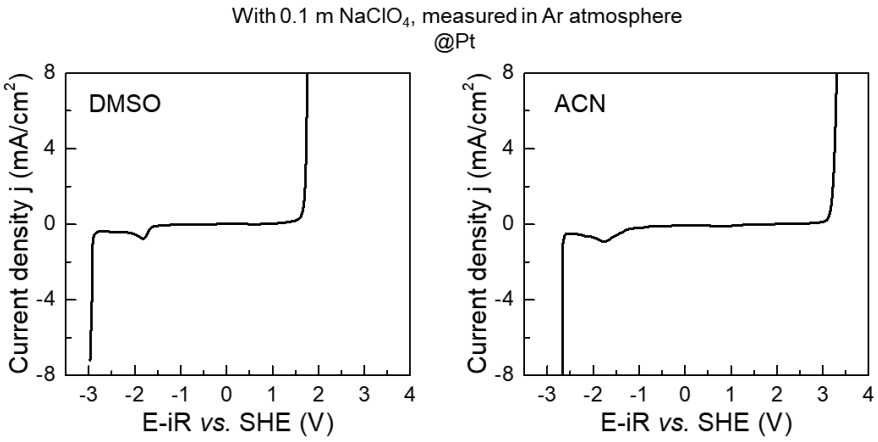

Fig. E-2 Stability of DMSO and ACN on Pt.

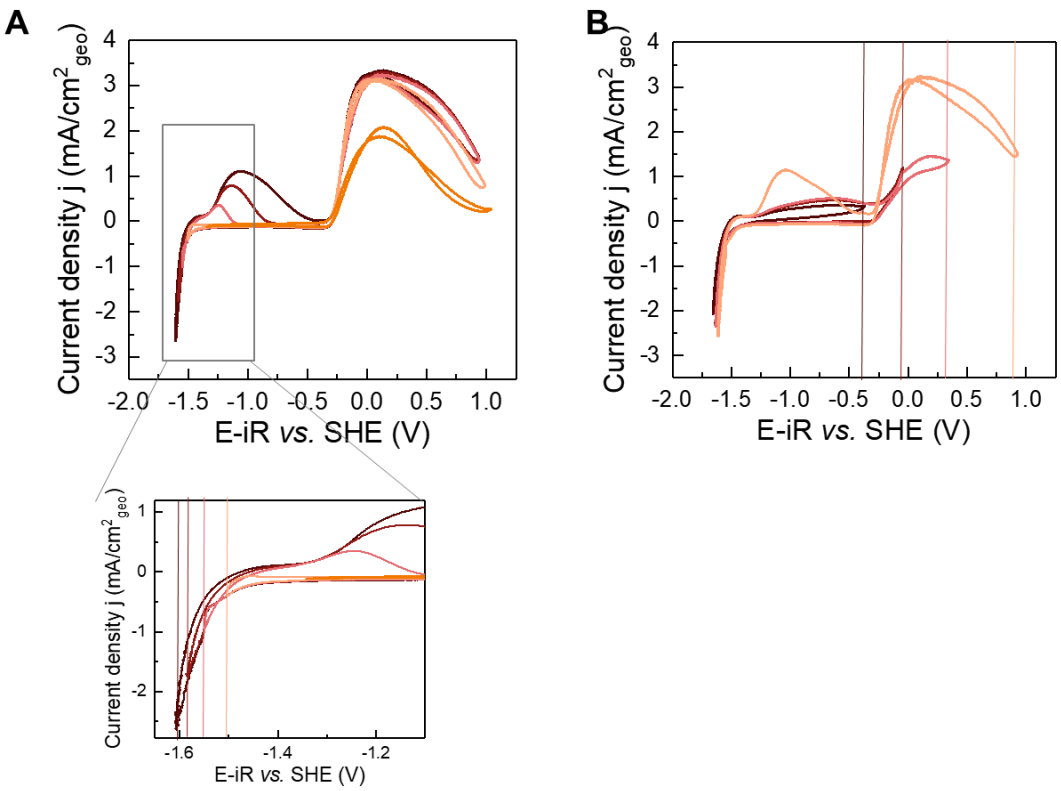

Fig. E-3 CV with different potential cutoffs for water-in-DMSO (H_2O:DMSO=1:40) in a H_2-saturated environment. (A) CV with different lower cutoff potentials ranging from -1.61 V_{SHE} to -1.5 V_{SHE}, with fixed upper cutoff at around 1 V_{SHE}. (A) CV with different upper cutoff potentials ranging from -0.4 V_{SHE} to 0.9 V_{SHE}. Electrolytes contained 0.1 m $NaClO_4$ as conducting ions.

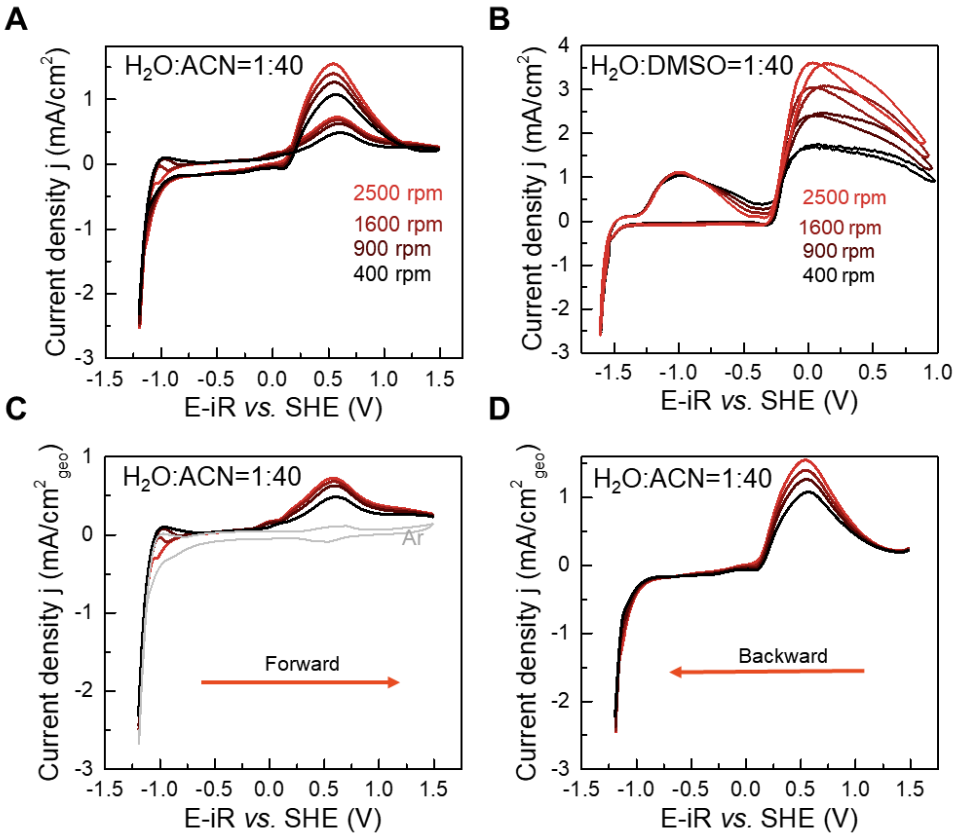

Fig. E-4 Comparison of CV for ACN and DMSO. HER/HOR for (A) H_2O:ACN=1:40 and (B) H_2O:DMSO=1:40 on Pt. (C) Forward and (D) backward scans of the CV of H_2O:ACN=1:40 in (A). Curves were measured at four rotation rates from 2500 rpm to 400 rpm in H_2 gas (red lines), and at 1600 rpm in Ar (grey lines). Electrolytes contained 0.1 m $NaClO_4$ as conducting ions.

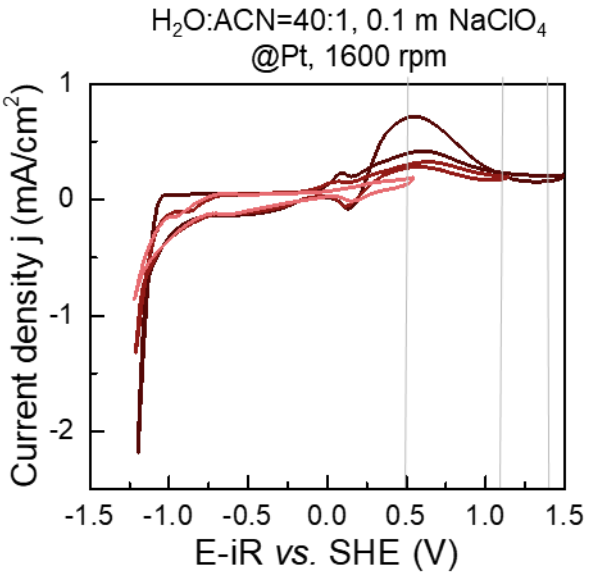

Fig. E-5 CV with different upper potential cutoffs for water-in-ACN (H_2O:ACN=1:40) in a H_2-saturated environment. Electrolytes contained 0.1 m $NaClO_4$ as conducting ions.

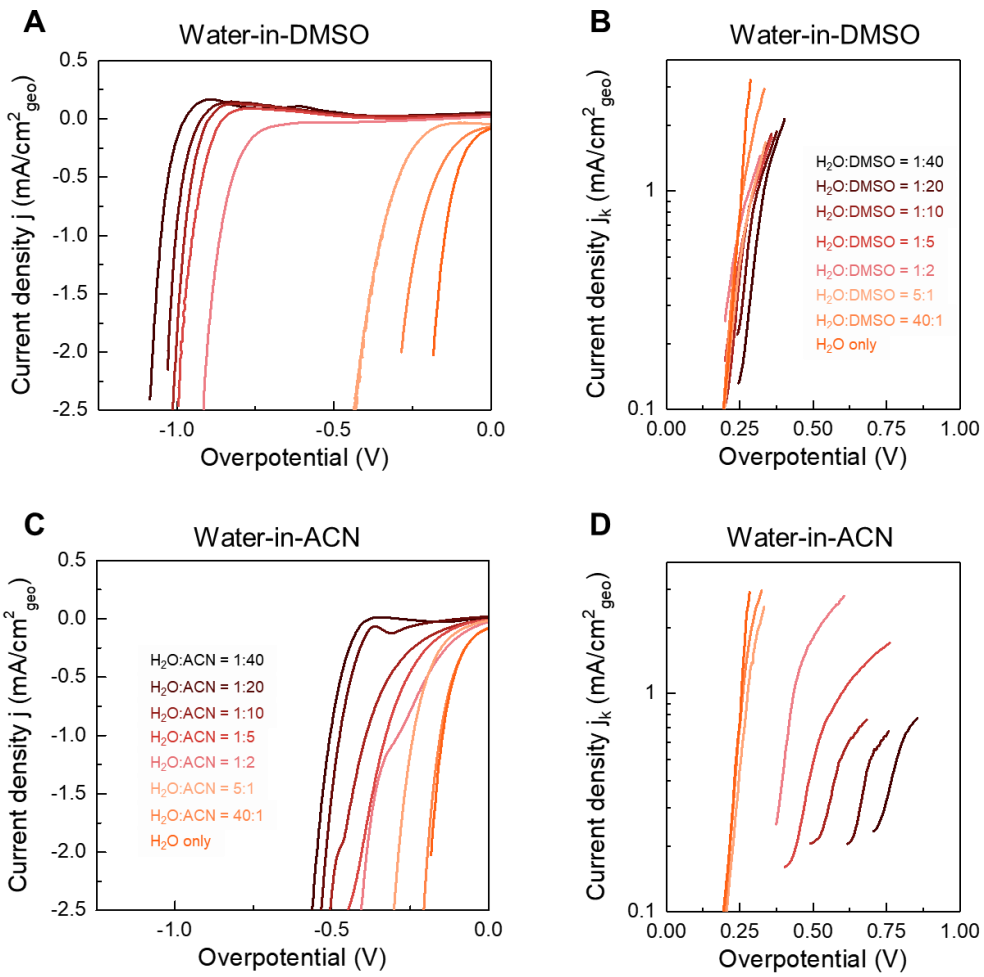

Fig. E-6 Summary of HER/HOR kinetic current densities for water in DMSO and ACN. (A) HER polarization curves and (B) HOR kinetic current densities for water-in-DMSO. (C) HER polarization curves and (D) HOR kinetic current densities for water-in-ACN. HER and HOR were measured in an Ar- and H_2-saturated environment, respectively. Electrolytes contained 0.1 m $NaClO_4$ as conducting ions.